LAGRANGIAN STUDIES OF TURBULENT MIXING IN A VESSEL AGITATED BY A RUSHTON TURBINE: POSITRON EMISSION PARTICLE TRACKING (PEPT) AND COMPUTATIONAL FLUID DYNAMICS (CFD)

by

FABIO CHITI

A thesis submitted to
The University of Birmingham
for the degree of
DOCTOR OF PHILOSOPHY

School of Engineering
Department of Chemical Engineering
The University of Birmingham
December 2007

to my parents

"... e questo sperimento farai con un vaso quadrato di vetro, tenendo l'occhio tuo circa almezzo d'una d'esse pariete; e nell'acqua [...] potrai mettere alquanti grani dipanico, perché mediante il moto d'essi grani, potrai speditamente conoscere il moto dell'acqua conseco che riporta; e che di questa tale esperienza potrai investigare molti belli moti che accaggiano dell'uno elemento penetrato nell'altro..."

(*Delle acque*, Leonardo da Vinci, 1452-1519)

Abstract

Stirred vessels are used in a wide variety of process industries such as fine chemicals, pharmaceuticals, polymers and foods. In order to design efficient mixing vessels, a deep understanding of the blending processes is required. In cases where the fluid is not completely transparent, traditional optical laser based techniques are ineffective. One of the most promising techniques to study opaque systems is based on the detection of a tracer that emits gamma rays. Positron Emission Particle Tracking (PEPT) has been developed at the University of Birmingham and has been used in a wide range of applications including stirred tanks. However, for agitated vessels, any attempt of validation of the PEPT technique versus other techniques cannot be found. Hence, this work aims to validate and explore the potential of Lagrangian data in a well known mixing system such as a standard baffled vessel stirred by a Rushton turbine. As part of the validation, comparison with Eulerian PIV/LDA data has been also undertaken and some underestimation of the high velocities in the system was found in the impeller region. By using a selective interpolation algorithm of the tracer locations, this problem was greatly reduced although a perfect match with optical technique is not feasible.

As further contribution to Lagrangian studies of mixing processes, Computational Fluid Dynamics (CFD) simulations have been undertaken to give both Eulerian and Lagrangian velocities and particle paths. However, it has been shown that traditional approaches to Lagrangian numerical simulation are unable to produce good trajectories that can be compared to experimental data. A novel three-step approach was suggested and implemented in order to achieve good paths, which then have been compared to the experimental trajectories.

Qualitative and quantitative analysis of experimental Lagrangian data showed that the trajectories are erratic and follow random paths; furthermore, frequency analysis applied to portions of trajectories does not reveal any dominant low frequency in the system. Finally, circulation studies were undertaken in order to characterise mixing processes. This focused on tracking the tracer every time it leaves and returns a control volume proving the value of analysing time and return length distributions, since it was possible to compare the circulation times achieved in PEPT with published work. The trajectography approach used in this work is the first attempt at using trajectories from PEPT as a tool to characterise mixing performance rather than only using the data to find Eulerian velocities and vector plots.

Acknowledgments

I wish to acknowledge both my supervisors Drs. Serafim Bakalis and Waldemar Bujalski for their support during my research. I am also thankful to Dr. Ed Wynn for his guidance in the early stages of my project.

A debt of gratitude is expressed to Professor Alvin Nienow for his endless guidance, encouragement and assistance throughout the course of this project.

I am deeply thankful to the financial assistance of Huntsmann, Brussels. Particular thanks must be extended to Dr. Archie Eaglesham for his precious support and advice.

I wish also to acknowledge the advice and assistance of Prof. David Parker and Dr. Xianfeng Fan at the Positron Imaging Centre, School of Physics and Astronomy, without whom the PEPT experimental work would not have been possible.

A special thank to my family, Luciano and Vally, my parents, Michela and Enrico, my siblings, and Sergio for their support and discussion, which often clarified my own thinking. I am also grateful to Sarah for her understanding and especially for her invaluable presence.

Finally, I would like to thank all the friends and colleagues who somehow accompany me during these years: Cristiano, Nicole, Francesco, Alessandra and Giacomo for their friendship, Hamza, Aman, Andrea, Luke, Antonio, Dr. Rachel and Dr. Idoko for the good time in the office and for all the stimulating conversations, and all the others I have met in Birmingham.

Table of Contents

Table of figures

Chapter 1

Introduction

1.1 Background

Stirred vessels are used in a wide variety of process industries such as fine chemicals, pharmaceuticals, polymers and foods. In order to design efficient mixing vessels, a deep understanding of the blending processes is required. Often in these geometries, chemical reactions occur and their efficiency, e.g., the selectivity and quality of products obtained, are limited by mixing issues. Assuring a good blend of the fluids is an important goal of mixing technologies. Despite the extensive use of stirred vessels in industry, the design of vessels is still primarily based on rules of thumb or empiricism: for example, the dimensionless groups such as of flow number, Fl, power number, Po; or scale-up criteria derived from results obtained in lab or pilot scale plant vessels. Regardless of the method used, the prediction of the hydrodynamics of mixing systems and their design is still very hard. The estimated cost to industry for poor initial design results in mixing related problems can be up to 3% of its total turnover, equivalent to \$2–11billion/year. Typical problems recorded include low production rates, high level of commissioning failures and increased downtime for maintenance. Badly affected processes are solid suspension plants where only 60% of plants achieve the design production figures (Butcher and Eagles, 2002).

Most of the techniques available for analysing the flow field generated within a vessel stirred by an impeller work on transparent media: Particle Image Velocimetry and Laser Doppler Anemometry are two techniques able to detect the velocities of seeding particles that follow the fluid motion. In cases where the fluid is not completely transparent, these laser based techniques are ineffective (e.g. Ducci and Yianneskis, 2005; Yoon *et al.*, 2005). Conductivity methods have been largely used when optical

techniques failed in order to achieve bulk information on the mixing performance in stirred vessels. A chemical dye is injected in the vessel and its diffusion or reaction with other reagents is tracked by means of several probes positioned around the vessel (amongst the pioneers, Holmes *et al.*, 1964). Basic Lagrangian techniques, developed for opaque systems, are based on recording the passages of a flow follower through certain regions. Radio and magnetic followers and aerial detection systems are commonly used for this type of study; however, only statistical information (visits per unit of time) around the aerials are achieved through these methods and the full description of the fluid dynamics of the system is still not achieved, as is extensively shown by Schmitz, 1996.

Finally, the most promising techniques to study opaque systems are based on the detection of a tracer that emits gamma rays. Computer-Automated Radioactive Particle Tracking (CARPT) and Positron Emission Particle Tracking (PEPT) are the main two techniques (Stellema *et al.*, 1998). Out of the two techniques, PEPT has been shown to be the most effective and the number of applications spreads from dry to liquids systems. Concerning dry systems, the technique has been validated for multiple cases such as: rotating drums (e.g. Cox *et al.*, 2003), fluidised and spouted beds (Parker *et al.*, 1997; Wong, 2006) and solid mixers (Kuo *et al.*, 2005; Tran *et al.*, 2006). PEPT has been also used for several liquid systems; Fairhurst *et al.*, 2001, studied high solid concentration flows in horizontal pipes tracking nearly neutrally buoyant particles. Furthermore, studies on solid suspensions and non-Newtonian fluids homogenisation in stirred vessel have been investigated by the means of the PEPT technique (e.g. Fangary *et al.*, 1999; Fangary *et al.*, 2002; Fishwick *et al.*, 2003; Fishwick *et al.*, 2005). However, in all these cases, any attempt of validation of the PEPT technique cannot be

found; in fact, most of the work published report that the system can track particles at velocities of $2m/s$ with an accuracy of $0.5mm$ and a frequency of $50Hz$ (e.g. Barigou, 2004) regardless of the fact that those capabilities are related to dry systems. When the tracer is immersed in a liquid, the gamma rays emitted are absorbed by the media surrounding the particle. For this reason, the assessment of the PEPT technique in liquid systems is needed.

1.2 My contribution

The main aim of this thesis is to assess the use of the PEPT technique in turbulent stirred liquid system. For such a demanding case, the generic developments of Parker *et al.*, 2002, have been assumed to be directly applicable. Thus, it is necessary to validate the technique for this application and to find what its limits of operability are. In addition, most of the published work is limited to the use of PEPT as a method to 'watch' inside opaque systems and thus translating Lagrangian data into Eulerian velocity information. Hence, this work also aims to explore the potential of Lagrangian data, firstly by studying the best way to determine Lagrangian velocities and then how to compare mixing processes based on different trajectories within the system. Nevertheless, as part of the validation, some comparison with Eulerian PIV data is also undertaken.

As a further contribution to Lagrangian studies of mixing processes, some Computational Fluid Dynamics (CFD) simulations have been undertaken to give both Eulerian and Lagrangian velocities. The Eulerian velocities have been used to simulate the tracking of a neutrally buoyant tracer and its trajectories have been compared to the

experimental measurement. The comparison of particle tracking data from CFD and experiment is novel.

Finally, as initially this study intended to quantify mixing in 'new' ways, in addition to the use of the PEPT technique, a compartmental model based on the resolution of the complex system of linear differential equation via the Eigenvalues approach is presented as a mathematical novel approach to determine mixing times. However, because it did not seem very fruitful compared to the PEPT approach, it is only reported in an Appendix (Appendix C) because it is considered to still have some potential for describing mixing quantitatively in new ways.

1.3 Thesis layout

The thesis is a summation of the all work that has been carried out since January 2005 on an experimental and numerical study of the Lagrangian characterisation of mixing in stirred vessels agitated by a Rushton Turbine. In Chapter 2 an overview of the basic concepts associated with mixing processes are explained together with a review of all the principal Eulerian and Lagrangian experimental methods used to study the hydrodynamics of stirred vessels. In Chapter 3 a theoretical review of the numerical methods available for Computational Fluid Dynamics (CFD) simulations and the methods used to calculate the flow and a power number are described. Furthermore, the equations used by the CFD codes to resolve Lagrangian tracking are also reported and explained. Chapter 4 gives full details of the equipment used, the other measurement techniques employed for this work as well as the details of the computational methods adopted in the numerical simulations. In Chapter 5, Chapter 6 and Chapter 7, all the results of this project are reported. Chapter 5 reports the validation of the Positron

Emission Particle Tracking technique applied to turbulent stirred vessels. An in-depth analysis of the parameters and the routines used to achieve the raw PEPT data is explained; successively, the test and optimisation of the routines used to find Lagrangian velocities is illustrated before reporting on the effect of tracer size, vessel size and viscosity on the technique results. Chapter 6 is concerned with CFD where a comparison between two types of meshes and two turbulence models is reported. In addition, the limitations relative to different methods of Lagrangian particle tracking obtained with the Ansys-CFX code are shown and an attempt to overcome them is proposed and explained in detail. Chapter 7 shows different ways to compare experimental and numerical Lagrangian particle tracking results; furthermore, it explores the use of trajectories to characterise homogenisation processes. Finally, in Chapter 8, Conclusions and Recommendations for Future Work in this field are given.

Chapter 2

An Introduction to Stirred Tanks and a Review of the Relevant Literature

2.1 Flows in stirred vessels

The flow pattern in a stirred tank is one of the most important considerations for industry as it affects the mixing performance in many ways in both continuous and batch mixing processes. The fluid motion inside the tank is achieved by using an impeller of which a large variety are used in industry, giving different flow patterns and hence uses. Some impeller common types are shown in Figure 2-1. Any impeller used in a cylindrical vessel produces a strong tangential swirling flow, with, depending on the impeller used, more or less weak radial and axial components (Dong et al., 1994). With turbulent flow, in order to interrupt the swirling motion and associated vortex at the surface of the fluid, and to achieve stronger radial and axial flows, the use of vertical strip baffles (typically four, each of width about 0.1 of the vessel diameter) is principally employed (see Figure 2-2). The introduction of these baffles leads to three

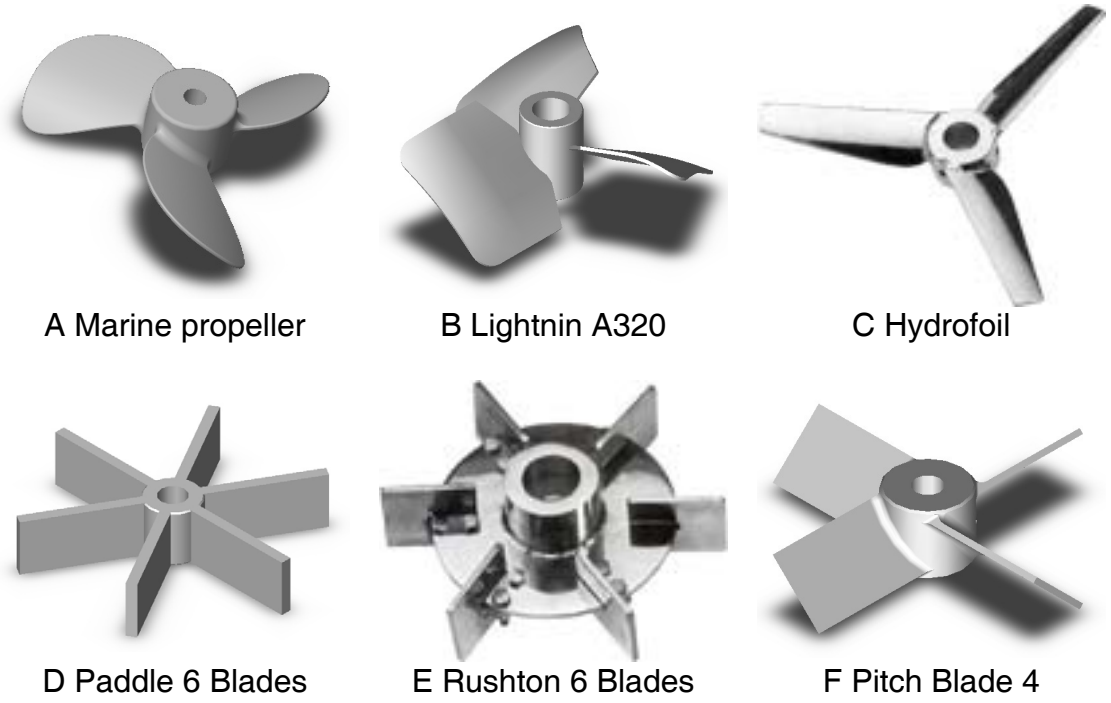

Figure 2-1: Some commonly used impellers (Courtesy of Post Mixing website)

main type of flows depending on the impeller type: (i) Radial flow, e.g. produced by the Rushton disc turbine (Figure 2-1E) and 6-blade paddle (Figure 2-1D); (ii) Axial flow, e.g. produced by the marine propeller (Figure 2-1A) or different forms of hydrofoil impellers (Figure 2-1B and C); (iii) or Mixed flow, e.g. produced by the pitched blade turbine (Figure 2-1F).

2.2 Mean flow patterns

2.2.1 Radial discharge flows, e.g. Rushton Turbine

Typical Rushton turbine (RT) has six flat blades (see Figure 2-1E) which produce a strong spinning radial flow. The flow field generated by this type of impeller has been extensively studied by means of LDA and PIV measurement techniques (e.g. Yianneskis et al., 1987; Stoots and Calabrese, 1995; Schäfer et al., 1997; Lee and Yianneskis, 1998; Ng, 1998; Sharp and Adrian, 2001). The radial flow associated with the swirling motion of the fluid, reaches the walls of the vessel and, by the effect of the vertical baffles, deflects in an upwards and a downwards separated flows creating two

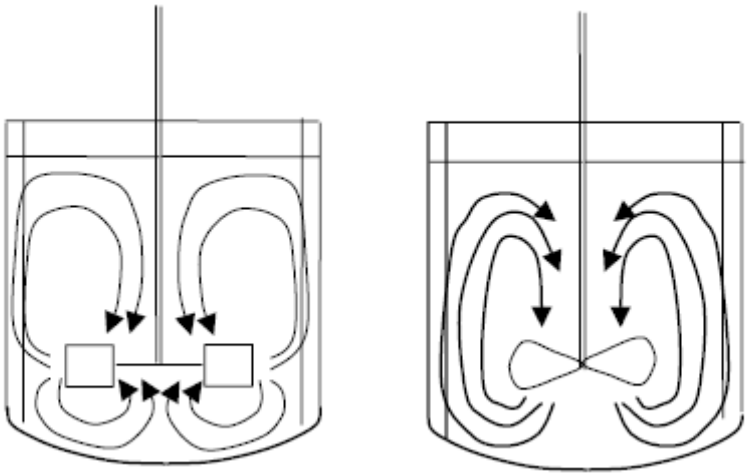

A) Radial flow pattern B) Axial flow pattern

Figure 2-2: Common flow patterns observed by various impellers (Harnby et al., 1985)

loops, as shown in Figure 2-2A. If the impeller off-bottom distance is reduced, the downwards loop may disappear, generating a much larger loop in the region above the impeller.

2.2.2 Axial discharge flows, e.g. Marine propeller or Hydrofoils

For this type of impeller, only one principal single loop is generated. Figure 2-2 shows the flow pattern induced by a down-pumping marine propeller or hydrofoil, the latter having largely replaced the former because of their lower fabrication cost and weight. The impeller jet is direct towards the bottom of the vessel, which deflects the flow outwards toward the walls of the tank. The fluid rises along the baffles, which break the swirl, to the surface. To maintain the mass balance of the vessel, the fluid has to move inwards towards the shaft region and finally it completes the loop back to the impeller.

Power consumption for this type of impeller is lower than for the Rushton turbine of the same diameter at the same speed. Furthermore, the axial flow towards the bottom of the vessel makes this impeller suitable for solids suspension. Compared to other impellers, literature for marine propeller applied to stirred vessel is quite limited (amongst the most recent Winardi and Nagase, 1991), but that for various hydrofoils is more extensive (e.g. Jaworski *et al.*, 1996; Mishra *et al.*, 1998; Nienow and Bujalski, 2004).

2.2.3 Mixed flow, e.g. Pitched Blade Turbine

A compromise between the two previous types of impeller is the so-called mixed flow impellers or pitch blade turbine (PBT). In this type of impellers, the blades are angled with respect to the vertical, typically at between 30° and 60°, and thus generate both an axial and a radial component, where the extent of each depends on the pitch of the blades. This type of impeller produces generally a principal single loop that extends to

the whole volume of the vessel. However, the geometry of the impeller and the distance from the bottom largely affect the flow generated by this type of turbines (Kresta and Wood, 1993a). Finally this type of impeller can be used either in down or up pumping configurations (Jaworski *et al.*, 2001).

Mixed flows impeller have been studied by numerous researchers, e.g Kresta and Wood, 1993a, 1993b; Hockey and Nouri, 1996; Nouri and Hockey, 1998; Schäfer *et al.*, 1998; Wu *et al.*, 2006; Simmons *et al.*, 2007.

2.3 Power number

The power drawn by a rotating agitator is one of the most important parameter for the design of mechanically agitated vessels and for the understanding of all of the mixing processes undertaken within them. Although the recent literature gives specific details for the power drawn for many impellers, the most generally accepted research on power consumption was undertaken during the 1950's, where it was shown that (2.1):

$$P \propto N^3 D^5 \tag{2.1}$$

where the power drawn P is related to the impeller diameter D and the rotational speed N. As explained by Bates *et al.*, 1963, a dimensional analysis can be obtained from Navier-Stokes equation of motion, and shows that:

$$F = \left(\frac{\rho v L}{\mu}, \frac{v^2}{Lg}, \frac{\Delta p}{\rho v^2} \right) = 0 \tag{2.2}$$

where v is the characteristic velocity; L the characteristic length, Δp is the pressure difference; μ is the fluid dynamic viscosity and ρ is the fluid density.

The first dimensionless group in equation (2.2), is the Reynolds number, Re, and represents the ratio of inertial forces to viscous forces. Substituting L with the diameter

of the impeller, D, and v with ND ($\propto \pi ND$, the tip speed of the impeller) where N is the impeller rotational speed, the Reynolds number can be written as:

$$Re = \frac{\rho N D^2}{\mu} \tag{2.3}$$

The group v^2 / Lg is known as Froude number, Fr, and represents the ratio of inertial to gravitational forces, which for impellers becomes N^2D/g.

Last term of equation (2.2), $\Delta p / \rho v^2$, represents the ratio of pressure differences producing flow to inertial forces. For mixer, Δp is related to power consumption since the pressure distribution over the impeller blades could be integrated to give torque acting on the impeller. In fact, the power can be calculated directly from the total torque and the rotational speed of the impeller as follows:

$$P = 2\pi NM \tag{2.4}$$

where P is the power draw and M is the shaft torque. It can also be shown that Δp and power are related by

$$\Delta p = \frac{P}{ND^3} \tag{2.5}$$

which gives the power number, Po, as the last group of equation (2.2):

$$Po = \frac{P}{\rho N^3 D^5} \tag{2.6}$$

For usual standard geometries stirred with a Rushton turbine, it has been found that a graph of Po against the Re has the shape shown in Figure 2-3. This curve can be divided into three different sections: the first at very low Re, where Po is inversely proportional to Re, is typical of the laminar region, with increasing Re the regime is considered transitional, and at high Re, turbulent flow is established, where Po is constant independent of Re.

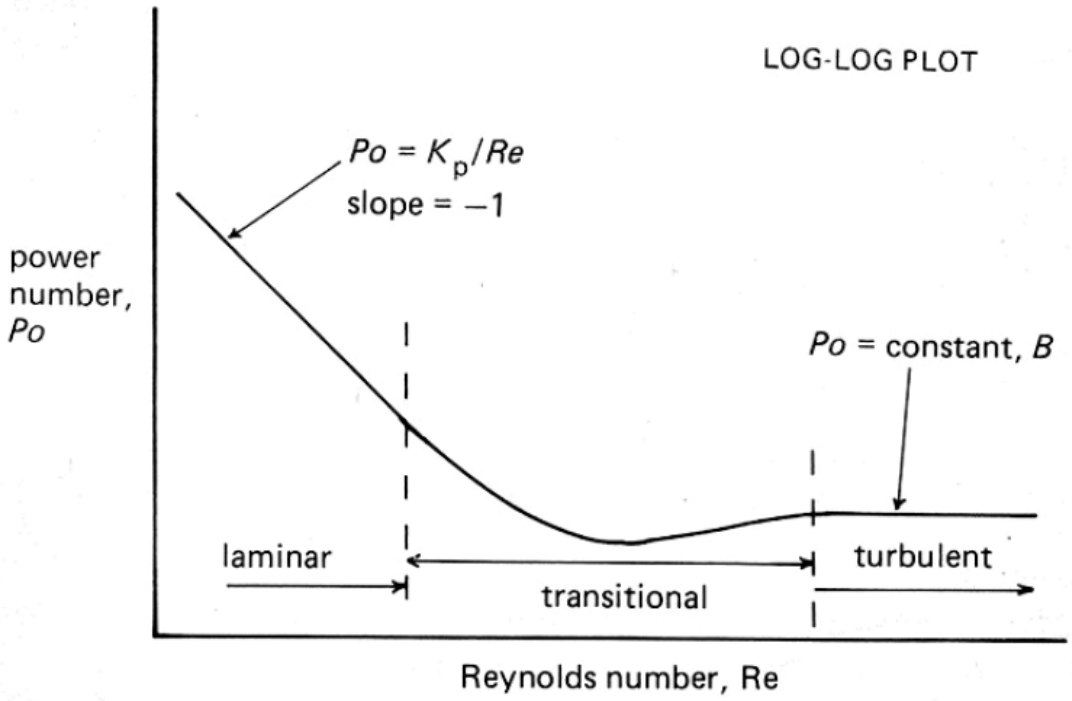

Figure 2-3: General characteristic of Power number curve versus Re number for a Rushton turbine in a stirred vessel (Harnby et al., 1985)

The absolute values of *Po* are strongly dependent on the impeller type and even relatively small changes in dimensions and position in the vessel, whilst the minimum in the transitional region is only found with the Rushton turbine.

2.4 Flow number

The turbine in a Newtonian liquid of low viscosity resembles a centrifugal pump and Q_p, the pumping capacity, is used to measure the impeller discharge. A number of theoretical and experimental models have been proposed to evaluate the pumping capacity for different types of impellers but the calculation is usually done using experimental results (Costes and Couderc, 1988a; Nienow, 1997). The radial velocity profile in a stirred tank reactor with Rushton impeller is shown in Figure 2-4 and *Qp* can be calculated from it by Equation (2.7) (where r is impeller radius and z is the

height of the blade) and the dimensionless flow number, Fl, for that impeller of diameter, D, can be obtained from Equation (2.8),

$$Q_P = 2\pi r \int_{-z/2}^{z/2} v_r dz \tag{2.7}$$

$$Fl = \frac{Q_p}{ND^3} \tag{2.8}$$

The flow number and the ratio of it to the power number can provide useful information regarding the liquid circulation in a stirred tank of a given geometry.

2.5 Circulation times

The fluid flow circulated by the impeller and its effectiveness in producing mixing/blending has been frequently investigated in order to help understand mixing processes. Bryant, 1977, introduced the technique of using a tracer emitting a radio signal and then tracking it. By using a neutrally buoyant plastic sphere ($2mm$) with a radio transmitter inside, it is assumed that it will act as 'an element of labelled fluid'. An aerial able to detect the signal emitted by the radio pill was introduced in the vessel; hence, each time the tracer passes in the proximity of the aerial, a signal is generated.

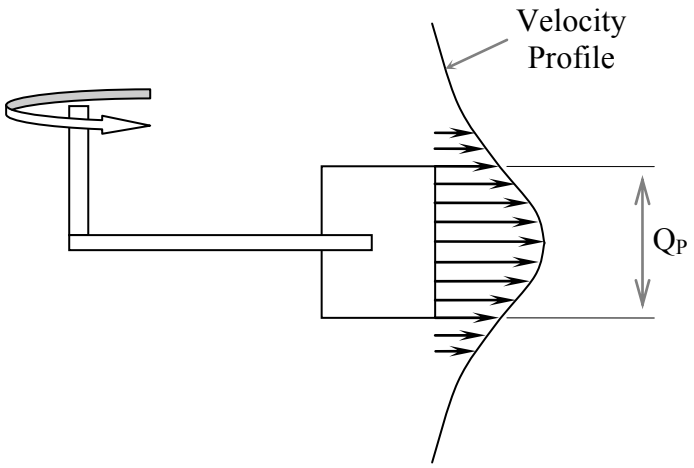

Figure 2-4: Definitions of flow rate, Q_P, for determining the flow number

This signal was then amplified by an external receiver and each passage is recorded on a data logger on a paper tape. The aerial was usually positioned around the impeller in such way that it was possible to monitor the time between consecutive visits and determine the impeller circulation time. Bryant and Sadeghzadeh, 1979, also suggested that the distribution of the circulation times could be approximated with a log-normal distribution, which can be expressed as:

$$f(t) = \frac{1}{\sqrt{2\pi\sigma_l^2}} \frac{1}{t} e^{\frac{-(\ln(t)-\mu)^2}{2\sigma_l^2}} \tag{2.9}$$

where t is the normalised circulation time, μ is the logarithmic mean and σ_l is the logarithmic standard deviation; which can be converted in terms of normalised values of mean and standard deviation to

$$\begin{aligned} \bar{t} &= e^{\left(\mu - \frac{\sigma_l^2}{2}\right)} \\ \sigma^2 &= \mu \cdot e^{\left(\sigma_l^2 - 1\right)} \end{aligned} \tag{2.10}$$

Bryant and Sadeghzadeh, 1979, actually applied the radio follower technique to a fully baffled tank (1 m^3 of volume) stirred by a Rushton turbine (D=T/3) at a clearance of $T/3$. The fluid used was water and each experiment was conducted until about 1500 circulations were obtained. Furthermore, the effect of gas aeration was investigated at different impeller speed leading to the conclusion that mean circulation time and standard deviation proportionally decreased with increasing air flow rate, while they are also directly proportional to the reciprocal of the impeller speed.

Middleton, 1979, using the same radio pill technique, studied the effect of vessel scale on return time distributions. In his work, the author investigated also two different positions of the impeller varying its clearance from the bottom ($C=T/2$ and $C=T/3$). Overall it was shown that mean circulation times were inversely proportional to the

impeller speed and are function of the T/D ratio as well as the volume of the tank. From the experimental results, the following empirical expression was obtained:

$$\bar{t} = 0.5V^{0.3}\left(\frac{T}{D}\right)^3\left(\frac{1}{N}\right) \qquad (2.11)$$

where V is the liquid volume [m^3], N is the impeller speed [rps], T and D are the diameters of the tank and the impeller, respectively. In these papers, the dimensions of the tracer detection zone as a function of the diameter of the impeller was also given. It was shown that the detection region consisted of a toroid with height= D/3, of inner diameter= 11/12 D, of outer diameter= 19/12 D and positioned at the impeller plane.

Van Barneveld *et al.*, 1987a, 1987b, also used radio follower in a large tank, in this case, equipped with two Rushton turbines. Distributions for the two impellers were obtained by means of using separated aerials for both the impellers. Experiments were carried out in water and in polymer solutions in order to compare circulation times and their distributions as a function of viscosity.

Another similar technique employs a magnetic follower. The method was introduced by Mukataka *et al.*, 1980, with a magnet inserted in a hollow plastic sphere of diameter equal to 5mm, adjusting the weight in order to make the pill neutrally buoyant. The technique is based on the basic principle of the generation of an induced current by a gradient in the surrounding magnetic field. The signal generation was acquired by a copper coil used as an aerial inside the vessel, induced by the movement of the magnetic pill. When the fluid follower passed close to the aerial, a current was induced where the strength of the current depended on the distance from it and the velocity of the pill.

The technique was developed and then applied to the study of Non-Newtonian fluids such as paper pulp (Mukataka *et al.*, 1981) or xanthan gum solution (Funahashi *et al.*, 1987). Mukataka *et al.*, 1981, measured circulation times in a stirred vessel equipped with dual impellers and presented a model describing the rate of fluid exchange between the upper and lower regions. Distributions achieved from the upper and lower impeller (the authors used two different aerial for each impeller) were the same for most of the experiments carried out. Funahashi *et al.*, 1987, used the magnetic flow follower in a flat-bottomed vessel stirred by a Rushton turbine (D=T/2) placed at a height equal to T/2 from the bottom. The fluids used were water and shear thinning solution of xanthan gum (0.9% - 4.6%). The authors found that the circulation times resulted in bimodal distribution, which could be explained by the use of a model consisting of a micromixer around the impeller with a high shear rate and a macromixer with a lower shear rate away from the impeller.

Furthermore, the magnetic flow follower was used also by Roberts *et al.*, 1995, who used the method to investigate the effect of impeller and tank scale on circulation time distributions in stirred vessels. In order to verify the reliability of the technique, they also made video recordings of smaller spherical acrylic flow followers plus laser Doppler anemometry. The authors correlated mean circulation time, $\bar{t}$ [s], with impeller speed, N [rps], by:

$$\frac{1}{\bar{t}} = 1.56\left(\frac{D}{T}\right)^2 N \qquad (2.12)$$

where D/T is the ratio between the impeller and the vessel diameters. The authors also confirmed that the circulation time distributions obtained with this technique have a bimodal shape and they suggested that longer circulation times were occurring when the

pill remained trapped in the eye of either the upper or lower circulation loop before returning to the aerial region.

Finally, Schmitz, 1996, applied the radio and magnetic follower techniques to Newtonian and non-Newtonian fluids. For both methods, mean circulation times and standard deviations were found to be inversely proportional to impeller speed. However, the use of the radiotracer was unsatisfactory for viscous and non-Newtonian fluids because it was unable to penetrate zones with low shear rates and therefore high apparent viscosity. He suggested that this was because its diameter was too large. He then adopted the magnetic follower and found that the circulation times achieved by using the magnetic tracer were higher than those obtain with the radio pill, because of the different volumes for the detection region for the two methods. Evidently, the size of the tracer, thus the ability to follow the fluid, and the calibration of the sensitivity of the signal detection, thus the definition of the detection areas, are very important factors influencing the results from the radio and magnetic follower techniques

2.6 Single phase turbulent mixing techniques

Having discussed in the previous Sections the main aspects of mixing covered in this thesis, there is need to distinguish between the different techniques available to describe the flow field developed in a stirred tank. In particular, for the study of the fluid dynamics of a single phase inside a turbulent vessel as undertaken here, it is possible to distinguish techniques based on an Eulerian reference frame or a Lagrangian reference frame.

2.6.1 Eulerian techniques

The Eulerian reference frame is a way of looking at fluid motion that focuses on specific points in the space through which the fluid moves. This concept can be visualized as sitting on the bank of a river and watching the water pass your location. Accordingly to the proportion of space observed, these flow mapping techniques are split into two categories: single point and whole flow field measurements. The former provides velocity values at one specific measurement point and are typically continuous in time; the latter leads to the acquisition of a velocity flow field over a portion of space, usually as an instantaneous distribution of velocity across a plane.

Typical examples of single point flow measurements used in a mixing vessel are the Pitot tube (Wolf and Manning, 1966), hot-wire anemometry (e.g. Cooper and Wolf, 1968) and laser Doppler velocimetry (e.g. Yianneskis *et al.*, 1987). The first to be used for characterising stirred vessels was the Pitot tube. It consists of a device able to measure the difference between the total pressure and the static pressure in a certain position. Since these two variables differ only by the dynamic pressure (i.e. $\frac{1}{2}\rho u^2$), it is possible to calculate the value of velocity in a specific point. Particular attention must be given to the measurements of high turbulent flows where the velocity fluctuation might affect the static pressure measurement, thus the final value of the velocity.

Figure 2-5 shows a diagram of a typical Pitot tube. It consists of two concentric pipes that are connected to an external manometer able to register the differences in pressures between the two pipes. The inner one facing the flow direction measures the total pressure of the flow, while the outer channel is used to measure the static pressure in the system. The Pitot probe has to be as small as possible in order not to affect the flow and thus to acquire true velocities. Different Pitot tube probes with multiples holes are

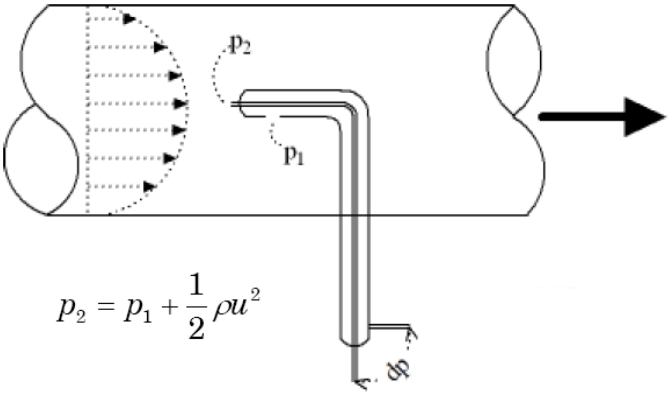

Figure 2-5: Scheme for Pitot Tube

available to measure velocities in different directions at the same time. They are subject to error when the tube is not aligned to the direction of flow. However, it can be useful for measuring velocities in solid-liquid, gas-liquid or gas-liquid-solid dispersions, where the bubbles and/or solid particle motion may interfere with other liquid-velocity determination techniques.

The second technique extensively used to measure velocities in stirred vessels is hot-wire (HWA) or hot-film anemometry, HFA (Cooper and Wolf, 1968; Gunkel and Weber, 1975; Bertrand and Couderc, 1985). Each consists of a probe, which measures the rate of cooling of an electrically-heated wire or film element with very low heat capacity. When the fluid flows past the heated element, changes in its velocity lead to variations of the heat loss which can be interpreted as a measure of the velocity. Due to the tiny size of the wire, it is fragile and thus HWA is suitable only for clean gas flows. However, in liquid flow, a HWA is used which is a platinum hot-film coated on a 25 ~ 150 *mm* diameter quartz fibre or hollow glass tube, as shown in Figure 2-6. Due to the electrical base of this technique, it gives a quick response in measurements of unsteady flows. Since the probe's electric resistance is relative to the temperature of the wire or film, the frequency of acquisitions depends on the heat capacity and the geometry of the

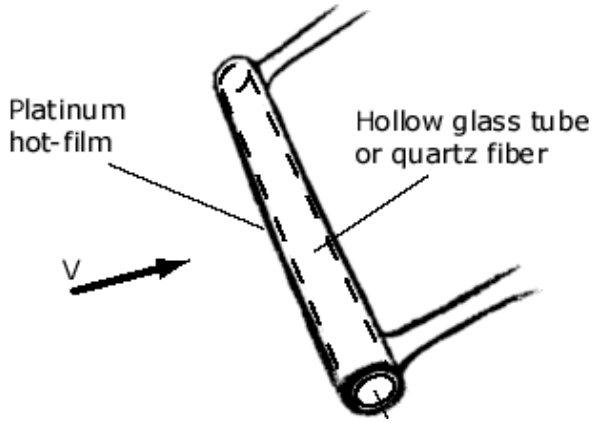

Figure 2-6: Schematic diagram of Hot-Film Anemometry

probe, being typically up to 10kHz. As in the previous method, the main limitation for this technique is the intrusive nature of the probe, which could locally influence the flow. Finally, the velocity measured using them is also highly affected by the orientation of the probe and its alignment with the flow.

More recently, experiments involving transparent media with laser techniques such Laser Doppler Anemometry (LDA) (also known as Laser Doppler Velocimetry, LDV) or Particle Image Velocimetry (PIV) have been developed. With LDA, laser beams illuminate a portion of the flow, and the light scattered from seeded particles in the flow is collected and processed. In practice, using a Bragg cell, a single laser beam is split into two equal-intensity beams, which are focused in the 'probe volume' (typically few millimetres). The light intensity at the beam intersection is modulated due to interference between the laser beams. This produces parallel planes of high light intensity, so called fringes (Figure 2-7). The fringe distance d_f is defined by the wavelength of the laser light, λ, and the angle between the beams, θ, as shown in Equation (2.13):

$$d_f = \frac{\lambda}{2\sin(\theta/2)} \tag{2.13}$$

Flow velocity information comes from light scattered by tiny "seeding" particles carried in the fluid as they move through the probe volume. The scattered light contains a Doppler shift, the Doppler frequency, f_D, which is proportional to the velocity component perpendicular to the bisector of the two laser beams. This relationship allows calculation of the velocity, v, of all the particles which pass trough the using Eq (2.14):

$$u = f_D \frac{\lambda}{2\sin(\theta/2)} \tag{2.14}$$

The data acquisition rate depends on the number of seeds present in the system and LDA can record velocities with frequencies up to $3kHz$.

In most of the applications, it is important to determine a velocity flow field rather than determining the value of velocity at a single point. To achieve that result, multiple

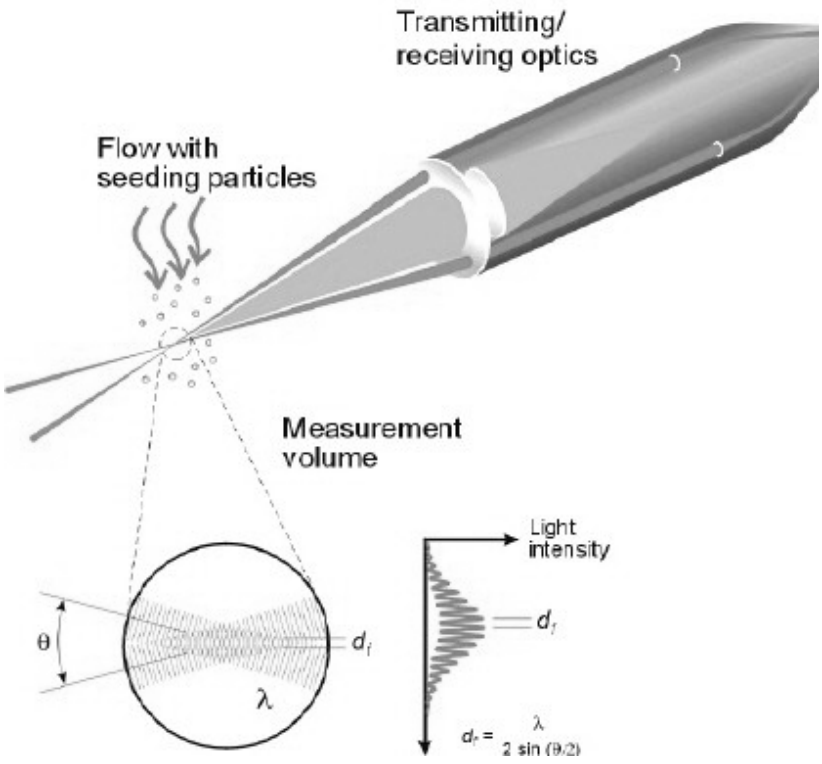

Figure 2-7: Schematic diagram of the principles used in LDA. With courtesy of Dantec Dynamics.

measurements have to be taken assuming that the fluid dynamics of the system does not change with time. The LDA technique has been extensively applied to stirred vessel to determine the flow field for a large number of applications and geometries (e.g. Ranade and Joshi, 1966; Van Der Molen and Van Maanen, 1978; Costes and Couderc, 1988a, 1988b; Wu and Patterson, 1989; Kresta and Wood, 1993a; Dong *et al.*, 1994). However, the main limitation to its use is the essential condition that the vessel and fluid must be transparent. The two phase systems liquid-gas and solid-liquid are really difficult to study with this technique though some work has been reported (Guiraud *et al.*, 1997; Haam *et al.*, 2000; Svensson and Rasmuson, 2004).

The technologies HWA/HWF and LDV mentioned so far, despite providing single-point measurements with a really good temporal resolution and quick response, do not offer the opportunity to obtain instantaneous information on the flow field and its velocity gradients across a significant portion of the flow. For a broader picture of the fluid velocity and the overall flow pattern, the Particle Image Velocimetry (PIV) technique has more recently been developed and applied to stirred tanks (La Fontaine and Shepherd, 1996). This technique permits spot and instantaneous velocity to be measured over an extended region of the flow. PIV systems measure velocity by determining particle displacement over time using a double-pulsed laser technique. A laser light sheet illuminates a plane in the flow, and the positions of particles in that plane are recorded using one or two digital cameras. After a known small fraction of time, Δt, another laser pulse illuminates the same plane, creating a second image of the same particles. Since particle images are in separate frames, every image is subdivided in a grid of cells, which are analysed by image software giving the particle displacement for the entire flow region observed. Figure 2-8 shows how the vectors have been

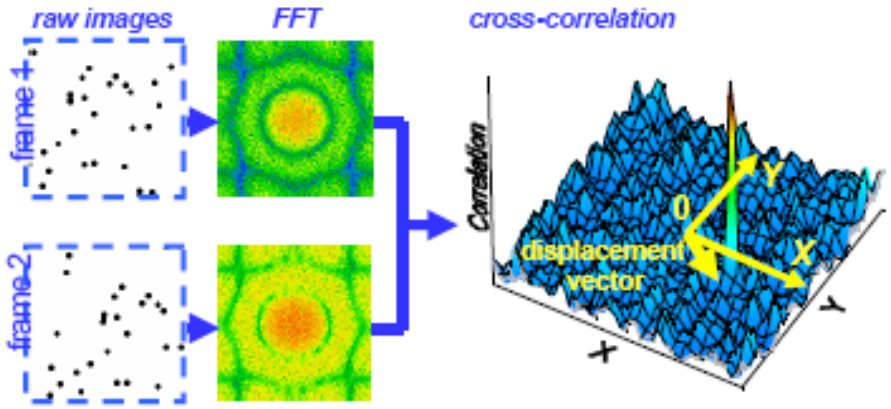

Figure 2-8: Software principles for particle displacements determination when using PIV

calculated by the analysis of the cells. If the particles in the flow field move by an amount Δx, in the x-direction, and Δy, in the y-direction, and the velocities in the x and y directions are u and v respectively, then:

$$v_x = \Delta x/\Delta t \quad \text{and} \quad v_y = \Delta y/\Delta t \tag{2.15}$$

Depending on the system to be analysed, several parameters need to be set before measurements are taken in order to achieve good results. These include, for example, the seeding density, the delay time between the two frames, number of pairs of images and collection frequency of the pairs of images.

2.6.2 Lagrangian studies

The Lagrangian reference frame is a way of looking at fluid motion where the observer follows individual fluid particles as they move through space and time. Plotting the position of an individual particle through time gives the pathline of the particle. This approach can be visualized as sitting in a boat drifting down a river. Only a few Lagrangian studies of stirred tanks have been reported and these are all fairly recent and include video trajectography (Wittmer *et al.*, 1998), computer-automated radioactive particle tracking (CARPT, Rammohan *et al.*, 2001) and positron emission particle

tracking (PEPT, Hawkesworth *et al.*, 1986). In all these cases, a neutrally density particle with respect to the liquid is tracked which it is assumed follows the liquid flow.

Video trajectography, as the name suggests, consists of the visualisation of a particle trajectory by the use of Charge-Coupled Device, CCD, cameras. In order to track the motion of a particle in three dimensions, the use of two or more synchronised cameras is necessary. The images collected by the cameras are then sent to a computer for image analysis that includes the subtraction of a background image, thresholding and object recognization, as well the conversion from pixels to linear dimensions. Despite the use of modern computers, the image processing and particle identification for all the frames is very time consuming. Furthermore, the size of the particle has to be sufficiently large, typically about 1.8 mm diameter, to allow it to be distinguished from the background image. Being an optical based technique, its other main limitation is the difficulty in obtaining a clear image without reflections on flat surfaces and with a good light contrast between the particle and the background (Pitiot, 1999).

The CARPT technique tracks a single radioactive particle labelled with radioactive scandium, ^{46}Sc, emitting γ radiations employed as the isotope. During the experiment, an array of 16 scintillation detectors monitors the γ radiation emitted by the particle, which is moving in the vessel following the liquid phase. The radiation intensity recorded at each detector decreases exponentially with increasing distance between the particle and the detector. In order to locate the spatial position of the tracer, calibration of the system is achieved by positioning the tracer at various known locations. Once the distance of the particle from the set of detectors is evaluated, a weighted regression scheme is used to estimate the position of the particle at a given sampling instant in time. By differentiating the successive particle positions, the instantaneous Lagrangian

velocities can be calculated as a function of time and position of the particle. From the Lagrangian particle velocities, ensemble averaging can be performed to calculate the average velocities. According to the developer of this technique (Rammohan *et al.*, 2001), due to the finite size of the particle (2.3*mm* in diameter), it is not possible to capture the true and fine-scale liquid turbulence. Thus, the big size of the tracer is probably the main limitation of this technique. However, it does not require transparent fluids and container and it can be used in multi-phase systems.

Similarly to CARPT, Positron Emission Particle Tracking is a non-invasive technique for following the motion of a single radioactively labelled tracer particle in any vessel and any media however complex. The technique is based on positron emission tomography, now widely used in medicine. Its application to engineering equipments was pioneered at Birmingham University by Hawkesworth *et al.*, 1986, and Parker *et al.*, 2002. According to the different type of experiment, tracer particles (down to 60μm) can be produced either by irradiating them directly or by adsorption of irradiated water onto the surface of the particles. In both the referenced cases, the type of irradiation consisted of a beam of ^{3}He ions from the Birmingham Radial Ridge Cyclotron, which converts oxygen to the radionuclide ^{18}F. In this isotope, a proton is converted to a neutron (n), a positron (a positive electron, β^{+}) and a neutrino (ν). This positron rapidly (essentially immediately with respect to the scale of the process being monitored) annihilates with a surrounding electron producing a pair of collinear back-to-back γ-rays photons, which carry equal and opposite momenta (511 *keV*), as shown in the following scheme:

$$\begin{aligned} p &\rightarrow n + \beta^{+} + \nu \\ \beta^{+} + e^{-} &\rightarrow 2\gamma \end{aligned} \qquad (2.16)$$

γ-rays are able to penetrate considerable thicknesses of material allowing the tracer to be detected through opaque equipment. The pair of γ-rays is detected using a "positron camera" consisting of two large rectangular detectors (600x300mm), operating in coincidence so that an event is recorded only if γ-rays are detected on both detectors within a resolving time of 12ns (Parker et al., 2002). For each event, the tracer particle must lie close to a line connecting the points on each detector where the pair of back-to-back γ-rays is detected within the resolving time of the system. Therefore, the particle position can be reconstructed by triangulation from a selected number of γ-ray pairs by minimising the distance between all the lines (see Figure 2-9). This triangulation process is iterative, which allows the elimination of those γ-rays that have been corrupted; for example, some of the detected γ-rays might have been scattered or two γ-rays coming from separate annihilation events might generate random coincidences within the same resolving time. All such events would lead to reconstructed paths far from the tracer position. The data obtained are then processed to give tracer position (x, y and z) as a function of time (t).

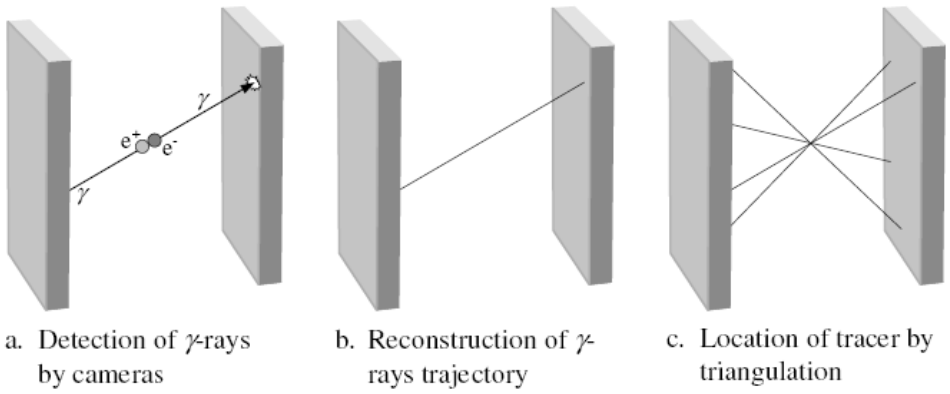

Figure 2-9: Algorithm scheme for location reconstruction

Chapter 3

Computational Fluid Dynamics modelling

Computational fluid dynamics (CFD) is one of the branches of fluid mechanics that uses numerical methods and algorithms to solve and analyze problems that involve fluid flows. Computers are used to perform the millions of calculations required to simulate the interaction of fluids and gases with the complex surfaces used in engineering. Software that can accurately and quickly simulate complex problems such as turbulent flows are an ongoing area of research. Most CFD codes use one of three approaches: the finite difference (FD), finite element (FE) or finite volume (FV) methods of which the latter two are most widely used. A detailed description of the FD, FE and FV methods is available in the literature (Anderson *et al.*, 1995). However, the finite volume methods are usually faster and have achieved the ability to model almost any type of geometry. Finite element methods, on the other hand, can create additional mesh structures and new element types for specific cases.

However, all the simulations in this work have been carried out using the commercial code, Ansys CFX 10, which is based on the finite volume method. This FV based software that CFX uses is similar to that employed by many of its competitors such as Fluent (despite the fact that recently Fluent has also become part of CFX's parent company, Ansys), Star-CD, Ocra, etc. Some claimed advantages (e.g. Anderson *et al.*, 1995) of CFD analysis over experimental work are:

- Use of CFD usually leads to a reduction in the time and the cost involved in implementing new designs.
- The analysis of systems that cannot be studied experimentally directly such as industrial scale equipment.

- Higher levels of detail can be obtained using CFD once a simulation has been established than is generally possible experimentally.
- Hazardous conditions can be investigated at or beyond their normal limit.
- Model parameters and geometries can be modified in a very easily and quickly.

On the other hand, CFD modelling requires continuous verification in order to assess the quality of the results and approximations done in order to set the model. In Ansys CFX 10, CFD simulations follow the path described in Figure 3-1.

3.1 Governing transport equations

Assuming an Eulerian reference system on a control volume where the fluid passes through, the mass and energy conservation equations lead to the formulation of the governing transport equations. With the hypothesis that the rates of change of linear momentum along the three directions are equal to the corresponding components of applied force, the fundamental Conservation equations can be written as for fluid flow, turbulence, chemical species transport and heat transfer. Since heat transfer and

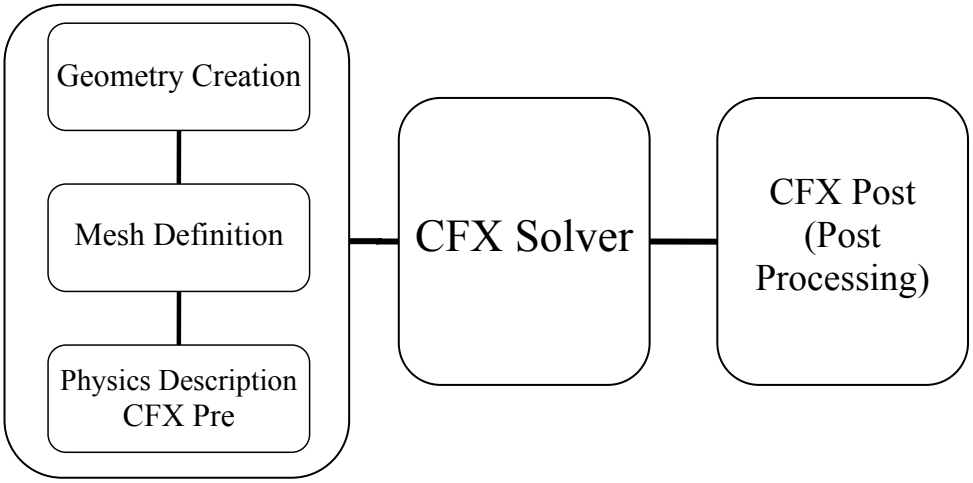

Figure 3-1: General representation of the CFD simulation process

chemical reaction phenomena are not considered in this project, only the equations governing fluid flow are presented.

By considering an arbitrary control volume, the mass conservation of the fluid passing through it can be written as follows,

$$\nabla \cdot (\rho \, \mathbf{v}) = 0 \tag{3.1}$$

where $\mathbf{v}$ is the velocity vector and the density, ρ, is assumed to be constant for incompressible flows as used here.

Equation (3.1) for an arbitrary control volume is a statement of conservation of momentum in each of the three component directions. The three momentum equations are referred to as the Navier-Stokes equations. Several momentum sources are also involved in addition to the momentum transport by diffusion and convection:

$$\frac{\partial(\rho v_i)}{\partial t} + \frac{\partial}{\partial x_j}(\rho v_i v_j) = -\frac{\partial p}{\partial x_i} + \frac{\partial}{\partial x_j}\left[\mu\left(\frac{\partial v_i}{\partial x_j} + \frac{\partial v_j}{\partial x_i} - \frac{2}{3}\frac{\partial v_k}{\partial x_k}\delta_{ij}\right)\right] + \ldots + \rho g_i + F_i \tag{3.2}$$

In equation (3.2), the convection terms are on the left. On the right hand side, the pressure gradient, a source term, which is the divergence of the stress tensor responsible for the diffusion of momentum, the gravitational force and other possible source terms are given.

For laminar flows, the equations governing the conservation of mass and momentum can be solved analytically and used to describe incompressible flows. Turbulence, however, adds complications since fluctuating velocities have to be taken into account; in this case, the calculation effort required to capture the temporal and spatial variation is extremely large since additional turbulence equations are needed.

3.2 Turbulence modelling

In fluid dynamics, turbulence is a flow regime characterized by random fluctuation of the flow field and thus continuous changes on the fluid properties. This flow characteristic results in a higher rate of momentum convection rather than diffusion, and a rapid variation of pressure and velocity in space and time. In the transition from laminar to turbulent flow, the flow behaviour becomes increasingly irregular and random so that the movement of the fluid becomes fundamentally unsteady even under constant imposed conditions. This type of flow can be observed in many industrial mixing processes with respect to the bulk flow, which is unstable and chaotic. Turbulent mixing consists of eddy diffusion at different length scales, leading to more rapid mixing than with laminar flow. Since turbulence is a random phenomenon, the computation based on a complete description of all the fluid elements is unrealistic and extremely demanding of computer power.

In considering turbulence, it is more appropriate to consider the instantaneous velocity at a point in two parts according Reynolds decomposition, a steady mean velocity $\overline{\mathbf{v}}$ with a fluctuating component $\mathbf{v}'(t)$ superimposed on it (Versteeg and Malalasekera, 1995) so that:

$$\mathbf{v}(t) = \overline{\mathbf{v}} + \mathbf{v}'(t) \tag{3.3}$$

By substituting equation (3.3) in (3.2) and taking a time-average of these equations, the Reynolds Averaged Navier Stokes (RANS) equation can be obtained as:

$$\frac{\partial(\rho v_i)}{\partial t} + \frac{\partial}{\partial x_j}\left(\rho v_i v_j\right) = -\frac{\partial p}{\partial x_i} + \frac{\partial}{\partial x_j}\left[\mu\left(\frac{\partial v_i}{\partial x_j} + \frac{\partial v_j}{\partial x_i} - \frac{2}{3}\frac{\partial v_k}{\partial x_k}\delta_{ij}\right)\right] + \ldots + \frac{\partial}{\partial x_j}\left(-\rho\overline{v_i' v_j'}\right) + \rho g_i + F_i \tag{3.4}$$

The new terms appearing in equation (3.4) are named the Reynolds stresses. The role of turbulence models is to close the system of mean flow equations. Direct numerical simulation (DNS) captures all of the relevant scales of turbulent motion, so no model is used at the smallest scales. Since to do this exceptionally fine mesh and huge computer power is needed, this approach is extremely expensive for complex problems even on modern computers. Hence models to represent the smallest scales of fluid motion have been developed to simplify the calculation process. Nevertheless, DNS simulations were carried out by Bartels *et al.*, 2002, where the authors simulated the flow in a vessel stirred by a Rushton turbine and made comparisons with the k-ε model (see Section 3.2.1.1). They compared mean flow patterns and turbulence kinetic energy finding that the DNS results were closer to the experimental values than the standard k-ε turbulence model.

3.2.1 Turbulence models overview

A turbulence model can be considered as a computational procedure for closing the system of mean flow equations so that a wide variety of flow problems can be calculated. Most CFD codes have the ability to model turbulence using the so-called classical models. These include the zero equation mixing length model, two equation k-ε and k-ω models and the Algebraic Stress Model (ASM). Another approach involves using techniques based on space-filtered equations such as the Large Eddy Simulations (LES). LES are turbulence models where the time dependent flow equations are solved for the mean flow and the largest eddies, while the effect of the smaller eddies is modelled. Since it is believed that the largest eddies interact strongly with the mean flow and contain most of the energy, LES results in more accurate predictions of the flow. Revstedt *et al.*, 1998, have published results based on LES in a stirred tank for a

Rushton turbine. They used a three dimensional grid and compared their results with some experimental data obtained by Costes and Couderc, 1988a, highlighting the accuracy of the model versus its high computing power demand, as well as the discrepancies still existing between the predictions and the experimental results. However, at present, the LES technique cannot be used at the University of Birmingham because its computational requirements are too high to be run on local workstation and also because the license for LES simulation is not available onsite. Geurts, 2001, has investigated in depth the role of turbulence models and more details can be found in that work.

3.2.1.1 The k-ε model

According to the literature (e.g. Deglon and Meyer, 2006), the k-ε mode remains the most widely used and validated CFD model and most published simulations for stirred vessel in the turbulent regimes have been undertaken using this model. The model uses two additional transport equations, one for the turbulence kinetic energy, k, and the other for the specific energy dissipation rate, ε, and they must be solved in order to compute the Reynolds stresses. The k-ε model is semi-empirical, based on observations in high Reynolds number flows. For incompressible, high Reynolds number flows, a transport equation to determine k can be written as,

$$\frac{\partial}{\partial t}\rho k + \nabla \cdot (\rho \mathbf{v} k) - \nabla \cdot \left(\left(\mu + \frac{\mu_T}{\sigma_k} \right) \nabla k \right) = P + G - \rho\varepsilon \qquad (3.5)$$

where G is the production of k due to the body forces (buoyancy and turbulence) and P is the shear production with each being defined respectively by,

$$G = -\frac{\mu_t}{\rho\sigma_\rho} g \cdot \nabla\rho$$
$$P = \mu_t \nabla\mathbf{v} \cdot \left(\nabla\mathbf{v} + (\nabla\mathbf{v})^T\right) - \frac{2}{3}\nabla \cdot \mathbf{v}(\mu_t \nabla \cdot \mathbf{v} + \rho k) \quad (3.6)$$

Similarly, the ε equation is,

$$\frac{\partial}{\partial t}\rho\varepsilon + \nabla \cdot (\rho\,\mathbf{v}\,\varepsilon) - \nabla \cdot \left(\left(\mu + \frac{\mu_T}{\sigma_\varepsilon}\right)\nabla\varepsilon\right) = C_1 \frac{\varepsilon}{k}(P + C_3 \max(G,0)) - \ldots$$
$$- C_2 \rho \frac{\varepsilon^2}{k} \quad (3.7)$$

In words, the equations can be described as,

Rate of change of k or ε	+	Transport of k or ε by convection	=	Transport of k or ε by diffusion	+	Rate of production of k or ε	-	Rate of destruction of k or ε

The C_1, C_2, C_3, σ_k and σ_ε are empirical constants. Since the C_3 is for buoyancy and here it is set to zero by default.

The turbulent viscosity, μ_T is derived from k and ε,

$$\mu_T = \rho C_\mu \frac{k^2}{\varepsilon} \quad (3.8)$$

where C_μ is also a constant. All these constants have a given default values in Ansys CFX 10 and they are: $C_\mu = 0.09$, $C_1 = 1.44$, $C_2 = 1.92$, $\sigma_k = 1.0$, $\sigma_\varepsilon = 1.3$.

A comprehensive study of the k-ε model carried out by Jenne and Reuss, 1999, suggests that the models need to be optimised with constants from further experimental results to give more accurate predictions of experimental results for stirred tank simulations. They also carried out a comparison with other turbulence models.

To summarise, it can be said that the k-ε model is simple and quite inexpensive computationally to use and has been successful in modelling shear and circulatory

flows. Though it does not provide accurate calculation of Reynolds stresses, it has been shown to be useful in providing mean velocity profiles and the distribution of k and ε spatially in the stirred tank.

3.2.1.2 The RNG k-ε model

The Renormalisation Group (RNG) k-ε model was developed in 1986 to improve on the empirical nature of the standard k-ε mode (Yakhot and Orszag, 1986). In fact, rather than using empirical constants, this method uses statistical methods developed in the area of renormalisation group theory to obtain them. The method is basically similar to the standard k-ε model but in particular it uses a different set of constants for the energy dissipation equation. The new set of constants performs well mainly in regions of high strain; i.e. flows around a blunt body where recirculation might occur. Concerning the turbulent viscosity constant, C_μ, a differential equation is solved, giving a value of 0.0845 for high Reynolds numbers that corresponds well with the value of 0.09 for the standard k-ε model. As a result of these changes, the RNG k-ε is claimed to work well in all turbulent conditions, from high Reynolds numbers down to the transitional regime (Schetz, 1996). In the RNG k-ε model, the energy dissipation equation (3.7) becomes,

$$\frac{\partial(\rho\varepsilon)}{\partial t} + \nabla\cdot(\rho\varepsilon\,\mathbf{v}) - \nabla\cdot\left(\left(\mu + \frac{\mu_T}{\sigma_\varepsilon}\right)\nabla\varepsilon\right) = \left(C_1 - C_{1RNG}\right)\frac{\varepsilon}{k}\left(P + C_3\max(G,0)\right) - C_2\rho\frac{\varepsilon^2}{k} \tag{3.9}$$

The constant C_{1RNG} is given by,

$$C_{1RNG} = \frac{\eta\left(1 - \frac{\eta}{\eta_0}\right)}{1 + \beta\eta^3} \tag{3.10}$$

and η can be written as,

$$\eta = \left(\frac{P_S}{\mu_r} \right)^{0.5} \frac{k}{\varepsilon} \tag{3.11}$$

The additional constants η_0 and β introduced in equation (3.10) have default values 4.38 and 0.015 respectively.

3.2.1.3 The k-ω model

The k-ω model of Wilcox, 1988, includes a low-Reynolds-number extension for near-wall turbulence. This model involves the solution of transport equations for the turbulence kinetic energy k and the turbulence frequency ω. Although the k-ω model is not as popular as the k-ε model, it does have several advantages, namely that:

- the model is reported to perform better in transitional flows and in flows with adverse pressure gradients;
- the model is numerically very stable, especially the low Re version, as it tends to produce converged solutions more rapidly than the k-ε models; and
- the low Re version is more economical and elegant than the low Re k-ε models, in that it does not require the calculation of wall distances, additional source terms and/or damping functions based on the friction velocity.

The main weakness of the k-ω model is that unlike the k-ε model, it is sensitive to the free-stream boundary condition for ω in free-shear flows. Modified variants exist which claim to remove this sensitivity, such as Baseline (BSL) k-ω model or Shear Stress Transport (SST) k-ω model; however, for clarity only the basic k-ω model equations are reported in equations (3.12) and (3.13).

$$\frac{\partial(\rho k)}{\partial t} + \nabla \cdot (\rho \, \mathbf{v} \, k) - \nabla \cdot \left(\left(\mu + \frac{\mu_T}{\sigma_k} \right) \nabla k \right) = P - \beta^* \rho k \omega \qquad (3.12)$$

$$\frac{\partial(\rho \omega)}{\partial t} + \nabla \cdot (\rho \, \mathbf{v} \, \omega) - \nabla \cdot \left(\left(\mu + \frac{\mu_T}{\sigma_\omega} \right) \nabla \omega \right) = \alpha \frac{\omega}{k} P - \beta \rho \omega^2 \qquad (3.13)$$

where P is the production rate of turbulence, which is calculated as in the k-ω model, see (3.10), and the constants used in Ansys CFX 10 are α=5/9, β=3/40, β^*=0.09, σ_k =2 and σ_ω=2. The k-ω model assumes that the turbulence viscosity is linked to the turbulence kinetic energy and turbulent frequency via the relation

$$\mu_T = \rho \frac{k}{\omega} \qquad (3.14)$$

By comparing equations (3.8)and (3.14), it can be seen that ω is also the ratio of ε to k, where ε is the dissipation rate of k.

3.2.1.4 Reynold stress model and algebraic stress model

In the previous two-equation models, the underlying assumption is that the turbulent viscosity is isotropic, i.e. the ratio between the Reynolds stress and mean rate of deformation is the same in all directions. The Reynolds Stress Model, RSM, has a higher level, more elaborate turbulence closure. Hence, it is also called a Second Order Closure. This modelling approach originates from the work by Launder *et al.*, 1975. In RSM, rather than using the eddy viscosity approach, the Reynolds stresses are computed directly. The exact Reynolds stress transport equations take account of the effects of the Reynolds stress fields in all the directions. The Reynolds stress model involves calculation of the individual Reynolds stresses, $\rho \overline{v_i' v_j'}$, using differential transport equations. These individual stresses are then used to obtain closure of the Reynolds-averaged momentum equation. This RSM can be simplified by using the

Rodi assumption (Rodi, 1980), which models the transport of the Reynolds stresses as being proportional to the transport of the turbulence kinetic energy, k, leading to the so called Algebraic Stress Model (ASM).

Bakker and Van Den Akker, 1994, used this approach. They modelled two and three-dimensional grids with two axial and one radial impeller and used the k-ε and the ASM model. Among the conclusions drawn were that the ASM predicted energy dissipation rates 15% higher than the k-ε model and that the single phase flow pattern simulations for stirred vessels can only be successful if the computations are done on a three-dimensional grid and the anisotropy of turbulence is taken into account. However, the ASM and the k-ε models were also compared using two different grid sizes and the results showed that the k-ε model still gave good flow field results in a somewhat shorter computational time than the ASM model.

3.2.1.5 Large eddy simulation model

Large Eddy Simulation (LES) is a numerical technique used to solve the partial differential equations governing turbulent fluid flow.

A common deduction of Kolmogorov's theory of self similarity is that large eddies of the flow are dependent on the flow geometry, while smaller eddies are self similar and have a universal character. For this reason, the LES method explicitly solves the Navier-Stokes' equations for the large eddies only, and, then, it adds the effect of the smaller and more universal eddies on the larger ones using a model. Thus, in LES, the large scale motions of the flow are calculated, while the effect of the smaller universal scales (the so called sub-grid scales) are modelled using a sub-grid scale (SGS) model. The most commonly used SGS model is the Smagorinsky model and it consists of the addition of an "eddy viscosity" into the governing equations.

LES requires less computational effort than direct numerical simulation (DNS) but significantly more than those methods that solve the Reynolds-Averaged Navier-Stokes equations (RANS). The computational demand also increases significantly in the vicinity of walls, and simulation of flows around complex boundaries might exceed even the limits of modern supercomputers. The main advantage of LES over RANS approaches is the increased level of detail it can achieve.

Comparison between the CFD results obtained by RANS and LES were performed in detail in a number of studies on flows in agitated tank. Yeoh *et al.*, 2004b, reported that, when they used LES applying the Smagorinsky model for the sub-grid scales, they obtained better agreement to the experimental results compared to RANS, which gave reasonable predictions only away from the impeller region. Micheletti *et al.*, 2004, also drew similar conclusions and in addition showed that LES was better at predicting the global turbulence energy dissipation rate, ε, than the RANS method. Finally, Hartmann *et al.*, 2004, reported simulations of a flow field generated by a Rushton turbine in a baffled agitated tank. They employed both the LES and RANS techniques. They also concluded that the agreement between the experimental measurements and LES predictions was better than those obtained by RANS, mainly for the turbulence kinetic energy near the impeller region but also for the flow field description.

All these studies have shown that flow fields in stirred vessel can be handled using the CFD methods when appropriate numerical techniques are employed. Nevertheless, there are still cases where simulations are unable to fully predict reality, e.g. complex fluids such as non-Newtonian liquid or multiphase systems. However, those mentioned fluids are beyond the scope of the simulation achieved in this work. In addition, with improving computer performances and technological developments as well as the

improvements in the numerical tools, the upper limit of the Reynolds number ($Re = \rho N D^2 / \mu$) in the computer simulations will be less and less limiting. Finally, the CFD models used have a huge impact on the predictions both qualitatively and quantitatively. For example, the RANS method provides sufficiently accurate results concerning the mean flow quantities. This may be sufficient to assess the effect of the geometry on the velocity field. However, accurate prediction of other flow quantities in stirred vessels, such as turbulence kinetic energy distribution and energy dissipation rate, can still be achieved through computationally very demanding LES and DNS methods.

3.2.2 Turbulence wall boundary conditions

According with physics, at the wall surface, the fluid velocity is zero. In computational fluid dynamics, this requirement is obtained by imposing the so called no-slip condition. The small fluid layer between the wall and the bulk flow is known as a shear layer and, in this case, also a wall boundary layer. The boundary layer is a very complex region characterised by large velocity gradients and diffusion dominated development. To model it precisely, it would necessitate an extremely fine grid. To overcome this problem, an empirical relationship, based on detailed experimental work and called wall function, can be used to describe the shape of the boundary layer so that only few grid cells near the wall are required. Further detail of the exact expression used in Ansys CFX can be found in the manual, Ansys-CFX, 2005.

3.3 Convergence control

Several factors play a crucial role in the convergence of the numerical simulation processes. The factors that can be said to play a significant role in determining

convergence are the residuals and the under relaxation. A brief discussion of these two concepts is given below.

The residual sum of each variable is computed at the end of each iteration. In a control volume, the error can be expressed as R_P,

$$A_P \Phi_P - \sum_{i,neigbours} A_i \Phi_i = R_P \tag{3.15}$$

where A is the area of a cell and Φ can be considered an arbitrary quantity such as mass. The total residual can be expressed as,

$$\sum_{P,cells} R_P = R \tag{3.16}$$

The residual is presented normalised in CFX output to gauge its changing value during the solution process.

Once a differential equation is solved iteratively, the solution makes use of information from the previous iteration. Instead of using the full computed change in variable, it is sometimes beneficial to use only a fraction of the change when several coupled equations are involved, leading to a stable convergence. The process is referred to as under relaxation and the fraction typically ranges from 0.1 to 1.0, depending on the complexity of the flow (turbulent or laminar regime), the variable being solved (pressure or momentum), the solution method being used and the state of the simulation (during the first few iterations or near convergence). A hybrid strategy was adopted in the simulations undertaken in this project. It consists of starting the solution with a small under relaxation, which was then made larger as the problem approached convergence.

3.4 Rotating boundaries in stirred vessels: modelling approaches

The presence of a moving boundary such as a rotating impeller, makes the CFD modelling much more complex than in more simple, stationery geometries. Early models of stirred vessels used two dimensional geometries, based on the assumption of axial symmetry. In those cases, the effect of the moving impeller was simulated by introducing a momentum source, while the presence of baffles was represented by a tangential momentum sink (Pericleous and Patel, 1987; Morud and Hjertager, 1996). The values used for the source-sink approach where taken from time averaged experimental velocity data (Kresta and Wood, 1991).

More recent developments of stirred tank modelling do not use experimental data, but they simulate the effect of rotating impeller by either sliding meshes or multiple frame of reference techniques. More details are given in the following Sections.

3.4.1 Experimental boundary conditions to accommodate the rotating impeller

As mentioned above, until relatively recent time, the most common way of dealing with this problem was to exclude the impeller region from the computational domain, and to replace it either by boundary conditions at its surface or by source terms distributed throughout its volume. The appropriate values were chosen with reference to experimental data and/or to simplified models of the impeller flow, in which the overall geometry of the vessel was neglected. Different variants of this general approach have been proposed, depending on the impeller type (radial versus axial), the availability of experimental data, the flexibility of different computer codes, and, of course, the personal preferences of the various authors.

This two-dimensional modelling was first extended to the three-dimensional case in 1986. Middleton *et al.*, 1986, were the first to carry out full three-dimensional simulations of flows in a stirred tank reactor. They also simulated competitive consecutive chemical reactions and compared the results with experimental data. The method by which empirical boundary conditions were imposed at the impeller boundary was not described in detail. The conclusion drawn was that three-dimensional simulations were necessary in order to predict the reaction yields.

The next development was the use of the so-called 'black box' approach, which has been extensively used. In this method, the impeller region was considered as being bounded by two surfaces as shown in Figure 3-2, one horizontal (Σ_H) and one vertical (Σ_V); profiles of v_r, v_h, k and ε were imposed on both surfaces and the flow equations were not solved in the interior grid nodes of the impeller region. A second, similar approach was also applied (Brucato *et al.*, 1998), where boundary conditions were

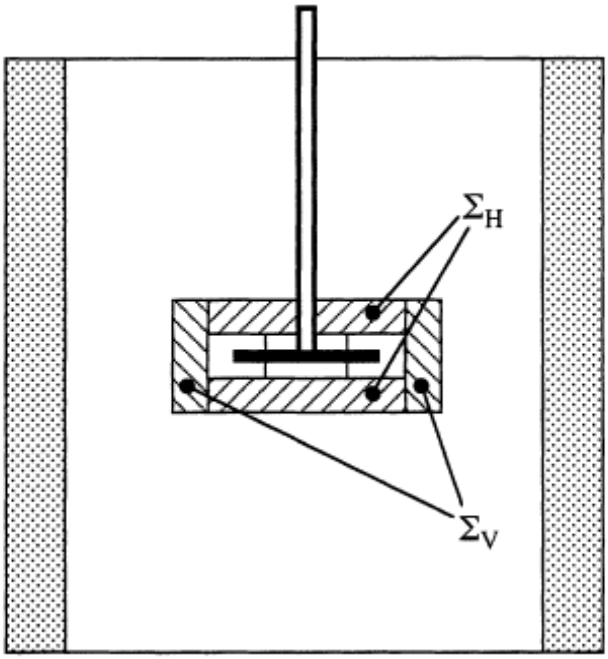

Figure 3-2 'Black box' region bounding the impeller swept region (from Brucato *et al.*, 2000)

imposed only on Σ_V and the equations for all variables were solved in the entire vessel, including in the impeller region. The best results were obtained by choosing the second approach and using empirical data from the authors' own experimental work (Brucato *et al.*, 1998) and from Wu and Patterson, 1989.

The experimental data for the boundary condition methods has usually been derived from LDV or PIV measurements that have also been azimuthally averaged; therefore, the near field flow produced by the particular impeller may also depend on the overall tank geometry and on the choice of the impeller boundary conditions, leading to significantly different flow fields being predicted. Therefore, this approach remains restricted to geometries for which experimental data is available and also for the impeller geometries which proved at the time to be too complex to model.

Some more modern work by Yoon *et al.*, 2001, used a novel procedure to obtain the experimental three component velocity field around the impeller region using stereoscopic PIV. They also attempted to fit with semi-empirical equations the flow induced by the impeller and use these models as boundary conditions for the CFD simulations. The tangential component of the flow was also considered in this approach unlike some other work carried out previously.

3.4.2 Direct computationally-based boundary conditions

The previously mentioned three dimensional approaches based on experimental results to provide the boundary conditions for the flow from the impeller have lead to direct simulation of the impeller and its mutual interaction with the stationary baffles. Out of these different methods that have been used in the past, newer techniques such as the rotating frame of reference, the inner-outer approach, multiple frames of reference

(MFR) and sliding mesh (SM) have been developed; the latter two being are the most used in Ansys CFX 10. All these modelling techniques use explicit modelling of the impeller without the need of any experimental input.

3.4.2.1 Rotating frame model

The rotating frame model uses the entire reactor domain and solves the momentum equations in a rotating frame. In this way, the Coriolis force can be included and solved in the simulations. The impeller is set to rest as it is given a negative angular velocity equivalent to that of the outer frame, which rotates with the rotational speed of the impeller. A different but similar approach is to keep the main domain still and to apply an external rotating wall. Unfortunately, this latter approach is not suitable as the simulation causes the movement of baffles through the liquid which is inappropriate. Thus, this approach is limited in its use.

3.4.2.2 Inner-Outer approach

In this method developed by Brucato *et al.*, 1994, the entire vessel is divided into two domains which partly overlap each other. The inner domain includes the impeller and the outer includes the baffles, as shown in Figure 3-3. The simulation is carried out first in the 'inner' rotating domain with boundary conditions imposed on the outer surface of the dark grey region. As the reference frame is non-inertial, the Navier-Stokes equations are modified to take account of the Coriolis and centrifugal forces. This method also uses an iterative process. A first trial flow field is thus computed in the whole impeller region, including the distributions of velocity, turbulence energy and dissipation on the boundary surface of the light grey region. The result from the simulation in this inner region is then used to compute the flow field in the outer domain. This domain is stationary and the simulation results in the prediction of the

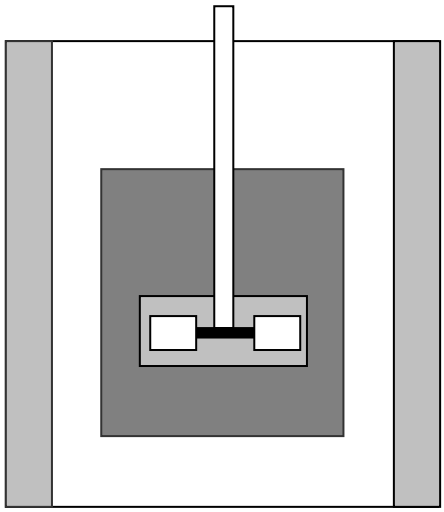

Figure 3-3 Computational regions for inner-outer approach

flow field in the rest of the vessel. The information from the simulation in the outer domain is used for boundary condition for another iteration and the procedure is carried out until the solution for the whole vessel converges.

3.4.2.3 Multiple frames of reference (MFR) approach

This method was developed by Luo *et al.*, 1993, and is based on the solution of the time-dependent form of the governing transport equations in two domains which were fixed to the respective frames of reference; the outer one being stationary and the inner one rotating with the impeller. At the interface, the finite volume mesh was allowed to shear and/or slide to accommodate the relative motion. The choice of the matching interface is not arbitrary and must be in a region where the flow does not change either tangentially or with time. Predictions were presented for a four-baffle tank stirred by a six-blade Rushton impeller for which measurements were available. The agreement with the experiments was better than that obtained by using a steady-state approach and a body-force impeller model. In this method, the impeller is always assumed static.

Therefore, it is not considered suitable for conditions where there is a strong impeller-baffles interaction.

3.4.2.4 Sliding mesh (SM) approach

In this case, developed initially by Tabor *et al.*, 1996 , the flow domain is divided into two cylindrical, non-overlapping sub-domains with each grid as a separate block. The outer one is fixed in the exterior reference frame, while the inner one rotates with the impeller (Figure 3-4). Unlike in the 'inner – outer' and in the MFR methods described above, the flow equations in the rotating sub-domain are formally written with respect to the specific reference frame, while it is the grid that rotates. However, the rotation of the grid results in acceleration terms which are completely equivalent to the body forces arising in non-inertial frames. The two regions are implicitly coupled at the interface separating the two blocks via a sliding-grid algorithm, which takes into account the

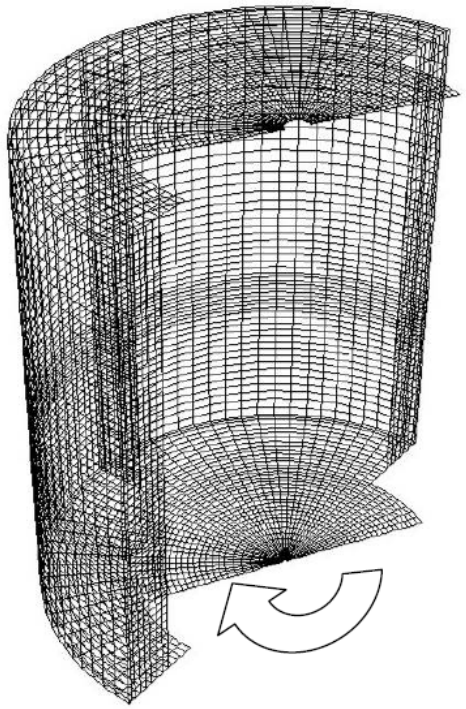

Figure 3-4: The computational grid with sliding mesh. The inner mesh is shown rotating with respect to the outer mesh.

relative motion between the two sub-domains and performs the required interpolations. In this case, simulations can only be conducted in a transient mode.

3.4.2.5 Hybrid MFR + SM approach

Campolo *et al.*, 2003, in their work used the previous two approaches in a joint way. They first obtained a steady state solution using a normal MFR approach and then used this solution to initialise the final SM simulation. Monitoring power input and kinetic energy, they observed that pseudo-steady state is attained after 20 impeller revolutions starting from fluid at rest, and after 5 impeller revolutions starting from the MFR flow field. Since to reach steady state using MFR is much quicker than 15 impeller revolution with SM approach, they estimated that this hybrid approach leads to the same final result in one third of the time needed to undertake a fully sliding mesh simulation.

3.5 Computational requirements

The simulations performed in this thesis have been carried out at the University of Birmingham on a local workstation. In fact, the workstation used was a Dell Precision 650 consisting of a two Xeon Intel processor units of 2.8GHz each, 2Gb of Ram and SCSI Hard Drive for quick storing access. The CFD software, Ansys CFX 10, was installed locally and configured to run in parallel processing if needed.

The number of total iterations carried out during a simulation can be summarised as follows:

$$N_i = Rev \times N_{ts} \times N_{its} \tag{3.17}$$

where N_i is the total number of iterations, Rev is the number of revolutions of the impeller, N_{ts} is the number of time steps in a revolution and N_{its} is the number of iterations in one time step. For example, if the simulation consists in resolving the

geometry every 5 degrees, N_{ts} assumes a value of 72, then the usual number of iteration per step is set to 10 and a minimum of 10 whole impeller revolutions are needed to stabilise the flow leading at a final value for N_i equal to 7200. In case at a particular time step, the residuals converge to the specified value before the 10 steps are completed, the solver passes immediately to the next time step, thus reducing the total number of iterations. The time needed for each iteration depends on two main parameters, the dimension of the mesh used to model the geometry and the type of turbulence model used. N_i multiplied by the CPU time needed to solve one iteration gives the total CPU time required to achieve the simulation.

3.6 Power number and flow number in CFD

3.6.1 Power number, Po, calculation techniques

The general approach of power number measurement based on summing the CFD simulations of the local specific energy dissipation rate, ε, over the whole vessel has been used by many researchers in the past, e.g., for the Rushton impeller in baffled vessels by Ranade, 1997. *Po* was under-predicted when compared with experimental results though the authors concluded that the power number could be improved by refining the grid. According to Ng and Yianneskis, 2000, for turbulence models such as k-ε, under-prediction of ε due to the assumption of isotropy throughout the vessel can lead to errors in power number calculation. It can be said that although the generation of k and ε are qualitatively well predicted, researchers have generally quoted under-predictions ranging from 20 to 50 percent (e.g. Ranade, 1997; Lane *et al.*, 2001; Aubin *et al.*, 2004).

A different method of power estimation in stirred tank reactors was published by Jaworski *et al.*, 1997. The authors investigated single impeller systems and derived methods for measuring the torque on the impeller blades and also on the baffles and walls of the reactor. They also correlated the torque from the two techniques and compared the results with experimental results. A good agreement was found in the laminar regime used. Therefore, in this work all the three approaches have been used and the results discussed.

3.6.1.1 Power number by energy dissipation rate integration

Power draw can also be defined in terms of the energy added to the fluid per unit time by the impeller (Bates *et al.*, 1963). An energy balance transforms the power drawn into power consumption in the fluid from which the power and power number can also be obtained. Power consumption is the volume integral of the specific energy dissipation rate over the vessel volume. The equation for this approach can be expressed as (3.18),

$$P = \rho \int \varepsilon_T dV \tag{3.18}$$

From this the Power number can be easily calculated using the following equation:

$$Po = \frac{P}{\rho N^3 D^5} = \frac{\int \varepsilon_T dV}{N^3 D^5} \tag{3.19}$$

Although, this can be difficult to establish accurately experimentally, it can be done by measuring the temperature rise and using the vessel as a calorimeter. On the other hand, it can be obtained computationally rather easily though, as mentioned above, it has proved rather difficult to get values in good agreement with experiments.

3.6.1.2 Power number using impeller torque

Power number obtained using this method has been referred to as the 'primary power number', Po_I throughout this thesis. The theory behind the torque calculation on blades is based on the pressure difference on the blades and shear on the hub and disc. By integration of the pressure and the viscous forces over all the surfaces of the turbine blade, the torque required to rotate the turbine could be calculated. At the end of a simulation, when the results become available, the following equation can be used to calculate the torque on the impeller surfaces,

$$M_I = M_{blades} + M_{hub+disc} \tag{3.20}$$

where,

$$M_{blades} = \sum_i \left(p_{up} - p_{down}\right)_i A_i r_i \tag{3.21}$$

In equation (3.21), i is the surface element that makes up a blade patch. The summation is done over a blade patch that is made up of surface elements. Here, p_{up} and p_{down} are the pressure upstream and downstream respectively. A_i is the area of the surface element and r_i the radial distance from the axis of tank shaft.

Apart from the blades, the primary power number also consists of contributions from the disc and hub. The equation can be given as,

$$M_{hub+disc} = \sum_H \tau_{H,t} r_H A_H + \int_D \tau_{D,t} r_D dr \tag{3.22}$$

The torque on the hub and disc surfaces is given by the summation of the tangential shear stress on each individual disc and hub elements.

It must also be mentioned that the contribution of the torque from the hub and disc surfaces are known to be minimal contributing only about 1 to 3 percent of the total value (Jaworski *et al.*, 1997). This approach to power number estimation can be

considered equivalent to the experimental method of the strain gauge technique where the torque is measured using net moments on the impeller and shaft.

The estimation of the primary power number can be done correctly even after 3-4 impeller revolutions with a time step of one computational cell. This short timescale is due to the quicker convergence of the flow near the impeller regions where the mesh is denser and the pressure profile develops immediately.

3.6.1.3 Power number using baffles and walls torque

The method known as secondary power number method, Po_{II}, has been used previously by other researchers (Jaworski *et al.*, 1997) who have used it to show the transfer of momentum from the impeller to the walls and baffles of the reactor. The method is based on the pressure difference upstream and downstream the baffle and is same in principle to the calculation on impeller blades. The overall secondary torque, M_{II}, is given by summation of the baffle torque and wall torque as in equation (3.23),

$$M_{II} = M_{baffles} + M_{walls} \tag{3.23}$$

The concept does not always predict the power number correctly and it can sometimes be misleading about the power number. The method is described in detail by Jaworski *et al.*, 1997, where the author has described the method to be based on the principle of conservation of angular momentum and found the method to be more accurate than the impeller torque due to the stability resulting from larger surface areas with respect to the first method. The wall torque, M_{walls}, was computed from the sum of the angular moment of the wall shear stress acting on the cylindrical wall, $\tau_{w,t}$, and bottom surfaces of the vessel, $\tau_{b,t}$, as shown in equation (3.24).

$$M_{walls} = r_w \sum_i \tau_{w,t} A_i + \sum_i \tau_{b,t} A_i r_i \qquad (3.24)$$

where A_i is the respective patch area and r_i the radial distance from the centre to the patch. The main contribution to the overall secondary torque comes from the baffles present in the vessel. The net normal pressure acting on the baffles can be expressed as reported in equation (3.25).

$$M_{baffles} = \sum_i \left(p_{up} - p_{down}\right)_i A_i r_i \qquad (3.25)$$

The computed total torque in both cases, i.e. the impeller blade and the vessel wall is then substituted into the general equation for power,

$$P = 2\pi N M_X \qquad (3.26)$$

where M_X can either be M_I or M_{II}. From this the power number, Po can be calculated using equation (3.19). Early experimental work using air bearings to measure vessel torque are equivalent to this approach (Nienow and Miles, 1969).

In the commercial CFD code used in this work, the post processing software gives the possibility to obtain the torque acting on any surface as a function of the axis direction chosen.

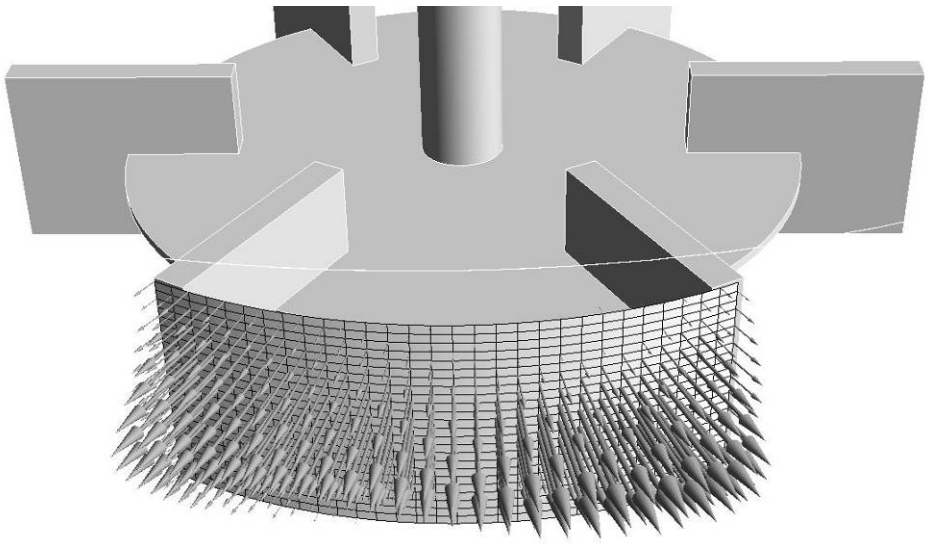

Figure 3-5: Surface of revolution to sample radial velocities in the impeller discharge

3.6.2 Flow number from CFD results

To apply the definition of Flow number reported in Section 2.4, equation (2.8), to CFD simulations, a surface of revolution around the impeller blades has been created in order to acquire the radial velocity component values in the Rushton impeller discharge stream. Due to the blade periodicity, only one sixth of the whole circumference was taken into account as shown in Figure 3-5. The surface of revolution was positioned at 1.5mm from the blades with a height equal to the blade height.

Once the surface was created, it was possible to export the radial velocity values from a sampling grid of 25 by 30 nodes. Finally, the pumping capacity, Q_P, can be calculated as:

$$Q_P = 6\sum v_r dA \qquad (3.27)$$

where dA is the integration area for each velocity. Since only a sixth of the circumference was used the sum of all the contributions is multiplied by 6.

The Fl can eventually be calculated by equation (2.8). Again, this method is essentially the same as that used with LDA or PIV.

3.7 Lagrangian particle tracking in CFD

The application of Lagrangian particle tracking in CFD involves the integration of particle paths through the vessel domain. Particle paths are tracked from their injection point until some integration limit criterion is met. Thus the tracking procedure is applicable to steady state flow analysis, rather than to transient regimes. The following Sections describe the methodology used here to track particles.

3.7.1 Integration

The particle displacement is calculated using forward Euler integration of the particle velocity over time step, dt.

$$x_i^n = x_i^o + v_{pi}^o dt \tag{3.28}$$

where the subscript o and n refer to old and new values respectively, while i indicates the time step and v_{pi} is the particle velocity. In forward integration, the particle velocity calculated at the start of the time step is assumed to be constant over all the time step. At the end of each time step, the new particle velocity is calculated equation (3.29):

$$v_p = v_f + \left(v_p^o - v_f\right)\exp\left(-\frac{dt}{\tau}\right) + \tau \cdot F_{all}\left(1 - \exp\left(-\frac{dt}{\tau}\right)\right) \tag{3.29}$$

where τ is a constant and F_{all} is the value of all the forces acting on the particle. The fluid properties are taken at the start of the time step at the particle location by interpolating the fluid properties of the volume element through which the particle is travelling.

3.7.2 Momentum transfer

According to (3.29), the fluid affects the particle motion through the viscous drag and a difference in velocity between the particle and fluid. On the other hand, there is an opposite action of the particle on the fluid flow due to the viscous drag. This effect is known as "coupling" between the phases. If the fluid is allowed to influence particle trajectories but particles do not affect the fluid, then the interaction is termed "one-way coupling". If the particles also affect the fluid behaviour, then the interaction is termed "two-way coupling". The flow prediction of the two phases in one-way coupled systems is relatively straightforward. The fluid flow field may be calculated independently from the particle trajectories, which can be calculated subsequently.

One-way coupling may be an acceptable approximation in flows with low dispersed phase loadings where particles have a negligible influence on the fluid flow. Two-way coupling requires that the particle source terms are included in the momentum equations. The momentum sources are due to turbulent dispersion forces or drag. The particle source terms are generated for each particle as they are tracked through the flow. Particle sources are applied in the control volume that the particle is in during the time step. However, since in this work, particle tracking is applied to only a single neutrally buoyant particle, one-way coupling is used in the simulations.

The forces acting on the particle travelling in a continuous fluid, which affect the particle acceleration, are due to the difference in velocity between the particle and fluid and due to the displacement of the fluid by the particle. The equation of motion for a particle in a rotating reference frame is:

$$m_p \frac{dv_p}{dt} = \underbrace{\tfrac{1}{8}\pi\rho_f d^2 C_D \left|v_f - v_p\right|\left(v_f - v_p\right)}_{I} + \underbrace{\frac{\pi\rho_f d^3}{6}\frac{dv_f}{dt}}_{II} + \underbrace{\frac{\pi\rho_f d^3}{12}\left(\frac{dv_f}{dt} - \frac{dv_p}{dt}\right)}_{III} + \\ + \underbrace{F_b}_{IV} + \underbrace{\tfrac{3}{2} d^2 \sqrt{\pi\rho_f \mu}\int_{t_0}^{t}\left(\frac{dv_f}{dt'} - \frac{dv_p}{dt'}\right)\left(t - t'\right)^{-0.5} dt'}_{V} - \\ \underbrace{-\frac{\pi d^3}{6}\left(\rho_p - \rho_f\right)\omega \times \left(\omega \times \vec{R}\right)}_{VI} - \underbrace{\frac{\pi\rho_p d^3}{3}\omega \times v_p}_{VII} \qquad (3.30)$$

where m_p is the particle mass, d is the particle diameter, v is velocity, ρ is density, μ is the dynamic viscosity, C_D is the drag coefficient, F_b is the buoyancy force due to gravity, ω is the vector of the rotational velocity directed along the axis of rotation. t_0 is used to denote the starting time, the subscript f refers to the fluid and the subscript p refers to the particle.

The term on the left-hand side is a summation of all of the forces acting on the particle expressed in terms of the particle acceleration.

- Term I is the drag force acting on the particle.
- Term II is the force applied on the particle due to the pressure gradient in the fluid surrounding the particle caused by fluid acceleration. It is only significant when the fluid density is comparable to or greater than the particle density.
- Term III is the force to accelerate the virtual mass of the fluid in the volume occupied by the particle. This term is important when the displaced fluid mass exceeds the particle mass, such as in the motion of bubbles.
- Term IV is the buoyancy force due to gravity, which for a spherical particle is given by:

$$F_b = \tfrac{1}{6}\pi d^3\left(\rho_p - \rho_f\right)g \qquad (3.31)$$

  where g is the gravitational acceleration.
- Term V is the Basset force or history term which accounts for the deviation in flow pattern from steady state. This term is not modelled in ANSYS CFX.

Term VI and VII are the centripetal and the Coriolis forces for rotating frames respectively.

3.7.3 Particle solver control parameters

In order to solve numerically equation (3.30) several parameters needs to be set for each simulation.

3.7.3.1 Number of integration steps per element

This setting controls the accuracy and timestep of the particle tracking integration. A timestep is chosen locally as the element length scale divided by the particle speed divided by the number of integration steps per element. The integration accuracy can be increased by using a higher number of integration steps at the expense of computational time. For the simulations in this work, a standard value of 10 has been chosen.

3.7.3.2 Maximum tracking time and maximum tracking distance

Maximum tracking time and distance are the real time and the actual distance over which the particle tracks are integrated. These parameters should be set to a time and length long enough for a particle to be tracked throughout the geometry but not too large or the computational cost of tracking particles, which may become trapped in recirculation zones, could become exceedingly large. In this thesis, the particles have been tracked up to 120*s*.

3.7.3.3 Maximum number of integration steps

The maximum number of integration steps is another control that can be used to terminate tracking of particles that may become trapped in recirculation zones. The number of integration steps is calculated as the number of integration steps per element multiplied by the number of elements crossed by a particle. The default value set in CFX10 is 10,000. This number has been increased in this study to 1,000,000 in order to allow the particles time to quit from some recirculation zones.

In the last two chapters, the experimental and numerical methods available in the literature that have been used to support this research have been presented. In the next Chapter 4, the actual material and methods used in the present study will be described, prior to the discussion of the results in later chapters.

Chapter 4

Material and Methods

4.1 Experimental set-up

4.1.1 The geometry

The whole set of experiments were carried out in geometrically similar systems at two different scales. The geometry consisted of a flat-based fully baffled cylindrical vessel in Plexiglas filled with fluid to a height, H, equal to the diameter, T. The four metallic baffles were T/10 in width and about T/100 in thickness, vertical and close to the wall. The stirrer used was a six blade Rushton turbine with diameter, D, equal to $T/3$, positioned at a clearance $C=T/4$ from the bottom of the tank. Each blade of the turbine had a length and a height equal to $D/4$ and $D/5$ respectively. In order to avoid optical distortion and to facilitate the qualitative observation of the system, the tank was surrounded by an outer square cross-section jacket made of the same material as the vessel, which was filled with the same fluid as that used for the experiments.

The impeller was driven, through a shaft with diameter equal to $0.09D$, by a $3kW$ motor

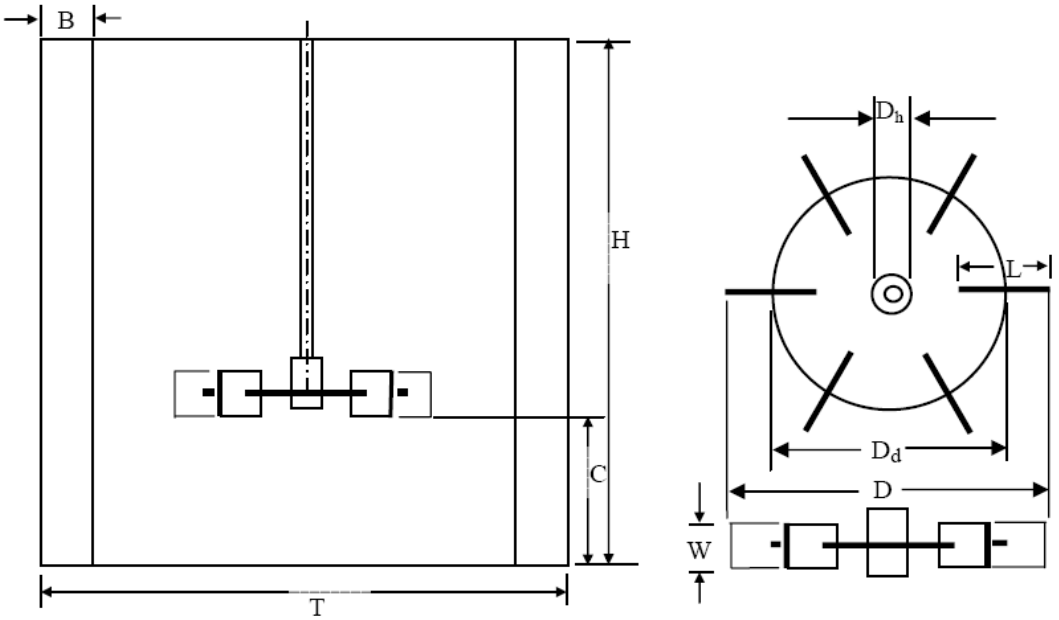

Figure 4-1: Rig diagram

with variable speed control. The two sizes, that have been used in this work, were a large one with T=287mm and a small one with T=204mm. For the larger vessel, only one rotational speed N $[rev/s]$ has been investigated N=300rpm, however for the smaller scale, the impeller speed was varied from N=100 to 600rpm.

4.1.2 The fluids

While for the larger vessel only one salt solution was used, for the small size two fluids have been considered, namely a salt solution and sucrose solutions. The reason for using the salt solutions was to match the density of the tracer used for the PEPT experiments, which, although it was supposed to be neutrally buoyant in water, was in general slightly different so that adjustments to the water density were needed. For the second set of experiments in the small vessel, where the effect of viscosity has been investigated, sucrose solution (50g/100ml of water) has been used; higher concentration in sugar would have resulted in liquid densities higher than the tracer. For the salt

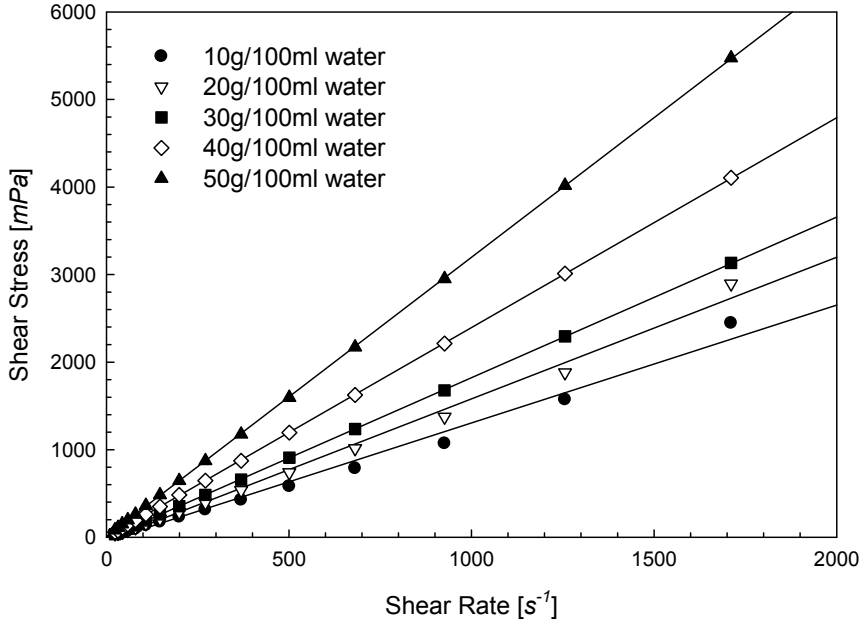

Figure 4-2: Shear stress vs. Shear rate for sucrose solutions at 20°C

solution, a viscosity similar to that of water has been assumed, but for the sucrose solution, experiments were undertaken to assess the exact value of the viscosity. The results obtained were compared to the data found in the literature (Norrish, 1967).

To determine the sucrose viscosity, a rotational viscometer, Rheomat 30, was used. Rotational viscometers use the idea that the force required to turn an object in a fluid can indicate the viscosity of that fluid. Since the sucrose solutions were of low viscosity, a double-gap cell was used. By monitoring the torque transmitted by the motor to the fluid at constant rotational speed, it is possible to calculate the torque and thus plot the graph in Figure 4-2 for different concentration of sucrose solution at constant temperature.

It is possible to calculate the viscosity of the solution by using the following relationship:

$$\tau = \mu \frac{du}{dy} \tag{4.1}$$

Equation (4.1) is valid for parallel flows between straight layers or one stationary and one moving pair of parallel plates, a Couette flow can be assumed in the cell gap since the diameter of the cylindrical cell is large with respect to the gap between the stationary cylinder and the rotating one. For Newtonian fluids, the shear stress is proportional to the shear rate giving a viscosity independent from the shear stress applied and that is seen in Figure 4-2. Thus, by fitting the data with a straight line, it is possible to find the viscosity of the solution as the slope of the straight line. The viscosity values for sugar solutions from 10 to 50g/100ml of water are reported in Table 4-1. In this table are also reported the values of density, specific gravity and increase in volume found in the literature (Norrish, 1967).

Table 4-1: Sucrose solution properties

Weight [g] of sucrose dissolved in 100 ml of water	Resultant solution				
	Sucrose by weight %	Viscosity Measured [mPa.s]	Viscosity Literature [mPa.s]	Specific gravity 20°/4°C	Increase in volume ml
10	9.10	1.34		1.034	6.165
20	16.69	1.62		1.066	12.357
30	23.11	1.83	1.931	1.095	18.570
40	28.61	2.40	2.459	1.120	24.801
50	33.37	3.19	3.246	1.143	31.048

The values measured are in good agreement with the literature, though they seem to be slightly under estimated by 1-5%. The reason is probably because the viscosity is highly dependent on temperature and even though the temperature of the laboratory was 20°*C*, it was not possible to control precisely the temperature of the fluid during the tests.

4.1.3 The tracer

As previously mentioned, the density of the tracer does not match the density of the water so, to make it neutrally buoyant, salt has been added to the water to raise the density to be as close as possible to the density of the tracer. The tracer used for this work is produced at the Centre of Tracer Production at the School of Physics and Astronomy of the University of Birmingham. The technique used to label the tracer consists firstly in producing a very dilute solution of radioisotope ^{18}F ions in deionised water. Then the ^{18}F exchanges with the counter-ions in ion-exchange resin bed so that the resin at this point is labelled leading to a quite high radioactive level (350-1000 μCi). Finally, the particle is coated with some water-proof paint to prevent the ^{18}F being removed from the resin during the experiments (Fan *et al.*, 2006). The particle density of this type of resin is about 1150 kg/m^3, but after being coated, the density is

uncertain and this makes it impossible to obtain a perfectly neutrally buoyant tracer, hence the amount of added salt is calculated to achieve a liquid density of 1150 kg/m^3. With this technique, tracer of 250 and 600μm diameter were prepared.

By matching as closely as possible the particle and liquid densities and by using a small tracer size in order to minimise its inertia, the tendency of the tracer to follow the fluid motion is maximised. Particle motion within a fluid of rapidly changing velocity is characterised by the use of Stokes number, $St = \tau_p / \tau_f$, where τ_p is the particle response time and τ_f is the fluid response time (to an external disturbance, in this case the impeller). Large Stokes number means that the particle responds slowly to changes in fluid velocity. Alternatively, small values of St indicate short particle response time with respect to the fluid, thus good tracking of the fluid streamlines and matching the fluid velocities. For Stokes numbers close to zero, the particle and fluid velocities behave identically (equilibrium flow); typically, equilibrium flow conditions can be assumed for $St < 0.1$ (Schetz, 1996). For these experiments, taking the worst case of $N = 600rpm$, and assuming that the flow is Stokesian (particle drag is therefore a linear function of the particle relative velocity and acceleration) τ_p ($\tau_p = \rho_s d_p^2 / 18\mu$) is approximately $0.0022s$ and τ_f (calculated as the ratio between impeller diameter and velocity of the tip) is approximately $0.024s$, giving a Stokes number of the order of 0.092. This value of the Stokes number will occur at the tip of the impeller where velocities are highest and τ_f is at its lowest. The fluid response time is calculated in a conservative way in fact nowhere else in the tank the fluid can have smaller response time. For the greater proportion of the vessel, St is much lower. This value of St, therefore, suggests that the neutrally buoyant tracer particle should follow faithfully the fluid motion. In fact, in the study of Rammohan *et al.*, 2001, somewhat larger tracers

(2.36mm in diameter) were used which were reported to closely follow the liquid provided the densities of the fluid and particle were closely matched.

4.1.4 The PEPT experimental set up

Despite which geometry size was used, each experiment consisted of positioning the rig between PEPT cameras, levelling the vessel and placing at an equal distance from the detectors to be most centred as possible. Once the rig has been set in position, it was filled up with distilled water and salt or sugar according the experiment needs. Finally, the impeller speed was set to the experiment value and left it run for a while giving the time to the system to stabilise the flow and to the motor to be able to keep a constant rotational speed. After the motor was steadily running, the tracer was introduced into the vessel and the recording started. For each change of experimental conditions the system was left to run for a few minutes before starting a new recording; this was to ensure that a steady state was achieved.

4.1.5 PIV configuration

The Particle Image Velocimetry equipment used to investigate the flow field developed in front and behind the impeller blades is composed of a dual head Nd:YAG laser (New Wave Research, Fremont, CA), a single frame-straddling CCD (TSI PIVCam 10-30, TSI Inc.) camera with a resolution of 1000x1016px, a synchroniser TSI LASERPULSE 610030 (TSI Inc., Shoreview, MN) and a DELL Precision 620 workstation running INSIGHT 5.1 (TSI Inc.) for image processing. The seeding particles used were silver-coated hollow sphere with a diameter of 10μm.

The camera was mounted on a computer-controlled traverse, able of controlling movements of the order of 0.5 mm.

The delay Δt between two consecutive images was chosen in function of the maximum displacement that a particle could travel in the interrogation window. This time was calculated as follows:

$$\Delta t < \frac{M \cdot Iw}{v_{tip}} \qquad (4.2)$$

Where M is the camera magnification $[mm/pixel]$, Iw is the pixels dimension of the interrogation window and v_{tip} is the impeller tip velocity which should give the maximum speed occurring in the system.

Since the work done was aiming to assess the tangential and radial velocity on the impeller plane, the laser sheet was set horizontal and entered the vessel laterally at a height equal to the impeller clearance. In order to reduce as much as possible the optical distortions due to the curvature of the wall tank the vessel was built with a surrounding square jacket filled with water. All the system was placed on a support that allowed a view of the tank from underneath. Below the tank was placed a 45 degrees mirror, which reflected the horizontal image towards the camera positioned on the side of the vessel. Finally, in order to freeze the impeller in the same position the aid of a shaft-mounted trigger was used, which triggered the flash and the camera acquisition with same frequency of the impeller rotation (see Figure 4-3).

Two-dimensional PIV velocities were obtained processing the images with a recursive Nyquist grid, the size of each interrogation area was 32x32*px* for the first pass, while a dimension of 16x16*px* has been adopted for the second pass. A 50% overlap between adjacent interrogation areas has been adopted in order to obtain an increment in the information on the flow.

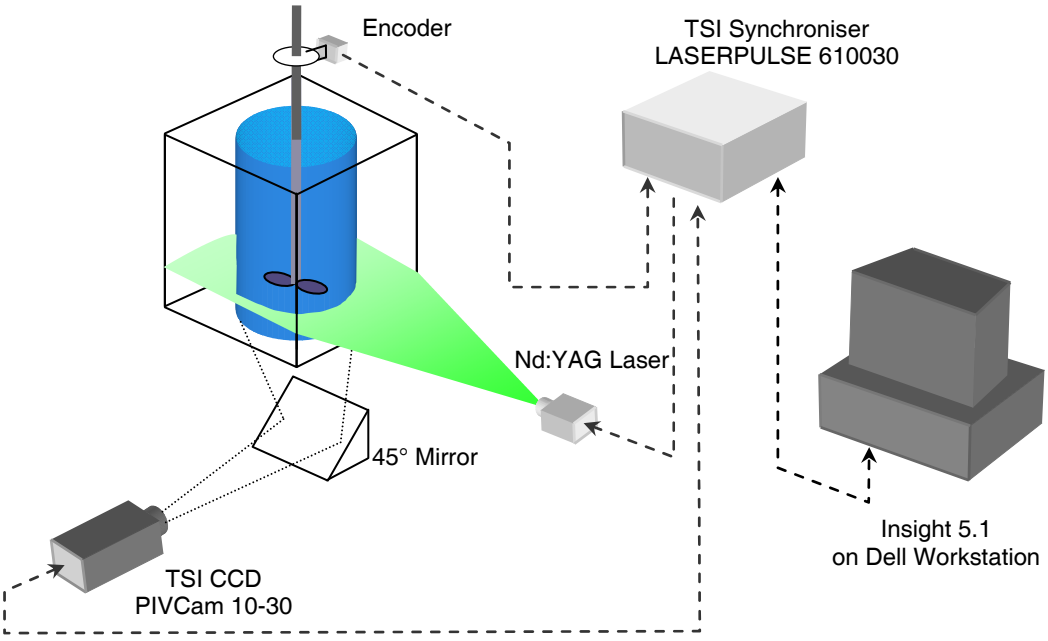

Figure 4-3: PIV configuration used for flow measurements behind the blades

For the experiment, 100 couples of images were captured; this amount of frames is enough in order to obtain a smooth averaged field although would not be good for turbulence studies. Each velocity field have been filtered validating each vector with the surrounding vectors (5x5) assuring the values stayed within two standard deviation of the population. This filtering step was achieved within the TSI Insight® software.

4.2 Computational set-up

4.2.1 Aim of CFD simulations

In this thesis, it is intended to simulate particle tracking using a Lagrangian approach to CFD simulations. In order to achieve the goal two set of simulations are conducted, a first standard single phase simulation to achieve a fully developed velocity flow field, whose results will be used as a base for the second set of simulations where Lagrangian solid particle tracking will be enabled. Finally, the results of these simulations will be compared with experimental results from PEPT.

4.2.2 CFD geometry and mesh definition

Over the last decades, computational modelling faced a quick and large improvement as has been described in the development of the different models mentioned in Section 3.4. The development of boundary conditions approaches affected also the structures of the grid type used to divide the studied geometry in finite volumes where to apply the different governing equations. Nowadays, there are two different approaches for the definition of stirred tanks meshes, namely structured or unstructured grids. In the past the majority of works have been carried out using only structured grids, because the flow, in stirred tanks, was thought as regular and very ordered, hence structured mesh were used in order to minimise numerical diffusion.

Numerical diffusion is usually exhibited in regions where flows are not perpendicular to element faces. Consider a 3-dimensional Cartesian coordinate system. On a mesh of quadrilateral elements, the flow direction may be normal to the faces of each element. In this case, the flow from one element to the next can be accurately represented to the limit of the mesh size.

In a case where the flow is not normal to the faces of the elements, for example in a region where the flow is swirling, the flow must move from one element to different elements. Consequently, some flow moves into each of the adjacent elements as shown in Figure 4-4a. Consider a similar flow, modelled on a totally unstructured tetrahedral mesh, as shown in Figure 4-4b. With this type of mesh, there is no flow direction which is more or less affected by numerical diffusion than any other. Consequently, the inaccuracy for simple unidirectional flows is greater than for a mesh of hexahedral elements aligned with the flow. However, the numerical diffusion errors for a mesh of tetrahedrons are consistent, and of the same order, throughout the flow domain. This

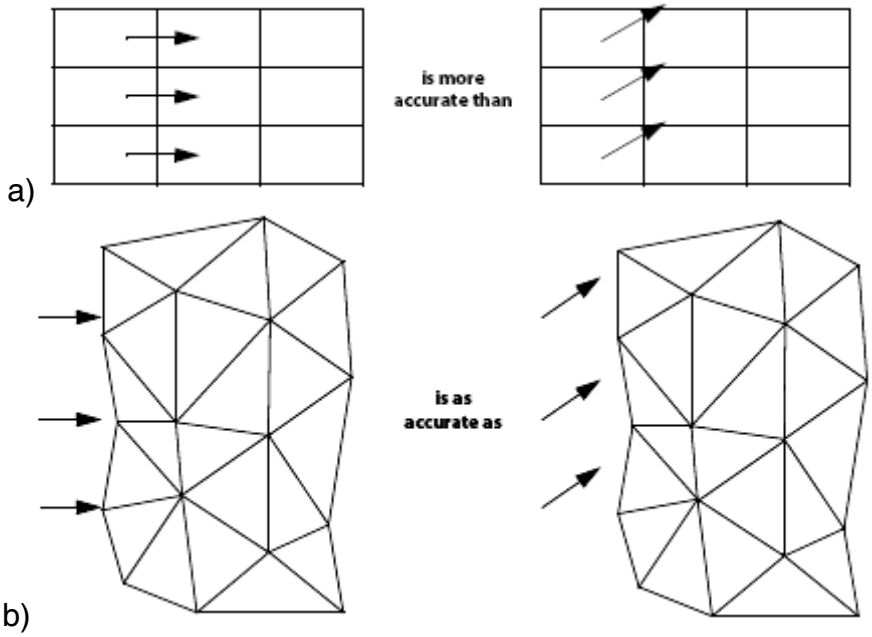

Figure 4-4: Numerical diffusion in a) structured and b) unstructured meshes

means that for real flows, tetrahedral control volumes will not exhibit additional inaccuracies in areas such as recirculation, because there is no single flow direction that may be aligned with the mesh.

A review of the CFD modelling techniques for stirred vessel hydrodynamics has been conducted by Sommerfeld and Decker, 2004. However, in this paper the authors do not refer to any simulations carried out in unstructured meshes. A comparison between structured and unstructured meshes can be found in the work of Kukukova *et al.*, 2005, where the influence of grid type on simulation results was studied for different impeller configurations; nevertheless, an exact indication on which mesh type leads to better results is not achieved.

Ansys CFX 10 package is provided with geometry and mesh tools, which allow to create solid geometries first and to mesh them with tetrahedral elements later. In the meshing stage the user is allowed to specify several parameters in order to control the mesh density in certain areas, such to control elements sizes close to the impeller, and to

create prismatic elements on walls where the flow is certainly parallel to them. In order to compare the effect of the mesh type on simulation results, a structured mesh, consisting of hexahedral elements, have been also created by using Ansys ICEM CFD 10.

Aiming to reduce the computational time needed to solve a simulation, it is popular to use only a portion of the whole vessel according the greatest common divisor of the number of blades and number of baffles, in this case having 6 blades and 4 baffles half geometry would be enough to describe the entire tank. However, since particle tracking will be performed in this work, periodic boundaries can not be used and the whole geometry needs to be modelled.

The model used for all the simulations is an exact copy of the large vessel used in the experimental work and described in Section 4.1.1, its dimensions are reported below in Table 4-2.

Table 4-2: Geometry ratios and dimensions used for CFD simulations

Description	*Symbol*	*Ratios*	*Dimension [mm]*
Vessel Diameter	T	-	287.0
Vessel Height	H	T	287.0
Baffles Width	B	T/10	28.7
Clearance	C	T/4	71.8
Impeller diameter	D	T/3	95.7
Disk diameter	D_d	4/5 D	76.5
Shaft diameter	D_h	0.09 D	8.6
Blade height	W	D/4	23.9
Blade width	L	D/5	19.1

As previously mentioned two types of meshes have been created in order to validate that the results found with the unstructured mesh matches the ones from the structured. In Figure 4-5 and Figure 4-6 are reported the two different grids for structured and

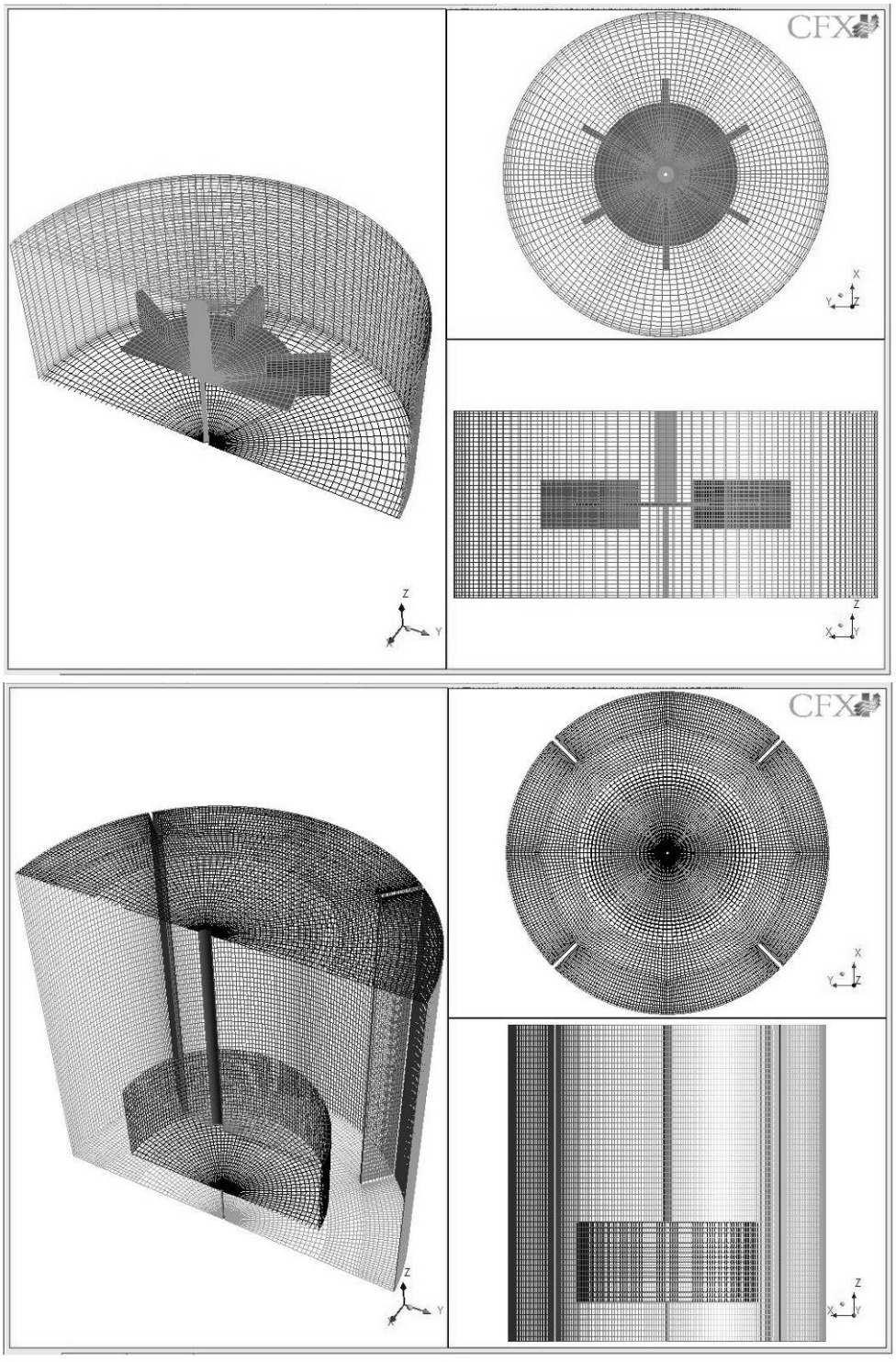

Figure 4-5: Structured mesh for impeller and tank regions (170006 and 507544 elements respectively)

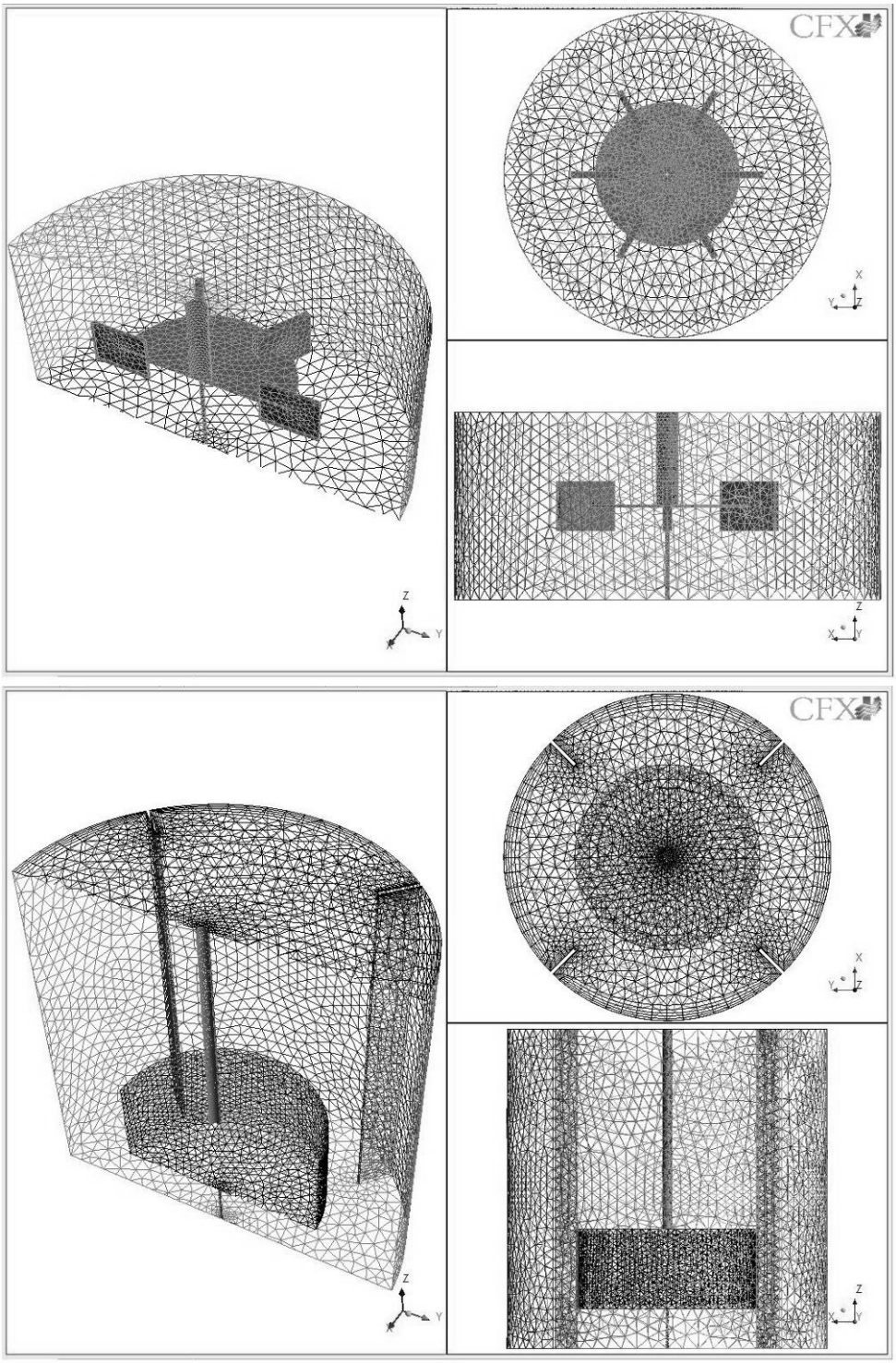

Figure 4-6: Unstructured mesh for impeller and tank regions (233888 and 407408 elements respectively)

unstructured mesh, respectively. In both cases the total geometry have been split in two: the impeller region (rotating frame) and the vessel (stationary frame). Particular attention has been given to the volume of the cells close to the regions interfaces and to the wall boundaries, in these zones a refining in cell size is needed to assure a smooth transition of the different variables from one domain to the other. Furthermore, around the external wall and on the impeller boundary, where high velocity gradients occur, there is need for smaller cells in order to achieve good results in the proximity of solid walls. Finally, for the structured mesh, on the top view in Figure 4-5 it can be noticed three main zones with a gradual cell refining from the centre to the periphery of the vessel, this is needed in order to have similar cell volume size throughout the vessel, otherwise structured mesh would generate small cells close to the shaft and much larger ones on close to the external walls and baffles. This problem does not emerge in unstructured grid, since a maximum cell edge is defined and the geometry is filled with tetrahedrons according with this maximum dimension.

In order to be able to compare the two geometries, the total number of elements for each grid has to be compared.

4.2.3 Choice of boundary condition and turbulence modelling

In depth review of the different boundary condition (see Section 3.4) and turbulence modelling (see Section 3.2) used in literature so far has been reported by Brucato *et al.*, 1998. This work assesses the different modelling approaches from direct impeller boundary condition to inner-outer approach finishing with sliding mesh approach. Brucato *et al.*, 1998, conclude that the SM approach gave the best agreement with experimental data as regards mean flow quantities, although it tended to under-predict the kinetic turbulence energy. On the other hand, requiring a fully time-dependent

simulation and a larger computational domain, it was the most computationally demanding among the three methods compared in their work. However, the huge progress of computer technology over the last years made computational time reduce drastically and the use of SM approach more possible. Still, to save some time a hybrid approach MFR + SM was used in this work, as described in Section 3.4.2.5 .

The k-ε model is the most established turbulence model for engineering flows and has been widely used for modelling turbulent flow in stirred tanks. In most of these studies, poor prediction of turbulence quantities has been attributed to deficiencies in this model, especially the inherent assumption of isotropic turbulence and limitations in predicting swirling or recirculating flow (Armenante *et al.*, 1997; Jenne and Reuss, 1999). Several authors have compared flow predictions in stirred tanks using variations of the k-ε model such as the Chen- Kim and Renormalized Group (RNG) k-ε models (Ranade *et al.*, 1989; Jenne and Reuss, 1999; Jaworski and Zakrzewska, 2002; Aubin *et al.*, 2004); however, the different variations have resulted in only slight changes in turbulence predictions. It has been suggested that a turbulence model that is not based on the assumption of isotropic turbulence should give better results. Armenante *et al.*, 1997, found that the Algebraic Stress Model indeed gave superior results to the standard k-ε turbulence model. However, in some published studies the Reynolds Stress Model based on non-isotropic turbulence was found to yield turbulence kinetic energy profiles showing a larger deviation from experimental values than those obtained using the standard k-ε model (Montante *et al.*, 2001; Jaworski and Zakrzewska, 2002). Furthermore, in mixing of turbulent vessel simulations the k-ω model has not been assessed as much as the standard k-ε. Hitomi *et al.*, 2006, carried out a comparison between the two models, using unstructured mesh, for an unbaffled vessel stirred by a

Rushton turbine. The authors concluded that the k-ω resulted in a better velocity flow field while the k-ε model predicted closer power number to the experimental values. Hartmann *et al.*, 2004, compared the results of RANS simulations versus LES. The turbulence model used in their work was the Shear Stress Transport turbulence closure model, which is a combination of the k-ω model near the wall and the k-ε model away from the wall. Overall, the RANS model was able to match LES performance in terms of flow field description, nevertheless it under-estimated the turbulence kinetic energy and the energy dissipation rate. The reason of this was associated to the assumption in the RANS model of isotropy turbulence in the whole vessel, where instead it has been showed to be only in the circulation loops, but not in the impeller discharge stream.

In order to better assess the two turbulence models and the effect of the mesh type on the velocity flow field, two simulations were carried out for each grid using the two turbulence models, RNG k-ε and k-ω.

Chapter 5

Positron Emission Particle Tracking Technique: Results

In this Chapter, the basic methods by which the concepts of PEPT are used to actually produce the data are discussed first. The actual method by which the location of the particle is obtained was developed by Parker *et al.*, 1993, giving a programme named `Track`, and initially the impact of the parameters inside this programme and their effect on the data obtained will be discussed. Next, having ascertained which are the best parameters to be used in `Track`, will follow a detailed description of the routines developed to analyse the current data including a test based on artificial data. Once it has been shown that the routines can be trusted, the effect of tracer dimensions will be studied in the large vessel and the first limitations of PEPT in stirred turbulent liquid system will be highlighted. In order to try to resolve the weaknesses revealed in the work up to this point, the smaller scale vessel was then used with two different viscosity fluids. Furthermore, an attempt is then made to improve the handling or structure of the data and the resulting improvements will be reported. Finally, some examples using the Lagrangian data obtained to define mixing are proposed and the results are presented.

5.1 Effect of the different parameters in `Track` used to produce the raw data

As briefly mentioned above , the location algorithm, actuated by the program `Track` was developed by Parker *et al.*, 1993. The data recorded by the PEPT cameras comprise a list of sequential events; `Track`, firstly, divides all the events in subsets of sequential events (*# of events/slice*); secondly; for each subset, it calculates the co-ordinates (*x, y, z*) of the point which is simultaneously closest to all of the reconstructed paths. Iteratively those events whose paths lie furthest from this point are then discarded as corrupted and a new point is recalculated using only the events left. This

reconstruction process is repeated until only a fraction, f_{opt}, of the all the events listed in the subset is kept. At this point, the algorithm passes to the processing of the following subset and finishes when all the subset have been processed, the final data have the form of a list of temporal positions, *t, x, y* & *z*. Figure 5-1 reports an example of the output of the program `Track` in form of a `.txt` file. The data to be analysed are divided in eight columns: the first four columns regards the time (*s*) and the three Cartesian position coordinates (*mm*); the fifth column gives a sort of error in the position location (*mm*) defined as the diameter of the confidence cloud where the particle has been located. While the sixth and seventh columns are not used, the eighth column gives the effective number of lines used to find the location.

The values of # *of events/slice* and f_{opt} are assigned for each experiment and they depend on the particular geometry, on the velocities involved in the system and also on

RT300d250

Separation= 658

f(opt) : 0.200 Displacement parameters : 300, 400, 1500

Fixed slices: 150 events/slice, 1 locations/slice

10.8	330.9	389.7	407.0	2.9	0.0	0.00	30
31.8	329.1	387.0	402.2	3.1	0.0	0.00	28
55.5	329.3	386.1	405.8	2.2	0.0	0.00	28
79.9	327.6	386.1	401.0	4.2	0.0	0.00	28
104.2	328.0	381.5	397.4	3.4	0.0	0.00	28
124.1	326.0	381.3	397.4	3.3	0.0	0.00	28
146.8	324.7	379.2	392.5	3.5	0.0	0.00	28
174.7	322.2	378.5	392.2	1.7	0.0	0.00	28
200.4	317.9	376.3	387.5	2.8	0.0	0.00	28
221.6	315.2	375.5	386.6	3.9	0.0	0.00	28
244.1	309.5	375.6	377.9	2.7	0.0	0.00	28
266.3	303.4	374.6	375.2	2.7	0.0	0.00	28
286.7	297.4	375.1	371.8	2.8	0.0	0.00	28
312.9	292.8	374.9	373.4	2.6	0.0	0.00	28
:	:	:	:	:	:	:	:
:	:	:	:	:	:	:	:

Figure 5-1: Typical `.txt` output file from `Track` program

the activity of the tracer during the period for which it is undertaken. Since the events are continuously recorded while the particle is moving, the choice of the # *of events / slice* and f_{opt} plays an important role in the generation of the raw location data.

Parker *et al.*, 1993, show in their work that, for a particle moving on a circular path at constant velocity, increasing the size of the event subset, up to a certain limit, results in more accurate reconstruction of the position of the particle; however, on extending it to still larger sets the accuracy decreases again. This suggests that, for a given speed, an optimum value of the number of events per slice exists, at which the best possible location is achieved. Furthermore, they show that with increasing velocity, the optimum value of the number of events for slice steadily decreases. Similarly to the number of events per slice, the f_{opt} parameter has a optimum value for a given set of events. In fact, a small f_{opt} should cut off all the corrupted events, leaving only the good ones; however, if the # *of events / slice* is small, e.g. 80, then a small f_{opt}, e.g. 0.05, would lead to the use of only 4 events for the triangulation process.

It should be quite clear at this point that it is impossible to define a general rule for the parameter definition, especially as they depend on the radioactivity of the tracer, its absolute velocity and fluctuation characteristics, including the rate of change of direction of the mean velocity of the tracer. The fully three dimensional turbulent flow in stirred tanks will therefore be among the worst cases to analyse. The analysis is made more difficult because in addition to the above points, the mass of water surrounding the tracer absorbs a portion of the γ-rays, reducing the effective radioactivity, and the absolute velocity of the tracer and its acceleration are high in the vicinity of the impeller, while when it is close to the external wall, it moves much more

slowly. Experience can help the first choice of these parameters, but only a trial and error approach leads to the finding of the optimum.

In order to quantify the effect of the processing parameters on the raw data the same experiment has been processed with different values of # *of events / slice* from 100 to 300 and f_{opt} from 10 to 30. For the first 20 minutes the relative standard deviation of the errors reported in the 5th column of the `.txt` file has been calculated for every combination of # *of events / slice* and f_{opt}. Figure 5-2 shows the effect of the processing parameters on the error values; it is clear how an optimum can be found for this type of experiment. In particular, the minimum relative standard deviation is obtained with values of # *of events / slice* and f_{opt} equal to 120 and 17, respectively, leading to a total number of lines used to find the locations of about 20. The parameters values obtained

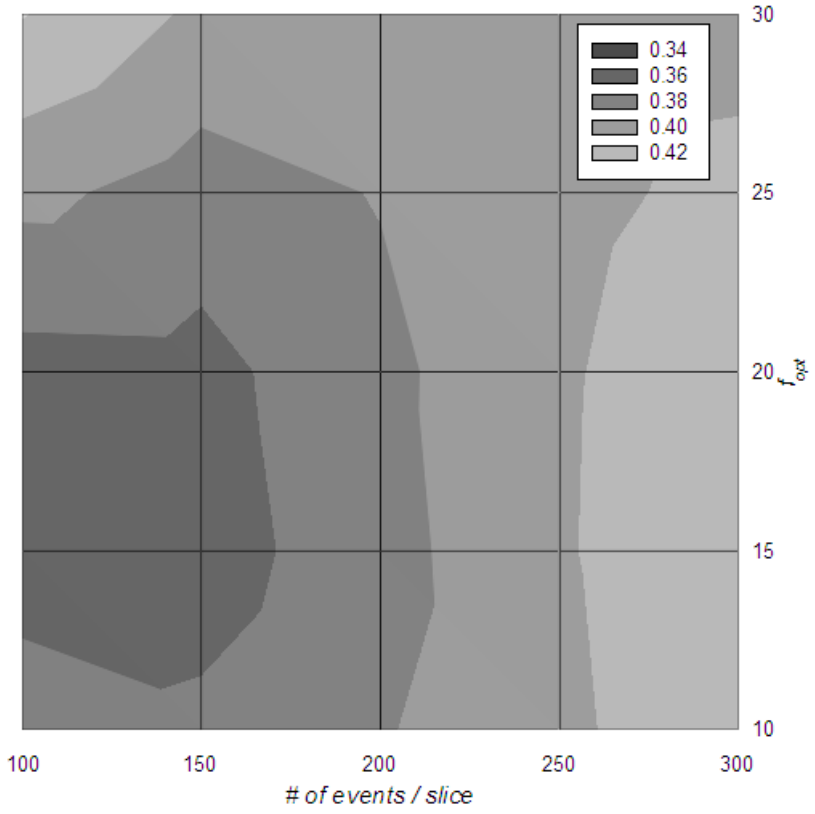

Figure 5-2: Relative standard deviation of the 5th column error for different values of *fopt* and *#events/slice*

in this way have been a guide for processing all the data collected in this type of geometry, naturally they needed to be adjusted for each experiment according the decaying of the activity of the tracer and with the change of impeller speed.

5.2 Real data structure

Once the optimum # *of events/slice* and f_{opt} parameters have been chosen for each experiment, the data need some pre-processing in order to be ready to be analysed and discussed in terms of the flow field. The raw data obtained from the Department of Physics and Astronomy of the University of Birmingham quite often presents two types of problem. The first one is related to the nature of the experiments. Since the tracer is small, it can get stuck in a small gap such as that between the baffles and the wall of the tank. The second is related to the triangulation algorithm. In this case the location found may be generated by a large number of corrupted data and as a result, it is not in line with the other close locations. To overcome these problems, two routines have been designed and created in this thesis, i.e. `cut.m` and `filtra.m`. The routine `cut.m` shows the data in graphical form as function of time. When it shows that the particle is stationary for a period of time so that it is deemed to be stuck by the user, the data in that time interval can be removed by clicking directly on the extremes of the region. The routine `filtra.m` acts in two stages, at the beginning, it calculates the spatial distance between each location and it plots them in a histogram. At this point, the user chooses the maximum length that should be accepted between two subsequent locations. Once that value is defined, the second stage of the routine filters out all the points having a distance either from the previous or from the following location larger than the maximum length defined. In addition, the `filtra.m` routine centres the data

according to the position of the tank between the two cameras. Inside the PEPT system, the *X* and *Y* system are on the plane of the detectors, while the *Z* is across the volume between the detectors. The origin of the PEPT reference system is on a corner of the detector 1: therefore, the values of *X, Y* and *Z* are all positive. Since stirred tanks have a vertical natural revolution axis, in the `filtra.m` routine, the data for the flow in the tank are centred on the axis of the vessel and the Y and Z axes are swapped in order to have the Z direction as vertical axis. To find the position of the vessel within the PEPT detection volume, a different weak radioactive tracer particle was attached around the bottom of the vessel and along the baffles; and by recording its different positions, it was possible to reconstruct the geometry of the vessel (circumference and height of the tank) and to find the coordinate of the vertical axis of the vessel.

Figure 5-3 shows the effect of the `cut.m` and `filtra.m` routines on the raw data. On

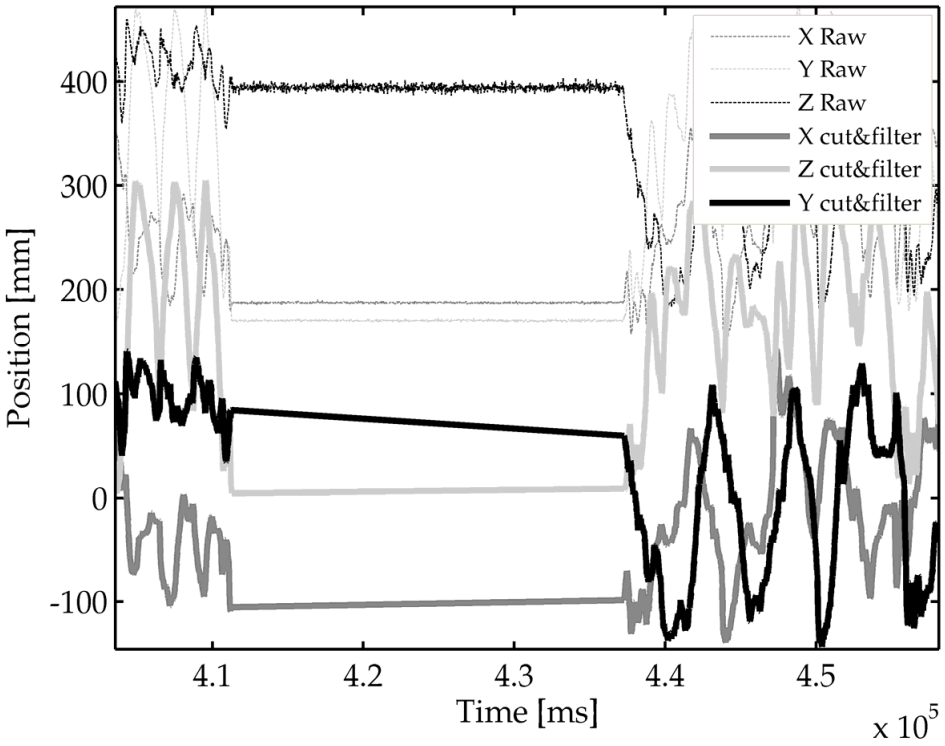

Figure 5-3: Data before and after the routines `cut.m` and `filtra.m`

the x-axis is reported the time [ms] and on the y-axis the tracer position [mm] along the three coordinate components; the thin lines are the three raw X, Y, Z coordinates as recorded in PEPT, while the thicker ones are the particle axis positions after the use of the routines to relate them to the tank. In the graph can be seen that the data are centred, e.g. the X coordinates range is shifted from [180 to 480] to [-150 to 150], the coordinates along Y and Z direction are swapped and the data when the particle was stationary between $4.11 \cdot 10^5$ and $4.37 \cdot 10^5 ms$ are removed.

The contour plot in Figure 5-4 shows on a horizontal plane x-y representing an integration over the whole volume of the total number of locations recorded by PEPT over a period of $2hr$ experiment and the position of the detectors have also shown. For a neutral density particle tracking the fluid in a well mixed closed system, intuitively it would be expected that the probability of the tracer being in any one position within the

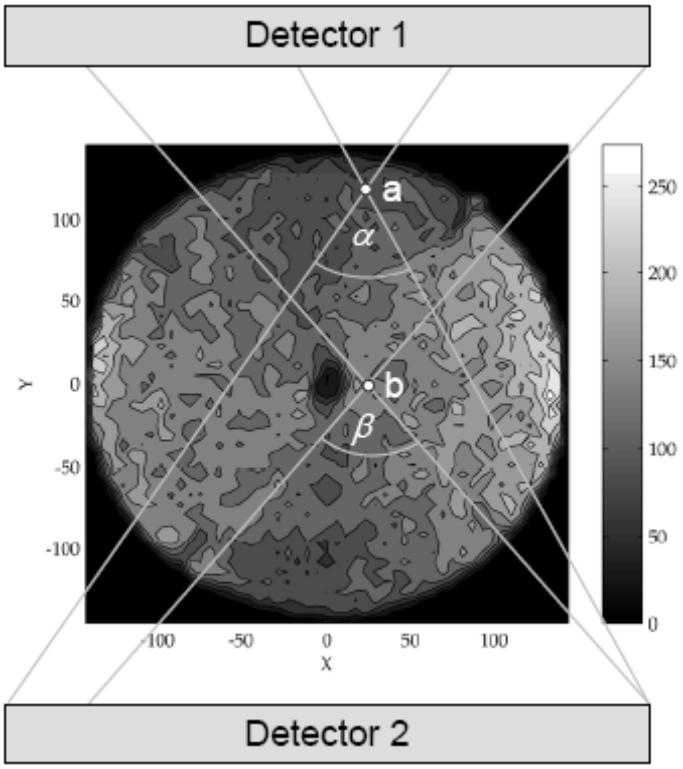

Figure 5-4: Total number of location recorded and integrated on the XY plane

vessel would be uniform. Moreover, the figure shows that close to the cameras a smaller number of locations are detected with respect to the ones that are further away. Consider a tracer at two different positions in the vessel, a and b, both on the same plane normal to the cameras and with the tracer emitting γ-rays in every directions. The number of γ-ray pairs detected by the cameras is proportional to the solid angle defined by the relative position of the tracer to the cameras and the dimensions of the cameras themselves. In the graph, it can be observed that the detection angle (α) for the tracer at position a close to the detector 1 is smaller than the angle (β) whom it is at position b, resulting in areas close to detector 1 with lower number of back to back pairs being detected and hence fewer locations. Finally, the right part of the figure shows more detections than the left part. This is probably because the vessel was not properly centred within the two cameras and indicates the difficulty of achieving accurate centring in spite of great care being taken.

5.3 Artificial data to perform and optimise the routines

5.3.1 Finding velocity using PEPT data

The simplest use of the PEPT data is to determine the local velocity of the tracer location by location. For this purpose several methods can been used: either the simple two point differentiation, equation (5.1), or a more sophisticate weighted average over a series of locations 5 steps apart using 11 data points, see Figure 5-5a, commonly used in the Physics Department and known as the 'six points' method (e.g. Fairhurst *et al.*, 2001; Stewart *et al.*, 2001), equation (5.2).

$$v_i = \frac{\overrightarrow{p_i} - \overrightarrow{p_{i-1}}}{t_i - t_{i-1}} \tag{5.1}$$

$$v_i = 0.1\left(\frac{\overrightarrow{p_{i+5}} - \overrightarrow{p_i}}{t_{i+5} - t_i}\right) + 0.15\left(\frac{\overrightarrow{p_{i+4}} - \overrightarrow{p_{i-1}}}{t_{i+4} - t_{i-1}}\right) + 0.25\left(\frac{\overrightarrow{p_{i+3}} - \overrightarrow{p_{i-2}}}{t_{i+3} - t_{i-2}}\right) + 0.25\left(\frac{\overrightarrow{p_{i+2}} - \overrightarrow{p_{i-3}}}{t_{i+2} - t_{i-3}}\right) + 0.15\left(\frac{\overrightarrow{p_{i+1}} - \overrightarrow{p_{i-4}}}{t_{i+1} - t_{i-4}}\right) + 0.1\left(\frac{\overrightarrow{p_i} - \overrightarrow{p_{i-5}}}{t_i - t_{i-5}}\right) \tag{5.2}$$

In equations (5.1) and (5.2), v_i is the velocity at the point $\overrightarrow{p_i}$ and time t_i. For these methods the location of the velocity vector is taken to be the average position of the points used to calculate the velocity.

A third method, proposed for the first time in this work, is based on finding for each component position the equation of the straight line of 'best fit' which passes across the set of data at the location as a function of time, Figure 5-5b. The gradient of this line is the velocity of the particle over that time. The spatial location of the vector lies on the 'best fit' line at an average time, *tm*, of the point used. In the case of systems with a

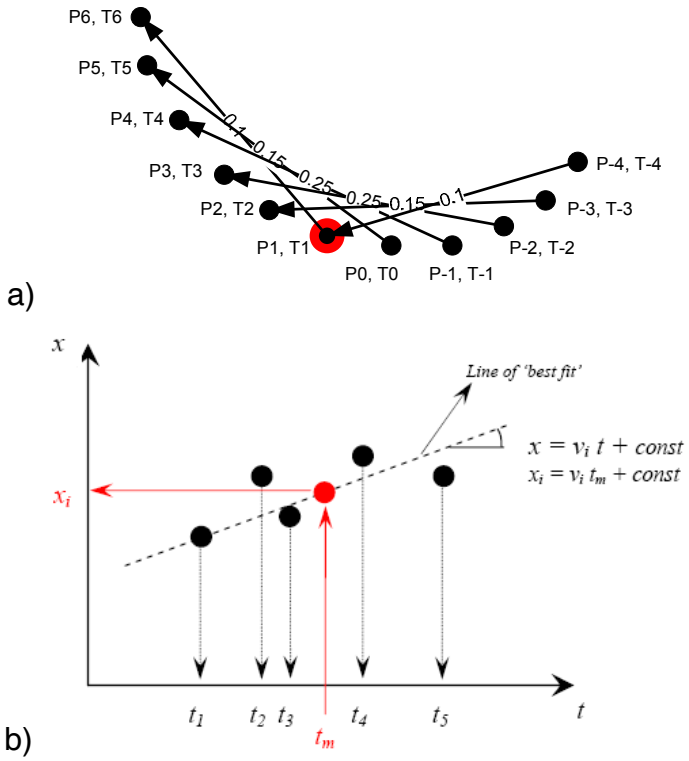

Figure 5-5: Scheme for a) 'six point' and b) linear fitting methods

well defined and known pattern or for particles running along certain trajectories, this method could be adapted using a different fitting polynomial.

For all the methods the total scalar velocity is calculated simply as vector summation:

$$v_{tot} = \sqrt{v_x^2 + v_y^2 + v_z^2} \tag{5.3}$$

To perform these calculations over the whole PEPT data, two routines have been developed in this study: `prep.m` and `velfit.m`. The first one prepares the data in a suitable form to be processed with one of the three methods, which are defined inside the routine `velfit.m`.

In order to assess if there were any errors in the previous routines a set of artificial data with known velocities have been created to simulate the PEPT data, but knowing the exact velocity involved in the artificial system. See Section 5.3.2 for further details.

5.3.2 Creation of artificial data

Expecting to work with a stirred vessel, a 2D spiral data set have been created according the following equations:

$$\begin{aligned} x &= R\cos(\omega t + rnd_{x1}) + rnd_{x2} \\ y &= R\sin(\omega t + rnd_{y1}) + rnd_{y2} \\ R &= (50 \div 150)mm \\ t &= (1 \div 1000)ms \end{aligned} \tag{5.4}$$

From the previous equations it is clear that the data emulates a particle moving along a spiral for a time t and with constant angular velocity ω. Some noise has been added, to match the experimental typical data, to the time, rnd_{x1} and rnd_{y1}, and to the final position, rnd_{x2} and rnd_{y2}; this noise has the form of random numbers generate with normal distribution with zero mean and standard deviation in accordance to the variable, $5ms$ and $1.5mm$ for the time and the position respectively.

Despite the name, the 'six points' method uses 11 locations to determine the local velocity of the tracer, as shown in the scheme in Figure 5-5a; if the use of a large number of locations assures a really smooth velocity profile, on the other hand, if data are not very frequent, during the whole time interval the particle can change its velocity and move substantially far from the first location. Furthermore, the final location of the vector will be averaged among all the positions of the 11 points. If this method gives good results in experiments where data are acquired with high time resolution or very slow velocities, it shows to be inappropriate when the time between locations results in large particle displacements (10 to 40 mm). In Figure 5-6 is shown a direct comparison between the 'six point' and the 'linear fitting' of 5 points methods applied to the artificial data with two different time resolutions, 8ms and 20ms for the first and second figure respectively. It is possible to see that as long as the time step is short both the methods are very similar and follow closely the locations, see Figure 5-6a. The discrepancy between the vector positions and the locations of the artificial data is due to the fact that these methods, although in different ways, use a mean of several location to position the velocity vector. In this case it is possible to see how the 'six point' method smoothes the data more than the other one, this is due to the fact that it uses 11 points instead of 5. Furthermore, the average theoretical velocity for this data is 1.68m/s; using the two methods the mean velocities obtained are 1.64 and 1.66m/s, for the 'six point' and the 'linear fitting' respectively. This denotes that using both methods the velocities detected are always underestimated with respect to the real velocities of the system.

In Figure 5-6b the time step is increased up to 20ms while the rest of the parameters were kept constant. In this case it is clear how the use of many points to interpolate

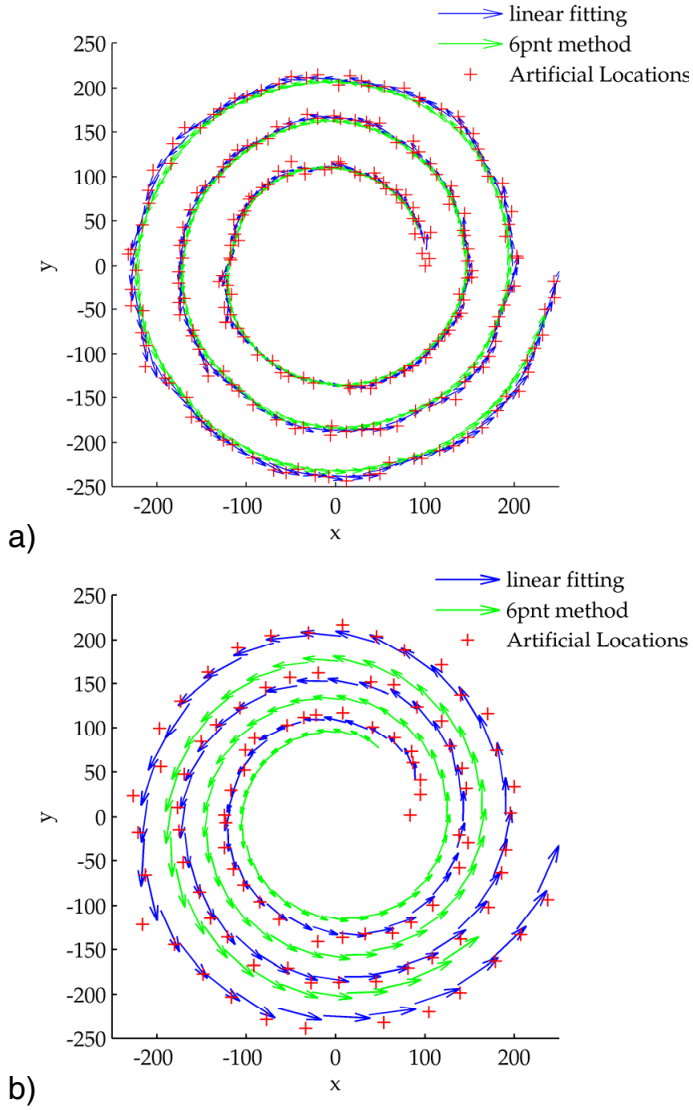

Figure 5-6: Vector plot comparison between the 'six points' and 'linear fitting' methods, a) time step equal to 8*ms* b) time step equal to 20*ms*

velocities could be a risk and leads to big error in the estimation of local velocities. While the 'linear fitting' method (using 5 points) keeps tracking closely the locations and predicting good velocities, the 'six points' method using 11 locations is not able to match the data since the position of the vectors are estimated by averaging the positions of the 11 locations. With these conditions the mean velocities recorded are 1.53 and $1.622 m/s$ for the 'six point' and the 'linear fitting' methods respectively, this shows how the 'linear fitting' method is more flexible and accurate.

5.3.3 Velocities in cylindrical reference system

In stirred tanks the fluid flows in a cylindrical motion around the vessel axis, ignoring the position of the baffles, most researchers report data in cylindrical coordinates using axial symmetric data or azimuthally averaged variables. To be able to compare the finding of this research to typical data published in the literature, the routine `prep.m` generates the velocities in cylindrical reference system as well as in Cartesian reference system. Looking to the structure of the artificial data in Figure 5-7, it can be noticed that the cylindrical coordinates shows almost linearity when plotted versus time. From a geometrical point of view, to transform Cartesian velocities to cylindrical reference system should give the same exact results as using cylindrical coordinates to find the cylindrical velocities. From a practical/numerical point of view, transforming velocities (found via interpolating Cartesian coordinates) is not the same as finding velocities via interpolating cylindrical coordinates. To see the differences the two approaches have been implemented and applied to these artificial data. In Figure 5-8 the results of this

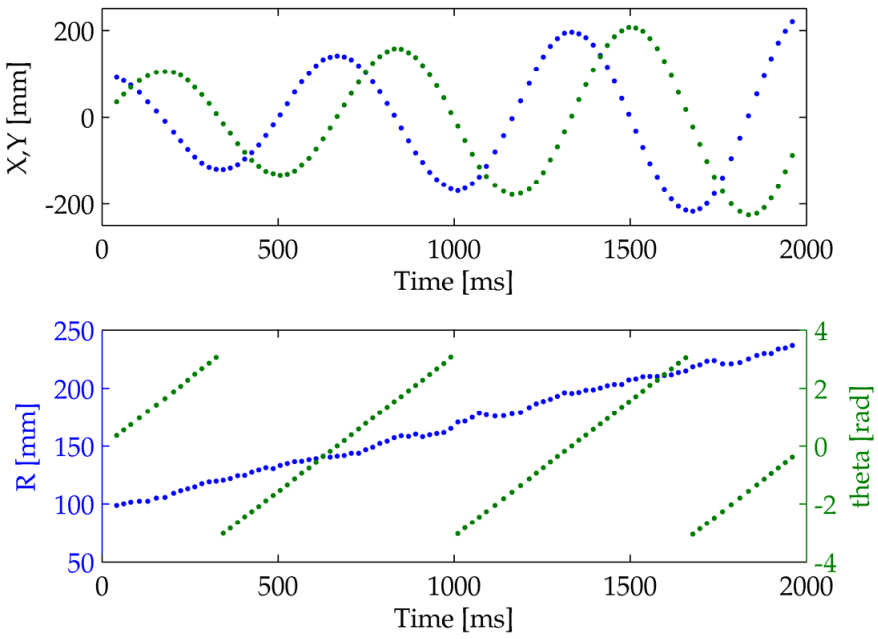

Figure 5-7: Cartesian and Cylindrical coordinates vs. Time for artificial data

comparison are shown; on the graph, on the left hand side are reported the cylindrical velocities obtained by converting the Cartesian velocities, while on the right hand side are reported the same velocities calculated by 'linear fitting' of the cylindrical coordinates. In both cases, the velocities are compared with the theoretical cylindrical velocities, which are found by converting the following Cartesian velocities into cylindrical coordinates:

$$\begin{aligned} \dot{x} &= -\omega R \sin(\omega t + rnd_{x1}) + rnd_{x2} \\ \dot{y} &= \omega R \cos(\omega t + rnd_{y1}) + rnd_{y2} \end{aligned} \tag{5.5}$$

The case a) shows to underestimate the tangential velocity, *vth*, for higher speeds and be not accurate for the radial component, *vr*, while the case b) shows to be very close the theoretical velocities for both the components. Despite this approach being well suited for the artificial data where the tracer moves along a spiral, it can be expected that in reality the tracer will rotate around the vessel axis following curved trajectories. For this reason all the PEPT data will be analysed with the second approach: in other words, the Cartesian velocities will be found from the Cartesian locations, while for the cylindrical velocities components the locations will be firstly transformed in cylindrical coordinate and then used to calculate the velocities.

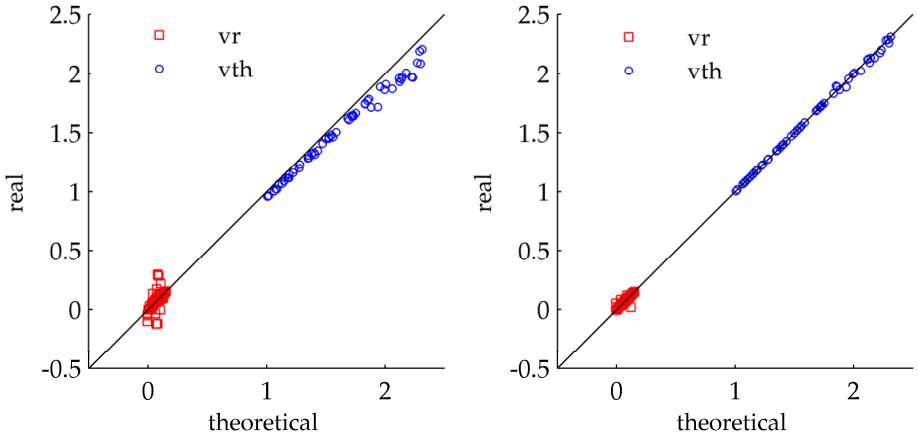

Figure 5-8: Cylindrical velocities vs. Theoretical achieved from a) converted Cartesian velocities b) calculated from cylindrical coordinates

5.4 Decaying activity effect on tracking time resolution

Once the routines to find local Lagrangian velocities were tested, they have been applied to real data coming from experiments in stirred vessels. The first experiment consists of a long run in the large vessel without changing the experimental conditions. During each experiment, the tracer loses its original activity according the following exponential law:

$$A = A_0 \exp(-\lambda t)$$
$$\lambda = \frac{\ln(2)}{t_{1/2}} \qquad (5.6)$$

Where A is the activity in function of the time, t, the initial activity, A_0, and the tracer half-time life, $t_{1/2}$ (=110min for ^{18}F). In Figure 5-9 is reported a table and a graph showing how the tracer activity decays with time; in the graph are also marked the values for the half-time life and its multiples.

For long experiments it is recommended to record the tracer movements on different files, in this way it is possible to process the different batches adapting the parameters #

Time [*min*]	Activity Percentage
0	100.0
10	93.9
20	88.2
30	82.8
40	77.7
50	73.0
60	68.5
90	56.7
120	46.9
150	38.9
180	32.2
240	22.0
300	15.1
360	10.3

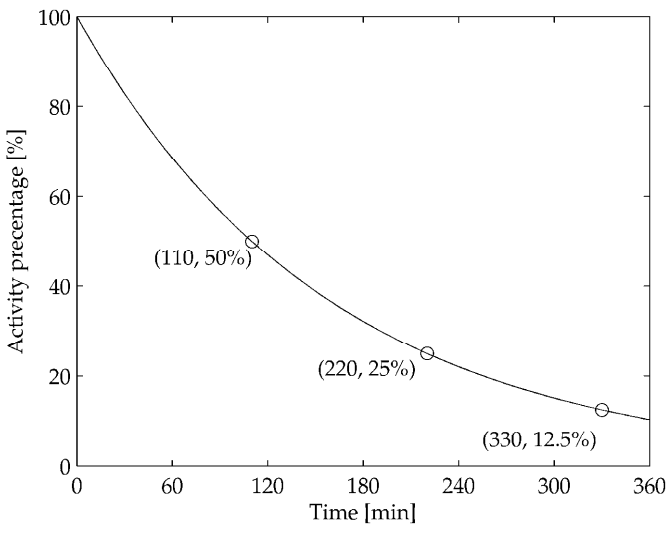

Figure 5-9: Table and graph of the activity percentage in function of time

of events / slice and f_{opt} to the frequency of the raw data. In fact, in the beginning of the experiments the tracer high activity leads to a large number of events per second recorded by the camera, up to 13-15$kevents/s$, this allows the use of large values of *events / slice* assuring an accurate positioning of the locations and good time resolution.

Due to the decaying activity, within a set of data the time resolution of the data has to increase; this can be seen in Figure 5-10 where is reported the mean and the standard deviation of the time resolution versus time. In this specific case, the experiment is carried out in the large vessel with impeller speed of $N=300rpm$, and the parameter used to process the data was 200*events / slice* with f_{opt} equal to 0.15. The mean values of dt and their standard deviation are calculated by averaging 500 consecutive time steps between pairs of locations. The average dt at the beginning of the set of data is about 40ms while it is 58ms towards the end of the set, which corresponds to an average of 5.0$kevents/s$ and 3.45$kevents/s$ (69% of the starting value) recoded by the cameras respectively. This agrees with the lost activity of the tracer, in fact,

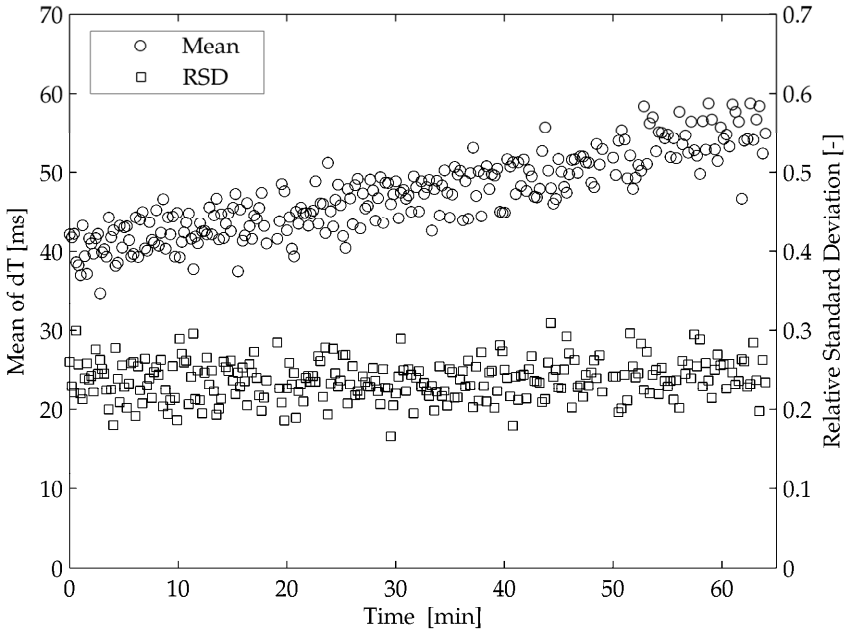

Figure 5-10: Time resolution vs. experiment time

accordingly to Figure 5-9 after one hour the tracer has a remaining 68.5% of its original activity. In addition, the relative standard deviation, defined as the ratio between the data standard deviation and its mean, was found to be constant during the experiment leading to the conclusion that the scattering of the dt depends only on its mean value.

5.5 Azimuthally averaged variables and velocities contours plots

The first set of data analysed with all the routines explained so far come from a long run experiment in a large geometry with an impeller speed of $300rpm$; the diameter of the tracer before painting was $600\mu m$ and the data were recorded for $5hrs$ until the number of events detected by the camera was too low (approximately $5kevents/s$). Since the data recording is divided into several files, before can be applied any of the routines they need to be unified into a single file. Then the routines `cut.m`, `filtra.m` and `prep.m` (which uses `velfit.m`) are applied to achieve the processed data consisting in position and velocities in function of time. Once all the positions and the velocities are calculated in cylindrical coordinates, they are averaged on an imposed grid. Due to the axial symmetric nature of stirred vessels, azimuthal averages are the most used in literature and easy to read for analysis. Azimuthal mean values are obtaining by averaging the values of the locations falling within a certain toroid volume neglecting their angular coordinates, as if they are all on the same plane. For stirred vessels, it is expected that the tracer spends equal time in each part of the entire tank. According to this, a 2D grid has been created in order to have equal volume toroids; hence, the radius has been divided into segments with different lengths. Once the grid is built, there are different approaches that can be used in order to define a mean values in a cell:

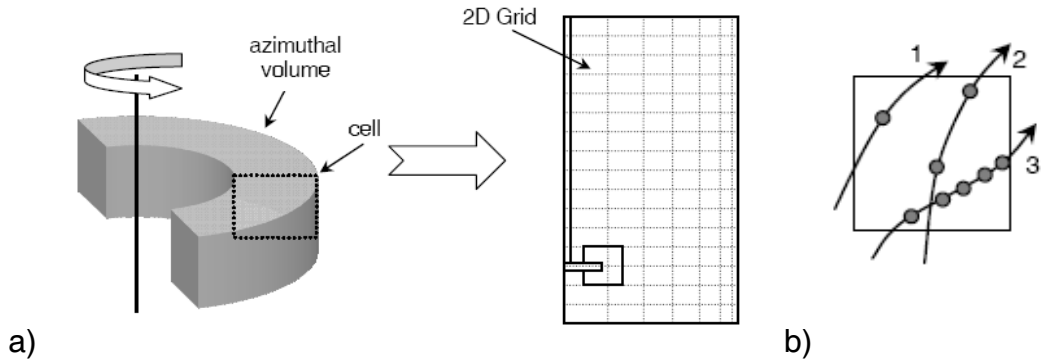

Figure 5-11: a) Azimuthal grid scheme b) locations and passes from a cell

- Average on the number of location recorded in a cell,
- Average on the passes from the cell,
- Weighted time spent in the cell average.

Figure 5-11b shows an example of a cell containing eight locations associated with three passes. From the example, since the locations belonging to pass 1 are sparser than the ones associated with pass 2 and pass 3, it is reasonable to assume that the velocity of pass 1 is higher than that of pass 2, which in turn is higher than pass 3. It is clear from this example that it would be wrong to obtain the average velocity for the cell based on the total number of location in the cell, because pass 3 would swamp the effect of the other two. On the other hand, the averaging of passes is computationally very demanding since it involves, firstly, identifying the different passes, secondly, finding an average velocity per pass and, finally, averaging the pass velocities. To overcome the complexity of this type of approach, a more simple method can be used. This method involves a time weighted average, where the single velocity associated with each location, being multiplied by the half interval time between the previous and the subsequent, location is added to all the other time-velocity products in the same cell.

Finally, this total time-velocity summation is divided by the total time spent in the cell. This method can be summarised as follows:

$$\overline{v} = \frac{\sum_j v_j \Delta t_j}{\sum_j \Delta t_j} \qquad (5.7)$$
$$\Delta t_j = \left(t_{i+1} - t_{i-1}\right)/2$$

where j is the j^{th} location and i indicates the index of that particular cell. This method also takes into account the effect of the radioactive decay of the tracer as, for two different passes having the same velocities but different tracer activity, the time spent in a cell will be the same, but in one case there are more locations than the other. By using equations (5.7) these two passes give the same velocity in each case as it should be expected. In the routine `Occ.m`, the grid and the azimuthal velocity are calculated. Since the total time spent by the tracer in each cell is recorded, it is possible to calculate the value of occupancy, defined as time spent in a cell divided by the total time of the experiment, as well as record the total number of times the tracer visits each cell. Finally, the average velocities are converted to dimensionless velocities by dividing them by the velocity of the impeller tip and the height and radial coordinates of the tracer position are also made dimensionless using the height and the radius of the vessel respectively.

The results of `Occ.m` can be seen in Figure 5-12 showing the dimensionless velocity components for the larger vessel (radial, tangential and axial respectively): at 300*rpm* (v_{tip}=1.52*m/s*) with the nominal 600μm neutrally buoyant resin tracer size.

However, it should be noted that the coating used to make the particle waterproof adds a thickness varying from 25 to 40μm. Finally, the grid used in this case consists in 25 and 50 cells in the radial and axial direction, respectively.

5.5.1 Results with a 600 μm tracer

Contour plots are really helpful in visualising the velocity flow fields and in a qualitative analysis of the results within the entire geometry. However, for a quantitative comparison with data reported in literature, a single velocity component profile as a function of position is really required.. From the literature, a suitable profile is the radial discharge velocity, which is available at various positions. The present values using the 600μm tracer are shown here in Figure 5-13 (as *RT300La*) at *r/R* equal to 0.25, 0.4, 0.55, 0.7 and 0.85 and compared with similar data reported in the literature (Wu and Patterson, 1989; Dyster *et al.*, 1993; Campolo *et al.*, 2003). For radial position far from the impeller, the present and literature profiles are all quite similar. However, close to the impeller, it can be seen that there are major differences with the present results. Here, the PEPT velocities are much lower than expected and it seems that close

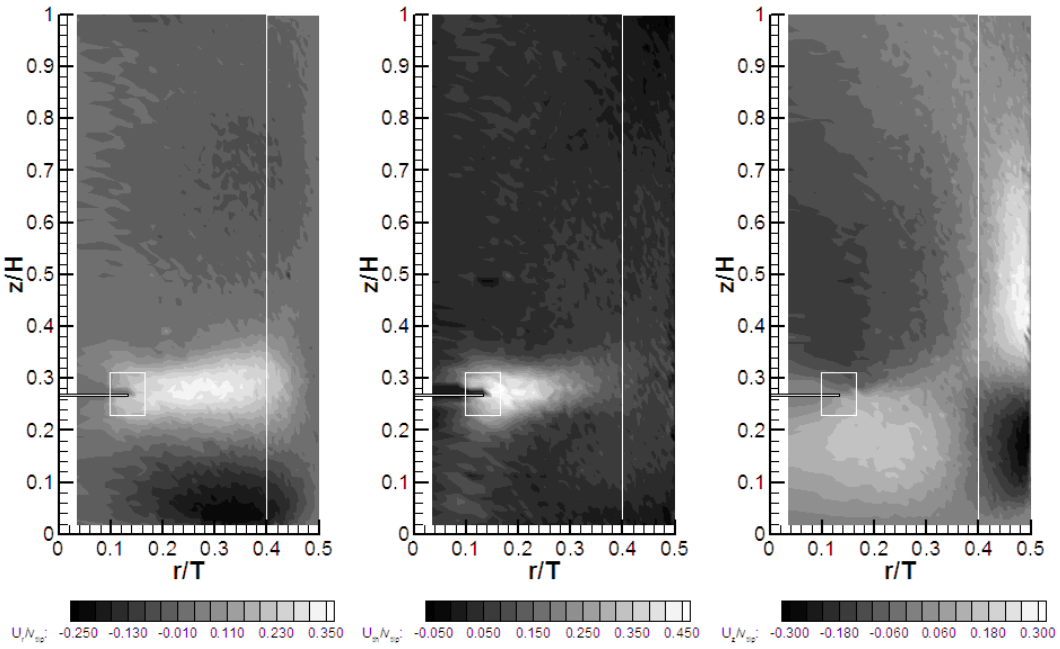

Figure 5-12: : Dimensionless velocity components from PEPT experiment a) u_r/v_{tip}; b) u_{th}/v_{tip} and c); u_z/v_{tip} (large vessel *N* = 300*rpm vtip* = 1.58*m/s*, tracer 600*micron* in diameter)

to the impeller, r/R=0.33, the PEPT velocities are close to zero instead of around 0.72 (Dyster *et al.*, 1993, and Wu and Patterson, 1989). This difference probably is due to the fact that in the region of the impeller, because the fluid moves most quickly, there are a smaller number of locations and hence it is harder to get accurate velocities. However, where the number of locations is sufficient to obtain accurate velocities away from the impeller but still in the radial discharge stream, the velocities found are in good agreement with the ones reported in the literature.

5.5.2 Results with a 250 μm tracer

After having realised that close the impeller, the number of location recorded are probably substantially smaller than elsewhere, it was felt that this might be because of the relatively large size of the tracer. Since a smaller tracer could be made, the second experiment consists of another long run without changing any of the system variables used in the previous experiment except that the size of the tracer before painting was 250μm in diameter rather than 600μm. In addition, this data set should help assess the reproducibility of the experiments. The results of this experiment are also reported in Figure 5-13 as *RT300Lb*. It can be seen that despite the use of a smaller tracer, the results do not show any improvement. This finding leads to the conclusion that the lack of data in the impeller region is not due by the ability of the tracer to follow the liquid since both the tracers follow the liquid in exactly same way. Furthermore, the results in Figure 5-13 show the reproducibility of the technique and routines which process the data recorded during the experiments. In addition, in Figure 5-14 is reported the axial velocity component for the two experiments in comparison with the results of Wu and Patterson, 1989.

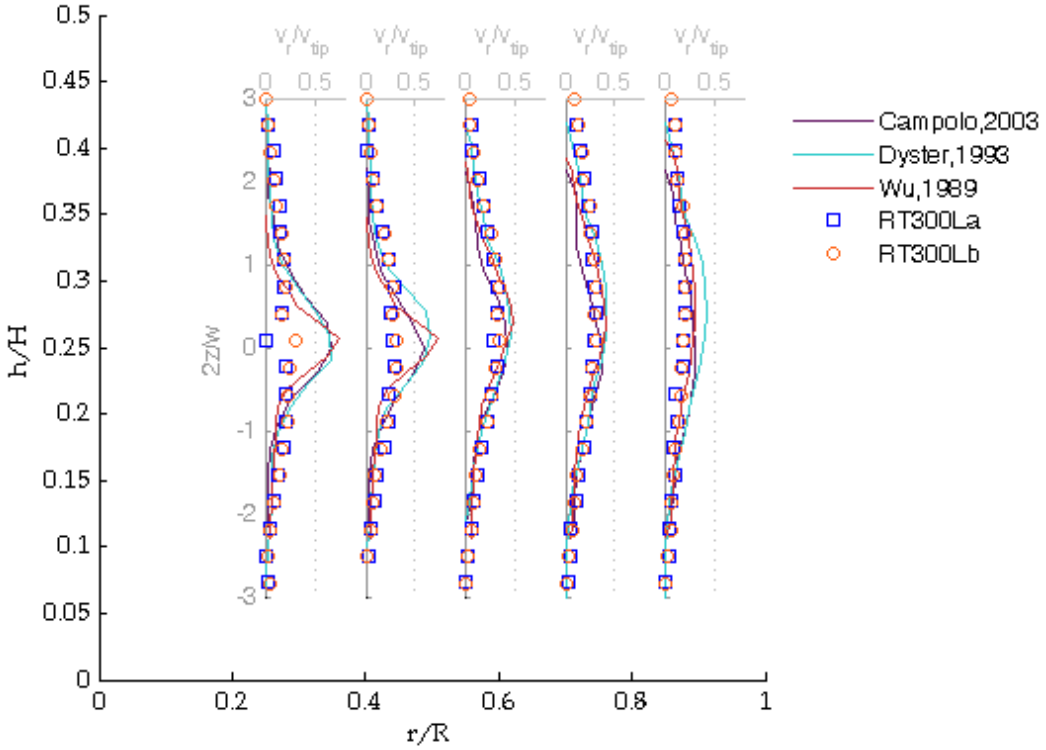

Figure 5-13: Discharge radial velocity profiles at various position compared with literature (PEPT data, *N* = 300*rpm*, *vtip* = 1.58*m/s*)

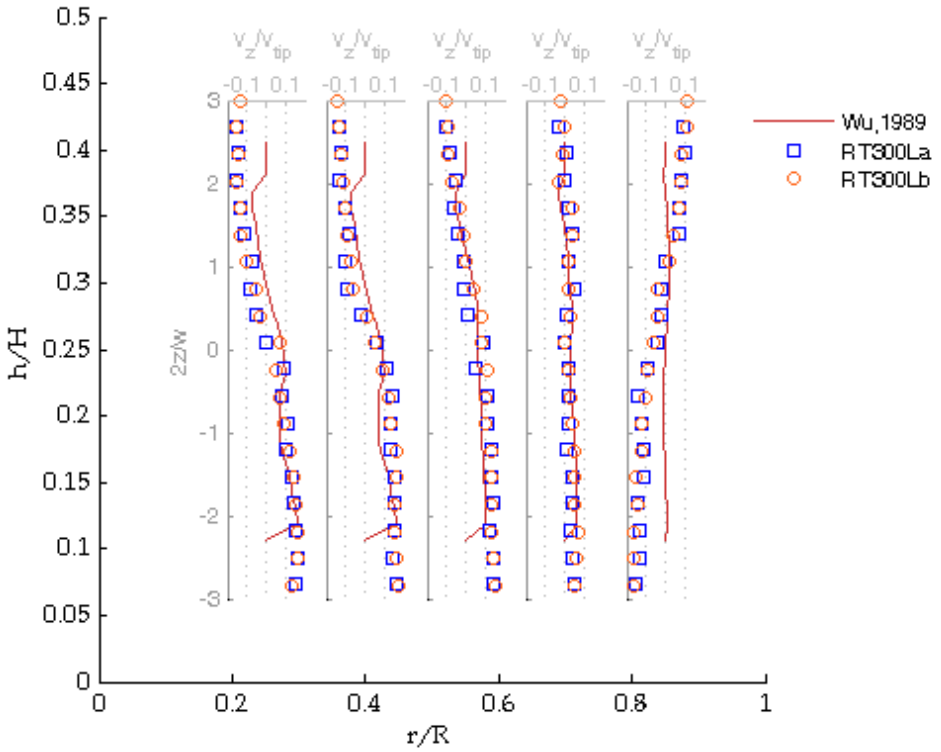

Figure 5-14: Discharge axial velocity profiles at various position compared with literature (PEPT data, *N* = 300*rpm*, *vtip* = 1.58*m/s*)

In this case, the results are more consistent with the literature, especially on the areas above and below the impeller plane. In particular, it is possible to notice that in proximity of r/R equal to 0.7, the axial velocities are close to zero, in this zone the flow is mainly tangential and radial, then the flow splits in two close to the wall and the axial component of the velocity rises again to almost $0.2v_{tip}$ (r/R=0.85). Close to the wall the velocities found from PEPT data are higher than those from Wu and Patterson, 1989. This discrepancy is probably because they used Laser-Doppler Velocimetry technique and close to the wall such systems have very high limitations due to optical distortion.

5.6 Improving the results by using selective interpolation

In the previous Section, it was suggested that close to the impeller where the velocities are at their maximum, there are less locations recorded by the PEPT cameras than the rest of the vessel where they are lower. This happens because the cameras have a constant acquisition time resolution so that the locations are more distant from each other when the particle moves faster. Thus, if the particle moves at $1m/s$ and the time between two locations is 30-40 ms, the positions will be 30-40 mm apart. In Figure 5-15a is reported frequency distribution over the axial locations for 40 intervals. Assuming the well-mixed condition proposed above, the average frequency for the vessel for 40 intervals should be around 2.5% per interval. In fact, in the proximity of the impeller, the value decrease to ~ 2% and rises to almost 3% in the regions of the upper and lower loop where the velocities are slightly lower. Furthermore, in Figure 5-15b the contour plot of the number of passes from each cell is reported. Since the radial discharge stream divides approximately equally into the upper and lower circulation loop, it is reasonable to expect the passes in the discharge stream to be of the

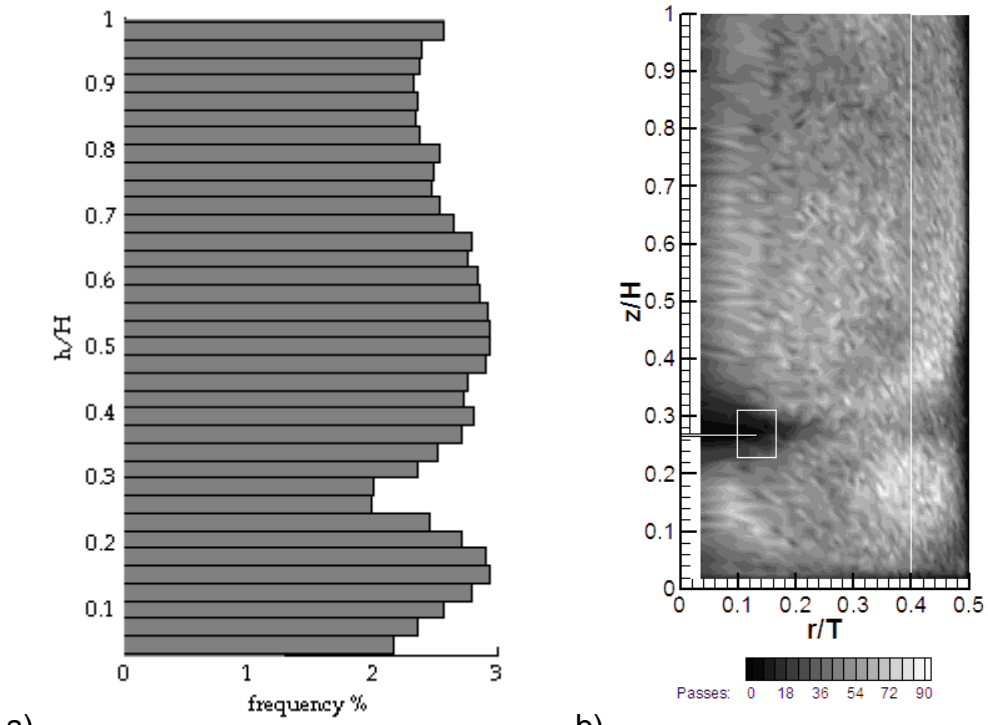

Figure 5-15: a)Axial locations frequency distribution; b) contour number of passes per cell (PEPT data, $N = 300rpm$, $vtip = 1.58m/s$)

order of twice those in the two loops. On the contrary, the plot does not show a large number of passes in the impeller stream at all. This low number of passes is because probably, due to the high velocity and close to the impeller the acceleration and change of direction, the particle location moves among cells apart without recording its pass from the cells within the interval.

In order to overcome this lack of information in such region, a selective linear interpolation can be applied to the data in the cases where the distance between locations are found to be more distant than a certain value. This value is chosen to be the cell dimension used for the azimuthal averaging process. Hence, if two locations have a relative distance larger than the cell dimension, a number of locations are interpolated in such way that the single relative distances between the new locations are smaller than the cell dimension. When instead, the particle moves slowly and the

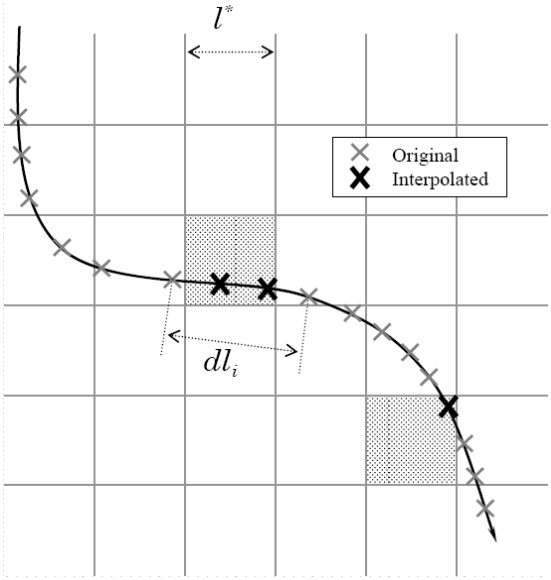

Figure 5-16: Selective interpolation working scheme

positions are close to each other, there is no need for interpolation. The concept and problem is shown schematically in Figure 5-16. In this figure, l^* is the dimension of the cell while dl_i is the distance between to consecutive locations. When dl_i is greater than l^*, the missing locations are interpolated and with them their time as well.

The results of the selective interpolation on the frequency distribution and passes are shown in Figure 5-17. Comparing these results to the previous ones in Figure 5-15, it is obvious that the interpolation has a big influence on the region around the impeller. The number of passes on the radial discharge stream is higher than everywhere else and much higher than before the interpolation. Although the new locations are interpolated, this improvement in the number of passes in the area close to the impeller suggests that re-calculating the velocities by processing the new set of data, with the interpolated locations, might well improve the results in the relation to the literature with respect to the actual velocities.

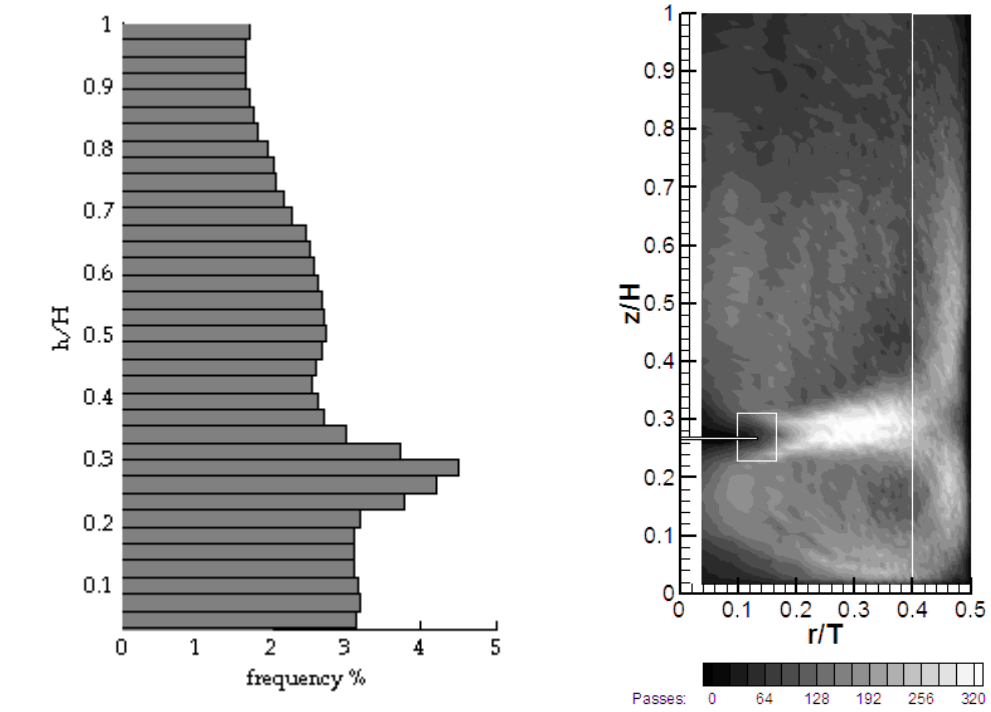

a) b)

Figure 5-17: Selective Interpolation: a)Axial locations frequency distribution; b) contour number of passes per cell (PEPT interpolated data, *N* = 300*rpm*, *vtip* = 1.58*m/s*)

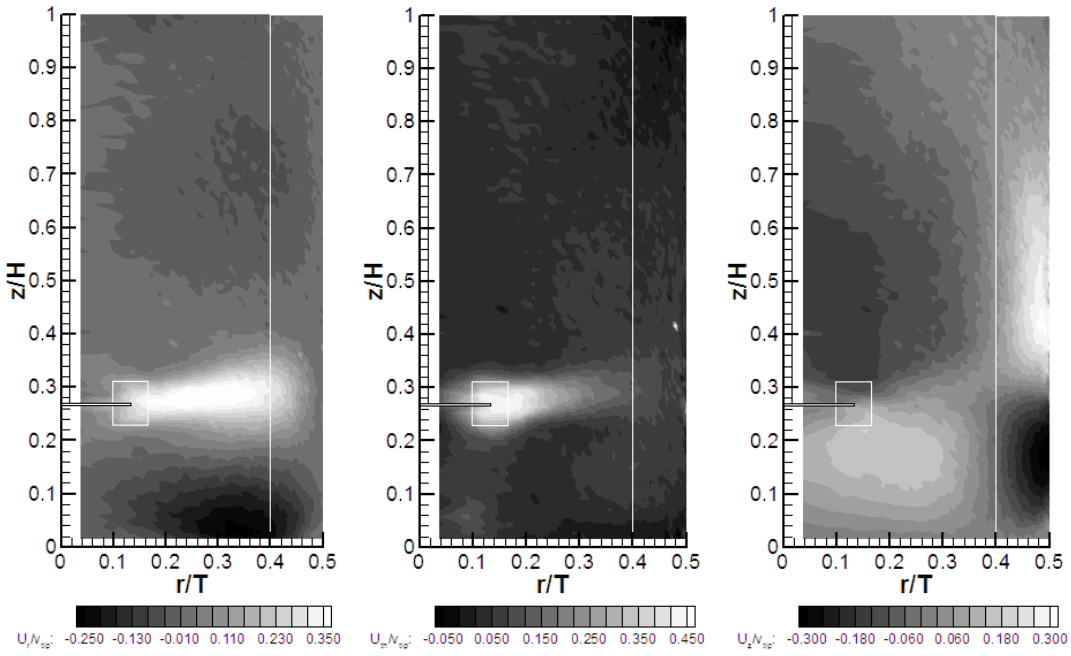

Figure 5-18: Selective Interpolation: a) u_r/v_{tip}; b) u_{th}/v_{tip} and c); u_z/v_{tip} (PEPT interpolated data, *N* = 300*rpm*, *vtip* = 1.58*m/s*)

Having applied the interpolation to the already filtered and cut data, the `filtra.m` and `cut.m` routines become unnecessary. Therefore, the routines used in this case were only `prep.m` and `Occ.m`. In Figure 5-18 the contour plots of the velocity components for the interpolated data are reported. Just by looking at these plots, it is not possible to appreciate the change with respect the original velocities reported in Figure 5-12. In fact, overall they are very similar and the largest improvement is in the radial component close to the impeller where the maximum velocity achieved is 0.43 times the velocity of the blade rather than 0.36 times as the previously, i.e. an increase of 17%. To quantify the difference following the introduction of data the percentage relative deviation, $\%E$, and relative root squared deviation, $\%RSE$, for the total velocity magnitude between the two cases defined as

$$\%E = \frac{v_{int}^{i} - v_{orig}^{i}}{v_{orig}^{i}} \cdot 100$$
$$\%RSE = \frac{\sqrt{\left(v_{int}^{i} - v_{orig}^{i}\right)^2}}{v_{orig}^{i}} \cdot 100 \qquad (5.8)$$

have been calculated. Where v_{int}^{i} and v_{int}^{i} are the i^{th} components of the interpolated and original velocity data, respectively.

The results are presented in Figure 5-19. In Figure 5-19a, where $\%E$ is greater than zero, the absolute velocity value has been increased by the data treatment and vice versa; while the $\%RSE$ in Figure 5-19b gives an indication of the absolute size of the difference between the two set of data. From the contour plot, it can be concluded that in the proximity of the Rushton turbine and close to the walls, there is the largest increase in velocities, and the only zones where there appears to be a decrease in

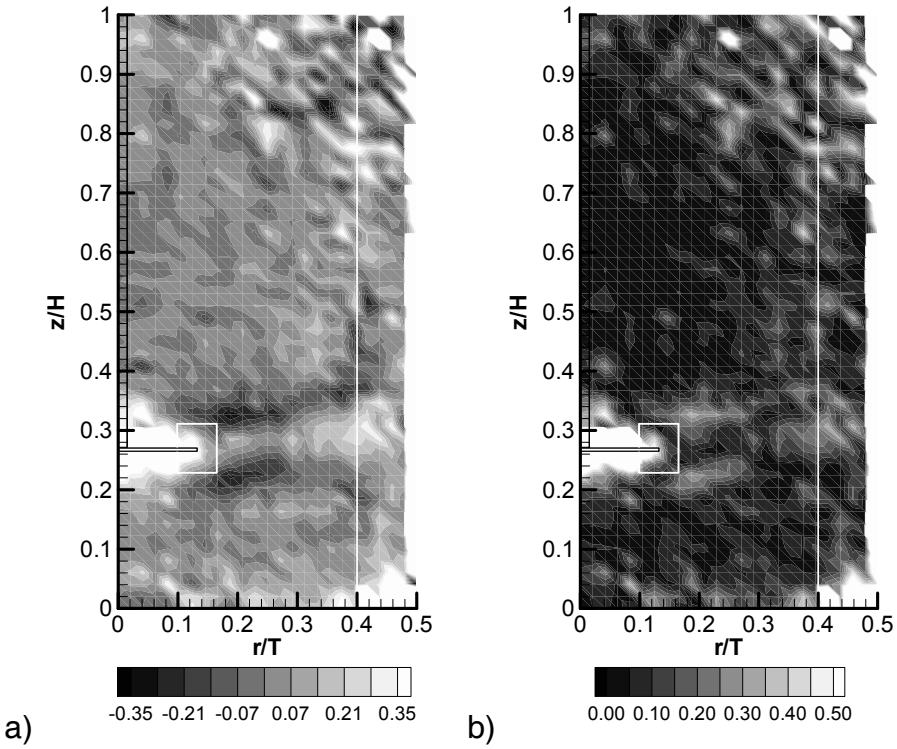

Figure 5-19: Selective Interpolation: a)%E and b) %RMS for total velocity (PEPT interpolated data, *N* = 300*rpm*, *vtip* = 1.58*m/s*)

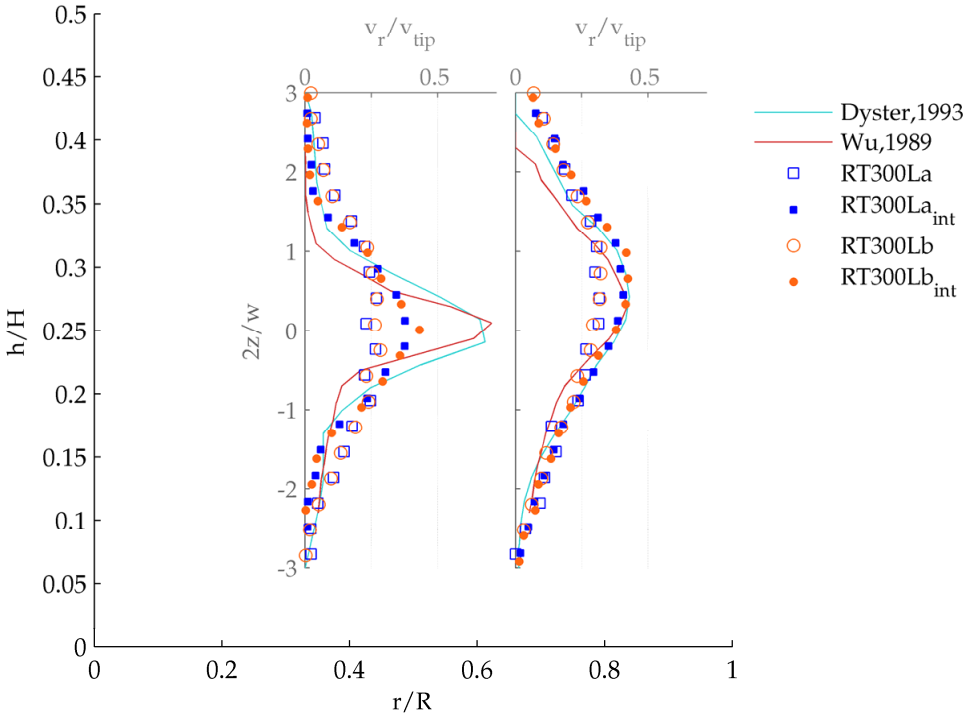

Figure 5-20: Comparison of Radial velocity profiles for original and interpolated data (PEPT, *N* = 300*rpm*, *vtip* = 1.58*m/s*, tracer a = 600*micron* & b = 250*micron*)

velocities is above and below the impeller blades. This enhancement occurs because the velocities calculated, through the routine `velfit.m`, use five consecutive points. Thus, since the locations are more apart in the original data, the velocities close to the impeller benefit from the greater number of locations in the impeller stream where the fluid is moving faster and deviating rapidly from the vertical to the horizontal direction, resulting in higher calculated velocities. Finally, two radial velocity profiles, at r/R equal to 0.33 and 0.66, for the original and interpolated data are shown in Figure 5-20. From the plot, it can be seen how the interpolated data shows larger radial velocity values in the impeller stream; furthermore, for values of r/R larger than 0.5 the agreement with literature data becomes much improved.

Overall, the reason for needing to use a selective interpolation on the original data have been justified and the benefits have been discussed and tested, clearly indicating improved results in regions of high velocity and rapid directional changes. Therefore, the rest of the results based on the PEPT measurements presented in this thesis will be based on using this selective interpolation.

5.7 Smaller scale results and effect of viscosity

As seen in Section 5.2, the number of locations recorded by the detector varies with the position of the tracer particle to the cameras. In fact, since the particles emit γ-rays in every direction the probability that a gamma ray will cross the detector is function of the distance from it. The two cameras are mounted on movable supports, which enable the cameras to be moved as close as possible to the used rig. Therefore, it can be speculated that flows in smaller sized equipment are easier to detect and analyse than in larger ones. To asses this idea experiments in the smaller geometrically similar vessel

were made. In addition, to prove the ability of the tracer to follow the liquid, the same experiments were undertaken using a media with higher viscosity. As described in Section 4.1 the smaller geometry has a diameter T=204mm instead of T=287mm with a corresponding volume of 6.28l and Table 5-1 lists the experiments carried out in it.

Table 5-1: List of experiments done and their operative conditions

Experiments done	N [*rpm*]	*Re*	*vtip* [*m s^-1*]
Large, SALT Solution			
RT300	300	1.61E+05	1.58
Small, SALT Solution			
RT600	600	1.38E+05	1.98
RT480	480	1.10E+05	1.58
RT200	200	4.60E+04	0.66
RT100	100	2.30E+04	0.33
Small, SUGAR Solution			
RT600	600	4.25E+04	1.98
RT480	480	3.40E+04	1.58
RT300	300	2.12E+04	0.99
RT200	200	1.42E+04	0.66

For a smaller geometry; as extensively shown in the literature (e.g. Khang and Levenspiel, 1976; Middleton, 1979; Nienow, 1997), by changing the scale of the system the different parameters and quantities involved in mixing change in different ways. In fact, comparing the different regimes in Table 5-1, it can be observed that similar Re values for the two geometries lead to dissimilar impeller tip velocities. In order to compare the two scales, a range of regimes has been chosen to assure either similar Re values, or similar tip velocities. However in the turbulent regime ($Re > 2\times10^4$), it is postulated and experimentally it has been shown many times (Costes and Couderc, 1988a; Dyster *et al.*, 1993; Dong *et al.*, 1994) that all velocities are directly proportional to the tip velocity. Hence, all the dimensionless velocities can be compared regardless of the Re or the impeller velocity (Khang and Levenspiel, 1976; Bujalski *et al.*, 1986; Costes and Couderc, 1988a).

5.7.1 Salt solution

Since in the smaller geometry, it is expected a larger number of locations should be detected per unit of time, resulting in a higher number of passes, the first comparison between this scale and the larger one is to compare the passes at different experiment length time using the same meshing grid. To do this, though the cell dimensions for the smaller geometry are less, the geometrical ratios must be kept constant over all the parameters used in the experiments. Figure 5-21 shows the contour plots of the passes for the large and small geometries as a function of time, i.e. after 5, 15, 30 and 60 *min*

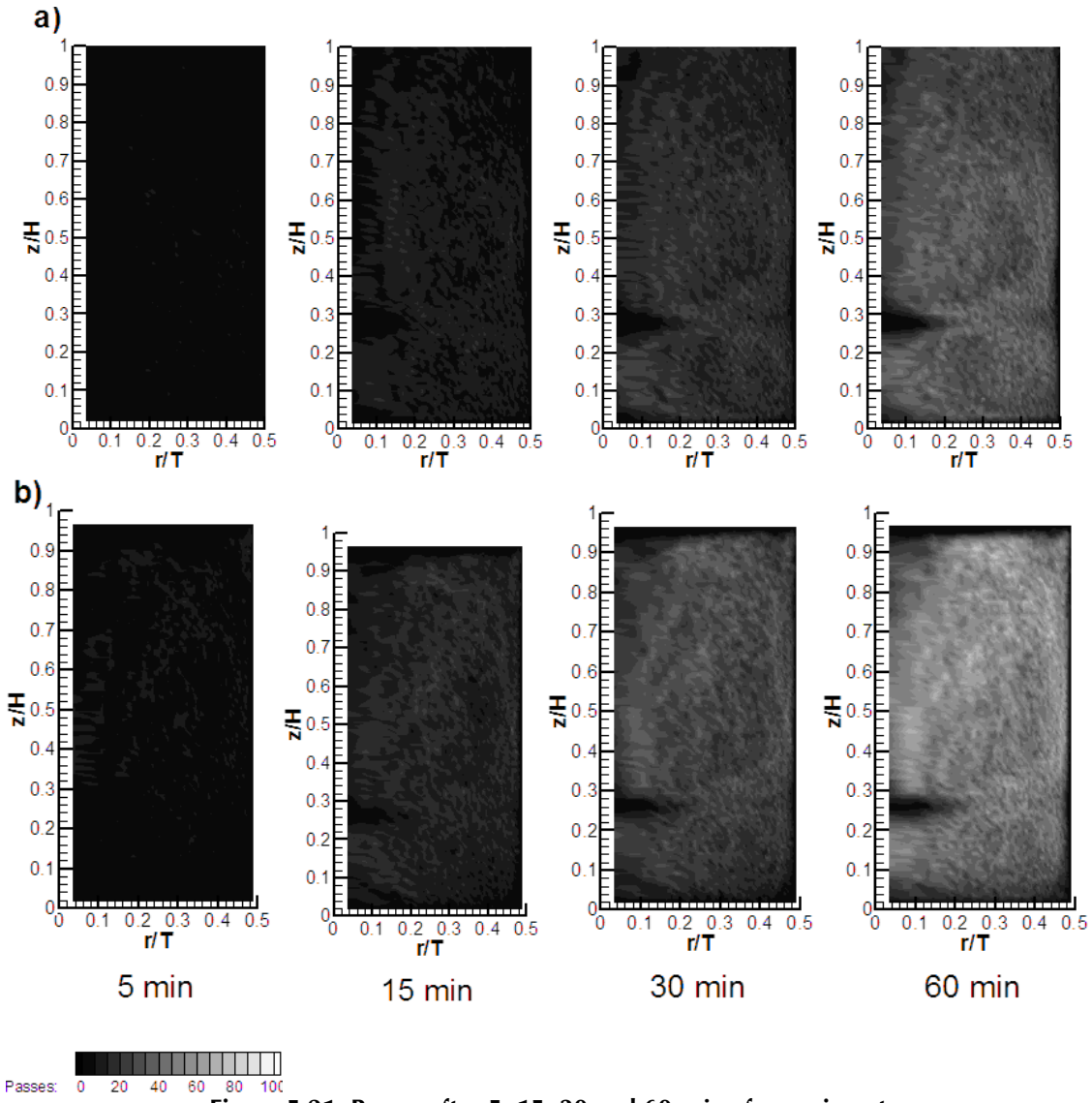

Figure 5-21: Passes after 5, 15, 30 and 60 *min* of experiment:
a) large geometry RT300 and b) small geometry RT480; in both case *vtip* = 1.58 *m/s*

at the same tip velocity in both so that N=480rpm in the smaller vessel.

Since the main interest of this comparison is to assess if the size has an effect on the acquisition of the data, the data used for this comparison are the non-interpolated ones to avoid selective interpolation influencing the comparison. For the small geometry, the number of passes increases much more quickly than for the large. After 30*min*, the number of passes recorded in the small geometry is almost the same as the number of passes recorded in 60*min* in the larger geometry. This result leads to the conclusion that

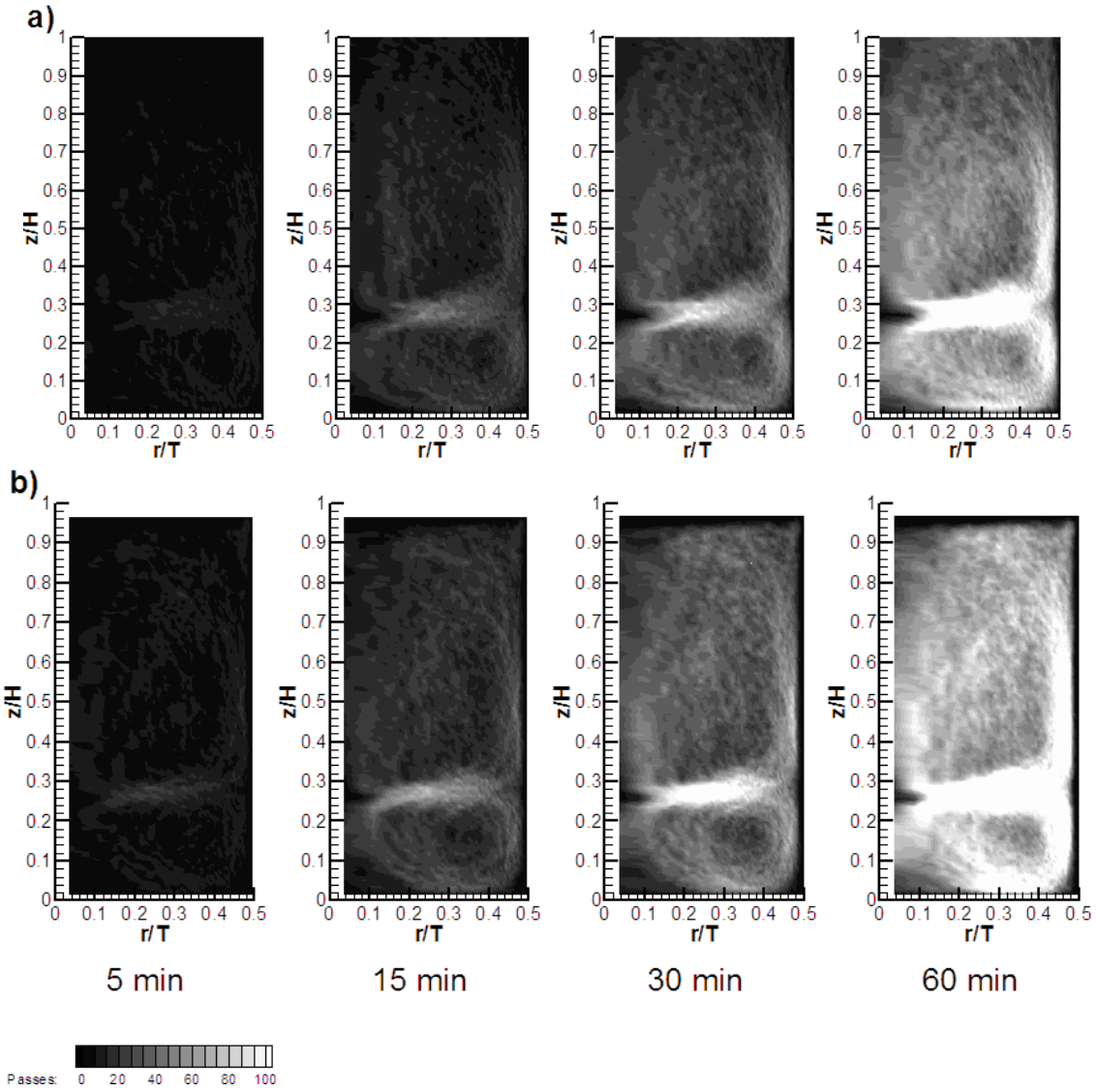

Figure 5-22: Interpolated passes after 5, 15, 30 and 60 *min* of experiment: a) large geometry RT300 and b) small geometry RT480; in both case *vtip* = 1.58 *m/s*

in a small tank the higher number of events per time recorded allows a quicker description of the system and the experiments can be run for a shorter time in order to achieve the same level of information. Similarly to Figure 5-21, Figure 5-22 shows the passes as function of time for the interpolated data. In this case, the difference between the two experiments is less evident even though for the small geometry there is still a huge benefit in using it. Having shown how the geometry influences the data acquisition process, it is important to assess if the accuracy of the velocities found within the small geometry in relation to the literature is better or worse than the large geometry. Hence the radial velocity profiles are again compared.

In Figure 5-23, it can be seem that, in terms of velocities, the small geometry gives very similar results to the large one. Close to the impeller, r/R=0.25 and 0.4, for the smaller size, the profile is more narrow around the impeller plane and the maximum

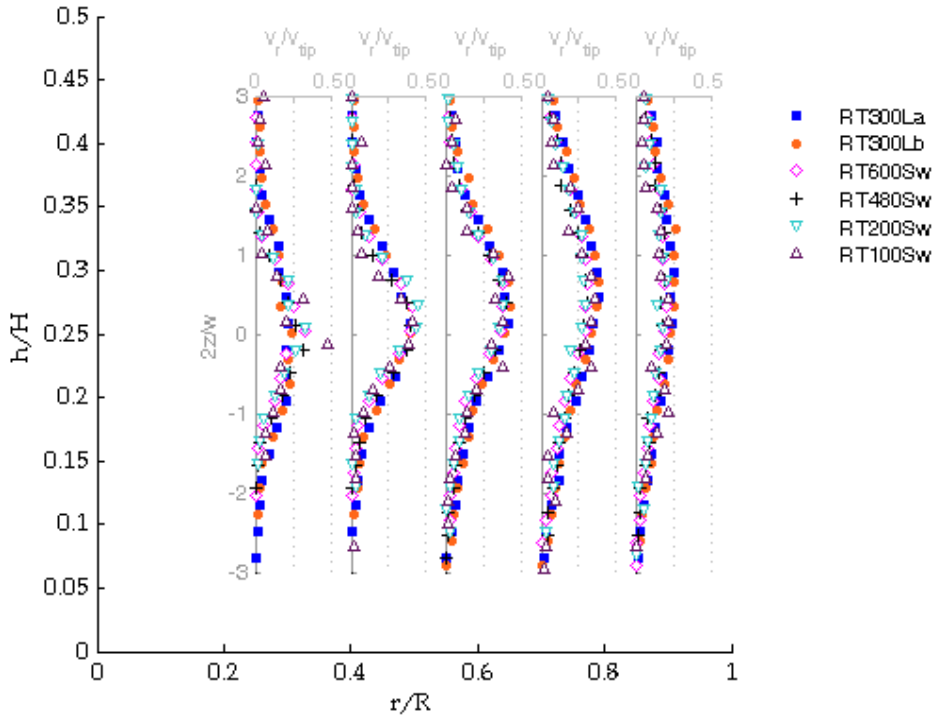

Figure 5-23: Comparison of Radial velocity profiles for large and small scales (PEPT, *L = large*, tracer a = 600*micron* & b = 250*micron, S = small, w = salt solution*)

dimensionless radial velocities are higher. On the other hand, further out, higher velocities are found with the larger vessel. This may be due to the fact that close to the wall, the cell dimensions for the small scale, are small compared to the accuracy of the locations position (see Section 5.1), so that the accuracy in those cell is worse. However, the maximum dimensionless velocities are still underestimated with respect to the ones reported in the literature.

Figure 5-24 shows all the dimensionless velocity components calculated during an experiment for a specific radius, r/R=0.3. On the vertical axis is reported the axial position while on the horizontal axis are reported the radial, tangential and axial component velocities. Looking at the radial components it is possible to notice how the single velocities at the impeller plane, z/H=0.25, can reach values close to the impeller tip velocity, however it can also be seen that there are values that are much lower than that, hence when all these values are averaged the final values is the one shown in Figure 5-23. The tangential component, overall the height of the vessel, shows positive values, i.e. same direction of the impeller rotation, as well as negative values, meaning that, regardless the rotational movement of the impeller, there are zones where the fluid moves in the opposite direction of the impeller.

Finally, the axial velocity component shows negative velocities obove the impeller plane and positive axial velocities below it. Such velocities are expected since the liquid flows into the impeller from the top and the bottom to be, subsequently, radially discharged.

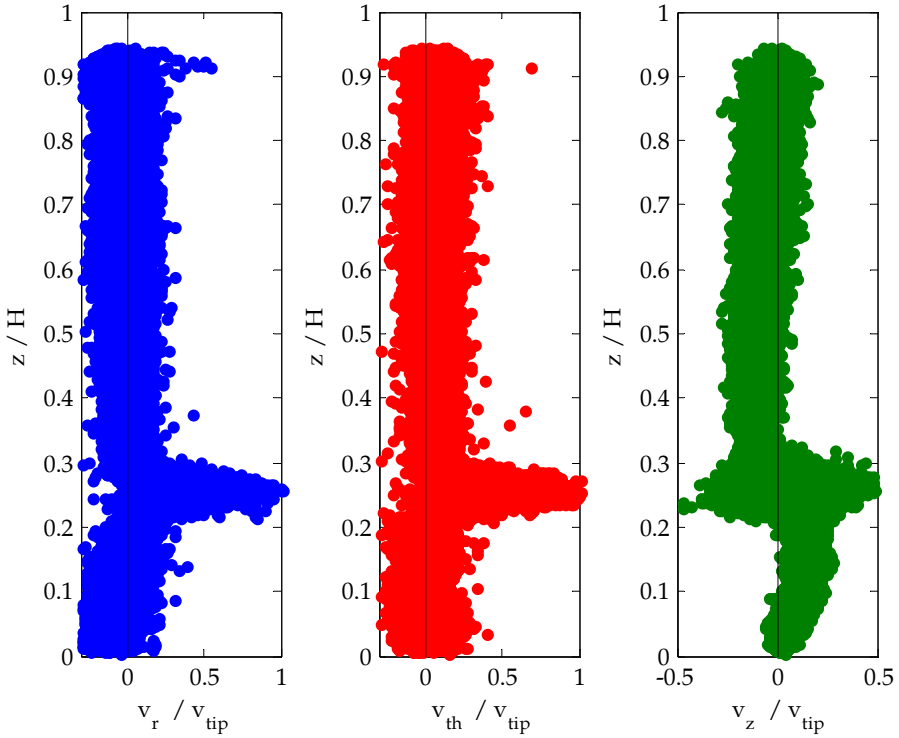

Figure 5-24: Velocity components at constant radial position $r/R = 0.33$ a) v_r/v_{tip}; b) v_{th}/v_{tip}; c) v_z/v_{tip}. (PEPT, small geometry, salt solution, $N = 480rpm$)

5.7.2 Sucrose solution

From the previous Section, it can be concluded that velocities in smaller geometries can be described in a shorter time with higher accuracy close the impeller while close to the wall the velocity are lower than the ones found on the large scale. The next parameter investigated for the small scale was how the liquid viscosity influences the velocity. This Section should prove if the tracer perfectly follows the liquid or if there is slip between particle and media; in other words, since the viscosity of sucrose solution is higher than the salt solution thus increasing the drag on the tracer particle, the possibility of slip should be minimised. Therefore, if the velocities recorded for this fluid are the same as the previous case since the flow is still turbulent, it can be assumed that the tracer reproduces perfectly the motion of the liquid. Velocity distributions for the salt and the sucrose solutions are reported in Figure 5-25; the velocities refer to the

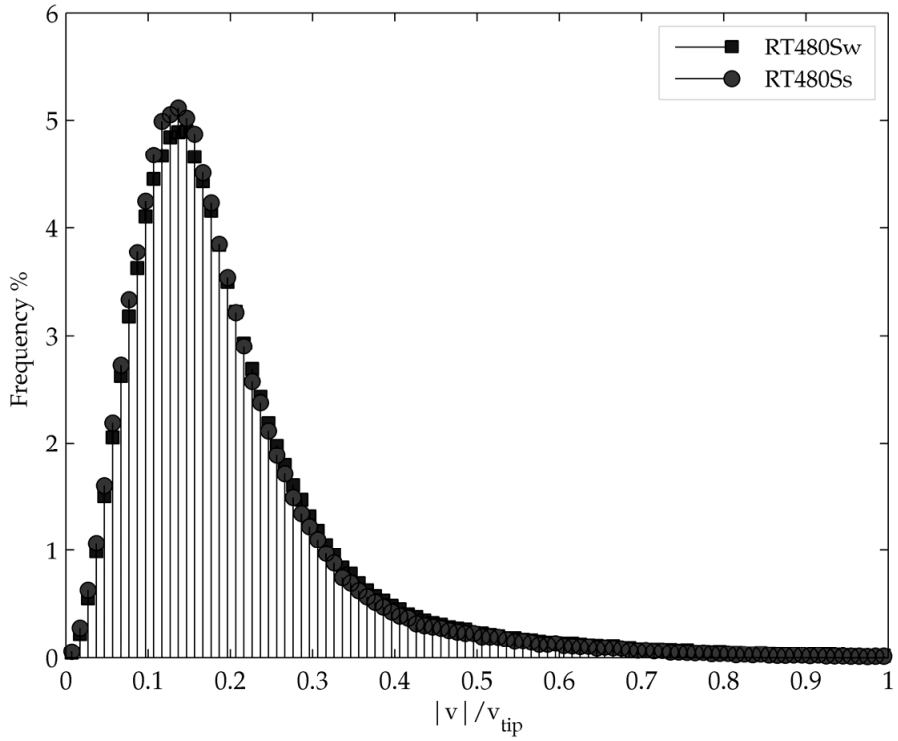

Figure 5-25: Velocity magnitude distribution for the small geometry (*N* = 480*rpm*, *w* = salt solution, *s* = sucrose solution)

absolute velocity overall the vessel. As shown in the graph, the two distributions look absolutely identical in the experimental error margins. Though the Reynolds number is different for the two experiments, $Re = 1.1\times10^4$ and 3.4×10^4 for the salt and sucrose solution, respectively; the flow is still turbulent since $Re > 1.1\times10^4$ velocities developed in the system are equal for the two cases, since the geometry and the impeller speed are the same. Considering the large similarity in the velocity distributions between these two experiments; rather than to plot the same type of graph for all the rest of experiments, which it would be pointless, the values of mean, mode, standard deviation as well as skewness of these distributions are reported in Table 5-2 and compared with the rest of the experiments done. While the mean values and standard deviation give information on the main flow velocity and how much the velocity values are spread, the mode is the most frequent velocity detected in the system and the skewness measures

the asymmetry of the distribution (positive values mean that the distribution is shifted towards right and vice versa). In probability theory the mean, standard deviation and the skewness are also known as first, second and third moment of the probability density function and have the form of:

$$\mu = \sum_{j=1}^{n} v_j \cdot F(v_j)$$
$$\sigma = \left(\sum_{j=1}^{n} (v_j - \mu)^2 \cdot F(v_j) \right)^{1/2} \qquad (5.9)$$
$$\gamma_1 = \sum_{j=1}^{n} \left(\frac{v_j - \mu}{\sigma} \right)^3 \cdot F(v_j)$$

Here n is the total number of bins used to calculate the velocity distribution, $F(v_j)$ is the probability density function of the velocity magnitude and v_j is the velocity value of the j^{th} bin.

Table 5-2: Mean, mode, STD and skewness for velocity distributions for all the experimental conditions used in PEPT

Experiment	N [rpm]	Re	v tip [m s^-1]	Mode	Mean	STD	Skewness
RT300La	300	1.61E+05	1.58	0.1767	0.2333	0.1308	1.612
RT300Lb	300	1.61E+05	1.58	0.1667	0.2347	0.1342	1.666
RT600Sw	600	1.38E+05	1.98	0.1464	0.2006	0.1341	2.072
RT480Sw	480	1.10E+05	1.58	0.1368	0.1929	0.1266	2.109
RT200Sw	200	4.60E+04	0.66	0.1266	0.1949	0.1300	2.141
RT100Sw	100	2.30E+04	0.33	0.1377	0.2089	0.1354	1.940
RT600Ss	600	4.25E+04	1.98	0.1264	0.1945	0.1260	2.029
RT480Ss	480	3.40E+04	1.58	0.1352	0.1864	0.1173	1.960
RT300Ss	300	2.12E+04	0.99	0.1371	0.1850	0.1157	1.846
RT200Ss	200	1.42E+04	0.66	0.1253	0.1647	0.1289	2.104

In the above table the data are divided in three groups: large scale, small scale salt solution and small scale sucrose solution. Looking at the values of the different statistical quantities within each group it is possible to notice how each case is consistent with the similar experiments. Comparing the large scale to the small, both the mode and the mean values are higher for the large scale, suggesting that the overall dimensionless velocity is higher in these cases; this might be possibly due to the higher

Reynolds number in the large vessel. In accordance to this conclusion, it can be notice also how in the small scale the experiments with the sucrose solution show slightly lower mean and mode values. In terms of skewness, the biggest difference occurs between the small and the large scale, larger positive values for the small vessel suggest that in this case there are higher velocities than in the large vessel; this agrees with what has been speculated in Section 5.7.1.

5.8 Conclusions

In this Chapter, for the first time, the PEPT technique has been tested and evaluated against a well-established set of data for the Rushton turbine for stirred liquid systems. The basic parameters in the program `track` used to produce the raw data have been proven to affect the accuracy of the final locations generated by the system. Thus, a study to assess the optimum parameters for each experimental set up is recommended.

Once the locations are obtained from the PEPT system, Lagrangian velocities are calculated by differentiating position versus time. Section 5.3 shows how Cylindrical or Cartesian coordinate systems lead to different results according to the type of fluid motion; i.e., for circular movements, the Cylindrical reference system leads to more accurate velocities.

The sizes of the tracer (250μm and the 600μm) used in this study had no influence on the results, since both of these sizes are small enough to follow the liquid closely.

Comparing radial velocities obtained with PEPT to published data (Dyster *et al.*, 1993, and Wu and Patterson, 1989), it is clearly seen that PEPT underestimates velocities (about 50% lower than literature values) in the region near to the impeller. This problem has been addressed and explained as being because of the limited spatial

resolution of PEPT in the high velocity region. Selective interpolation of the raw data has been proposed (and justified) in this region, leading to an increase in the calculated velocities, which significantly brings them closer to the literature values.

Finally, the effects of scale and viscosity have been investigated and no major effects on dimensionless velocities (measured values normalised by impeller tip speed) for this system have been observed. This finding confirms the assumption that, at the same Re in turbulent conditions, the liquid velocities can be scaled with the impeller tip velocity.

Chapter 6

Computational Fluid Dynamics: Results

In this Chapter 6 the results of CFD simulations are reported. In the first Section 6.1 the two different meshes (structured hexahedrons and unstructured tetrahedrons) and the two different turbulence models (*RNG* k-ε and k-ω) are compared to each other in terms of velocity profiles, energy contours, power numbers and flow number. By analysing the velocity profiles some unexpected high velocity values were found behind the impeller blades. Thus, in Section 6.2, an in-depth study of the velocity flow field developed behind a blade was carried out. In the last Sections of this Chapter (Sections 6.3 and 6.4), particle tracking simulations were performed and discussed.

The simulations of this Chapter refer to the geometry described in Section 4.2.2 with impeller speed, N, equal to $5rps$ ($300rpm$).

6.1 Mesh type and turbulence model comparison: steady state simulations

6.1.1 Velocity Profiles

The dimensionless radial, tangential and axial velocity components for the four models analysed in this Section are reported in the contour plots in Figure 6-1, Figure 6-2 and Figure 6-3 respectively. The top row of contour plots concern the two turbulence models, *RNG* k-ε and k-ω, for the structured mesh; while, the other two graphs are the results of the same turbulence models applied to the unstructured mesh. For all the plots the legend used was the same and it is reported underneath them for each case. For each condition, a side view and a bird eye view of a xy plane are shown.

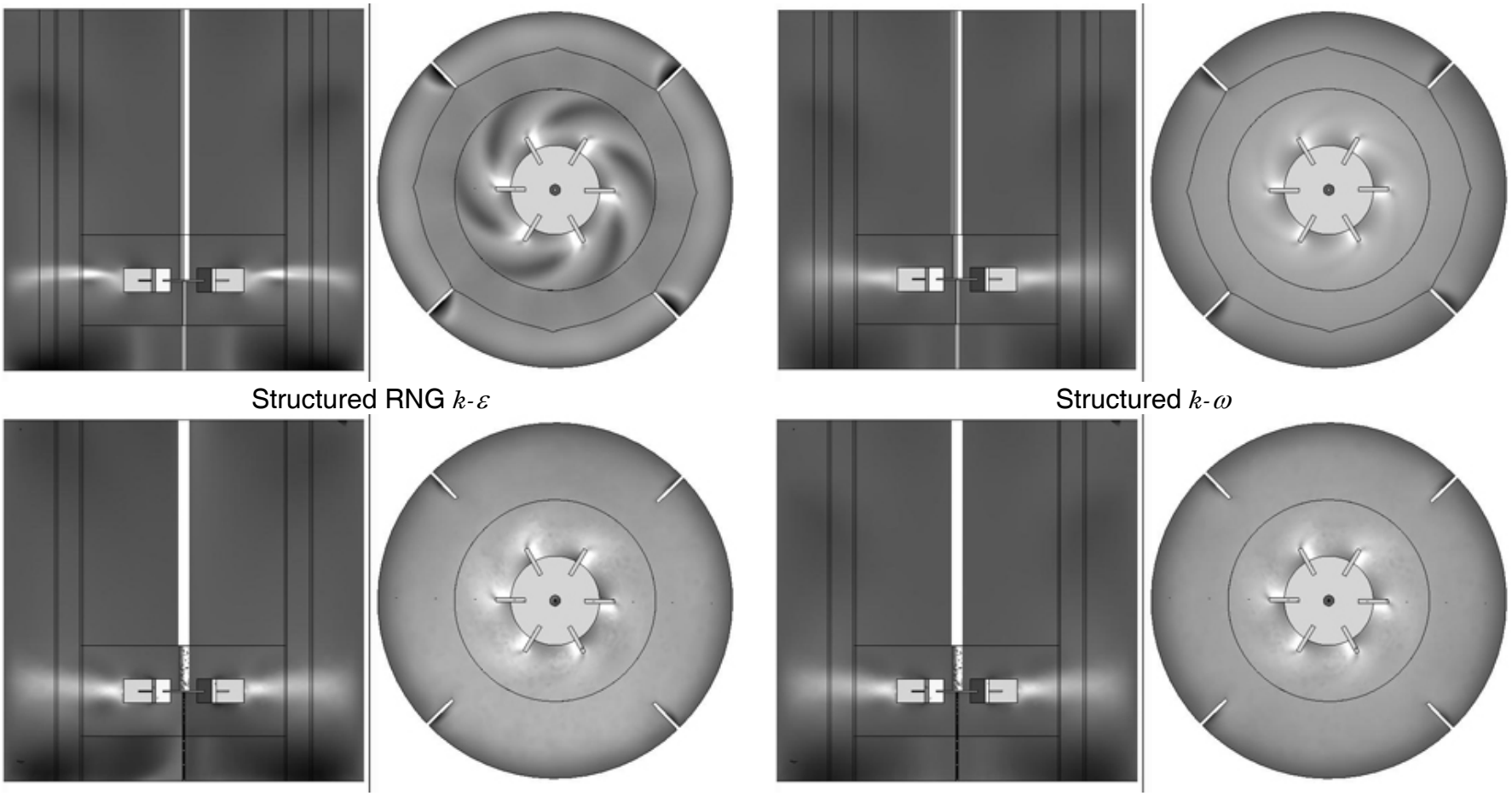

Figure 6-1: Radial Velocity

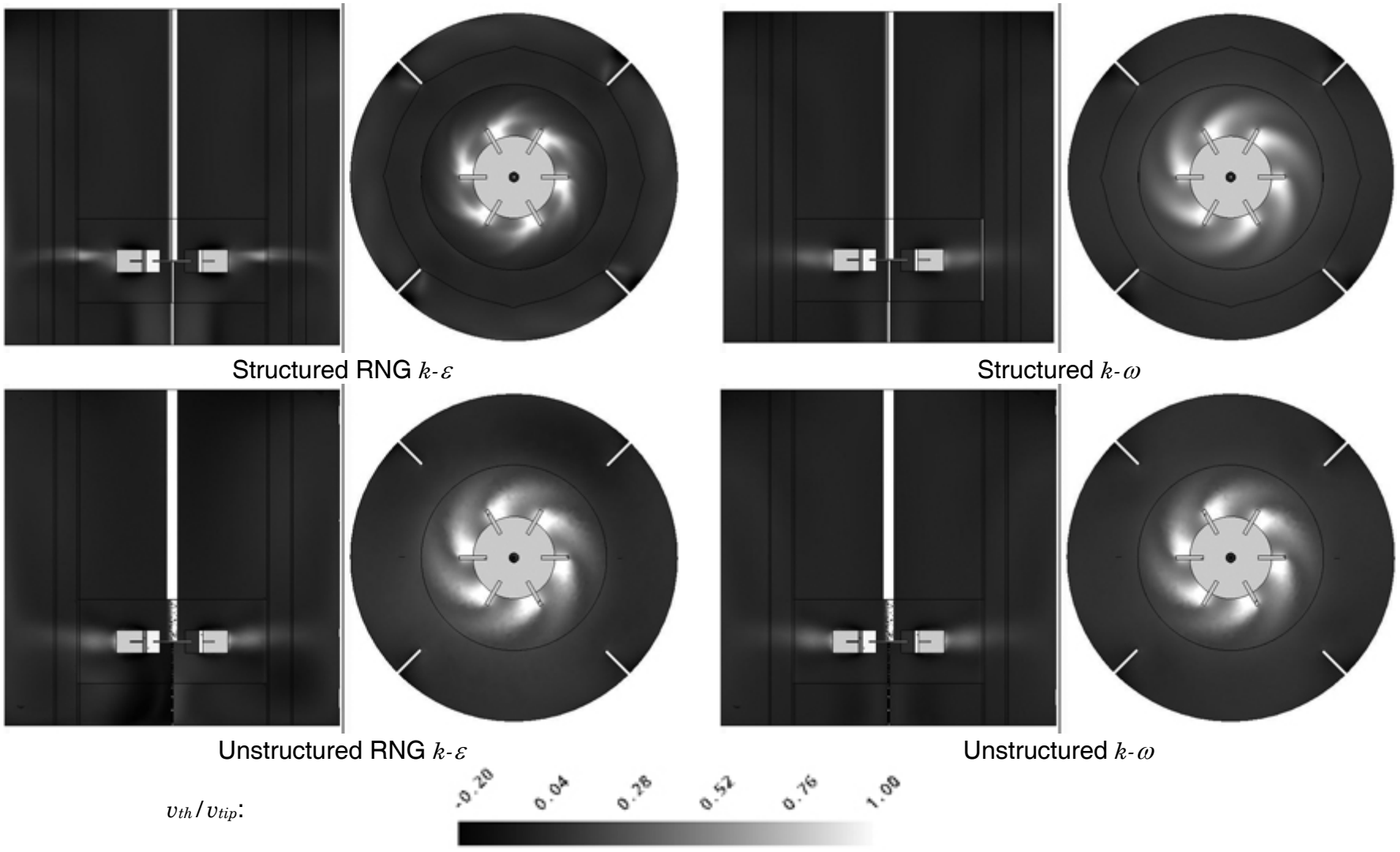

Figure 6-2: Tangential Velocity

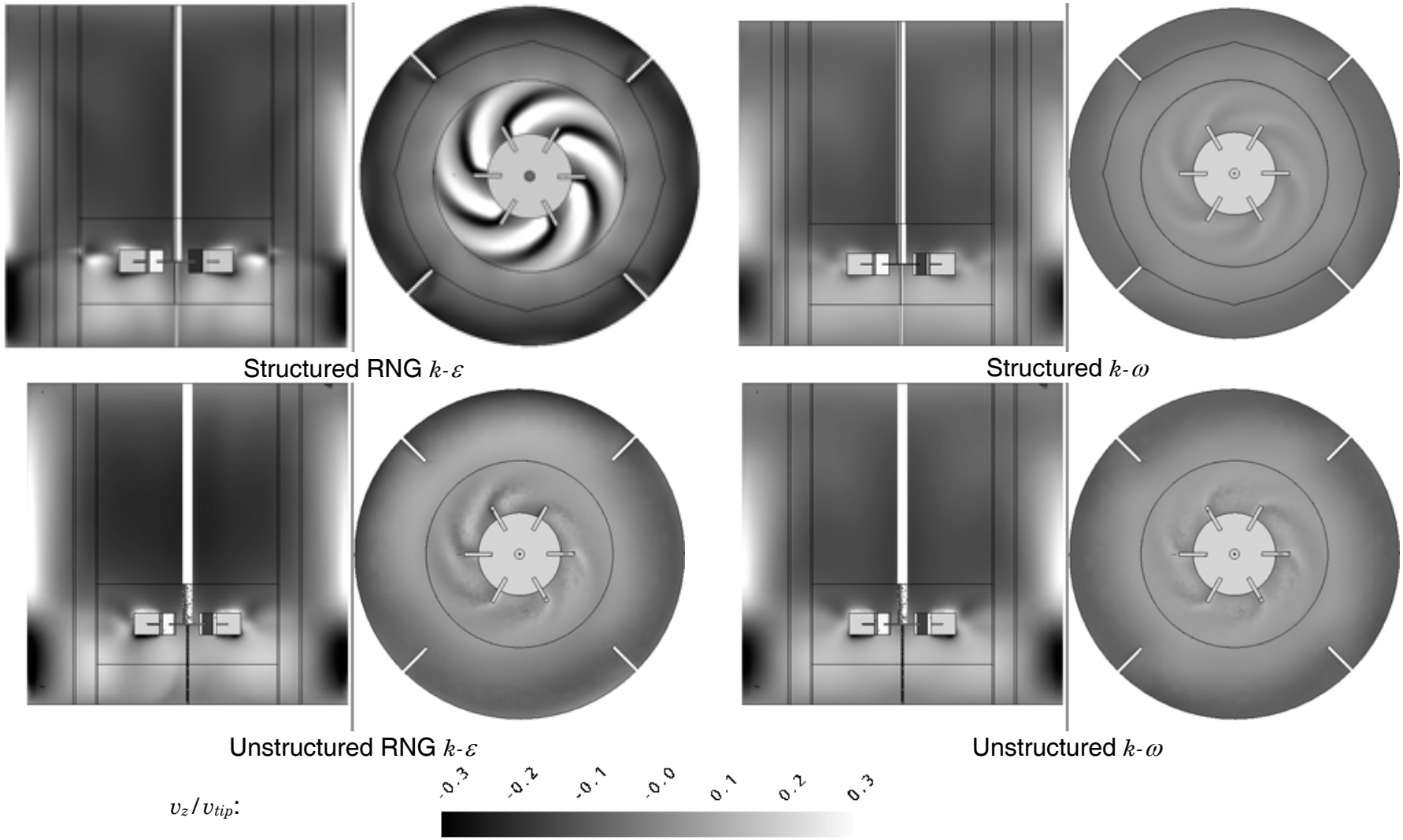

Figure 6-3: Axial Velocity

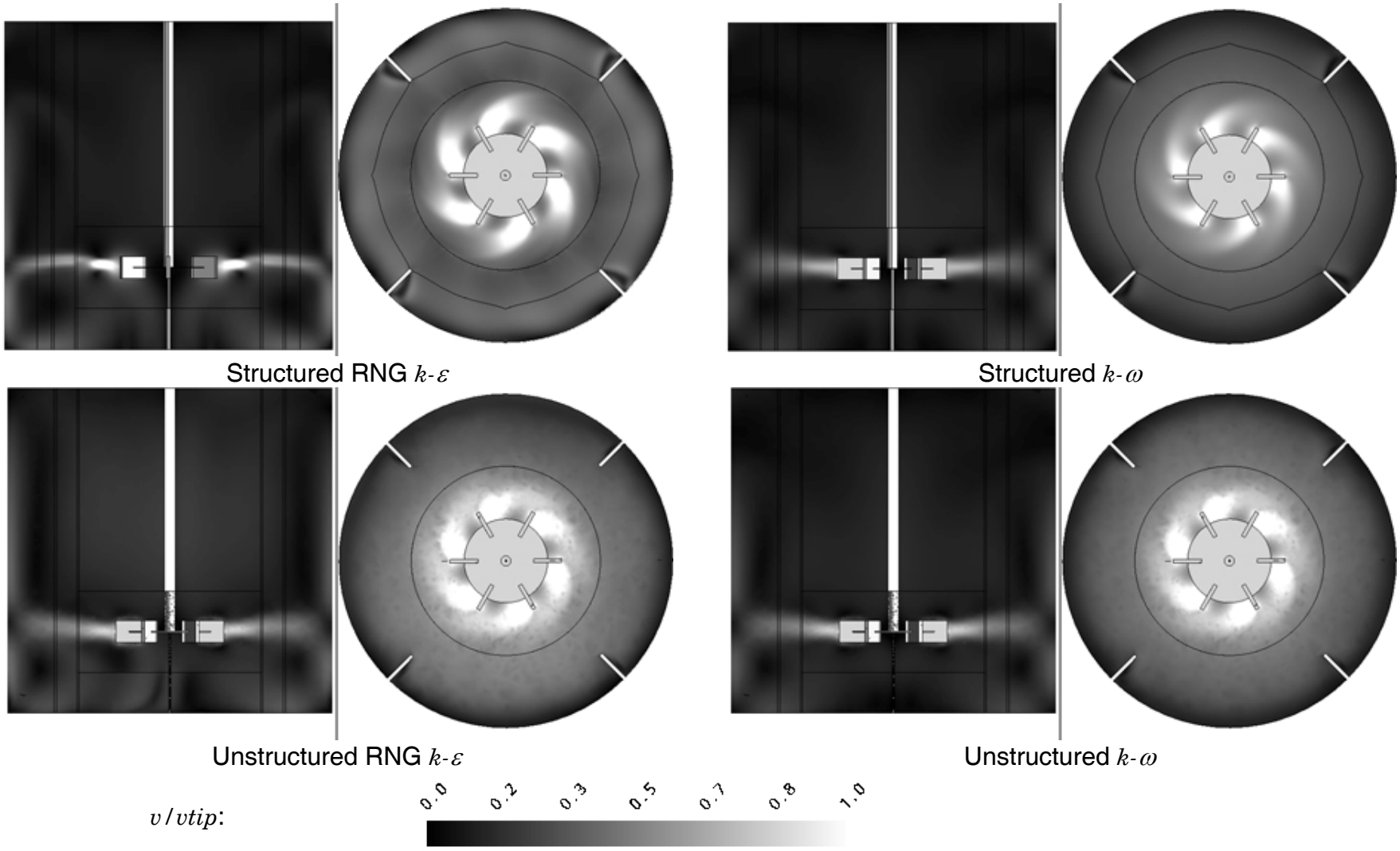

Figure 6-4: Velocity magnitude

Side by side comparison of the contour plots show how the models and mesh types lead to different velocity flow field. The radial velocity in Figure 6-1 illustrates how the k-ω model is not affected by the mesh type while the *RNG* k-ε model gives different results for the two different meshes. In addition the unstructured mesh is not affected by the model used resulting in very similar contour plots. The *RNG* k-ε model applied to structured grid is the only case, which shows some zero radial velocities in the proximity of the impeller on the *xy* plane view. Also the k-ω model on the hexahedral grid shows the same pattern but less evidently.

Concerning tangential and axial component velocities similar conclusions can be drawn: the tetrahedral mesh is not affected by the model used and it is consistent along the three component of velocity. The k-ω model applied to the structured mesh provides velocity contours which have intermediate values between the unstructured cases and the *RNG* k-ε model on the structured grid. The largest discrepancy between the four cases appears for the axial velocity, where the *RNG* k-ε model shows, for the structured mesh, zones with alternative positive and negative axial velocities as if it would be a Section of a circumferential vortex. This could be associated to the trailing vortex of the lower tip of the blade. In effect, for this case, in the radial and tangential side views it can be noticed how the impeller discharge stream directs upwards compared to the other cases. Therefore, the two trailing vortices are possibly not symmetric to the impeller plane, thus the *xy* plane intersects the lower one resulting in the axial contour of Figure 6-3.

Figure 6-4 shows the contour plots of the absolute velocity in the same four cases previously. To be noticed in this set of plots it is the high velocity region

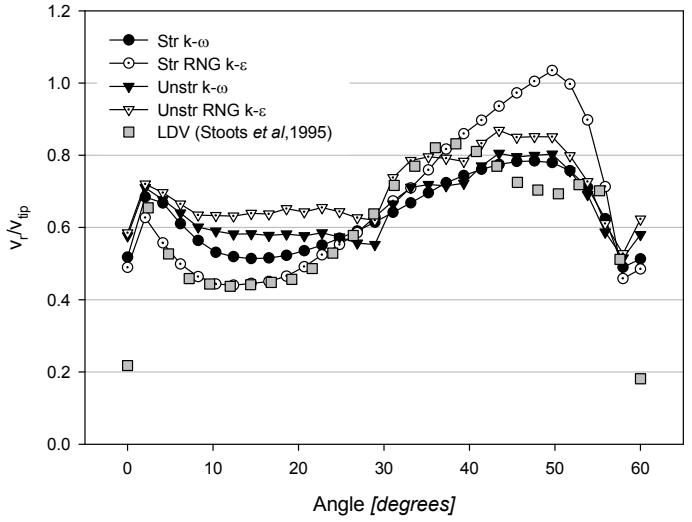

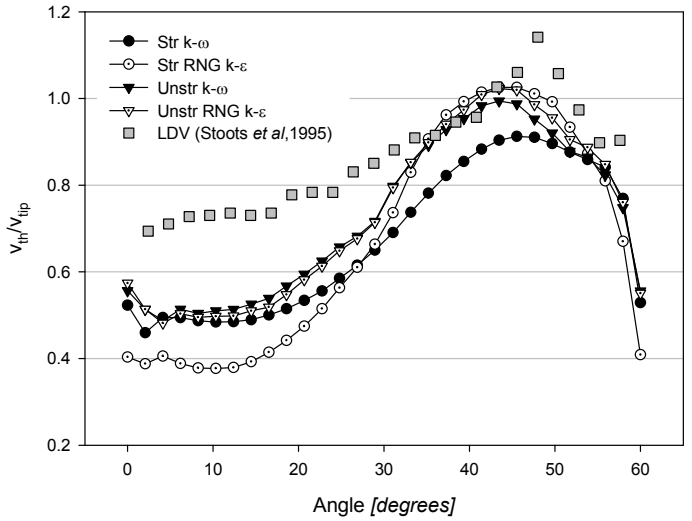

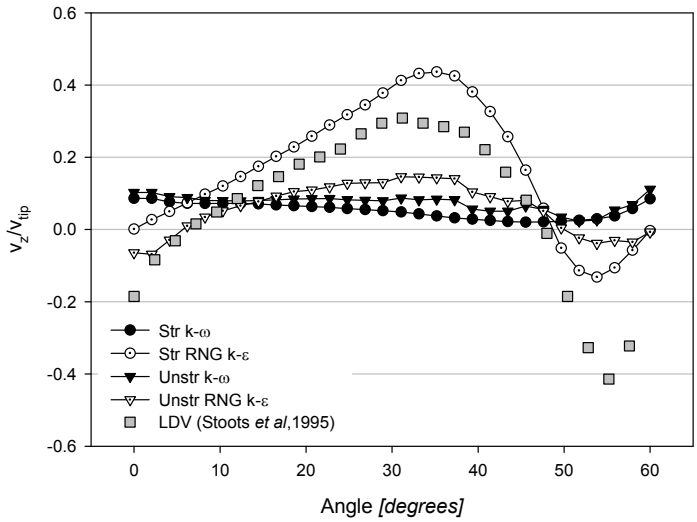

Figure 6-5: Azimuthal radial, tangential and axial velocities at the disc plane at r/R = 0.344

appearing behind the blades of the impeller; furthermore, this velocity appears from the legend to be higher than the velocity of the tip blade (up to 40-50% greater than v_{tip}). Despite this result seems to be wrong some researcher shown in their graphs similar experimental results even thought they do not highlight the phenomena (Yianneskis and Whitelaw, 1993; Stoots and Calabrese, 1995). Further work focusing on this issue is reported in Section 6.2.

After the discussion of the qualitative analysis of the flow field velocity generated by the four models, Figure 6-5 shows the azimuthal radial, tangential and axial velocity components, normalised to the impeller tip velocity, at the disc plane and 1.5mm off the blade tip (r/R=0.344). The motion of the blade in this plots is from left to right, thus angle values between 0 and 30 degrees are considered in front of the blade pass and values between 30 and 60 degrees behind it. The angular profiles are also compared to the experimental data published by Stoots and Calabrese, 1995, using LDV technique. The model results show a general agreement with experimental data, however some models results in lower discrepancies with the LDV velocities than others. Concerning radial velocities prediction, only the *RNG* k-ε models applied to the structured grid matches exactly the experimental profile, but only for angles between 0 and 40 degrees. Just after the blade passage all the models overpredict the radial velocity (+14-50% depending on the model). This can be associated to the fact that the high turbulence in that zone is not well predicted by the different models. On the other hand, the models shows a better agreement to the experimental data for the tangential velocity components in this zone, while they all underpredict the tangential velocity for angles between 0 and 35 degrees (–30-45% depending on the model). Finally, for the axial velocity, only the *RNG* k-ε model applied to the hexahedral mesh follows closely the

experimental profile though the values are overpredicted for angles between 0-50 degrees and undepredicted the rest. The other three cases do not show even a similar trend to the LDV data.

From this analysis the *RNG* k-ε applied to the structured mesh seems to perform the best in terms of velocity components close to the impeller, in regions far from the turbine all the models are comparable and results in very close flow patterns. Kukukova *et al.*, 2005, also confirm that the k-ε applied to structured grids results in better velocity profiles than if it is applied to unstructured meshes. In contrast, Hitomi *et al.*, 2006, concluded in their work that the k-ω predicted the tangential flow more accurately than the k-ε, this is probably due to the fact that they simulated an unbaffled vessel and the turbulence models might give different response.

6.1.2 Energy Contours

Turbulence kinetic energy and turbulence kinetic energy dissipation rate have been often analysed to assess the goodness of turbulence models (Kresta and Wood, 1991; Schäfer *et al.*, 1997; Jenne and Reuss, 1999; Ng and Yianneskis, 2000; Aubin *et al.*, 2004; Micheletti *et al.*, 2004; Yeoh *et al.*, 2004a; Deglon and Meyer, 2006). All the authors, who have published their work using RANS models, agree that these models do not predict correctly turbulence properties. The main reason for this is considered to be the assumption in the RANS model that the turbulence in stirred vessels is isotropic. In fact, it has been proven, amongst others by Kresta, 1998; Lee and Yianneskis, 1998, that in the proximity of the impeller discharge stream the turbulence is anisotropic while it can be considered isotropic in the rest of the vessel. Therefore, the model usually results in underestimation of these turbulence properties in particular in the stirrer zone. Since the aim of this work is focused on the flow field developed in the vessel rather

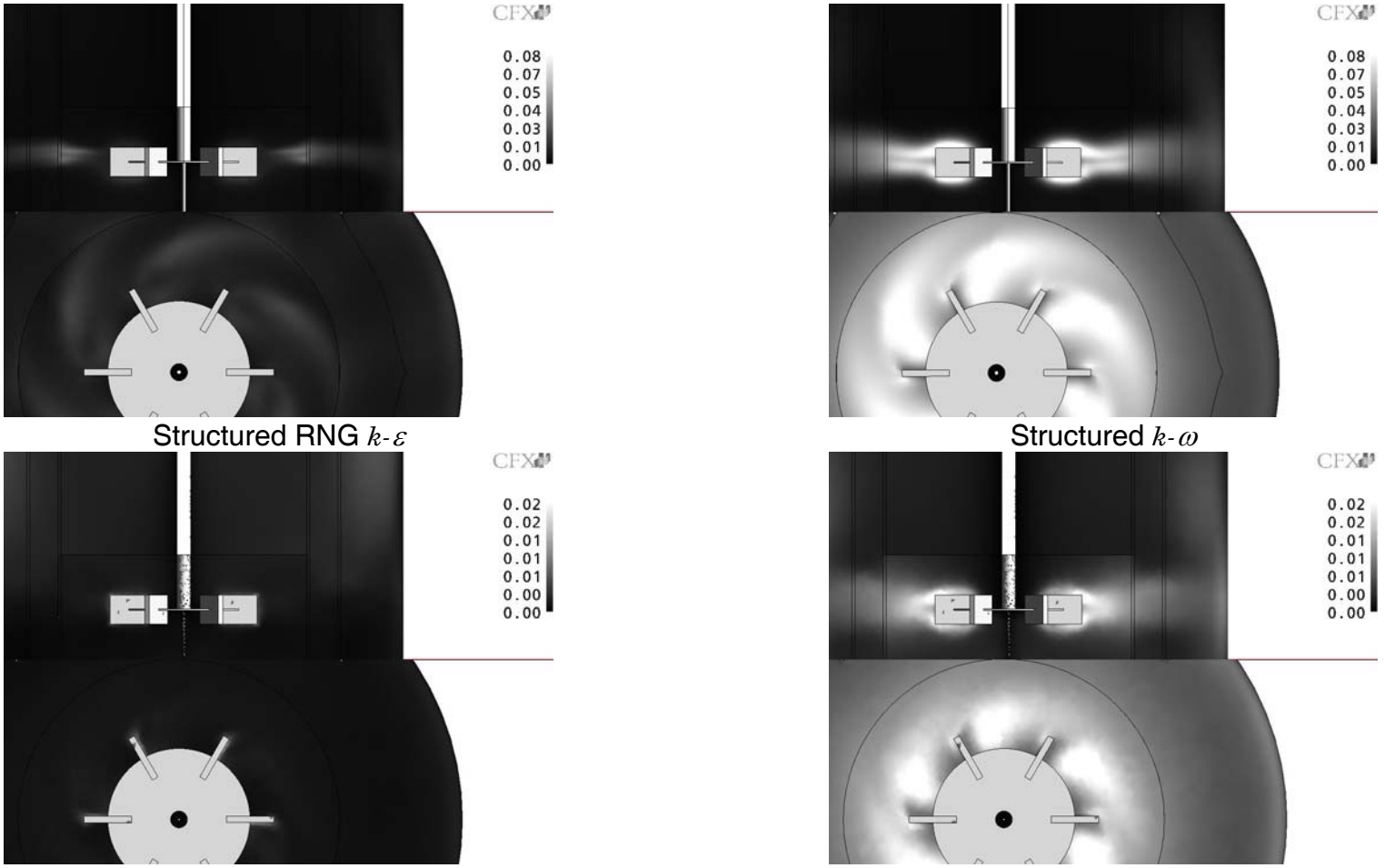

Figure 6-6: Normalised turbulence kinetic energy contour plots

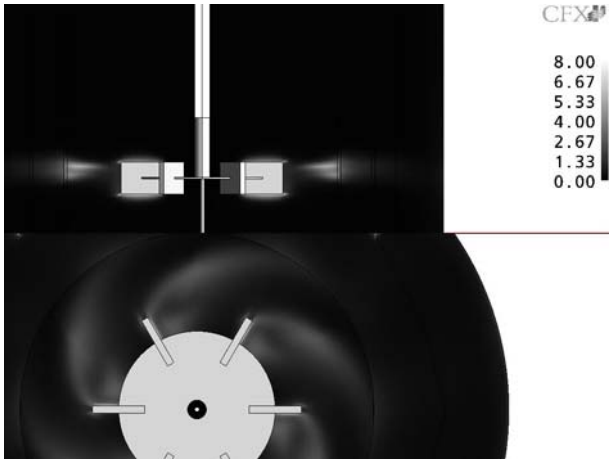

Structured RNG k-ε

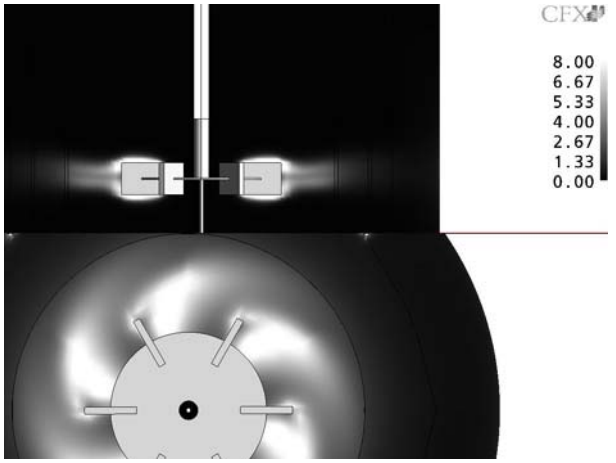

Structured k-ω

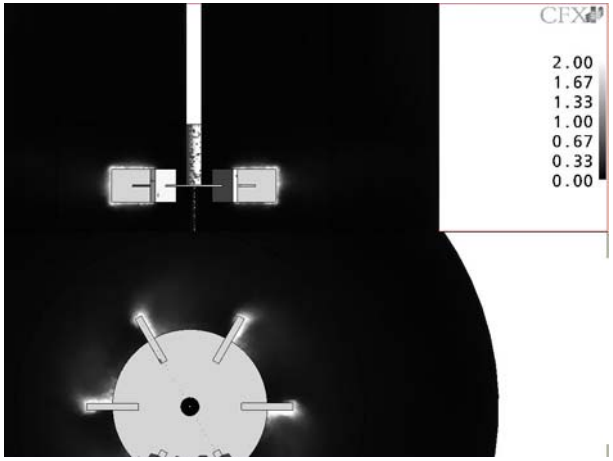

Unstructured RNG k-ε

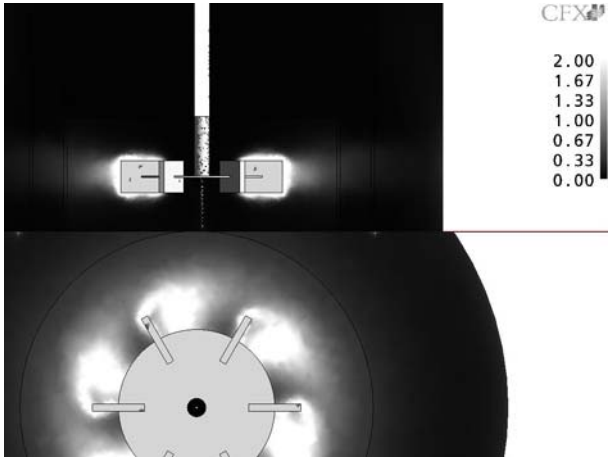

Unstructured k-ω

Figure 6-7: Normalised turbulence kinetic energy dissipation rate contour plots

than a comprehensive study on turbulence, the lack of agreement between model and experimental results it is considered only marginally significant. However, a comparison of the turbulence properties between the different models used in this work is reported in this Section.

Turbulence kinetic energy, k, and kinetic energy dissipation rate, ε, contour plots are reported in Figure 6-6 and Figure 6-7, the variables used here were normalised versus v_{tip}^2 and N^3D^2 respectively. From the graphs, two main considerations emerge clearly: the structured grid models lead to turbulence properties about four times higher than the results achieved using the unstructured mesh and within a type of grid the k-ω model predict the turbulence properties more accurately than the *RNG* k-ε. The latter result should suggest to investigate more the k-ω model and to explore its real potentials in predicting turbulence quantities. For this kind of assessment the simulations carried out for this thesis are inappropriate since the time step used (on step every 15degrees) is too large for turbulence studies (one step every degree).

6.1.3 Power Number and Flow Number

Power number and flow number, calculated for the different models as described in Section 2.3, are compared hereafter.

In Table 6-1 there are reported the values of *Po* calculated in the three methods described in 3.6.1 and the *Fl* determined by using equation (2.8) and (3.27): values in the first column were obtained by integrating the turbulence energy dissipation rate overall the vessel, in the second column there are collected the *Po* obtained by calculating the torque acting on the impeller and on the shaft, where the values in the third column refer to the torque acting on the baffles and on the external walls of the

vessel, finally the last column values are the *Fl* calculated on a surface of revolution at r/R=0.34, just off the blade tips.

In the previous Section 6.1.2, the underestimation of turbulence properties for RANS models was highlighted and confirmed; as consequence the power number calculated by integrating the turbulence energy dissipation is also largely underpredicted. However, it can be noticed how the *Po* values obtained using the k-ω models are substantially larger than the values obtained from the *RNG* k-ε models using the same type of grid. Concerning the primary and secondary power numbers calculated using the torque acting on the impeller and on the baffles; it is possible to see how a better prediction is achieved. Experimental evaluations of power number are reported in literature, Bujalski *et al.*, 1986, studied the power number dependency on material thickness and scale and they found that for a geometry similar to the one used in this research *Po* values between 4.4 and 5.1 depending on the thickness of the blades. Yianneskis *et al.*, 1987, reported for a similar geometry a power number equal to 4.8. In more recent time Rutherford *et al.*, 1996, assessed again the effect of disk and blades thickness on the mixing characteristics of Rushton turbines finding values of *Po* equal to 4.8 – 5.5, which are in good agreement with the work of Bujalski *et al.*, 1986. For the structured grid the *RNG* k-ε model gave consistently higher *Po* than the k-ω, while for the tetrahedral grid the two models predicted very similar power numbers. This disagree with Nayan, 2004,

Table 6-1: Power number and Flow number comparison

	Po - ε	*Po* - *I*	*Po* - *II*	*Fl*
Struct RNG k- ε	1.90	4.61	5.02	0.72
Struct k- ω	3.30	4.18	4.24	0.69
Unstruct RNG k- ε	0.50	4.68	4.65	0.71
Unstruct k- ω	1.19	4.49	4.89	0.66

in fact, the author obtained Po_I about 9-30% higher than Po_{II}; however, he attributed the discrepancy in the results to the coarser mesh resolution used on the external walls and the baffles. The Fl is calculated by integrating the radial velocities on the surface of revolution positioned at the impeller tips as described in Section 3.6.2. According to the profile of the radial velocities on the impeller plane showed in Figure 6-5, the profiles for the *RNG* k-ε models have higher values than the others which results in larger Fl as showed in Table 6-1. The Fl obtained from the *RNG* k-ε is in perfect agreement with the ones published in literature equal to 0.72 (Costes and Couderc, 1988a; Dyster *et al.*, 1993; Nienow, 1997).

6.2 High velocities behind the blades

6.2.1 Velocity contours

As already mentioned in Section 6.1.1 in the region behind the blades the velocity of the fluid can reach values higher than the velocity of the tip itself. This phenomenon is present in literature graphs several times, but it never been highlighted or discussed. In Figure 6-8 there are plotted the velocity profiles vs. the angular position of the blade at the impeller plane for the four models analysed above. The profiles are compared with two set of data from literature; Stoots and Calabrese, 1995, who achieved their experimental results by using LDV techniques, and Revstedt *et al.*, 1998, that performed LES simulations in stirred tanks. As it can be noticed in the plot, the RANS models used in this thesis are in a very good agreement with the experimental data, while the LES values result in an overestimation of these same values.

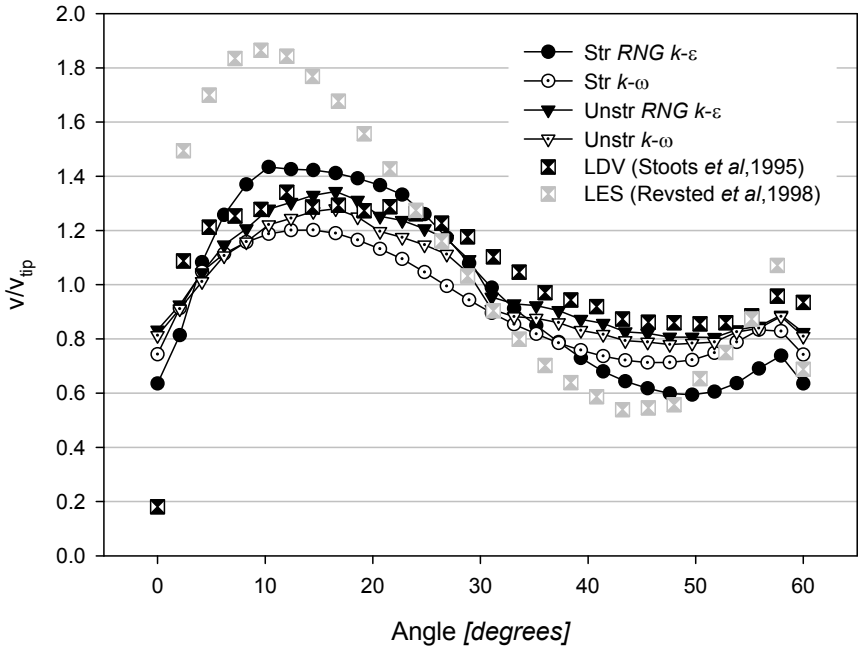

Figure 6-8: Azimuthal velocity magnitude at the disc plane at r/R = 0.344

Yianneskis and Whitelaw, 1993, noticed that there is a considerable amount of suction behind the blade and circulation is evident at angle 10° and 20° (see Figure 6-9). The vector plot, shown in Figure 6-9, indicates velocities relative to a rotating frame of reference which is solid to the blade, therefore, all the vectors refer to the relative motion between the fluid and the blade; since the impeller is moving from right to left with velocity ωr (where ω is the impeller angular velocity and r is the distance from axis of revolution), the vectors pointing towards left have a velocity higher than the impeller speed. Using the results of the *RNG* k-ε model applied to the structured mesh, a similar plot to Figure 6-9 was obtained by defining a z-θ plane positioned at r=0.38D (see Figure 6-10) and by plotting the velocity vectors belonging to this plane, as reported in Figure 6-11a. In Figure 6-11b the velocity magnitude vectors relative to the stationary frame of reference are also reported; the difference between the velocity in

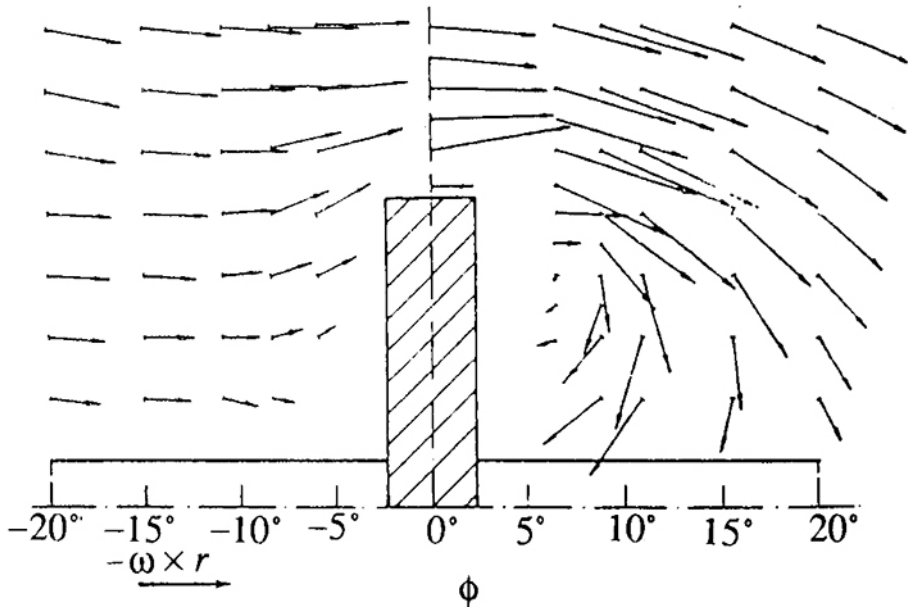

Figure 6-9: Mean velocity vectors around the impeller blade at r = 0.38D z-θ plane from Yianneskis and Whitelaw, 1993.

the stationary and in the rotating frame of reference can be expressed by the equation (6.1), as follows:

$$v_{rot}^{i} = v_{stn}^{i} - \omega r^{i} \qquad (6.1)$$

where the superscript i refers to a general vector positioned at r^i distance from the rotation axis and the subscripts *rot* and *stn* refer to the rotating and stationary frame of reference, respectively. The circulation behind the blade, which is probably the cause of the high velocities in that area, is generate by the negative pressure acting on the back of the impeller blades, in this region the fluid dragged by this depression accelerate to assure the mass conservation creating strong recirculation and turbulence.

6.2.2 PIV Comparison

In order to validate further the presence of high velocities behind the blades of the impeller PIV experiments have been carried out. Two different impeller speeds have

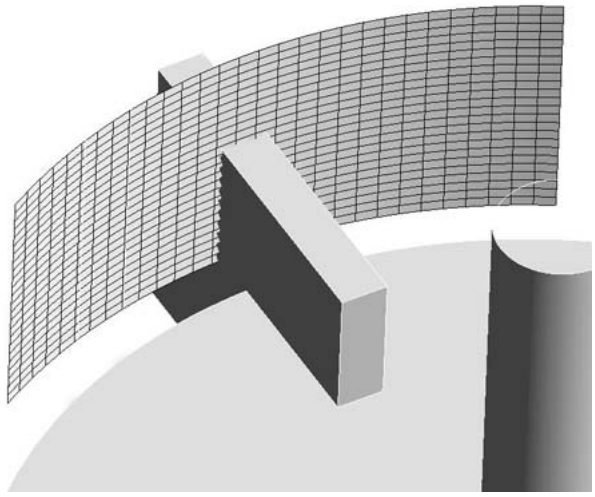

Figure 6-10: Scheme of the position of the z-θ plane at r = 0.38D

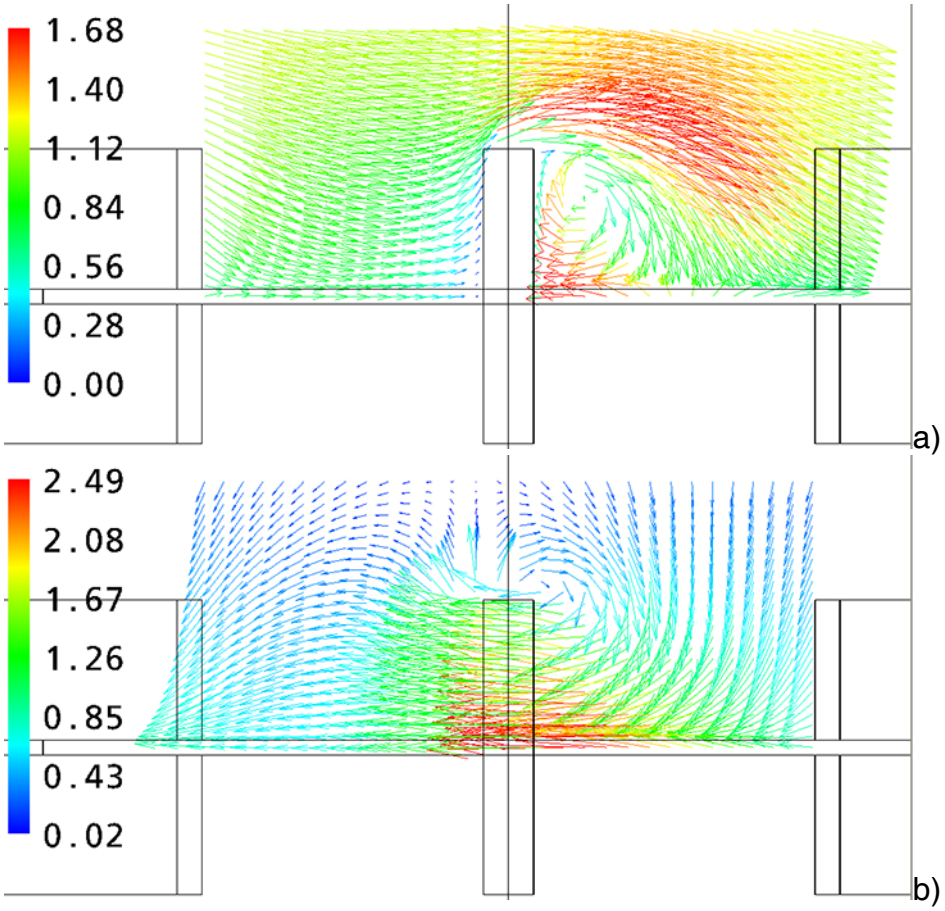

Figure 6-11: Mean velocity vectors around the impeller blade at r = 0.38D z-θ plane (RNG k-ε model on structured mesh): a) rotating system of reference, b) stationary system of reference

been investigated which both led to the same results, this was done to assure the reproducibility of the experiments and the consistency of the results.

As described in Section 4.1.5, the PIV equipment was configured in order to obtain the horizontal velocity profile on the *xy* plane positioned at the impeller disc. The results of the experiment carried out in the small geometry with an impeller speed equal to N=300rpm, which gives a v_{tip} of 0.99m/s, are reported in Figure 6-12. The velocity vector plot in Figure 6-12, shows how the fluid follows the movements of the blades

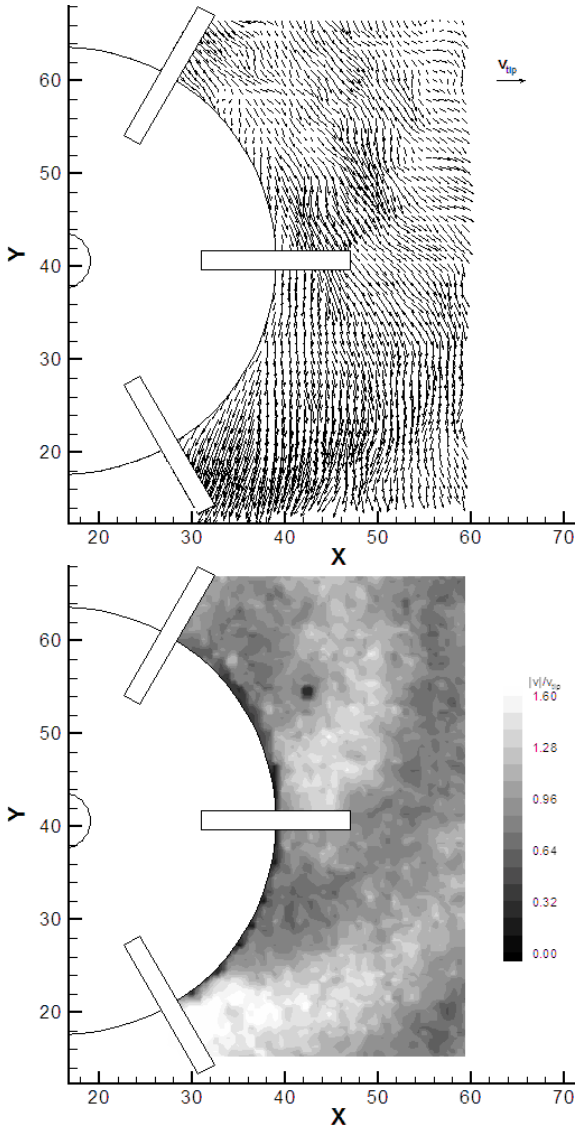

Figure 6-12: Velocity vector plot and velocity magnitude contour for PIV experiment in the small geometry with baffles at 45° with respect of the horizontal blade (*vtip* = 0.99*m/s*).

and in the zones behind the blades it is directed towards them, however in this plot is not evident the circulation around the tip of the blade. Probably the strong radial velocity component at the tip blade nullify that effect, which is evident in the z-θ plane passing trough the middle of the blade in Figure 6-11b. On the other hand, the contour plot of Figure 6-12 displays clearly how the velocities behind the blades can reach values up to 70% higher than the v_{tip}. Finally, it can also be observed that the velocities at the blade, positioned at the lower part of the plot, are higher than the ones at the rear of the central blade; this is probably because the quality of the images was superior in that area and, thus, the PIV software could get velocities that are more accurate.

6.3 Particle Tracking in CFD

In this Section, an overview of the different type of approaches that have been tried in order to achieve particle tracking results using CFD, will be described and discussed.

6.3.1 Integrated Streamlines

The easiest way to obtain trajectories from CFD simulation is undoubtedly the use of streamlines. A streamline is the path traced by a massless particle placed at an arbitrary location in a steady-state vector field. This approach consists of obtaining paths through integration of the velocity flow field according equation (6.2):

$$x_i^n = x_i^o + v^o dt \qquad (6.2)$$

where the superscript o and n refer to old and new tracer position respectively, while the subscript i indicates the time step and v^o is the fluid velocity over the integration time step dt. Streamlines calculation is obtained in post processing (i.e. after the solver have resolved the fluid dynamics of the simulation) and is optimised to achieve effective and quick results giving a good idea of the main flow behaviour. However, being based

only on the fluid vector field, streamlines do not take into consideration any interaction between the particle and the solid boundaries of the system, resulting in non realistic trajectories. Streamlines found for a standard simulation in CFD are shown in Figure 6-13. From the streamlines reported in Figure 6-13, it is possible to notice the regularity in the trajectory overall the vessel; furthermore, since the fluid velocity vectors in a steady state are used to interpolate the streamlines, two different trajectories starting from the same point are identical. Finally, streamlines starting from a location below the impeller plane tends to remain contained in the inferior part of the tank; vice versa, the ones starting from above the impeller never visit the region underneath it.

6.3.2 Steady State Lagrangian Particle Tracking using Sliding Mesh Models

Lagrangian particle tracking in CFD models, as described in details in Section 3.7, consists in solving the fluid dynamics of a system first and then use the results achieved to apply the momentum transfer to a particle determining its velocity, equation (3.29); thus, it is possible to calculate the trajectory of the particle over an integration time step

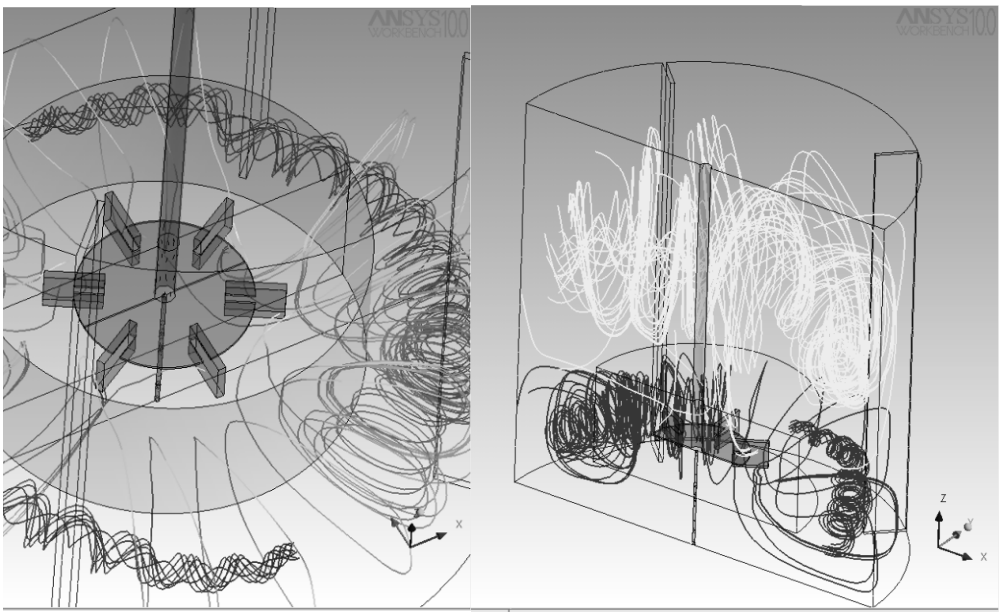

Figure 6-13: Integrated streamlines for CFD simulation (N = 300 rpm, *RNG k-ε* turbulence model).

using equation (3.28). This process can be applied either to steady state simulation or to transient simulations; in this Section, the results of the steady state case will be shown and discussed.

As explained in Section 4.2.3, the motion of the impeller is modelled by dividing the whole vessel in two domains: a spinning domain, which contains the impeller and part of the shaft, and a stationary domain, which contains all the rest. The fluid velocities, therefore, can be associated either to the rotating frame of reference (solid to the impeller) or to the stationary frame of reference (solid to the baffles). The difference between the values of these velocities applies only to the rotating domain and can be expressed using equation (6.3):

$$v_{rot}^{i} = v_{stn}^{i} - \omega r^{i} \qquad (6.3)$$

where the superscript i refers to a general velocity vector positioned at r^i distance from the rotation axis and the subscripts *rot* and *stn* refer to the rotating and stationary frames of reference. Concerning the stationary domain the two velocities are identical since there is no rotating velocity component to take into account.

Equation (3.30) uses the fluid velocities associated to the rotating frame of reference to calculate particle velocity in the turning domain; unluckily Ansys CFX 10 does not allow the user to impose the solver to use the velocities relative to the stationary frame of reference. This leads to the results shown in Figure 6-14, where the trajectories calculated are plot on top of the vector velocity flow field: on the left and right figures are reported the velocity vector fields respect the rotating and stationary frame of references (notice that in the stationary domain there is not difference between the two fields). Comparing the direction of the vectors in the spinning domain, it is possible to notice how on the rotating frame of reference the fluid appears to move towards the

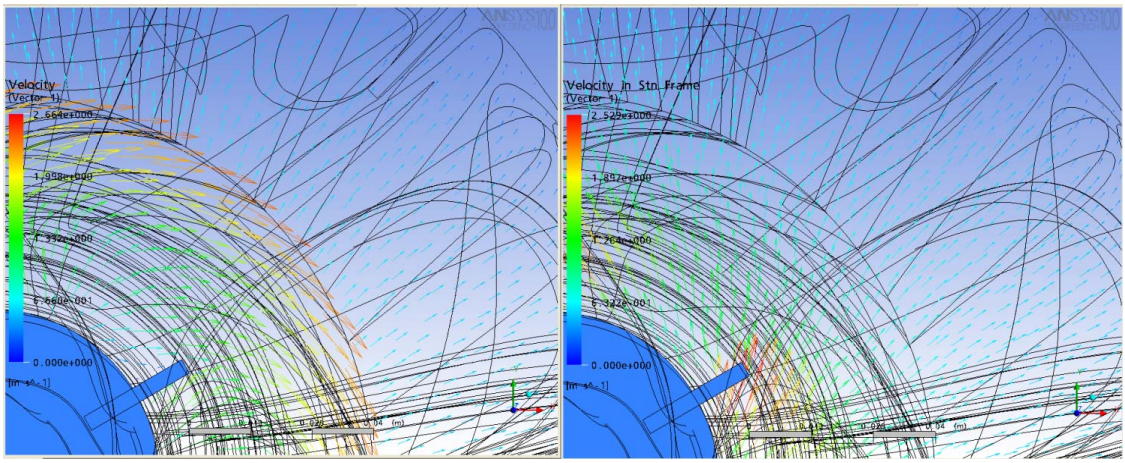

Figure 6-14: Particle trajectories for CFD Particle Tracking simulation and velocity vectors associated to rotating and stationary frame of reference (N = 300 rpm, *RNG k-ε* turbulence model).

blades of the impeller, while it is pushed by the impeller in the rotating frame of reference. It is also clear how the trajectories have been calculated using the velocities in the rotating frame of reference; in fact, they follow closely the fluid vector field showing a big discontinuity at the interface. Evidently, these trajectories are an artefact of the code and they cannot be compared with the experimental results.

In order to obtain correct particle trajectories in the spinning domain, Ansysy CFX 10 gives the possibility to subtract the rotating velocity component from the trajectories belonging to the inner domain. This correction process is carried out after the trajectories have been calculated. The outcome of this post processing is shown in Figure 6-15, where the trajectories in the rotating domain are now corrected and well aligned with the velocity vector field of the stationary frame of reference, the drawback of this approach is that, since in the stationary domain there is not rotating component, the trajectories in that domain remain exactly the same, leading to misalignments at the interface as shown in Figure 6-15b.

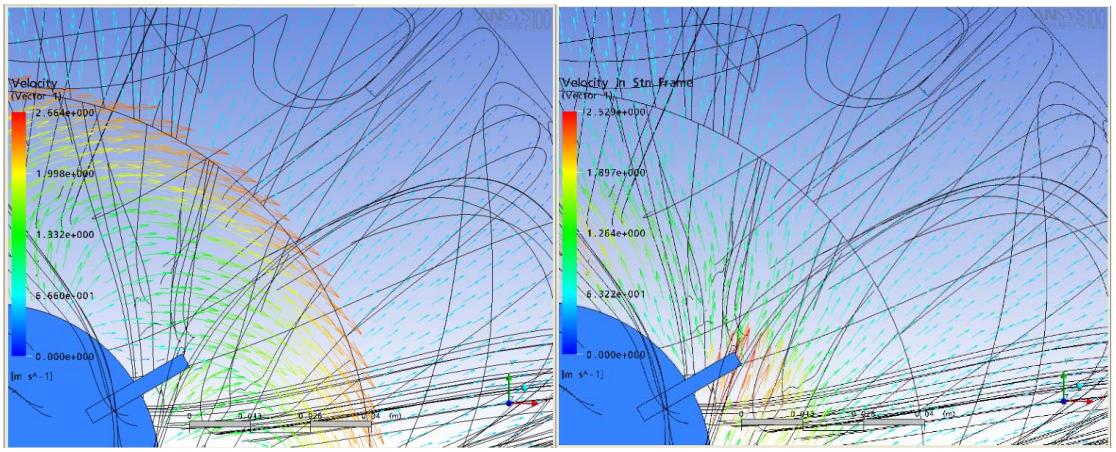

Vectors on rot. frame of reference Vectors on stn. frame of reference

Figure 6-15: Particle trajectories corrected in the rotating domain for CFD_PT and velocity vectors associated to rotating and stationary frame of reference (N = 300 rpm, *RNG k-ε* turbulence model).

6.3.3 Transient Lagrangian Particle Tracking simulations

After having tried to model Lagrangian particle tracking in steady state simulations, transient simulations have been attempted. In this case, the Lagrangian particle tracking integration is performed at the end of each transient time step once the fluid dynamics is resolved. In this way the velocities taken into account to resolve the momentum transfer equation are associated to the stationary frame of reference, therefore, the trajectories follow closely the velocity vector field. However, when the particle crosses the interface between the inner and outer domain, its trajectory shows a discontinuity related to the rotation of the spinning domain at each time step. Trajectories in transient simulations are shown in Figure 6-16, it can be seen that close to the impeller a swirl in the trajectories appears indicating the good quality of the simulated trajectories; however, at the interface between the two domains the particle paths shown are not continuous. Furthermore, the wedge that goes from the shaft to the interface indicates the amount of rotation made by the inner domain each time step.

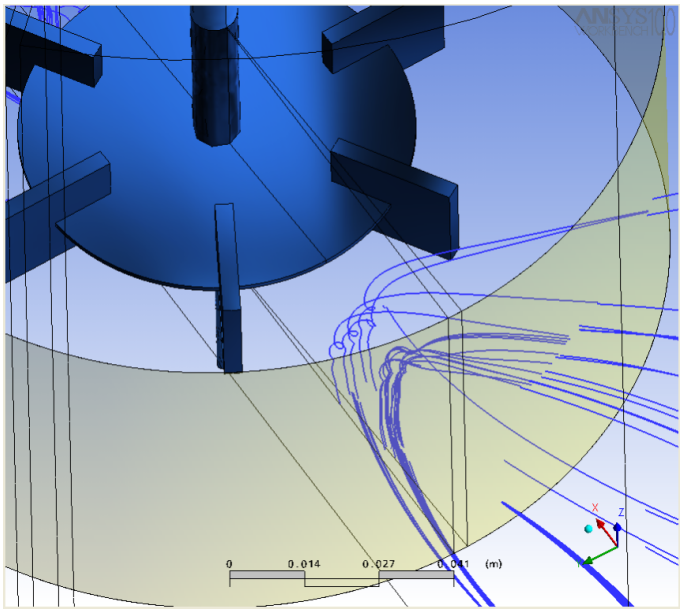

Figure 6-16: Particle trajectories for CFD_PT in transient simulation (N = 300 rpm, *RNG k-ε* turbulence model).

Aiming to keep the interface discontinuities at a minimum a very small time step should be used, this means that the computational time needed to track long paths would rise massively. For example, to track a particle for 10*min* using one degree time step, it would require 360 steps for each rotation and considering that for an impeller speed of 300*rpm* a full impeller rotation lasts 0.2*s*, 10*min* of particle tracking corresponds to 3000 impeller revolutions and 1.08 million steps, with an indicative computational time of 1 minute per step, to solve the whole simulation it will need 2 years of computational power. Evidently this approach is not feasible despite would give accurate results. In fact, to obtain the solution reported in Figure 6-16, which tracks the particle for only 10*sec*, the simulation needed two weeks to be completed.

6.4 Lagrangian Particle Tracking with Non-rotating Frame

6.4.1 The Approach

In the previous Section Lagrangian particle tracking for steady state and transient simulations were performed and discussed. In all the simulation the major problem has been the presence of the two domains, the stationary and rotating. The idea to go around the problem is to apply particle tracking to non-rotating domains. In order to achieve the aim, a standard simulation like the ones has been carried out in Section 6.1 is accomplished. A second simulation is then defined with both the domains set as stationary; the results of the first simulation are thus interpolated and used as initial conditions for this simulation. Since with non-rotating domains the simulation would converge to the solution of a still fluid, in Ansys CFX 10 the fluid dynamics solver was disabled and a solution of frozen domains was achieved. At this point keeping the same approach used for the second simulation, a third and final simulation was defined for Lagrangian particle tracking and the solutions previously obtained were used to initiate the solver which was set to solve only the particle tracking. A scheme of the three simulations used to achieve particle trajectories is reported in Figure 6-17.

Ansys CFX 10 does not permit the use of stationary velocities as initial conditions for simulations where rotating domains are not modelled and defined. Therefore, to overcome this issue a user's additional variable was created as copy of the stationary velocities; then, in the second simulation, the additional variable values were used as initial conditions (see Appendix B for the external routine needed to employ the additional variable as initial condition).

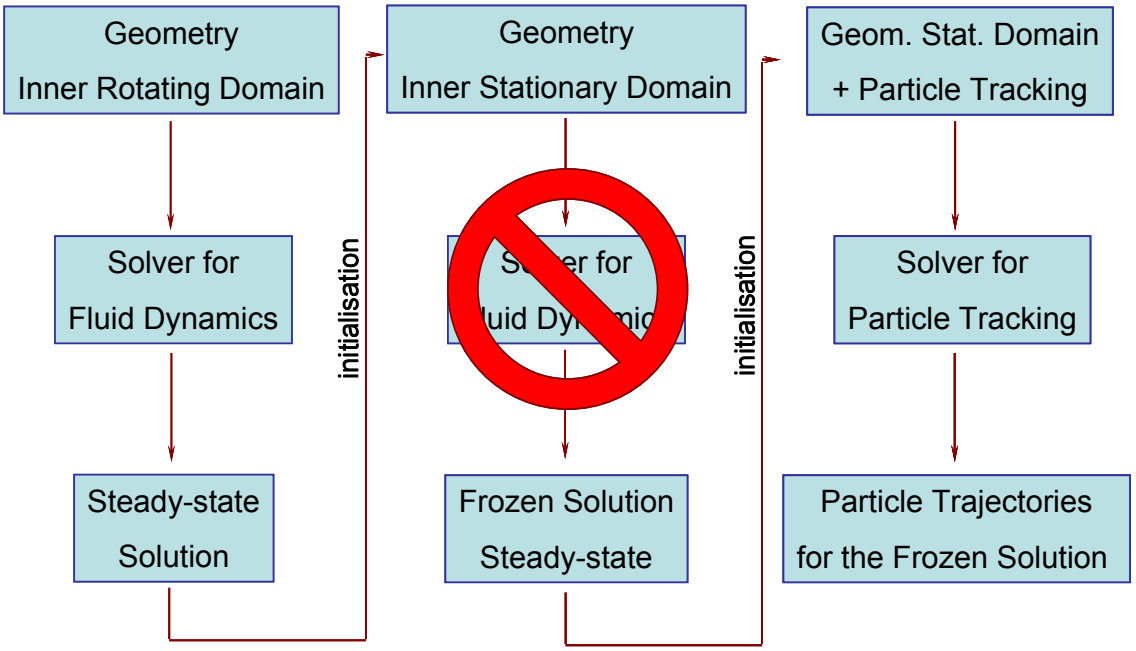

Figure 6-17: Simplified scheme for the frozen frame approach

6.4.2 The Results

In this Section the results achieved by implementing the frozen frame approach described in the previous Section 6.4.1 are explained and discussed. The first results achieved for CFD Particle Tracking are reported in Figure 6-18 where the trajectory of a single particle is shown on top and azimuthal views. For these results, the particle injection point was positioned in the impeller discharge stream, namely r=0.25T and h=0.33H; the tracking lasted until the maximum number of integration step, set equal to 1000000, have been achieved which corresponded to a total tracking time of two minutes (120s). From Figure 6-18 it can be seen how the trajectory looks much more real than the other types of approaches; however, from the side view emerges that in the region of the lower loop the tracer has the tendency to move in regular loops along the walls of the tank, while for the region above the impeller follows different paths with less regularity.

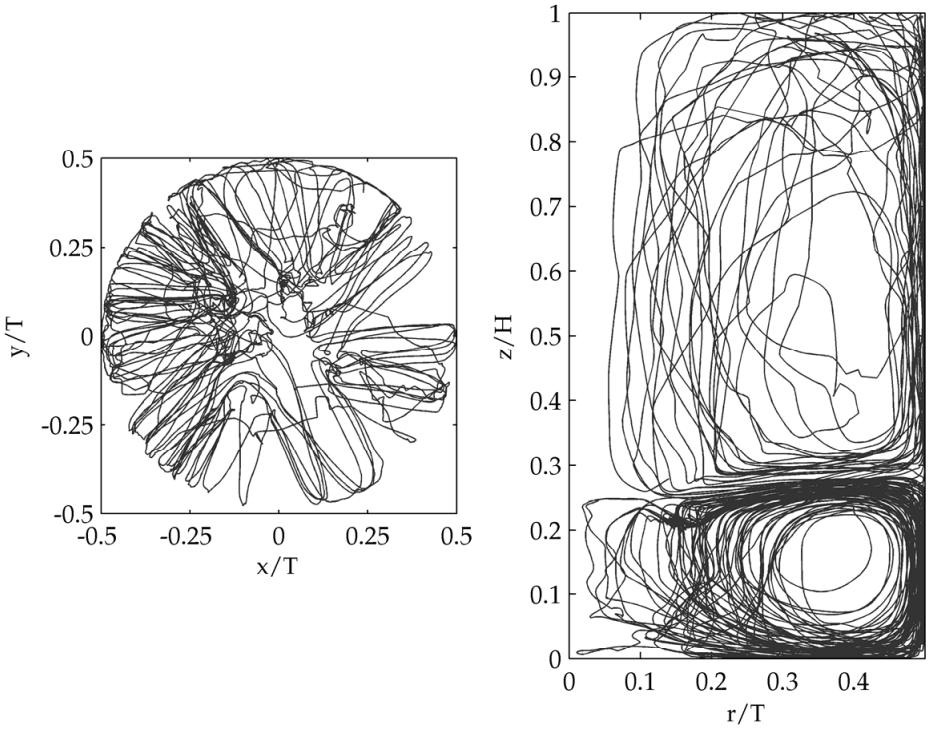

Figure 6-18: Top and azimuthal views of CFD Particle Tracking trajectory tracked for 120s (N = 300 rpm, *RNG k-ε* turbulence model).

The particle paths are then processed using the same routines that have been developed to analyse PEPT results and described in Section 5.5. Occupancy and number of passes are reported in Figure 6-19, from the figure is clear how two minutes of tracking are not sufficient for a proper description of the system, in fact, the occupancy is not uniform as supposed to be and there are different parts of the vessel not yet visited by the particle.

One way coupled condition was set in this simulation, this means that the fluid affects the particle motion but the particle does not affect it. Therefore, to track one particle or many essentially does not make any difference. For this reason 20 different particles have been tracked and the trajectories have been listed in a queue as belonging to one single particle, resulting in a single trajectory over a period of one hour. For these trajectories the occupancy plotted in Figure 6-20 results more uniformly distributed and the number of passes is naturally larger than the previous case; however, there is still a

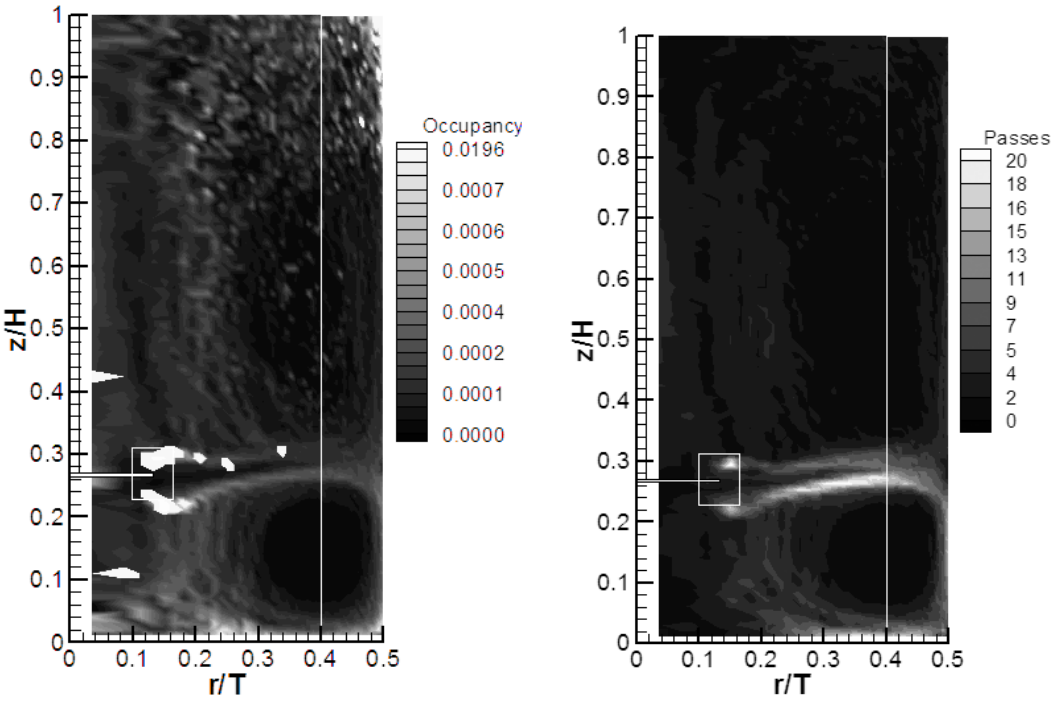

Figure 6-19: Azimuthal occupancy and passes for CFD Particle Tracking (1 particle, N = 300 rpm, *RNG k-ε* turbulence model).

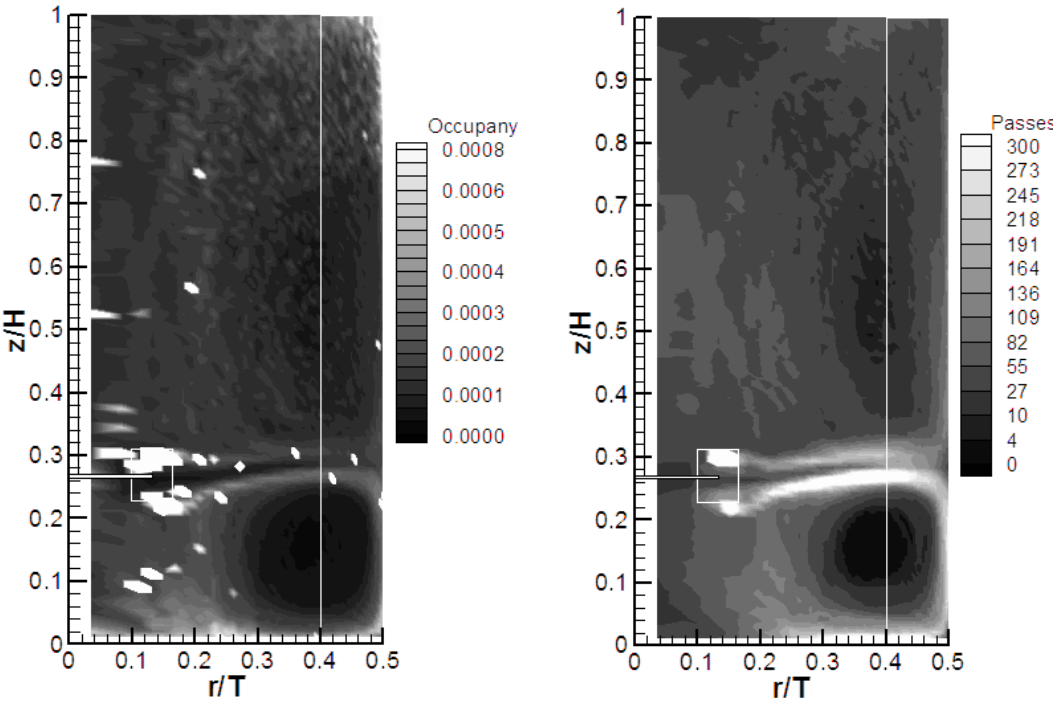

Figure 6-20: Azimuthal occupancy and passes for CFD Particle Tracking (20 particle, N = 300 rpm, RNG k- *ε* turbulence model).

region at the centre of the lower loop where the particle never passed. In the next Chapter, the comparison between the PEPT trajectories and the CFD trajectories will be performed and different methods to analysed trajectories will be discussed.

6.5 Conclusions

This Chapter reports the work done on CFD simulations of stirred tanks. From the comparison of structured versus unstructured meshes, it can be concluded that, using a similar number of cells for both mesh types, the results are similar and thus not affected by the type and orientation of the cells. However, the choice of the turbulence model does affect the results of the simulations. *RNG* k-ε and k-ω models, despite being able to predict similar velocity profiles, show quite large differences in the prediction of energy quantities such as the kinetic energy and the energy dissipation rate. Both methods underpredict the energy quantities in the proximity of the impeller; however, the k-ω model predicts overall higher values, which are closer to those obtained experimentally. The dimensionless numbers, *Po* and *Fl*, have been calculated from the CFD results. Regardless of the turbulent model implemented and the mesh used, the flow number calculated by integrating the impeller discharge flow is on average 0.7, which is close to the values reported by a number of authors (Costes and Couderc, 1988a; Dyster *et al.*, 1993; Nienow, 1997).

From the CFD simulations, fluid velocities higher than the tip speed have been found behind the impeller blades. Although, it sounds impossible to obtain such high velocities, a careful review of the literature showed that such speeds had been measured experimentally previously but not recognised as such. This prediction has also been validated in this study by PIV.

Due to the presence of a stationary and a rotating frame, particle tracking in CFD is not well simulated. Thus, the limitations of Lagrangian particle tracking have been assessed by investigating the different ways to set up simulations in Ansys-CFX. Stationary simulations are impossible to achieve since the particle tracking codes do not take into account the artificial rotation of the rotating domain; which is used to emulate the rotation of the impeller. Large discontinuities at the interface between the two domains are thus created. Transitional simulations, instead, are possible to achieve, although they require huge computer numerical power and thus are not practical at present. Eventually, in order to work around these problems, a new method for particle tracking has been proposed and described. The results obtained with this method have finally been reported and shown to be promising for further work and development

Chapter 7

A Comparison of Particle Tracking using Positron Emissions and Computational Fluid Dynamics

7.1 How to compare trajectories

This chapter aims to illustrate how it is possible to use particle trajectories to describe a stirred vessel. Until this point, the work done was focused on achieving a good trajectory from both PEPT experiments and numerical simulations. In Chapter 5, the trajectories from PEPT have been analysed and used to find Eulerian velocities and other information such as occupancy and the number of time the tracer passes through each part of the tank. Again in Section 6.4 the trajectories obtained from CFD simulations have been processed using exactly the same routines as those used for the experimental results.

However, trajectories contain much more information useful for quantifying mixing than just velocity flow fields and occupancy. and in the next few Sections, different approaches are used to show how to do so and to compare PEPT and CFD-PT techniques whilst doing so.

7.2 Qualitative comparison

7.2.1 Trajectories side by side

The simplest approach, that can be used to compare trajectories obtained from different systems or methods, is by plotting them side by side and by looking for qualitative differences and similarities. Trajectories are three-dimensional curves obtained from a data set of consecutive locations recorded over a certain time. To show trajectories on two-dimensional plots, their projections on different planes can be plotted and thus compared. Figure 7-1 shows the typical trajectories obtained from experimental and numerical results; these trajectories refer to a tracking time, in the larger geometry, of

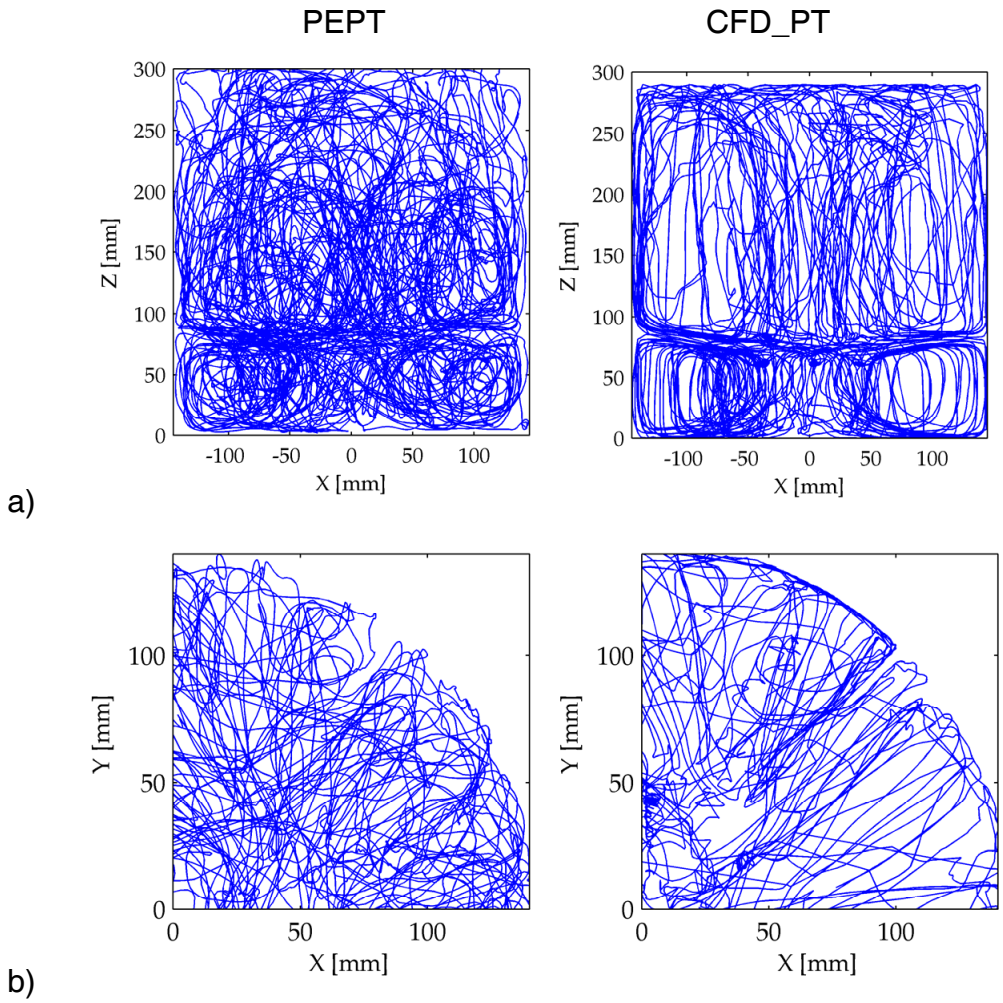

Figure 7-1: Trajectories obtained after 5*min* of PEPT experiments (left hand side) and CFD_PT simulations (right hand side). Trajectories projection on a) the *xz* plane and b) the *xy* plane.

5*min* since a longer time would have made it impossible to distinguish single passes.

Furthermore, in order to have a closer picture of the trajectories projection on the *xy*-plane, only one quarter of the tank is shown in Figure 7-1b. Figure 7-1 illustrates how the trajectory obtained from the CFD-PT simulation is more regular and uniform than the real trajectory recorded in PEPT. It can also be seen that projections on the *xz*-plane are not very useful since paths perpendicular to this plane result on vertical straight lines when projected and they hide other trajectories.

To solve this problem, the same trajectories are reported in cylindrical coordinates and plotted on the *rz* and *r-th* planes respectively, as shown in Figure 7-2. By using the

cylindrical coordinates, it is possible to plot data for 20*min* without losing clarity of representation. Again, in Figure 7-2, the trajectories obtained from CFD-PT are more regular than the experimental ones, which appear more disordered and random. It can also been observed that the tracer in the numerical simulation does not visit the centre of the lower and upper loops leading to a lack of data in those areas as shown by the low number of passes as already shown in Figure 6-20, Section 6.4.2.

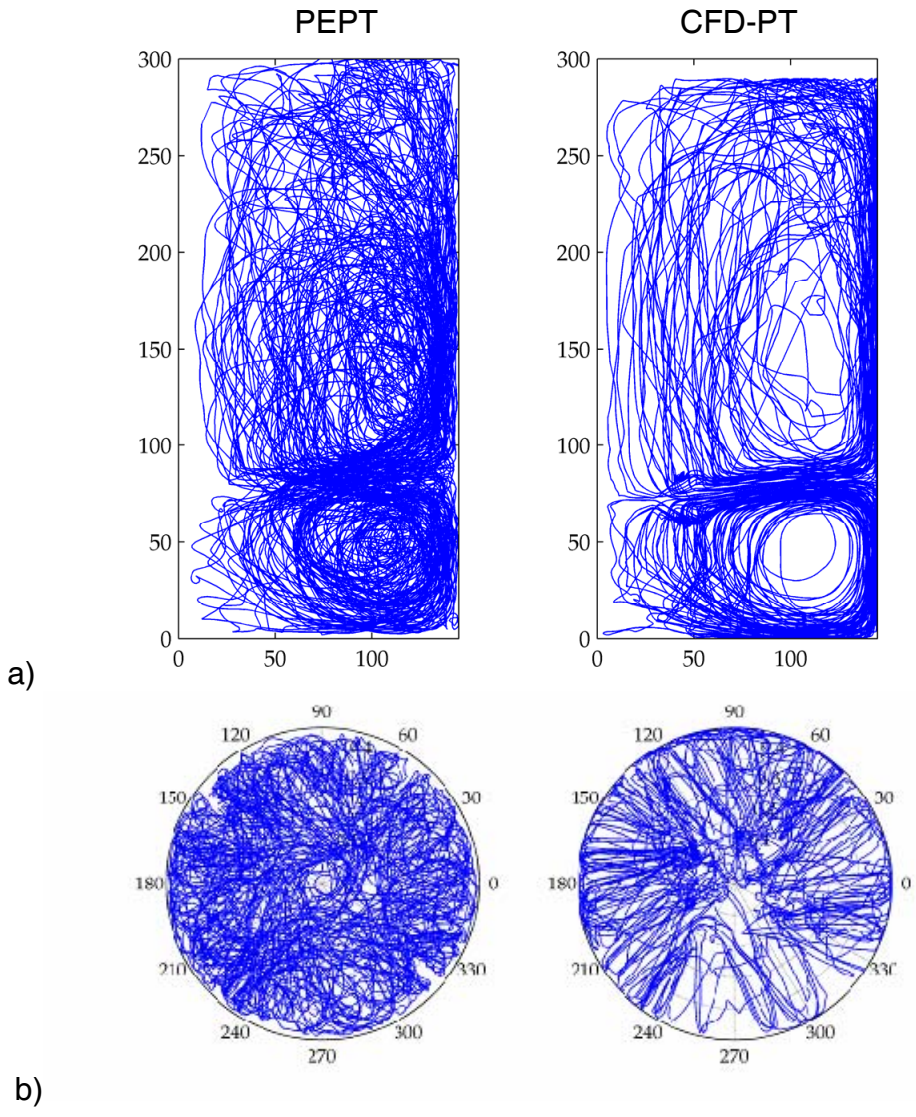

Figure 7-2: Trajectories obtained after 20*min* of PEPT experiments (left hand side) and CFD_PT simulations (right hand side). Trajectories projection on a) the *rz* plane and b) the *r-th* plane.

7.2.2 Poincaré Maps

The second method used to analyse different trajectories is by mean of the Poincaré maps. Poincaré maps consist of recording periodicities or irregular recurrences on 2D plots; in the case of Lagrangian particle tracking the tracer positions are recoded every time they cross a predefined plane. In order to achieve some further information, the crossing points on the maps in this work have been plotted in two different colours according to the direction which the particle passes the plane, i.e. red and blue for crosses in the positive and negative direction respectively.

Several different planes have been considered to obtain a full description of the system; specifically horizontal, azimuthal and vertical planes have been used in this work. Figure 7-3 collects the horizontal Poincaré sections for the PEPT and CFD trajectories at height equal to 0.03, 0.1, 0.18, 0.25, 0.29, 0.5, 0.71 and 0.92 H. The blue cross marks indicate where the particle crossed the plane directing towards the bottom of the vessel and vice versa for the red circles. Concerning the PEPT data representation, it is possible to see the shape of the lower and upper loops since for height lower than the impeller plane (z=0.25 H) the downwards blue intersections are around the external wall while the upwards intersections appear to be in the inner part of the vessel. On the other hand, for sections above the impeller planes the trends of the crossing directions are inverted. From the comparison of the experimental and the numerical Poincaré maps, it emerges clearly that, while the experimental data looks randomly and uniformly distributed on the sections, the numerical CFD-PT trajectories are more segregated in particular for sections placed in the proximity of the centre of the lower loop. Furthermore, it is interesting to notice the effect of the baffles on the flow

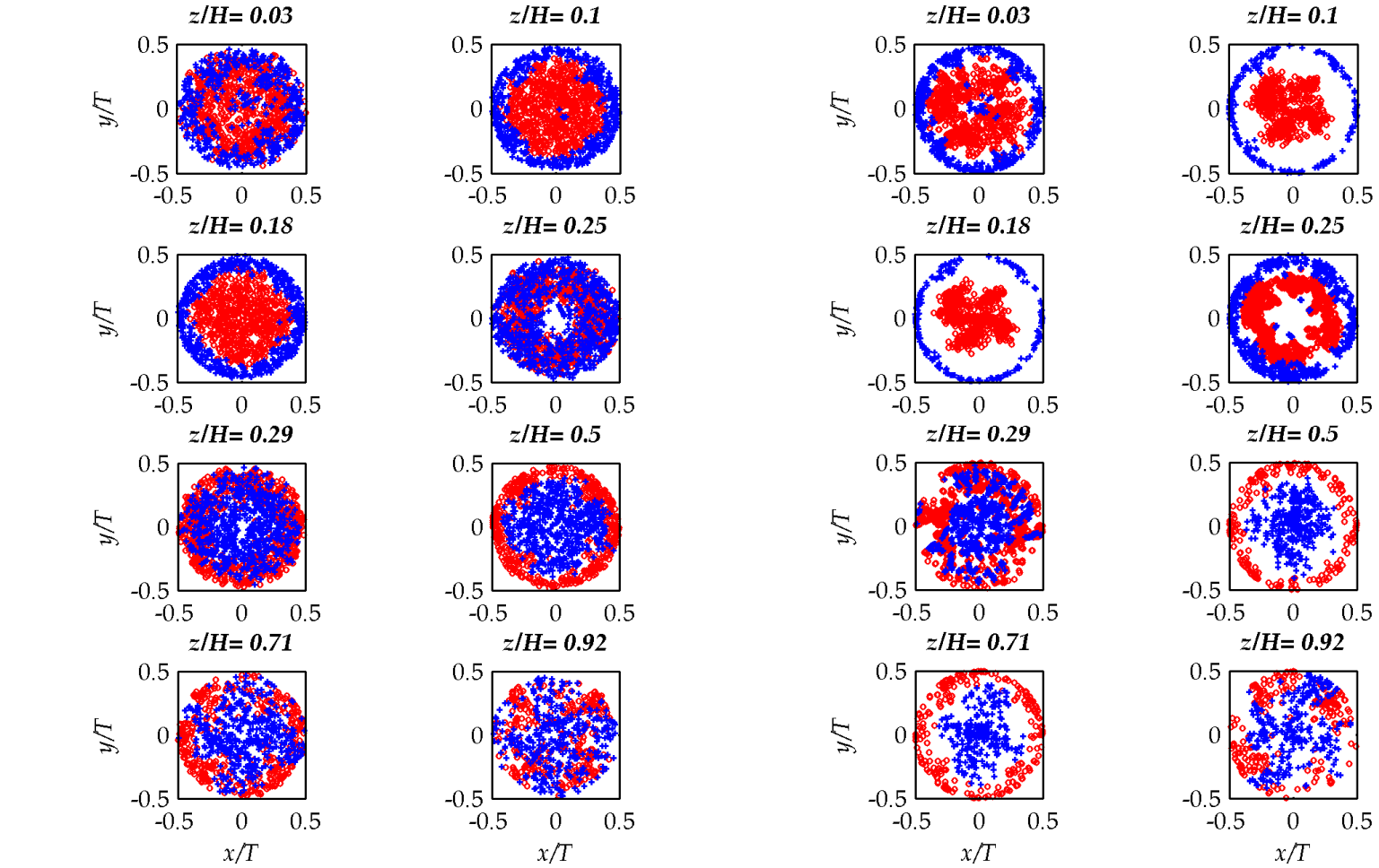

Figure 7-3: Poincaré maps at different height on the *x-y* plane for a) PEPT and b) CFD_PT data. (red circles – crossing the plane towards the top of the vessel; blue cross – towards the bottom)

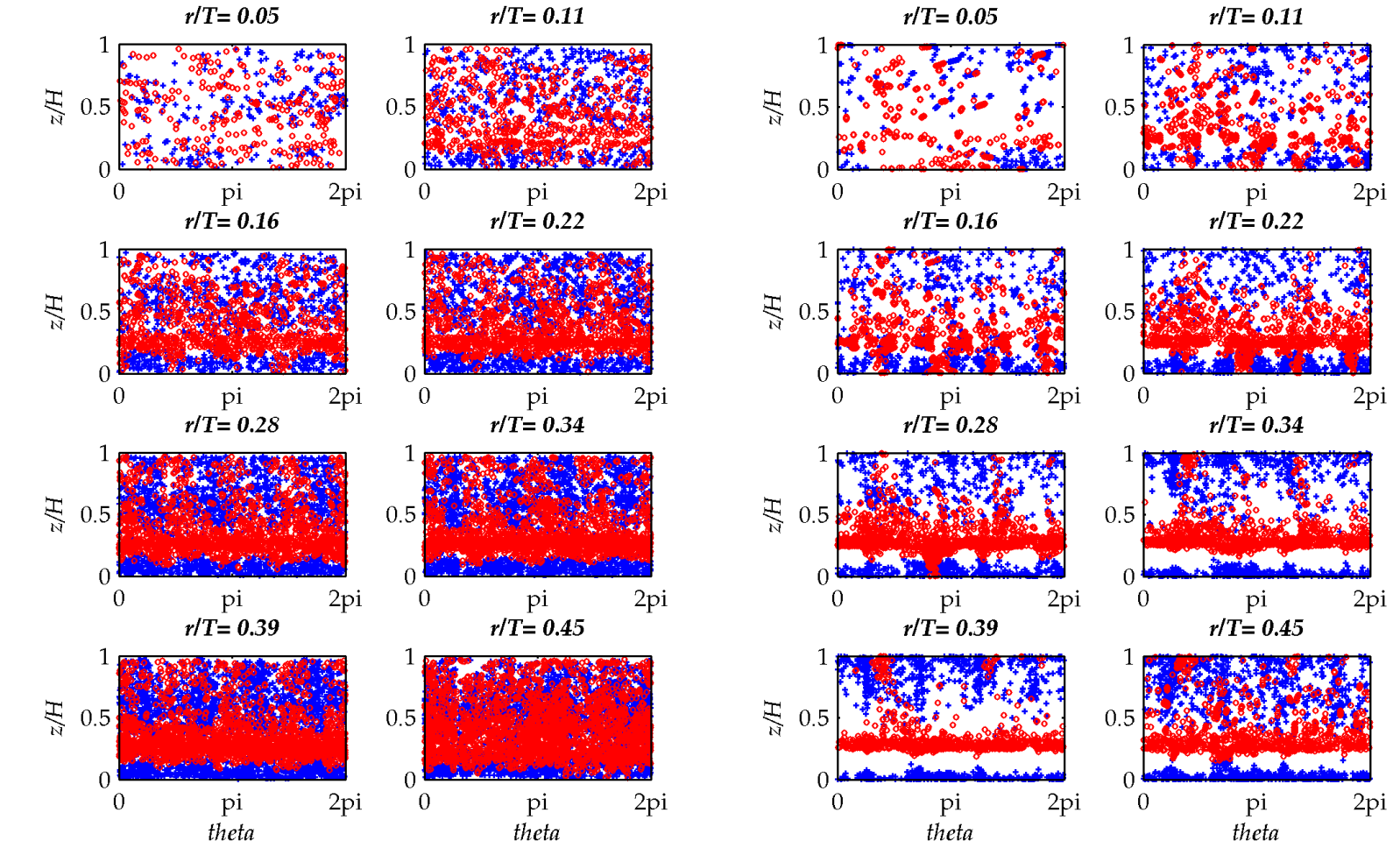

Figure 7-4: Poincaré maps at different radii on the *th-z* plane for a) PEPT and b) CFD_PT data. (red circles – crossing the plane towards the external wall; blue cross – towards the centre)

direction for height between 0.71 and 0.92 H; in fact, in these maps, four upwards (red) crossing areas appear in the region of the four baffles. Similar to Figure 7-3, Figure 7-4 shows the Poincaré maps at different radii on the th-z plane, where the red circles and the blue crosses indicate the particle crossing an azimuthal plane towards the external wall of the vessel and vice versa, respectively. The azimuthal planes were obtained for radii equal to 0.05, 0.11, 0.16, 0.22, 0.28, 0.34, 0.39 and 0.45 T. From both the experimental and numerical maps, a horizontal band of red circles at a height approximately equal to 0.25 H can be observed, which denotes the strong radial flow generated by the Rushton turbine. This phenomena also causes the regions of blue crosses above and below the impeller plane generated by the upper and lower flow loops. Finally, the effect of the baffles is very clear in the experimental maps for radii between 0.28 and 0.39 T, resulting in an alternation of red and blue vertical areas, which is also evident for the maps obtained from the CFD simulations.

Overall from these first sections, it can be seen that the numerical simulations provide trajectories with very similar trends to the experimental ones, though the fine details are not matched in these plots.

7.3 Frequency Analysis

7.3.1 Fast Fourier Transforms

In mathematics, the discrete Fourier transform is a transform for Fourier analysis of finite-domain, discrete-time signals. It is widely employed in signal processing and related fields to analyse the frequencies contained in a sampled signal, which here consists in the positions of the particle over a time period. One of the several ways to compute efficiently the discrete Fourier transform is by using a fast Fourier transform

(FFT) algorithm. This method is designed for evenly spaced time data. However, there are various ways to get evenly spaced information from unevenly spaced data of the type available here. For example, interpolation onto a grid of evenly spaced times can be used for this purpose. Such interpolated data can then be treated by FFT spectral analysis methods. However, the experience of practitioners of such interpolation techniques is not reassuring (Roussinova *et al.*, 2004) and such techniques sometimes perform poorly. In addition; long gaps in the data often produce an erroneous grouping of different frequencies at low frequency values in the power spectrum (Press *et al.*, 1992; Britz and Antonia, 1996). If this technique were to be used to characterised dominant frequency in the system lower than the impeller speed, it is probable that the above-mentioned errors may be encountered, which could lead to false prediction of peak frequencies in the power spectrum.

7.3.2 Lomb-Scargle Method

A different approach proposed by Lomb, 1976, first and Scargle, 1982, later, can be used for unevenly spaced data which mitigates these difficulties. The method consists of a generalization of the classical periodogram for unevenly sampled data, based on the method of least squares. This method was shown by Scargle, 1982, to be invariant with respect to time translation and to provide a statistical significance test for a supposed periodic signal. In the literature, the Lomb-Scargle method has been widely described and used mostly in the study of astronomical signals. However, it has been used in mixing research for the study of macroinstabilities (Britz and Antonia, 1996; Roussinova *et al.*, 2000; Roussinova *et al.*, 2003). The Lomb algorithm is functionally and mathematically equivalent to the direct application of the discrete Fourier transform and a rigorous and simplified mathematical description can be found in Roussinova *et*

al., 2004. Because it operates directly on unevenly spaced data, it is a more precise method than FFT, which requires interpolation of the signal to obtain evenly spaced data.

7.3.3 Frequency analysis application: Results

7.3.3.1 Method description and test

The concept behind the application of frequency analysis to the trajectories found from PEPT experiments, comes from the idea that the tracer moves on circular motion in each directions, therefore its position recorded versus time should follow a sinusoidal pattern or similar to it. Ideally it could be imagined that using the horizontal positions along the axes x and y the tracer would rotate with a frequency that is a portion of the impeller speed, while using the vertical positions z the frequency found would be related to the upper and lower loops.

Before applying this frequency analysis technique to the experimental trajectories obtained from this study of the stirred vessel, this approach has been performed on paths obtained in a different geometry where periodic motion is more accentuated. The geometry consisted of a vertical high shear mixer used for granulation processes; where

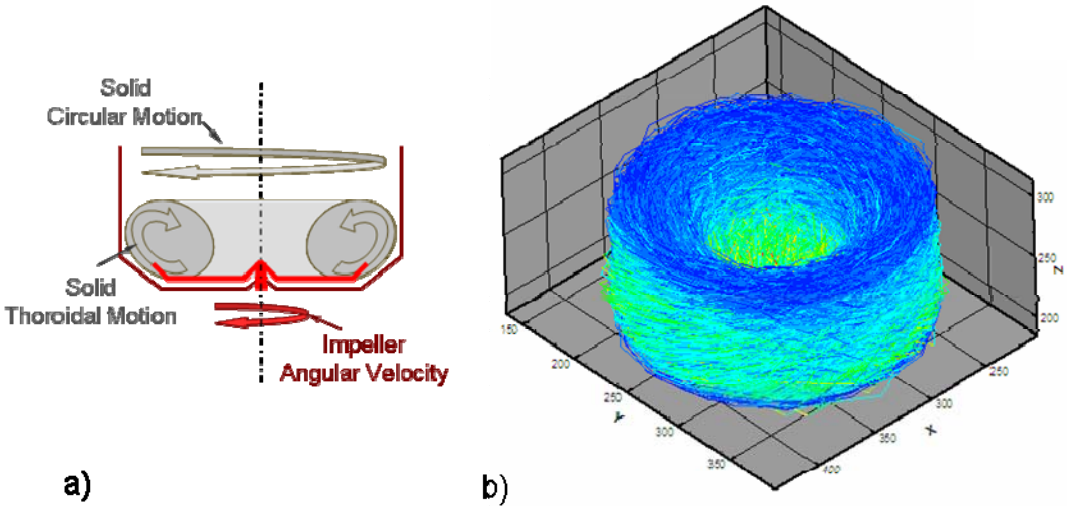

Figure 7-5: Vertical high shear mixer a) toroidal motion scheme, b) trajectories

the particle motion is mainly toroidal as can be seen schematically in Figure 7-5a, though in Figure 7-5b the real particle paths from PEPT look more circumferential.

The size of the granulator is 200*mm* in diameter and about 80*mm* in height. Further details of the geometry and results can be found in Tran *et al.*, 2006. In order to show the toroidal motion, the tracer position along the three Cartesian axes has been plotted versus time in Figure 7-6 for 20*s* of the total experiment length. From Figure 7-6 , it can be seen that the Z component oscillates a lot as result of the toroidal motion as explained above. However, it can also be noticed that there is a harmonic pattern associated with the other two coordinates around the origin, which well describes the main movement of the solid powder pushed by the blade. By applying frequency analysis to these high shear granulator data using both the FFT and Lomb-Scargle methods, it is possible to obtain for the *z*-component the frequency spectra shown in

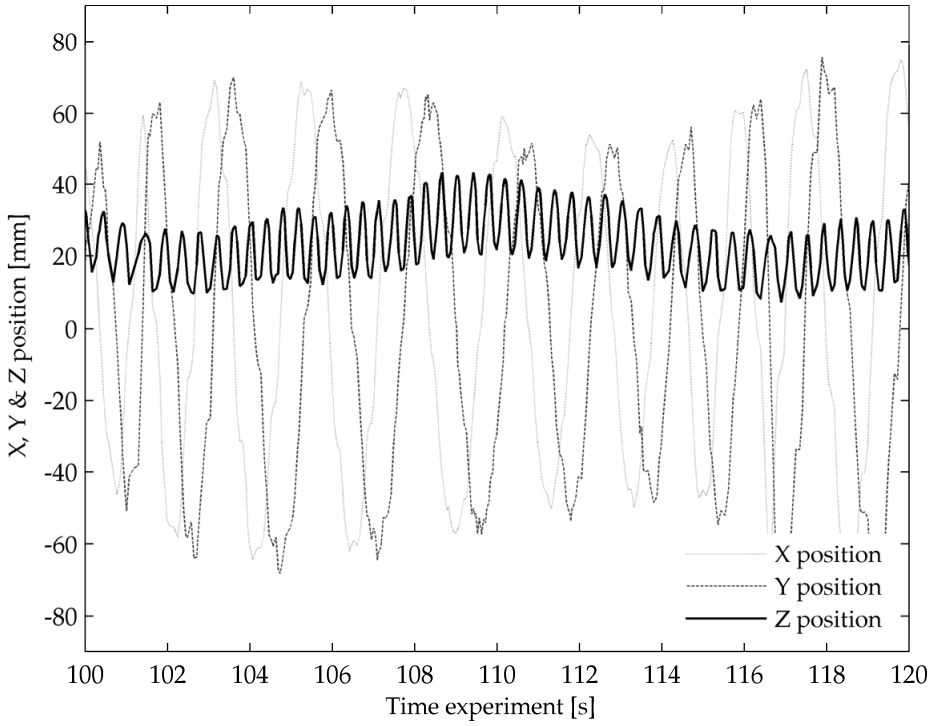

Figure 7-6: Cartesian tracer position versus time for vertical high shear mixer rotating at 500rpm

Figure 7-7. Regardless of the method used, the two spectra are very similar and detect two main frequencies in the system. However, the Lomb-Scargle method seems to be able to spot some more details in the spectrum between 2.5 and 3Hz resulting in two separate peaks instead of only one. This difference is probably due to the fact that the data used for this method do not need to be interpolated onto an evenly spaced time grid as they are for the FFT application, thus it can provide narrower peaks that allow a more accurate identification of the frequency involved.

7.3.3.2 Frequency analysis applied to the stirred vessel

In this Section, the FFT and Lomb-Scargle frequency analysis methods are applied to the data obtained during the first set of PEPT experiments (see Section 5.5.1 which consists of tracking the 600μm particle in the larger geometry agitated by the impeller rotating at 300rpm. As explained in Section 7.3.1, the FFT frequency analysis cannot be performed with unevenly spaced data without prior interpolation. To allow for this requirement, for both the PEPT and CFD_PT data, the interpolation grid resolution has been chosen equal to the minimum of all the time intervals used to find the frequency spectrum. The average minimum time interval recorded during the PEPT experiments is around 30ms, which enables one to detect frequencies up to 33.3Hz (the reciprocal of 30ms). On the other hand, the frequency in the system related to the blades of the impeller rotating at 5rps (300rpm) is 30Hz, (multiplying the impeller speed by the number of the blades). Since in-depth studies of turbulence are not possible with the PEPT technique and were not pursued in the current work, the acquisition frequency of about 33Hz is adequate for the study of the low dominant frequencies. However, the lower limit of frequencies that can be detected has to be higher than the reciprocal of the

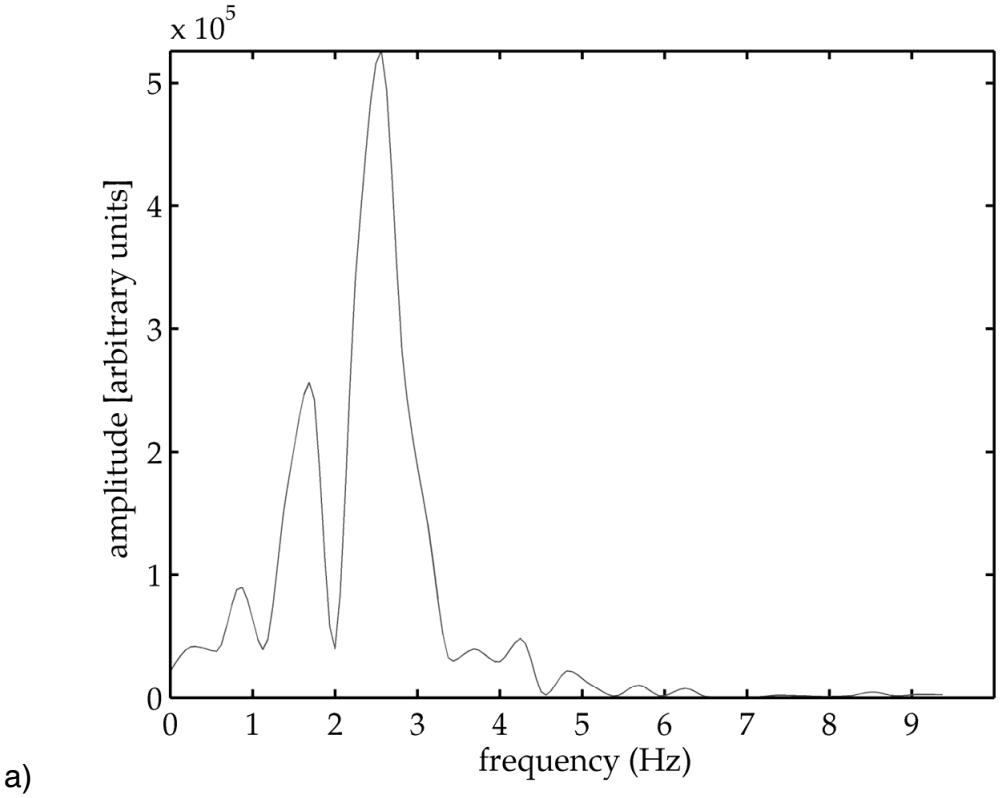

a)

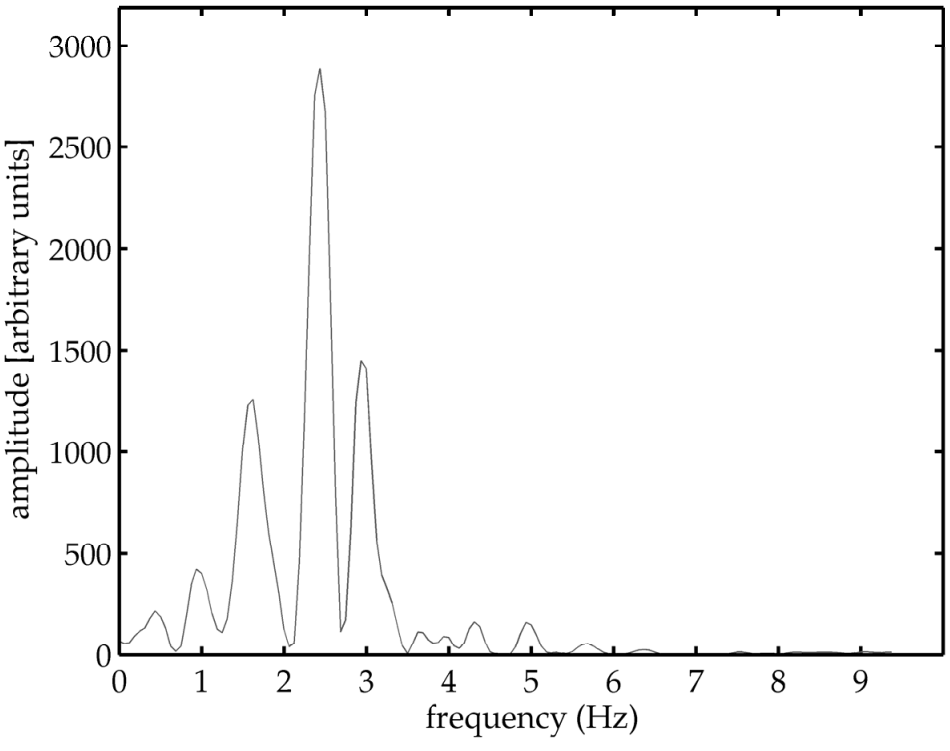

b)

Figure 7-7: Frequency analysis applied to the z-coordinate of vertical high shear granulator. a)FFT and b)Lomb-Scargle methods

half of the time observed since it is impossible to find recurrent trends longer than the time observed. The experimental trajectories, as seen in Section 7.2, are quite irregular. Thus the frequency analysis has been applied to different portion of data, according to their length and time of acquisition. Figure 7-8 shows the data used to try to find any dominant frequencies in the system. The coordinate used as the axis of symmetry in this approach was the vertical axis, in order to find the frequencies related to the flow in the upper and lower circulation loops, since using the x and y axes would not give any useful information in this respect. The plot of the z-coordinate versus time for the PEPT data and the CFD_PT data are reported respectively in Figure 7-8a and Figure 7-8b. For both the experimental and numerical results in Figure 7-8, the data used for each case consists of four sets of positions. In fact, the z-position has been tracked for 20*sec* and 120*sec* for the left and the right hand side graphs, respectively. However, it should be noted the recording time started at two different moments during the experiment (after 60*sec* for the top two graphs and after 1380*sec* for the bottom two). Comparing the position of the tracer versus time for the stirred vessel (Figure 7-8) to the one obtained for the vertical high speed mixer (Figure 7-6), it can be seen that the results in the present case are very different and much less regular though the CFD_PT data shows a more evident sinusoidal trend than the PEPT data.

In addition, the FFT frequency analysis has been applied to all the data sets reported and the results are shown in Figure 7-9. For each portion of data, the frequency spectrum is expressed as a plot of the system frequencies on the horizontal axis and their amplitude on the vertical axis. The frequency spectra in Figure 7-9 show how hard it is to pick up frequencies from these data, despite the set of data used. For the 20*sec* data set, the

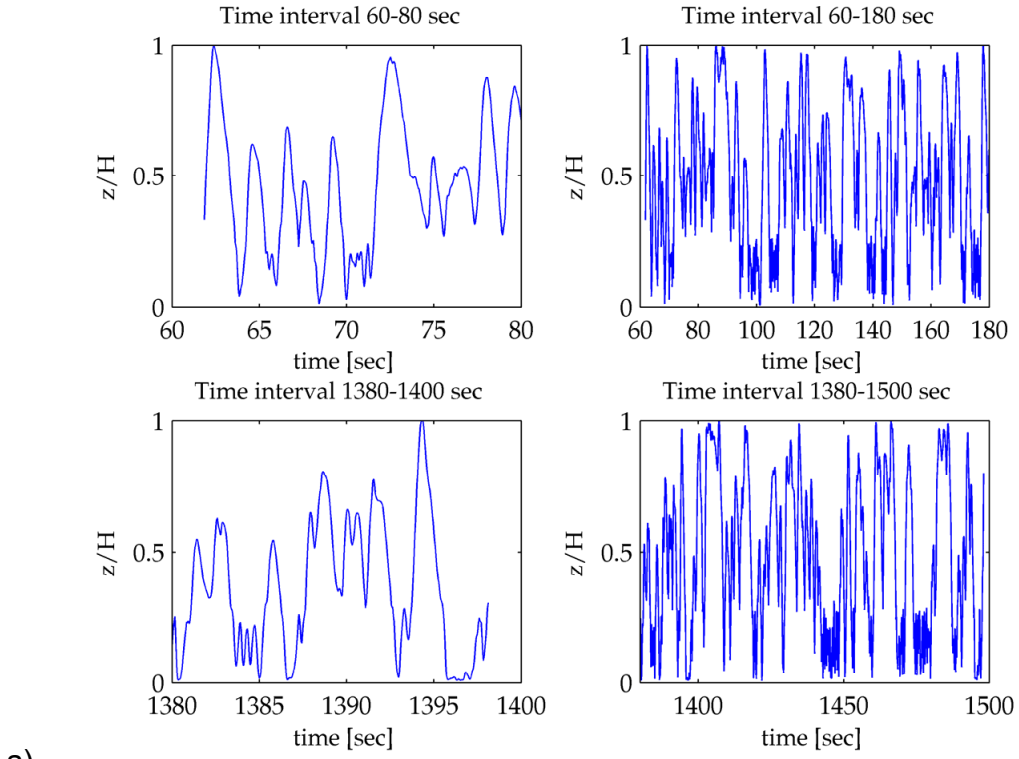

a)

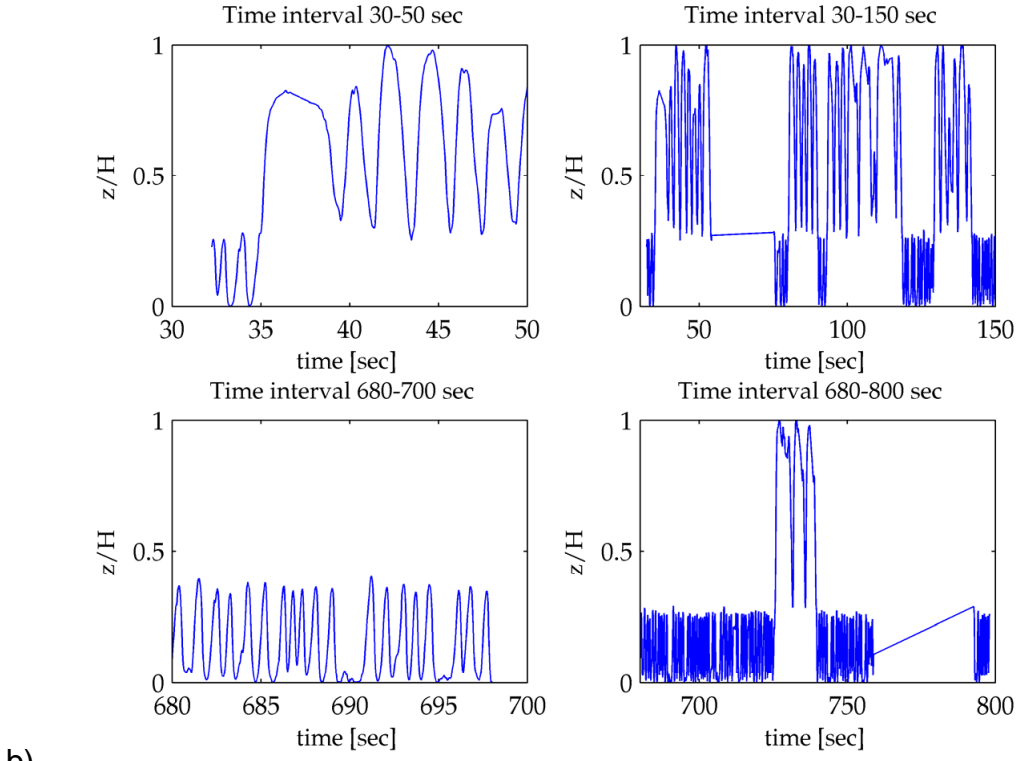

b)

Figure 7-8: Cartesian tracer position versus time for the stirred tank agitated at 300rpm a) PEPT and b) CFD_PT

minimum physical frequency is $0.1Hz$ $(=(20sec/2)^{-1})$ while for the $120sec$ is $0.0167Hz$ $(=(120sec/2)^{-1})$. The frequencies picked up using FFT that are smaller than the minimum physical one are the results of the noise in the data, while for frequencies higher than that values, there are not any peaks to give any information on the system.

The lack of dominant frequencies could depend on the fact that the data have been interpolated in a regular grid losing the nature of the data. In order to understand if this is the reason, the Lomb-Scargle method have been applied to the same data and the frequency spectra obtained are reported in Figure 7-10. Despite many more peaks appearing using this method, it is impossible distinguish a clear pattern or dominancy. Even within the same type of experiment, just by changing the set of data, the analysis gives completely different spectra as can seen in the four plots in Figure 7-10a. Although the trajectories obtained from the CFD_PT simulations looked very regular from a qualitative point of view, the frequency analysis results are still unable to extract any type of information from this data.

As a last attempt to use frequency analysis on the trajectory data, the spectra shown in Figure 7-9 and Figure 7-10 are re-plotted on logarithmic scales in Figure 7-11 and Figure 7-12, respectively. This change would highlight small amplitude frequency values if they existed. Again, however, using this representation does not give any useful quantitative information which can be used in order of characterise the mixing phenomena occurring in a stirred vessels with a Rushton turbine.

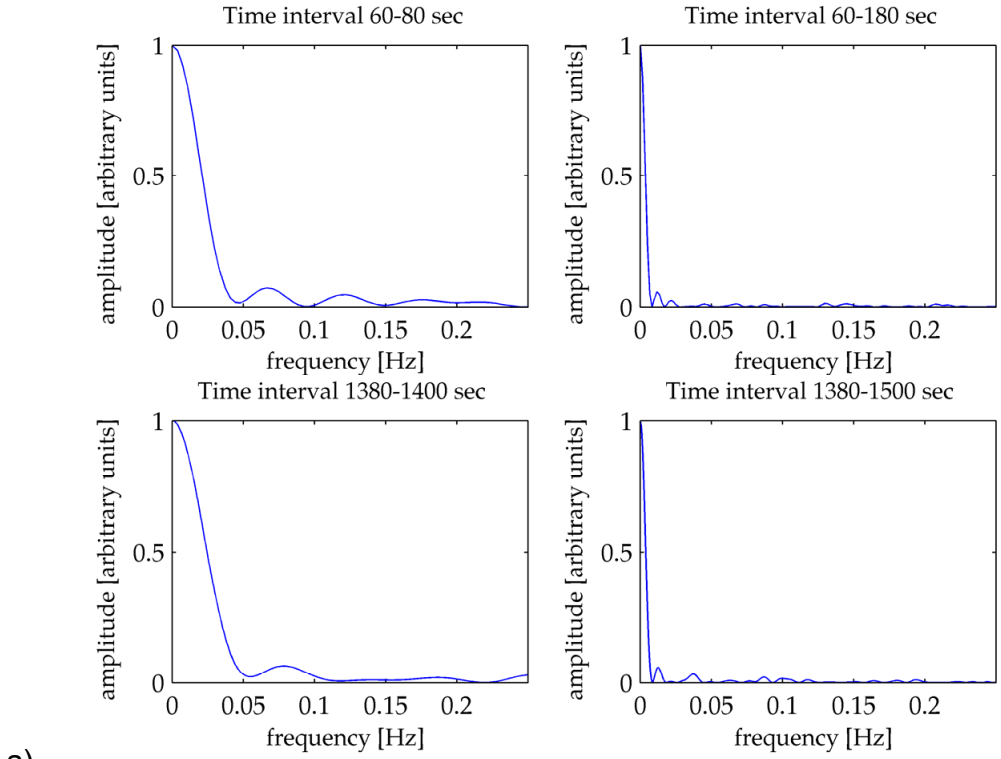

a)

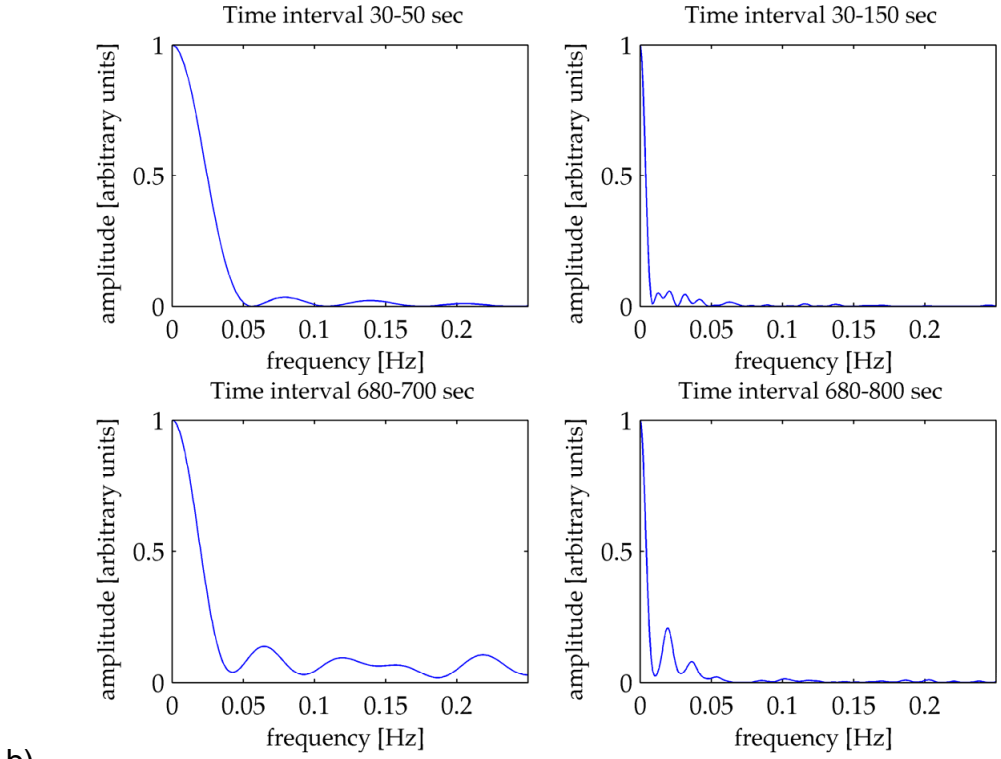

b)

Figure 7-9: FFT Frequency spectra for the stirred tank agitated at 300rpm a) PEPT and b) CFD_PT

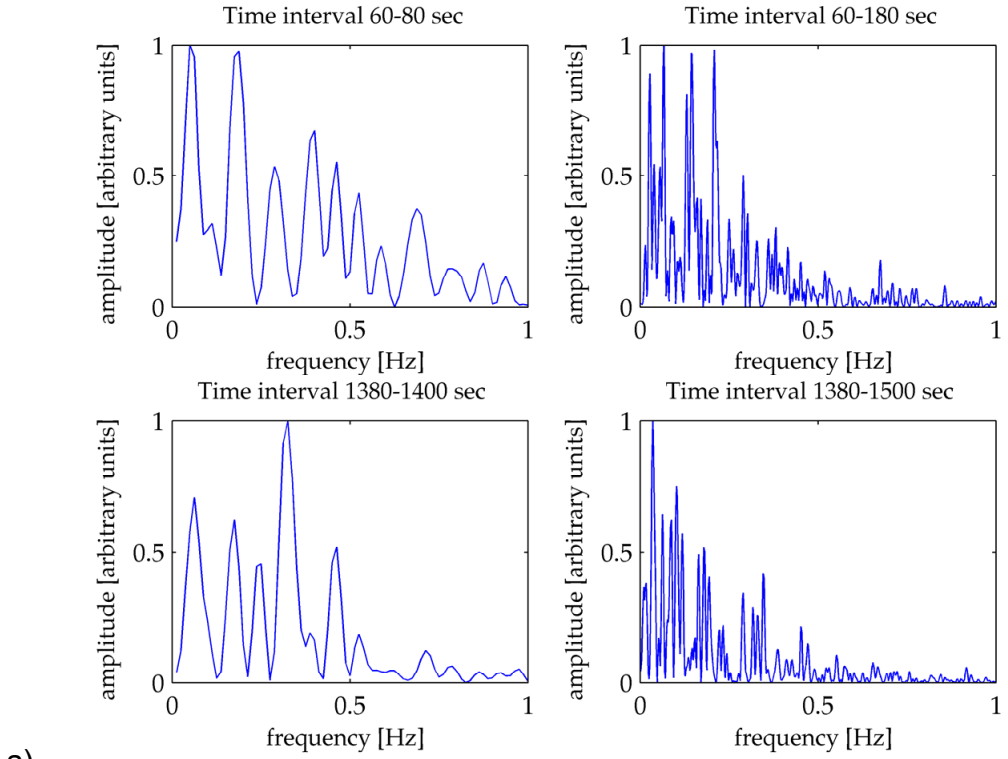

a)

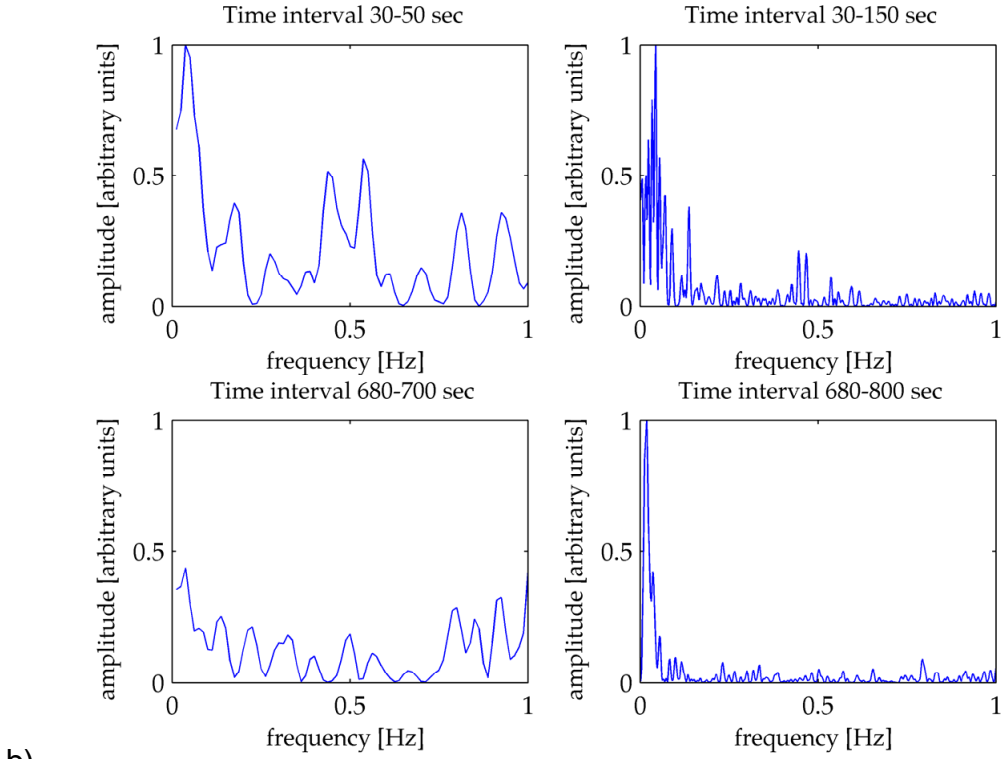

b)

Figure 7-10: Lomb-Scargle frequency spectra for the stirred tank agitated at 300rpm a) PEPT and b) CFD_PT

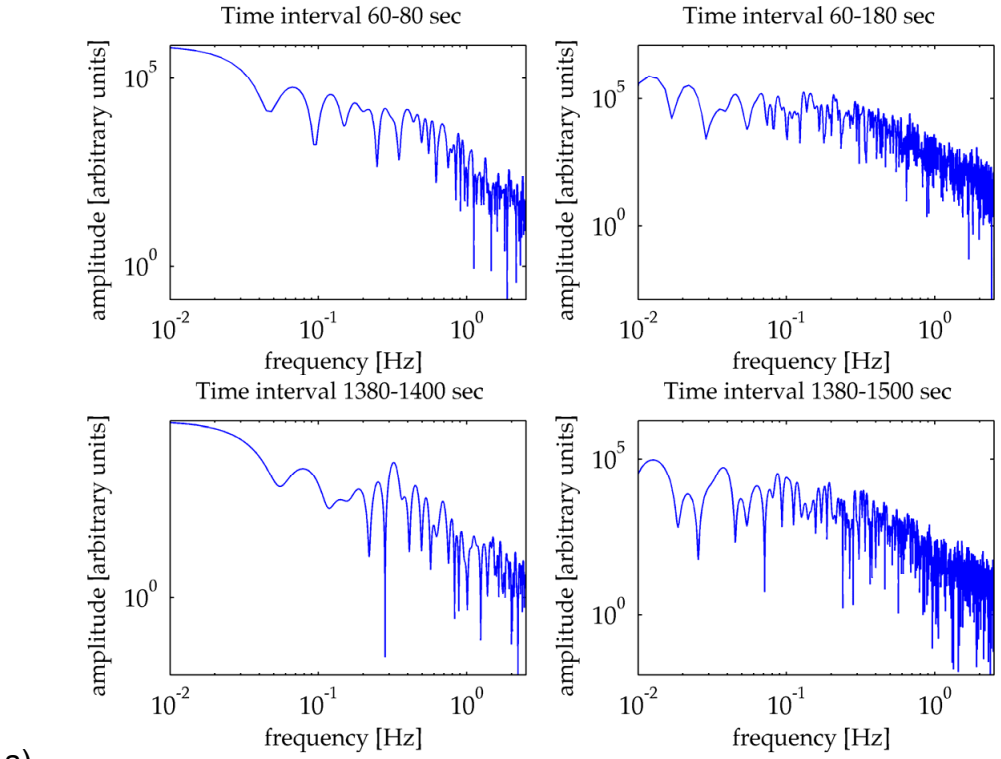

a)

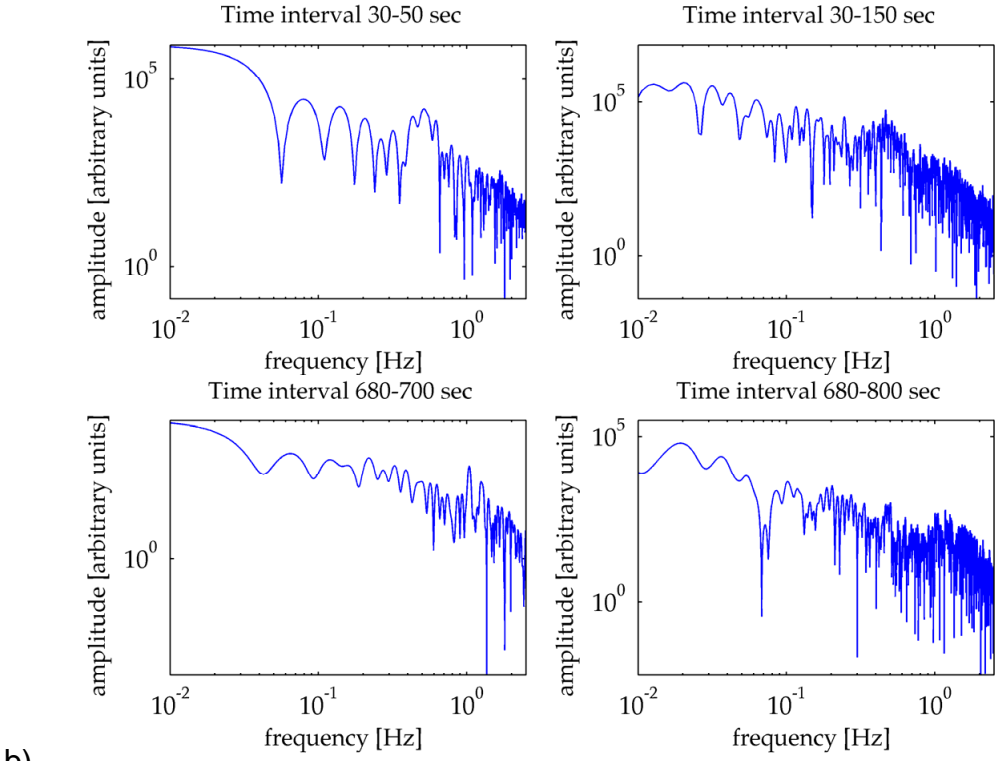

b)

Figure 7-11: FFT Frequency spectra for the stirred tank agitated at 300rpm a) PEPT and b) CFD_PT

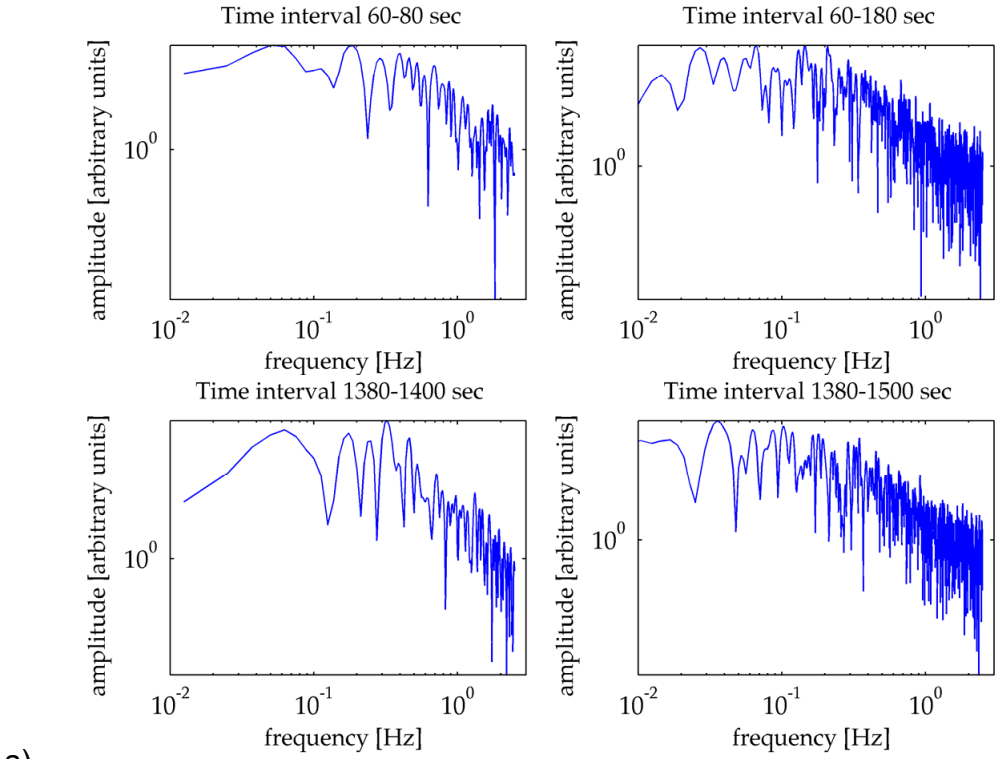

a)

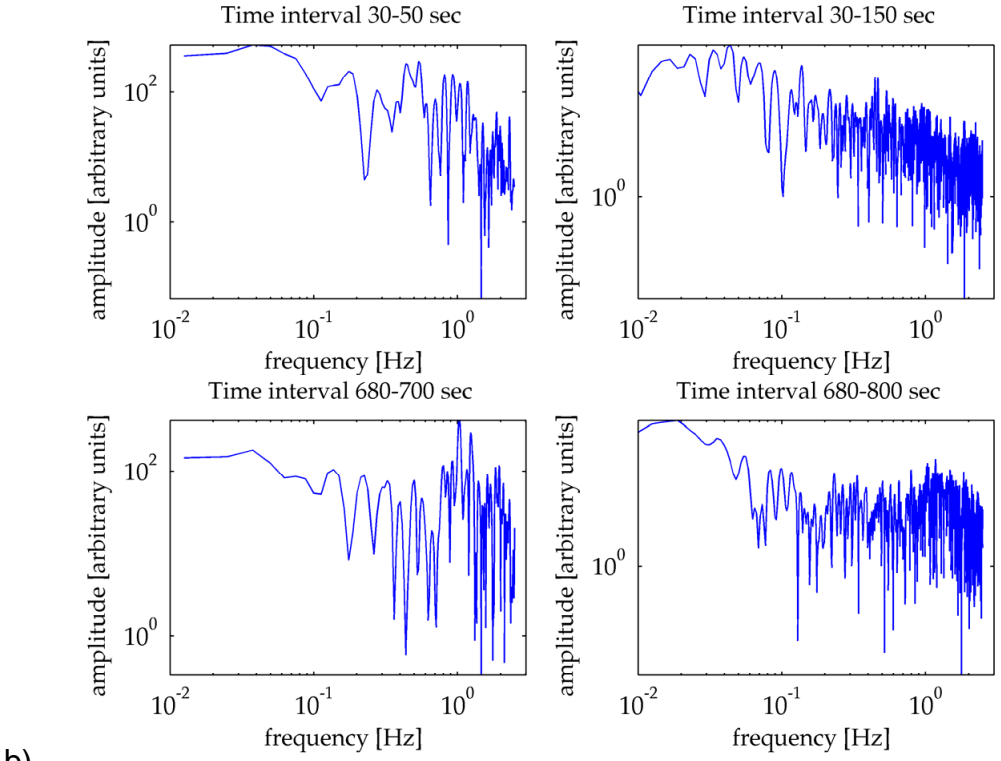

b)

Figure 7-12: Lomb-Scargle frequency spectra for the stirred tank agitated at 300rpm a) PEPT and b) CFD_PT

7.4 Return Time & Length Distributions for Trajectories

7.4.1 What are Return Time & Length Distributions?

A different way to characterise mixing using trajectories is by analysing return time and length distributions. Return time and length quantities are related to portions of particle trajectories that start from and end at a defined position. By following the tracer every time it leaves a defined region and recording the distance travelled and the time spent before it returns to the original starting position, it is possible to obtain useful data, which can be used to characterise the system investigated. Furthermore, the average trajectory velocity can also be calculated by dividing the length of the trajectory by its return time. The control region chosen in this work, as the starting and ending points of the trajectories, is similar to that used by Middleton, 1979, when studying the flow generated by Rushton turbines using a radio pill. The region consists of a toroid with height= $D/3$, inner diameter= 11/12 D, outer diameter= 19/12 D and positioned at the impeller plane (see Figure 7-13). The best way to analyse all these return quantities is

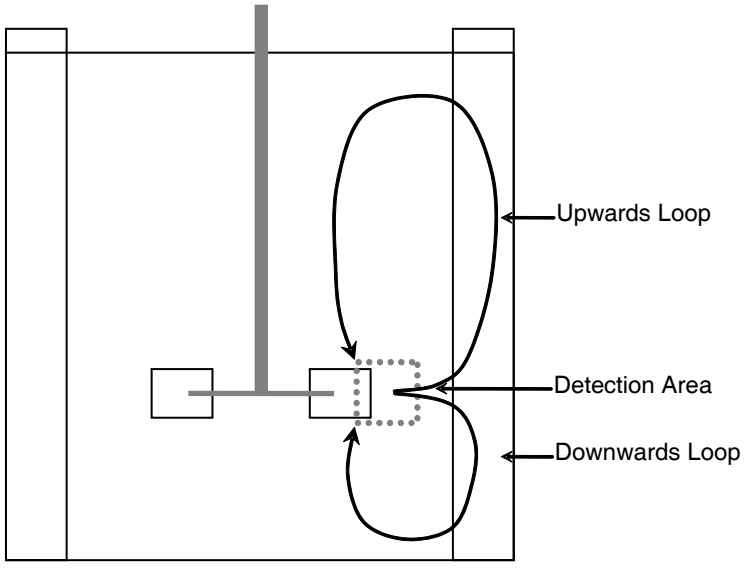

Figure 7-13: Schematic diagram of the control region chosen for return time and length measurements.

by plotting them on histograms as a function of the frequency with which every trajectory occurs. Considering the typical qualitative representation of the flow in a tank agitated by a Rushton turbine at a clearance of $C=T/4$ as shown in Figure 7-13 one would expect that the flow in the upwards loops would result in longer times and distance travelled than those in the downwards loops. Possibly, with a clearance equal to $C=T/2$, the two loops would give comparable results (Roberts *et al.*, 1995). A typical return length distribution found from the trajectories that leave from and return to the detection region obtained for the large geometry used in this work are reported in Figure 7-14a From this distribution, it is possible to distinguish a main peak for return lengths at $180mm$, which is probably related to the flow in the downward loop.

However, there is not another clear peak that might be expected due to the upwards flow loop. In order to better distinguish the distributions of the return trajectories according the upward and downwards loops, the trajectories have been split in two groups depending on which part of the vessel they pass through prior to passing through the interrogation area. This information is readily available from the raw PEPT data. The result of analysing the data that way is shown in Figure 7-14b where the dark and light grey data are associated with the downwards and upwards trajectories respectively. Comparing the two trajectories for the different regions in Figure 7-14, it can be seen that the distribution obtained using all the trajectories (Figure 7-14a) is largely dominated by the trajectories that occur in the lower part of the vessel. In addition the number of trajectories occurring in the upper and lower part of the vessel represent on average 46% and 54% of the total number of trajectories, respectively.

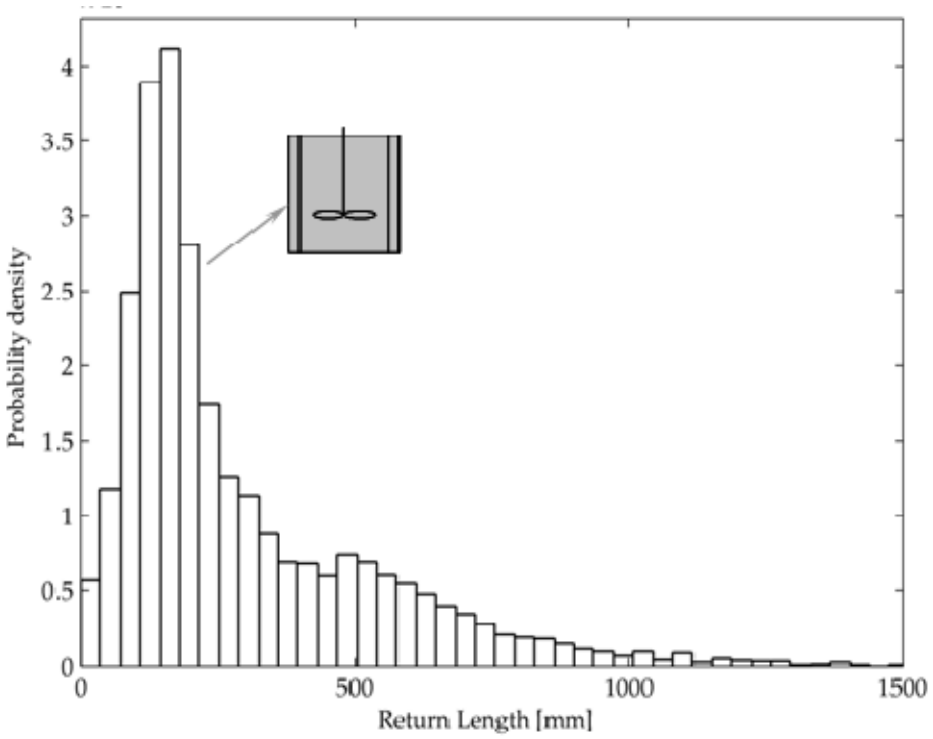

a)

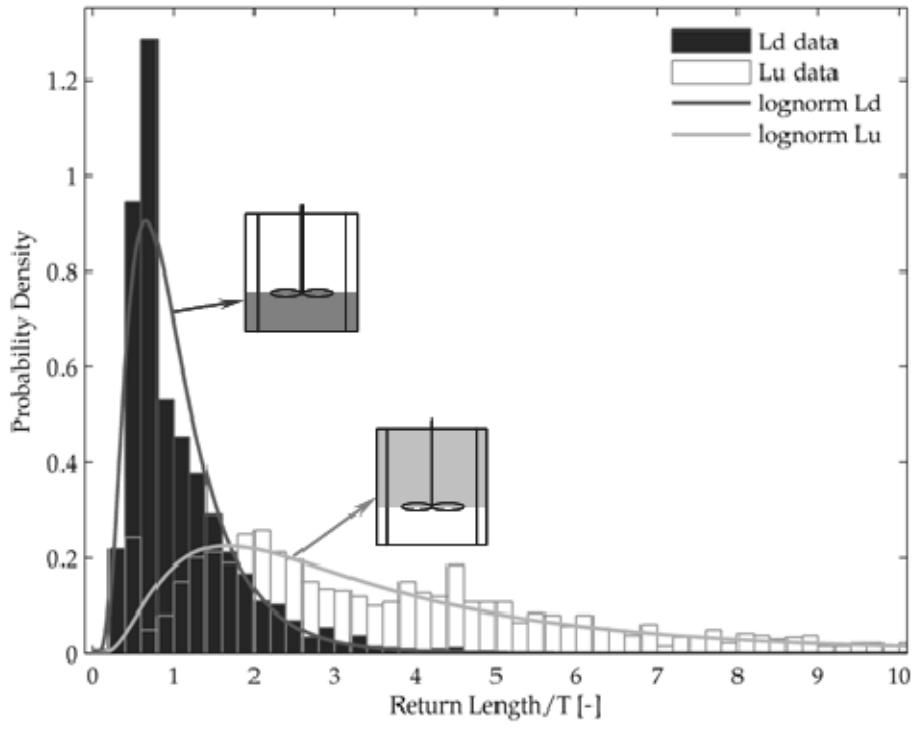

b)

Figure 7-14: Return length distribution for large stirred vessel agitated at 300rpm: a) using all the trajectories and b) grouping them in two groups.

In the remainder of this Section, the trajectories will be grouped as being in the upper and lower part of the vessel as described above and in addition, the return lengths will be made dimensionless with respect to the diameter of the tank (T) for all the distributions. Finally, each distribution has been best fitted with a log-norm distribution as reported previously (Middleton, 1979; Roberts *et al.*, 1995; Wittmer *et al.*, 1998). A similar approach has been adopted with the return time distributions and velocities, which have been made dimensionless by means of the impeller speed ($1/N$) and the impeller tip velocity (v_{tip}), respectively. An additional feature that can be illustrated by this type of analysis is the complexity of a single trajectory or a set of trajectories by defining a particular condition that they have to meet. For example, it is possible to select a family of trajectories based on particular return length or the return time criterion.

Figure 7-15a shows the upwards and downwards trajectories with a return length equal

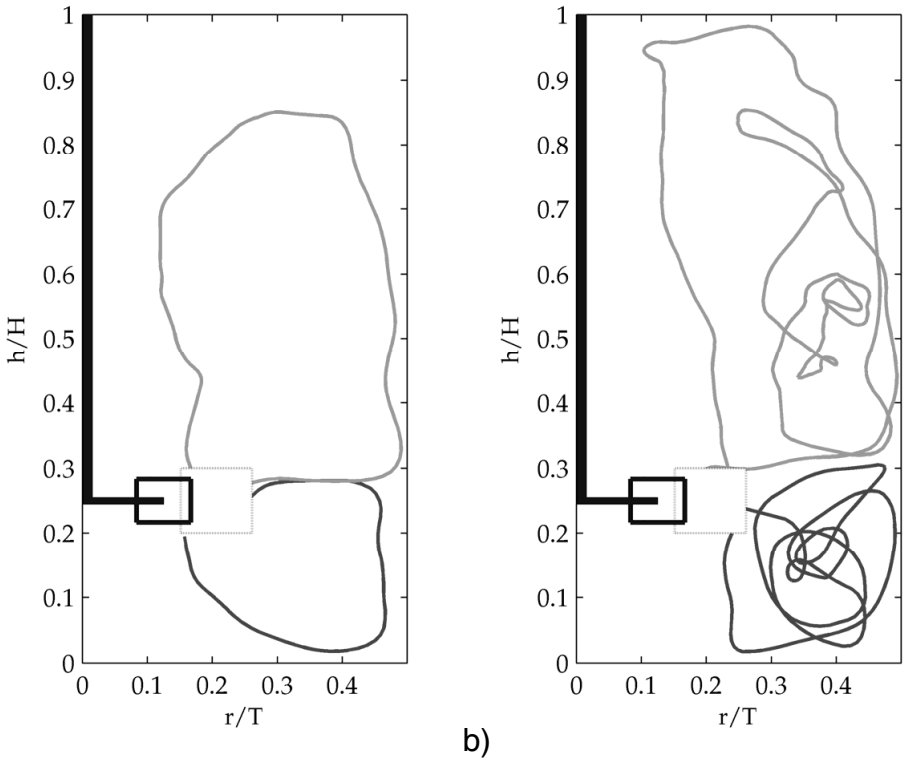

Figure 7-15: Typical return trajectories for large stirred vessel agitated at 300rpm on a *rz*-plane: a) short pattern and b) long pattern.

to 3.5 and 1 times the diameter of the tank respectively. Similarly, Figure 7-15b reports two trajectories associated with the upper and lower tank region with return path length equal to 5 and 3 times the diameter of the vessel. In this way, it is possible to better understand discrepancies between different distributions or achieve a better insight of typical phenomena occurring in the geometry. In particular, in Figure 7-15b it can be seen how certain trajectories contribute to the tail of return length distributions as a result of several loops occurring in the upper or lower regions of the vessel without ever crossing the impeller plane. On the other hand, Figure 7-15a shows how similar trajectories, which intersect the impeller plane, generate single loop paths, which are also the most frequent in the vessel.

7.4.2 Return distributions for real data

In this Section, the return length, time and velocity distributions for different experiments are reported and compared in order to show the useful information that can be obtained by this method. As explained in the previous Section, the return length, time and velocity distributions have been made dimensionless in order to compare data from different impeller speeds and different scales. Recapping, the experiments done consist of:

- two runs at 300rpm for the large scale vessel using two different tracer sizes,
- four runs in the small scale vessel using a salt solution with impeller speeds varying from 100 to 600rpm,
- four similar runs in the small scale using sucrose solution

In addition, the results from one simulation run with CFD have been included.

Figure 7-16 and Figure 7-17 shows the distributions obtained from two experiments, one in the large and one in the small scale geometries agitated at 300 ($Re = 161 \cdot 10^3$, $v_{tip} = 1.58 m/s$) and 200rpm ($Re = 48 \cdot 10^3$, $v_{tip} = 0.66 m/s$) respectively. It can be seen clearly that the distributions obtained for the two cases are so similar to each other that it seems difficult to draw any quantitative conclusion other than that they are essentially the same.. This similarity between the distributions agrees with the generally accepted concept that, for stirred vessels under turbulent conditions and with geometrical-similarity, velocity quantities made dimensionless by means of the tip velocity and dimensions by tank diameter are constant throughout the entire turbulent regime. Furthermore, the dimensionless return velocity distributions show that the most frequent dimensionless velocities in the upper and lower loop are comparable, though the velocity distribution for the upper region has a longer tail, which is probably an indication of a larger variety of potential trajectories; in particular, there is more room to exhibit multiple loops. The distributions obtained from all the experiments carried out in this work are very similar to each other, hence in order to compare quantitatively the different experiments, the data in each case have been fitted with a log-norm probability function as suggested by Bryant and Sadeghzadeh, 1979. The mode value for each probability density functions was obtained by finding the value for which the function was a maximum; hence, the most frequent event.

In Table 7-1 the data for the different experiments are divided into three main groups, the first set is for the two experiments carried out in the large geometry (T=287mm), the second and the third sets are for the small geometry (T=148mm) for the salt solution and the sucrose solution, respectively. Furthermore, the return values are reported in

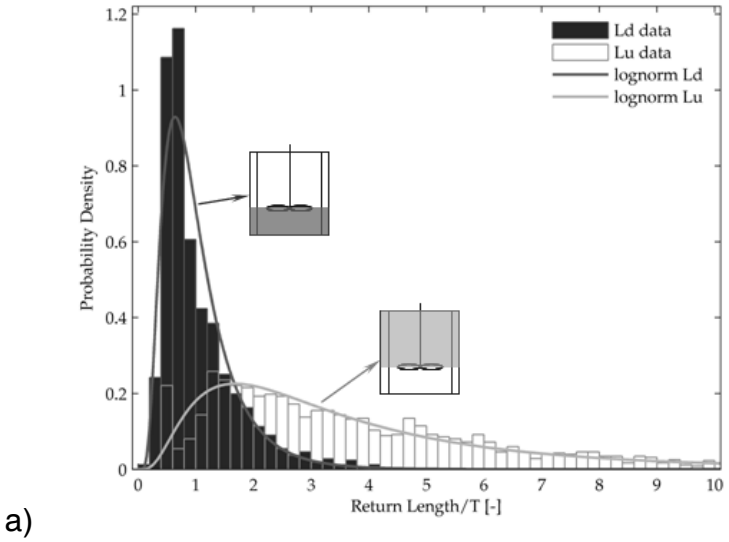

a)

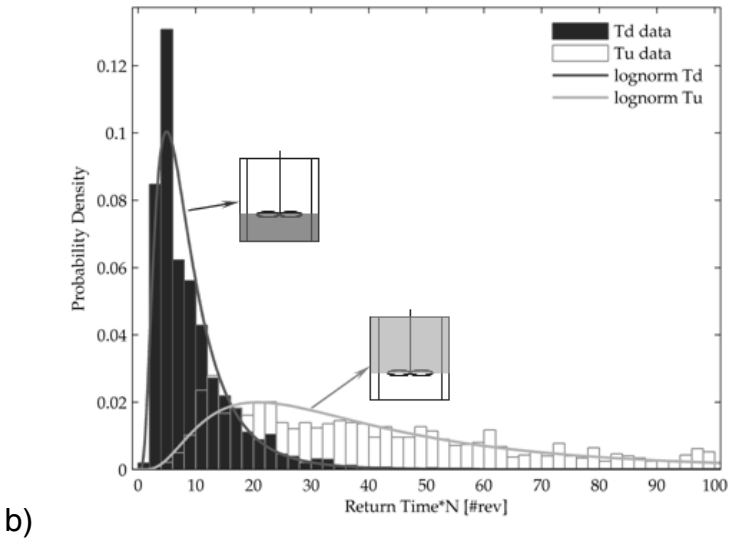

b)

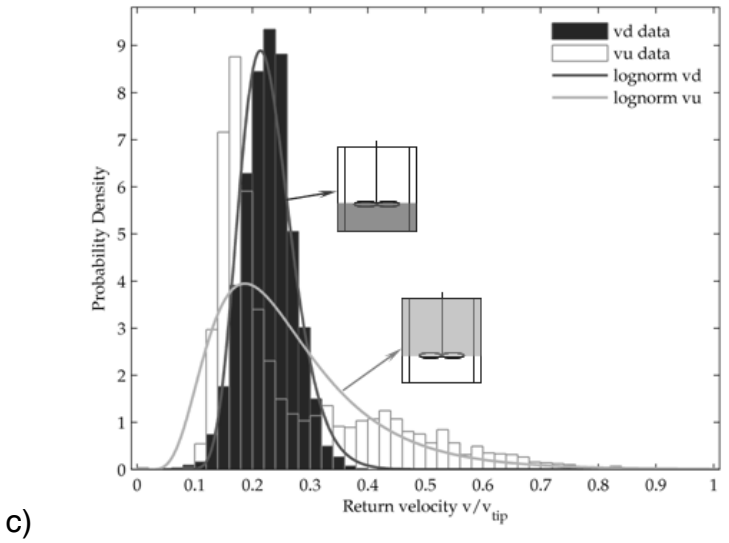

c)

Figure 7-16: Return trajectory distributions for the large stirred vessel agitated at 300rpm using 250μm tracer. Return a) length, b) time and c) velocity distributions.

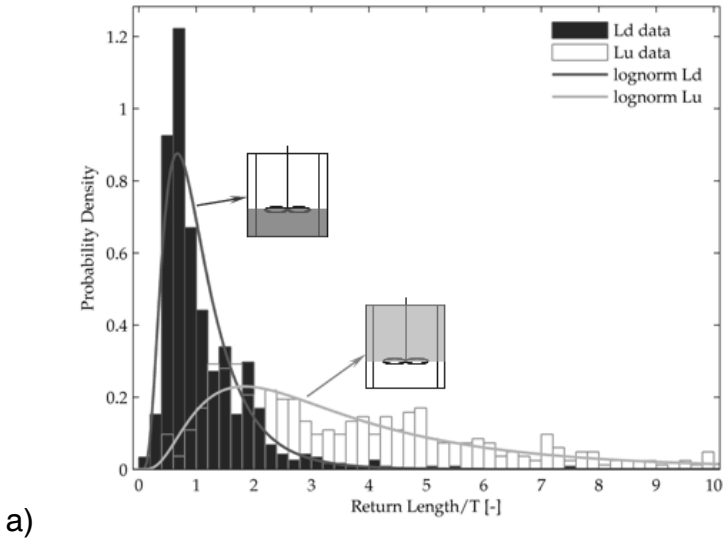

a)

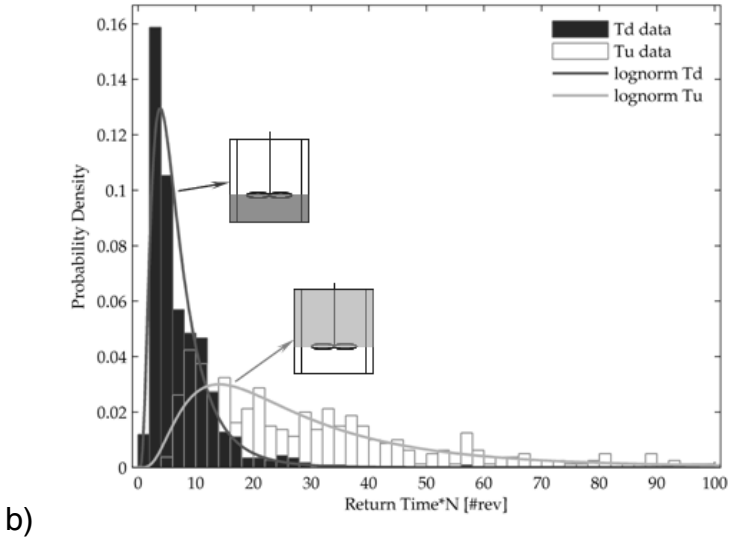

b)

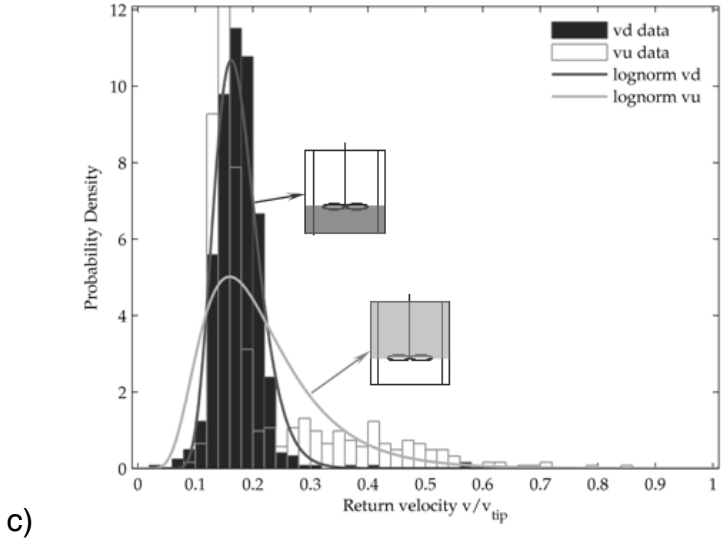

c)

Figure 7-17: Return trajectory distributions for the small stirred vessel agitated at 200rpm using salt solution and 250μm tracer. Return a) length, b) time and c) velocity distributions.

both the dimensionless and their original dimensional forms. By looking at the mode values for each group of data, it is possible to notice how these values are constant in all the experiments, except for experiments *RT100* and *RT200suc*. However, these latter experiments were run at lower speeds and even though the density of the tracer had been carefully matched by that of the fluid, the PEPT data occasionally showed the tracer resting on the bottom of the vessel. Hence, ignoring the values obtained for these two experiments, several conclusions have been deducted from this approach.

The most frequent return lengths for the lower region (*Ld*) are very similar for the experiments carried out in the salt solution at both scales, while slightly smaller values are obtained for the sucrose solutions (about 0.90 versus 0.86 times the tank diameter). For the upper part of the vessels, though there are fewer results, the values of *Lu* range from 1.88 to 3.13 times the tank diameter. However, it can be observed that the experiment in the smaller vessel and with the sucrose solution give the shortest relative trajectories, while the longest are obtained from the experiments in the large vessel. These differences can be explained in terms of the irregularity and relative randomness of the particle paths. Larger values of return length denote that the particle follows a longer and more complex trajectory; since the sucrose solution is more viscous than the

Table 7-1: Summary of the most frequent values for return length, time and velocity distributions.

Experiment =	*RT300d250*	*RT300d600*	*RT100*	*RT200*	*RT480*	*RT600*	*RT200suc*	*RT300suc*	*RT480suc*	*RT600suc*	CFD_PT20
N [rpm]	300	300	100	200	480	600	200	300	480	600	300
1/N [sec]	0.20	0.20	0.60	0.30	0.13	0.10	0.30	0.20	0.13	0.10	0.20
D [mm]	97	97	48	48	48	48	48	48	48	48	97
T [mm]	287	287	148	148	148	148	148	148	148	148	287
Most frequent value:											
for Ld / T [-]	0.92	0.90	0.90	0.91	0.90	0.87	0.80	0.83	0.87	0.88	0.88
for Lu / T [-]	3.04	3.08	2.00	2.36	2.39	3.13	1.71	1.88	2.14	2.14	2.99
Ld [m]	0.26	0.26	0.13	0.13	0.13	0.13	0.12	0.12	0.13	0.13	0.25
Lu [m]	0.87	0.88	0.30	0.35	0.35	0.46	0.25	0.28	0.32	0.32	0.86
for Td · N [-]	2.98	3.19	3.70	4.62	4.51	4.11	3.19	4.21	4.62	4.62	3.59
for Tu · N [-]	12.58	15.34	11.46	15.23	16.26	19.22	11.46	13.09	14.72	14.32	17.07
Td [sec]	0.60	0.64	2.22	1.38	0.56	0.41	0.96	0.84	0.58	0.46	0.72
Tu [sec]	2.52	3.07	6.87	4.57	2.03	1.92	3.44	2.62	1.84	1.43	3.41
for vd/v_{tip}	0.24	0.24	0.12	0.19	0.19	0.20	0.11	0.14	0.17	0.18	0.20
for vu/v_{tip}	0.17	0.17	0.15	0.15	0.14	0.15	0.14	0.14	0.14	0.15	0.10

salt solution, it can be speculated that the larger viscous forces might lead to more regular paths and hence shorter return length values. Concerning the different values for the larger scale compared the smaller one; it is hard to find the reason why on the larger vessel the dimensionless return trajectories seem to be longer compared with the trajectories found for the smaller scale. Furthermore, in the small vessel with salt solution the spread of these values is larger than in the other two groups; for the sugar solution instead, it is possible to notice how increasing the impeller speed, hence the Re, the return length for the upper region increases, possibly, because at higher Re corresponds faster mixing and larger randomness. Furthermore, Baldyga *et al.*, 2001, introduced the concept of intermittency, where bursts in the specific energy dissipation rate occur more often for increasing Re and, therefore, further variation in the flow field pattern can be caused by intermittency phenomena at higher impeller speeds.

Regarding the dimensionless return time mode values (Td and Tu), there is good consistency for the smaller geometry for the lower region of the vessel, Td, (discrepancies are smaller than 5% of the mean value), while there is a larger spread of values for the upper region, Tu. This finding is probably due again to the possibility of the tracer following some longer trajectories, which might also influence the fitted log-normal function and thus its mode. For the larger vessel, again there is good agreement for the return times for the lower part and a slightly wider spread for the upper part; overall, the dimensionless return times for the large vessel are substantially shorter than the return times for the small scale. This observation may imply that return time cannot be compared between two scales based on only impeller speed; or that at the larger scale, the trajectories average velocity is slightly higher than in the small tank.

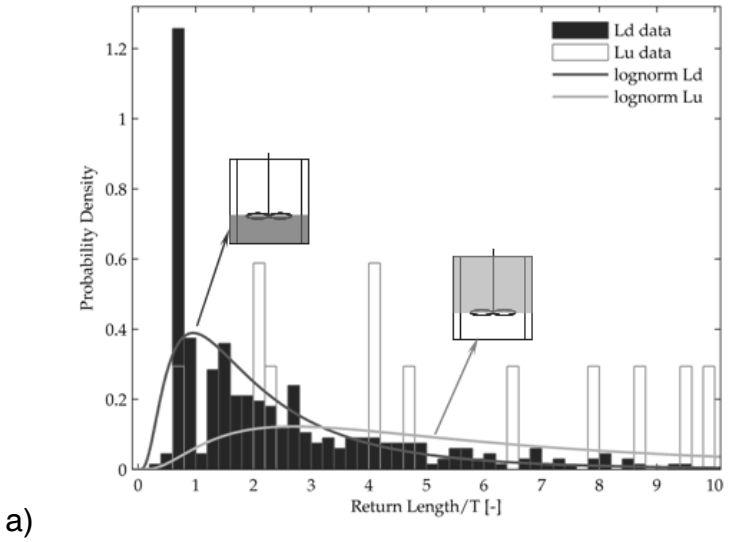

a)

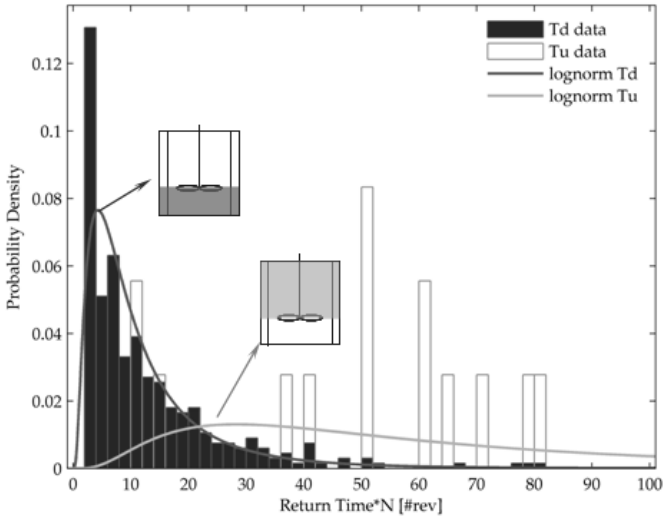

b)

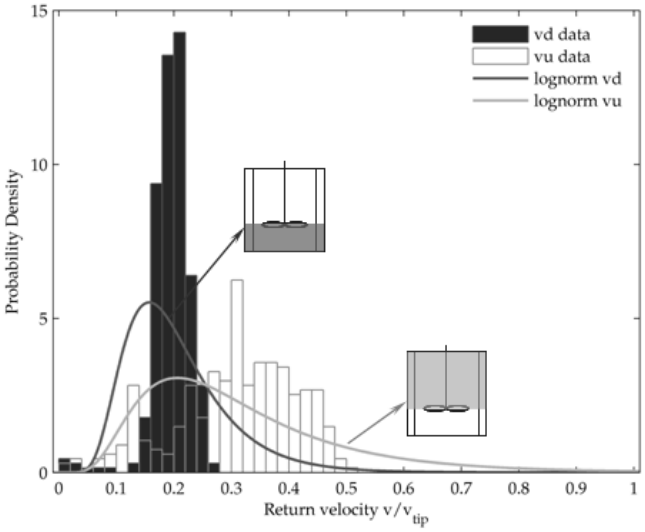

c)

Figure 7-18: Return trajectory distributions for the large stirred vessel agitated at 300rpm obtained from CFD_PT simulation. Return a) length, b) time and c) velocity distributions.

Regarding this last observation, it can be seen that the dimensionless average trajectories velocities (vd/v_{tip} and vu/v_{tip}) found in the large scale are higher than the other two set of data; where, in addition, the velocities for the salt solutions seem to be slightly larger in the lower region compared to the sucrose solution, 0.19 versus 0.16 respectively.

In order to complete this type of analysis, similar distributions can be obtained for the trajectories found from the CFD data. Figure 7-18 shows the return distributions with the probability density fitted function for the data obtained from the CFD Particle Tracking simulation. As already highlighted in Section 7.2 the trajectories found with CFD are much more regular than the ones obtained experimentally, the tracer tends to follow always the same trajectories without exploring the whole tank resulting in more discrete distributions than continuous as for the PEPT cases. Despite this, it is still possible to fit these distributions using a log-normal probability density function, even though the shape of the fitting function is quite different from the previous cases. Therefore, quantitative analysis is likely to be imprecise and not accurate. However, the predictions are best for the lower part of the vessel, with the modes within 25% of the experimental ones.

7.4.3 Circulation times and homogenisation times

In the literature, most workers report that mean circulation times for stirred vessels are inversely proportional to impeller speed, as reported in Section 2.5. In order to compare the present work with the literature, the most frequent return times for all the experiments have been plotted versus the reciprocal of the impeller speed in Figure 7-19. The data obtained for the upper and lower distributions have been split into three sets Table 7-1, i.e. for the salt solution in the large and in the small vessel and for the

sucrose solution in the small vessel. Figure 7-19 confirms that for this work too, the return times are linearly dependent on 1/N for both loops. For the return times for the upper loop in the small vessel, the values in the salt solution are larger than with the sucrose solution. Furthermore, the scale seems not to have a major effect on the return time; in fact, for impeller speed equal to 300*rpm* ($1/N$=0.2*s*), experiments carried out in the two sizes result in similar values for the return times. In addition, the return times for the sucrose solution are smaller than the return times for the salt solution, particularly for lower impeller speeds, i.e., higher values of $1/N$. This result suggests that the return times depend not only on the size of vessel used and on the impeller speed, but probably also on the viscosity of the fluid in the system and thus on the *Re* of the system. In the literature, a few workers have correlated mixing and circulation times and linked them to impeller speed (Holmes *et al.*, 1964; Ruszkowski, 1994; Grenville *et al.*, 1995 or Nienow, 1990).

In an attempt to understand better both the validity of those relationships and the meaning of return times, Figure 7-20 shows on the same plot, the return times found here for the PEPT experiments and the values predicted by using the equations in the literature and collected in Table 7-2. From Figure 7-20 it can be seen how the

Table 7-2: Mean circulation, $\bar{t}$, and mixing time, θ, based on equations from literature

Holmes et al., 1964	$\bar{t} = 0.64\left(\frac{T}{D}\right)^2 \frac{1}{N}$
Middleton, 1979	$\bar{t} = 0.5V^{0.3}\left(\frac{T}{D}\right)^3 \frac{1}{N}$
Nienow, 1990	$\bar{t} = \frac{V}{Fl \cdot N \cdot D^3}$
Ruszkowski, 1994; Grenville et al., 1995	$\theta = 5.3\left(\frac{1}{N}\right)\left(\frac{1}{Po}\right)^{0.33}\left(\frac{T}{D}\right)^2$

prediction based on the ratio between the volume of the tank and the pumping capacity of the impeller proposed by Nienow, 1990, which is essentially a conceptual time only, is very large compared to the measured circulation times of the others. In addition, the prediction of mixing time is expected to be higher than the circulation time since it has been shown, for example, byKhang and Levenspiel, 1976, that a system is homogenised after about 5 circulations. Concerning the Holmes *et al.*, 1964, and Middleton, 1979, expressions, both of them are close to the return time obtained for the lower loop, while the values for the upper loop are significantly different. Thus, these predictions tend to fit only the lower loop values because the techniques, used by the authors of these expressions, did not allow one to distinguish between the upper and lower loop and because the lower loop is so much more common, as resulted in distributions similar to Figure 7-14a which is itself dominated by the lower loop data. Holmes *et al.*, 1964, used a tracer concentration response technique while Middleton, 1979, used a radio pill and the difference in the two techniques may possibly explain the discrepancies between the two predictions.

Finally, PEPT allows the effect of the detection area used with respect to these mixing parameters to be analysed. Figure 7-21 indicates how the most frequent return times, obtained for the large vessels, change as a function of the detection area used to define the starting and ending point of the trajectories. It can be seen from Figure 7-21 that the dimensions of the detection area have a major influence on the circulation time results.

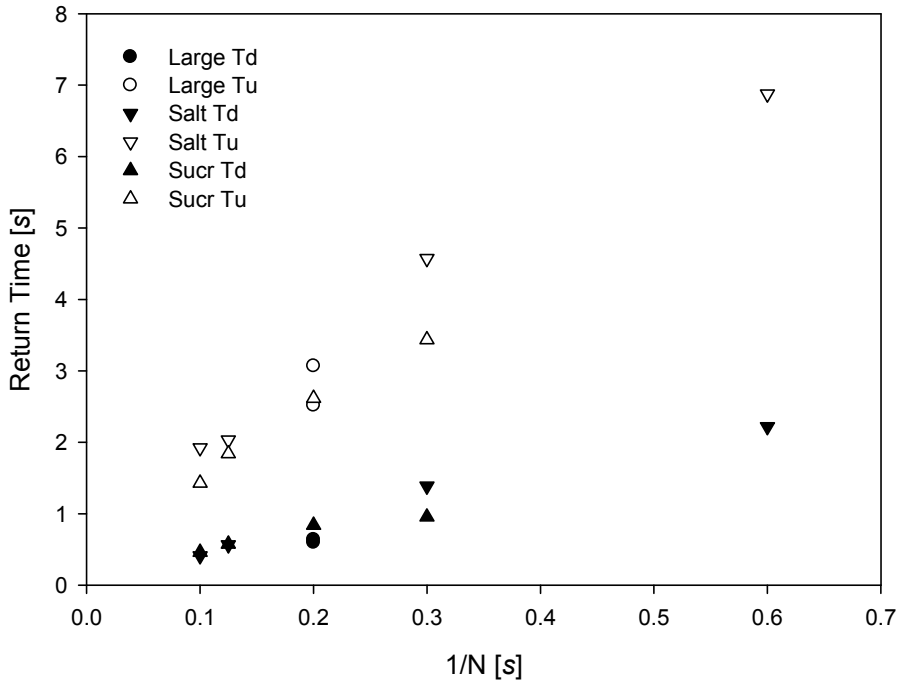

Figure 7-19: PEPT Return times obtained from the different experiments plotted versus the reciprocal of the impeller speed

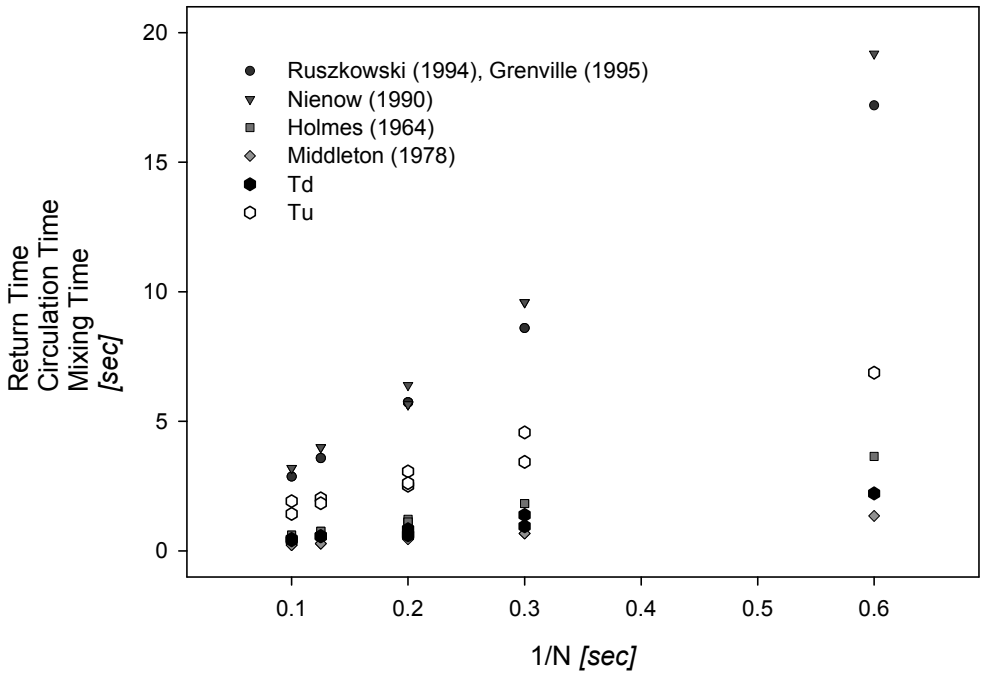

Figure 7-20: PEPT Return times plotted versus the reciprocal of the impeller speed compared to different relationship found in literature

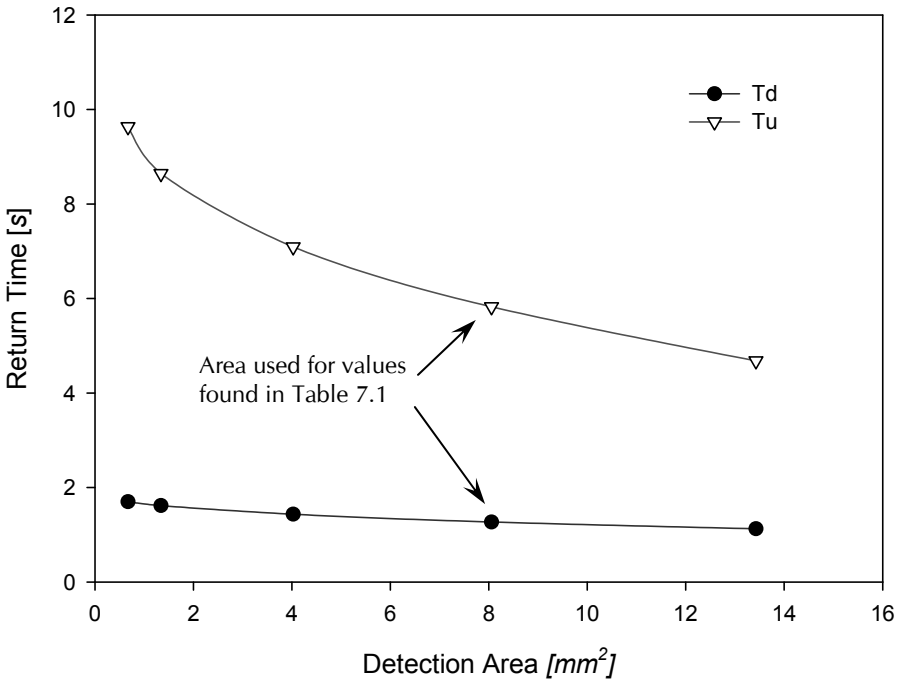

Figure 7-21: Effect of the detection area on the return times for RT300Large experiment

Furthermore, in those techniques where the calibration of the system is difficult, very different results can be obtained using the same technique. For example, with the radio pill, the sensitivity of the receiver needs to be set so that the pill detects passages close to the aerial without detecting the ones far away and great care is needed when doing so. Schmitz, 1996, compared the circulation time distribution obtained using both the radio and the magnetic pill techniques; the magnetic pill showed much larger circulation times. The finding was explained as being because the two tracers had different sizes and the two methods have different sensitivities and hence detection area.

At this point, it can be concluded that when circulation times are used to characterise mixing, particular attention must be paid to three main factors:

- the size of the tracer affects its ability to follow the liquid motion, especially when system with higher viscosity than water are analysed;

- the detection area has a major effect on the magnitude of the circulation times measured, hence quantitative comparisons between different techniques and different workers can be misleading;
- the detection area also affects the magnitude of the circulation times, hence again quantitative comparisons between different techniques and studies can easily be of doubtful value;
- for stirred vessel equipped with radial flow impellers positioned as in the present geometry, circulation times are largely governed by the lower loop, which represents only 55% of all the circulations that occur, thus they are not fully representative of what happen in the whole system. This problem can also occurs in other system where secondary loops are present.

7.5 Conclusions

In this last Chapter reporting the results from this study, experimental and numerical trajectories have been thoroughly analysed and compared. Starting from qualitative methods, experimental trajectories have been shown to be very erratic and with a high level of randomness. On the other hand, the trajectories found by using CFD models are much more regular and uniform, resulting in zones with a high number of passages and regions with an absence of information since no passes are recorded. The impact of these two important and different characteristics has been assessed by side-by-side comparisons of Poincaré maps and particle trajectories.

In order to find a quantitative approach, frequency analysis as well as return time and length distributions have been analysed. Both the two frequency analysis methods, applied to the trajectories obtained experimentally, have not been successful, since the

trajectories do not show any regular frequency, leading to the conclusion that the ideal flows where the fluid moves in regular lower and upper loops is a simplification of what happens in a real system. The tracer may follow one of the loops for a short while, but then it leaves immediately for another direction. Only the average of all these paths creates those regular loops that can be idealised as two main toroids present above and below a radial flow impeller in the typical off bottom clearance of T/4 to T/3.

Finally, return time and length distributions confirmed that geometrically similar stirred vessels under turbulent conditions can again be compared to each other on the basis of dimensionless velocities. Furthermore, the tracer spends a longer period of time above the impeller (up to 10% longer) and circulation times are dominated by what happens in the upper region.

Chapter 8

Conclusion and Recommendations for Future Work

In this Chapter, the main conclusions reported in each part of the thesis are summarised.

8.1 Positron Emission Particle Tracking applied to turbulent mixing processes

In Chapter 5, the PEPT technique has been tested and evaluated for the quantification of the fluid flow in a vessel stirred by a Rushton turbine under turbulent conditions. For fluid moving mainly in a circular motion, as is the case of stirred vessels, the use of cylindrical reference coordinates leads to more accurate velocities.

Where high velocities gradients, especially when associated with rapid changes of direction, occur, e.g. in the region near to the impeller, it is possible that PEPT underestimates velocities (up to about 50% lower than the true value as measure by PIV, for example, and in the literature). This problem has been revealed and partially resolved by adopting a selective interpolation extra locations in the raw data where the experimental locations are further apart than a certain prescribed distance. This interpolation results in an increase in the measured velocities, bringing them closer to the true values. Despite the problem PEPT has in dealing with high velocity gradients, the technique is still an outstanding tool for the study of opaque systems and its use can be extended to all liquid/paste systems, though still keeping in mind that where high velocity gradients are found, the velocities in those regions could be underestimated. The ability to follow a tracer in an opaque system is a great advantage over many other techniques; in addition, it is essential for the study of all the countless industrial application where only an empirical approach has been used until today.

8.2 Numerical Particle Tracking

In Chapter 6, CFD simulations of stirred tanks were reported. From the comparison of two turbulence models, *RNG* k-ε and k-ω models, it can be concluded that, despite both predicting similar velocity profiles, they show differences in the prediction of kinetic energy and energy dissipation rate. Underestimation of the energy quantities close to the impeller has been assessed for RANS simulations (see Section 6.1.2); however, the k-ω model results in greater turbulence estimations, which are closer to the experimental values whatever the mesh used.

From CFD simulations, it has been possible to find fluid velocities higher than the tip speed behind the impeller blades. Further investigation of the literature and PIV experimental work has validated these velocities.

The rest of the work done in CFD aimed to simulate the Lagrangian particle tracking achieved by means of PEPT. The idea was to solve a standard simulation and subsequently track a single particle numerically. For the simulation of stirred tanks, the use of two domains (rotating and stationary) is needed, thus creating a moving interface, which makes it impossible to track the particle correctly across it. This limitation has been overcome by creating a three-step simulation: a standard rotating-stationary simulation was used as the initial condition leading to a second one, where the rotating domain was frozen and finally, the particle tracking routine was implemented , which gave sensible results. This method was successful in terms of usability though the results still need to be validated and improved by tuning the particle solver parameters.

8.3 Trajectography

Chapter 7 investigates how to use trajectories in order to compare different systems both experimental and numerical. From a qualitative point of view, the trajectories obtained experimentally are erratic and follow random paths. The trajectories obtained from the CFD simulations instead follow a uniform pattern and tend to pass several times from the same region without visiting the rest of the vessel. Quantitatively, the analysis of trajectories led to the conclusion that the tracer follows random trajectories and certainly not any regular pattern. In fact, a frequency analysis study (Section 7.3.3) failed in finding any dominant frequencies.7.3.3.2

Finally, the circulation study proved the value of analysing time and return length distributions since it was possible to compare the circulation times achieved in PEPT with published work. Furthermore, thanks to the large quantity of data obtained with this technique, it has also been possible to understand the effect of the detection area on the circulation time, thus, the wide discrepancy in results between radio follower and magnetic follower techniques.

8.4 Further work and recommendations

In terms of the validation of the PEPT technique applied to turbulent liquid systems such as agitated vessels, the work achieved in this thesis is believed to be exhaustive and accurate. The in-depth and methodical approach used in this thesis should be used as a basis for other workers who intend to use this technique to study turbulent systems and also viscous complex rheology opaque systems of 'real' materials as found in industry where there is no chance of validating PEPT against PIV, for example. For the latter cases, the velocities and rates of acceleration are likely to be lower and the PEPT

technique with the considerations established here really comes into its own and the range of such mixing problems that can be tackled becomes almost infinite.

Knowledge of the limitations of PEPT and how to accommodate them also will be of great value for handling the fluid flow in turbulent two phase (gas-liquid, liquid-liquid and solid liquid) and three phase (G-L-S) systems and by labelling the solid phase, the velocity of that phase in two and three phase systems. Also by labelling one size at a time, the flow of one size of particle in a range of sizes should be tractable. The method should also be extendable to cover the spatial distribution of different sizes (their occupancy).

Finally, the trajectography approach used in this work is the first attempt at using trajectories from PEPT as a tool to characterise mixing performance rather than only using the data to find Eulerian velocities and vector plots. Pitiot, 1999, using a different technique, namely video trajectography, investigated different ways on how to use trajectories for mixing characterisation purposes; some of that work could be extended to PEPT results directly. Many of these topics are now being pursued in the Chemical Engineering Department at the University of Birmingham.

Concerning the numerical approach with CFD, the main area of improvement and further work would be the validation of the trajectories obtained by using the method proposed in Section 6.4. The effect of the particle solver parameters on the final paths should also be investigated. However, if new releases of Ansys-CFX fix the boundary issue for particle tracking, the method proposed in this thesis would automatically lose its value.

Bibliography

ANDERSON, J.D., CORRIGAN, J.J. and CASTELLANO, E., "Computational Fluid Dynamics. The basics with applications" (*McGraw-Hill, Inc., Singapore,* 1995).

ANSYS-CFX, "ANSYS CFX-Solver, Release 10.0: Theory" (2005).

ARMENANTE, P.M., LUO, C., CHOU, C.C., FORT, I. and MEDEK, J., "Velocity profiles in a closed, unbaffled vessel: Comparison between experimental LDV data and numerical CFD predictions", *Chemical Engineering Science (20) 52* (1997) *3483-3492*.

AUBIN, J., FLETCHER, D.F. and XUEREB, C., "Modeling turbulent flow in stirred tanks with CFD: the influence of the modeling approach, turbulence model and numerical scheme", *Experimental Thermal and Fluid Science (5) 28* (2004) *431-445*.

BAKKER, A. and VAN DEN AKKER, H.E.A., "Single-Phase Flow in Stirred Reactors", *Trans. Inst. Chem. Engrs. (A) 72* (1994) *583-593*.

BALDYGA, J., BOURNE, J.R., PACEK, A.W., AMANULLAH, A. and NIENOW, A.W., "Effects of agitation and scale-up on drop size in turbulent dispersions: allowance for intermittency", *Chemical Engineering Science (11) 56* (2001) *3377-3385*.

BARIGOU, M., "Particle tracking in opaque mixing systems: An overview of the capabilities of PET and PEPT", *Chemical Engineering Research and Design (9 SPEC. ISS.) 82* (2004) *1258-1267*.

BARTELS, C., BREUER, M. and DURST, F., 'Comparison Between Direct Numerical Simulation and k-ε Prediction of the Flow in a Vessel Stirred by a Rushton Turbine.' *10th European Conference on Mixing* (*Delft, Netherlands,* 2002).

BATES, R.L., FONDY, P.L. and CORPESTEIN, R.R., "An Examination of some Geometric Parameters of Impeller Power", *I&C Process Design and Development 2* (1963) *310-314*.

BERTRAND, J. and COUDERC, J.P., "Evaluation of the Power Consumption in Agitation of Viscous Newtonian or Pseudoplastic Liquids by Two-Bladed, Anchor or Gate Agitators", *Chemical Engineering Research and Design (4) 63* (1985) *259-263*.

BEZZO, F. and MACCHIETTO, S., "A general methodology for hybrid multizonal/CFD models: Part II. Automatic zoning", *Computers and Chemical Engineering (4) 28* (2004) *513-525*.

BEZZO, F., MACCHIETTO, S. and PANTELIDES, C.C., "A general methodology for hybrid multizonal/CFD models: Part I. Theoretical framework", *Computers & Chemical Engineering (4) 28* (2004) *501-511*.

BRITZ, D. and ANTONIA, R.A., "A comparison of methods of computing power spectra of LDA signals", *Meas. Sci. Technol. (7) 7* (1996) *1042-1053*.

BRUCATO, A., CIOFALO, M., GRISAFI, F. and MICALE, G., "Complete numerical simulation of flow fields in baffled stirred vessels: The inner-outer approach." *Proceedings, IChemE, Symposium Series 136* (1994) *155-162*.

BRUCATO, A., CIOFALO, M., GRISAFI, F. and MICALE, G., "Numerical prediction of flow fields in baffled stirred vessels: A comparison of alternative modelling approaches", *Chemical Engineering Science (21) 53* (1998) *3653-3684*.

BRUCATO, A., CIOFALO, M., GRISAFI, F. and TOCCO, R., "On the simulation of stirred tank reactors via computational fluid dynamics", *Chemical Engineering Science (2) 55* (2000) *291-302*.

BRYANT, J., "The characterization of mixing in fermenters", *Advances in Biochemical Engineering, Volume 5* (1977), *pp. 101-123*.

BRYANT, J. and SADEGHZADEH, S., 'Circulation rates in stirred and aerated tanks', *Third European Conference on Mixing* (*BHRA Fluid Engng, YORK, U.K,* 1979), *pp. 325-336*.

BUJALSKI, W., NIENOW, A.W., CHATWIN, S. and COOKE, M., 'The dependency on scale and material thickness of power numbers of different impeller types', *International Conference on Mechanical Agitation* (*Toulose, France,* 1986).

BUTCHER, M. and EAGLES, W., "Fluid Mixing re-Engineered", *Chemical Engineer 773* (2002) *28-29*.

CAMPOLO, M., SBRIZZAI, F. and SOLDATI, A., "Time-dependent flow structures and Lagrangian mixing in Rushton-impeller baffled-tank reactor", *Chemical Engineering Science (8) 58* (2003) *1615-1629*.

COOPER, R.G. and WOLF, D., "Velocity profiles and pumping capacities for turbine type impellers", *Canadian Journal of Chemical Engineering 46* (1968) *94-100*.

COSTES, J. and COUDERC, J.P., "Study by laser Doppler anemometry of the turbulent flow induced by a Rushton turbine in a stirred tank: influence of the size of the units - I. Mean flow and turbulence", *Chemical Engineering Science (10, 1988) 43* (1988a) *2751-2764*.

COSTES, J. and COUDERC, J.P., "Study by laser Doppler anemometry of the turbulent flow induced by a Rushton turbine in a stirred tank: influence of the size of the units - II. Spectral analysis and scales of turbulence", *Chemical Engineering Science (10, 1988) 43* (1988b) *2765-2772*.

COX, P.W., BAKALIS, S., ISMAIL, H., FORSTER, R., PARKER, D.J. and FRYER, P.J., "Visualisation of three-dimensional flows in rotating cans using positron emission particle tracking (PEPT)", *Journal of Food Engineering (3) 60* (2003) *229-240*.

DEGLON, D.A. and MEYER, C.J., "CFD modelling of stirred tanks: Numerical considerations", *Minerals Engineering (10) 19* (2006) *1059-1068*.

DONG, L., JOHANSEN, S.T. and ENGH, T.A., "Flow induced by an impeller in an unbaffled tank - I. Experimental", *Chemical Engineering Science (4) 49* (1994) *549-560*.

DUCCI, A. and YIANNESKIS, M., "Direct determination of energy dissipation in stirred vessels with two-point LDA", *AIChE Journal (8) 51* (2005) *2133-2149*.

DUFF, I.S. and SCOTT, J.A., "Computing selected Eigenvalues of Sparse Unsymmetric Matrices using subspace iteration", *ACM Transaction on Mathematical Software (2) 19* (1993) *137-159*.

DYSTER, K.N., KOUTSAKOS, E., JAWORSKI, Z. and NIENOW, A.W., "LDA study of the radial discharge velocities generated by a rushton turbine: Newtonia fluids, Re > 5", *Chemical Engineering Research and Design (A1) 71* (1993) *11-23*.

FAIRHURST, P.G., BARIGOU, M., FRYER, P.J., PAIN, J.P. and PARKER, D.J., "Using positron emission particle tracking (PEPT) to study nearly neutrally buoyant particles in high solid fraction pipe flow", *International Journal of Multiphase Flow (11) 27* (2001) *1881-1901*.

FAN, X., PARKER, D.J. and SMITH, M.D., "Enhancing ^{18}F uptake in a single particle for positron emission particle tracking through modification of solid surface chemistry", *Nuclear Instruments and Methods in Physics Research, Section A: Accelerators, Spectrometers, Detectors and Associated Equipment (2) 558* (2006) *542-546*.

FANGARY, Y.S., BARIGOU, M., SEVILLE, J.P.K. and PARKER, D.J., "A Langrangian study of solids suspension in a stirred vessel by Positron Emission Particle Tracking (PEPT)", *Chemical Engineering and Technology (5) 25* (2002) *521-528*.

FANGARY, Y.S., SEVILLE, J.P.K. and BARIGOU, M., "Flow studies in stirred tanks by positron emission particle tracking (PEPT)", *Institution of Chemical Engineers Symposium Series (146)* (1999) *23-34*.

FISHWICK, R., WINTERBOTTOM, M., PARKER, D., FAN, X. and STITT, H., "The use of positron emission particle tracking in the study of multiphase stirred tank reactor hydrodynamics", *Canadian Journal of Chemical Engineering (1) 83* (2005) *97-103*.

FISHWICK, R.P., WINTERBOTTOM, J.M. and STITT, E.H., "Explaining mass transfer observations in multiphase stirred reactors: Particle-liquid slip velocity measurements using PEPT", *Catalysis Today 79-80* (2003) *195-202*.

FRIEDLY, J.C., "Dynamic Behaviour of Processes" (*PRENTICE-HALL, INC., Englewood Cliffs, New Jersey* 1972).

FUNAHASHI, H., HARADA, H., TAGUCHI, H. and YOSHIDA, T., "Circulation Time Distribution and Volume of Mixing Regions in Highly Viscous Xanthan Gum Solution in a Stirred Vessel", *Journal of Chemical Engineering of Japan (3) 20* (1987) *277-282*.

GEURTS, B.J., "Modern simulation strategies for turbulent flow" (*Edwards, Philadelphia, SA,* 2001).

GODFREY, K., "Compartmental Models and Their Application" (*Academic Pressi Inc. LTD, London* 1983).

GRENVILLE, R.K., RUSZKOWSKI, S. and GERRED, E., 'Blending of miscible liquids in the turbulent and transional regimes.' *15th NAMF Mixing Conference* (*Banff, Canada,* 1995).

GUIRAUD, P., COSTES, J. and BERTRAND, J., "Local measuremts of fluid and particle velocities in a stirred suspension", *Chemical Engineering Journal (2-3) 68* (1997) *75-86*.

GUNKEL, A.A. and WEBER, M.E., "Flow Phenomena in Stirred Tanks. Pt. 1. The Impeller Stream", *AIChE Journal* (1975).

HAAM, S.J., BRODKEY, R.S., FORT, I., KLABOCH, L., PLACNIK, M. and VANECEK, V., "Laser Doppler anemometry measurements in an index of refraction matched column in the presence of dispersed beads: Part I", *International Journal of Multiphase Flow (9) 26* (2000) *1401-1418*.

HARNBY, N., EDWARDS, M.F. and NIENOW, A.W., "Mixing in the process industries" (*Butterworths & Co. Ltd,* 1985).

HARTMANN, H., DERKSEN, J.J., MONTAVON, C., PEARSON, J., HAMILL, I.S. and VAN DEN AKKER, H.E.A., "Assessment of large eddy and RANS stirred tank simulations by means of LDA", *Chemical Engineering Science (12) 59* (2004) *2419-2432*.

HAWKESWORTH, M.R., O'DWYER, M.A., WALKER, J., FOWLES, P., HERITAGE, J., STEWART, P.A.E., WITCOMB, R.C., BATEMAN, J.E., CONNOLLY, J.F. and STEPHENSON, R., "Positron Camera for Industrial Application", *Nuclear instruments and methods in physics research (1) A253* (1986) *145-157*.

HITOMI, D., KATO, Y. and KUBO, T., "Finite element analysis of a flow induced by a Rushton turbine in an unbaffled stirred vessel", *Journal of Chemical Engineering of Japan (3) 39* (2006) *275-283*.

HOCKEY, R.M. and NOURI, J.M., "Turbulent flow in a baffled vessel stirred by a 601 pitched blade impeller", *Chemical Engineering Science (19) 51* (1996) *4405-4421*.

HOLMES, D.B., VONCKEN, R.M. and DEKKER, J.A., "Fluid flow in turbine-stirred, baffled tanks--I : Circulation time", *Chemical Engineering Science (3) 19* (1964) *201-208*.

JAWORSKI, Z., DYSTER, K.N. and NIENOW, A.W., "The effect of size, location and pumping direction of pitched blade turbine impellers on flow patterns: LDA measurements and CFD predictions", *Chemical Engineering Research & Design (A8) 79* (2001) *887-894*.

JAWORSKI, Z., NIENOW, A.W. and DYSTER, K.N., "An LDA study of the turbulent flow field in a baffled vessel agitated by an axial, down-pumping hydrofoil impeller", *Canadian Journal of Chemical Engineering (1) 74* (1996) *3-15*.

JAWORSKI, Z., WYSZYNSKI, M.L., MOORE, I.P.T. and NIENOW, A.W., "Sliding mesh computational fluid dynamics-a predictive tool in stirred tank design", *Proceedings of the Institution of Mechanical Engineers, Part E: Journal of Process Mechanical Engineering (3) 211* (1997) *149-156*.

JAWORSKI, Z. and ZAKRZEWSKA, B., "Modelling of the turbulent wall jet generated by a pitched blade turbine impeller: the effect of turbulence model", *Chemical Engineering Research and Design (A8) 80* (2002) *846-854*.

JENNE, M. and REUSS, M., "A critical assessment on the use of k-ε turbulence models for simulation of the turbulent liquid flow induced by a Rushton-turbine in baffled stirred-tank reactors", *Chemical Engineering Science (17) 54* (1999) *3921-3941*.

KHANG, S.J. and LEVENSPIEL, O., "New scale-up and design method for stirrer agitated batch mixing vessels", *Chemical Engineering Science (7) 31* (1976) *569-577*.

KRESTA, S., "Turbulence in stirred tanks: anisotropic, approximate, and applied", *Canadian Journal of Chemical Engineering (3) 76* (1998) *563-576*.

KRESTA, S.M. and WOOD, P.E., "Prediction of the three-dimensional turbulent flow in stirred tanks", *AIChE Journal (3) 37* (1991) *448-460*.

KRESTA, S.M. and WOOD, P.E., "The flow field produced by a pitched blade turbine: Characterization of the turbulence and estimation of the dissipation rate", *Chemical Engineering Science (10) 48* (1993a) *1761-1774*.

KRESTA, S.M. and WOOD, P.E., "Mean flow field produced by a 45: pitched blade turbine: changes in the circulation pattern due to off bottom clearance", *Canadian Journal of Chemical Engineering (1) 71* (1993b) *42-53*.

KUKUKOVA, A., MOSTEK, M., JAHODA, M. and MACHON, V., "CFD prediction of flow and homogenization in a stirred vessel: Part I vessel with one and two impellers", *Chemical Engineering and Technology (10) 28* (2005) *1125-1133*.

KUO, H.P., KNIGHT, P.C., PARKER, D.J. and SEVILLE, J.P.K., "Solids circulation and axial dispersion of cohesionless particles in a V-mixer", *Powder Technology (1-3) 152* (2005) *133-140*.

LA FONTAINE, R.F. and SHEPHERD, I.C., "Particle image velocimetry applied to a stirred vessel", *Experimental Thermal and Fluid Science (2) 12* (1996) *256-264*.

LANE, G.L., RIGBY, G.D. and EVANS, G.M., "Pressure distribution on the surface of Rushton turbine blades-experimental measurement and prediction by CFD", *Journal of Chemical Engineering of Japan (5) 34* (2001) *613-620*.

LAUNDER, B.E., REECE, G.J. and RODI, W., "Progress in the Development of a Reynolds-Stress Turbulence Closure", *Journal of Fluid Mechanics (3) 68* (1975).

LEE, K.C. and YIANNESKIS, M., "Turbulence Properties of the Impeller Stream of a Rushton Turbine", *AIChE Journal (1) 44* (1998) *13-24*.

LEHOUCQ, R.B., SORENSEN, D.C. and YANG, C., "ARPACK Users' Guide: Solution of Large Scale Eigenvalue Problems with Implicitly Restarted Arnoldi Methods" (*SIAM, Philadelphia,* 1998).

LOMB, N., "Least-Squares frequency analysis of unequally spaced data", *Astrophysics and Space Science 39* (1976) *447-462*.

LUO, J.Y., GOSMAN, A.D., ISSA, R.I., MIDDLETON, J.C. and FITZGERALD, M.K., "Full flow field computation of mixing in baffled stirred vessels", *Chemical Engineering Research and Design (A3) 71* (1993) *342-344*.

MARON, M.J., "Numerical Analysis: A Practical Approach" (*Collier Macmillan Publishers, London* 1982).

MICHELETTI, M., BALDI, S., YEOH, S.L., DUCCI, A., PAPADAKIS, G., LEE, K.C. and YIANNESKIS, M., "On spatial and temporal variations and estimates of energy dissipation in stirred reactors", *Chemical Engineering Research and Design (9 SPEC. ISS.) 82* (2004) *1188-1198*.

MIDDLETON, J.C., 'Measurement of circulation within large mixing vessels', *Third European Conference on Mixing* (*BHRA Fluid Engng, YORK, U.K,* 1979), *pp. 15-36*.

MIDDLETON, J.C., PIERCE, F. and LYNCH, P.M., "Computations of Flow Fields and Complex Reaction Yield in Turbulent Stirred Reactors, and Comparison with Experimental Data", *Chemical Engineering Research and Design (1) 64* (1986) *18-22*.

MISHRA, V.P., DYSTER, K.N., JAWORSKI, Z., NIENOW, A.W. and MCKEMMIE, J., "A study of an up- and a down-pumping wide blade hydrofoil impeller: Part I. LDA measurements", *Canadian Journal of Chemical Engineering (3) 76* (1998) *577-588*.

MONTANTE, G., LEE, K.C., BRUCATO, A. and YIANNESKIS, M., "Numerical simulations of the dependency of flow pattern on impeller clearance in stirred vessels", *Chemical Engineering Science (12) 56* (2001) *3751-3770*.

MORUD, K.E. and HJERTAGER, B.H., "LDA measurements and CFD modelling of gas-liquid flow in a stirred vessel", *Chemical Engineering Science (2) 51* (1996) *233-249*.

MUKATAKA, S., KATAOKA, H. and TAKAHASHI, J., "Effects of Vessel Size and Rheological Properties of Suspensions on the Distribution of Circulation Times in Stirred Vessels", *Journal of Fermentation Technology (2) 58* (1980) *155-161*.

MUKATAKA, S., KATAOKA, H. and TAKAHASHI, J., "Circulation Time and Degree of Fluid Exchange between Upper and Lower Circulation Regions in a Stirred Vessel with a Dual Impeller", *Journal of Fermentation Technology (4) 59* (1981) *303-307*.

NAYAN, N., "Computational And Experimental Study Of Power Input, Flow Field And Mixing Time In Reactors Stirred By Single And Multiple Impellers", *University of Birmingham,* 2004.

NG, K., "Assessment of sliding mesh CFD predictions and LDA measurements of the flow in a tank stirred by a Rushton impeller", *Chemical Engineering Research and Design (A6) 76* (1998) *737-747*.

NG, K. and YIANNESKIS, M., "Observations on the distribution on energy dissipation in stirred vessels", *Chemical Engineering Research and Design (3) 78* (2000) *334-341*.

NIENOW, A.W., "Agitators for Mycelial Fermentations", *Trends Biotechnol. (8) 8* (1990) *224-233*.

NIENOW, A.W., "On impeller circulation and mixing effectiveness in the turbulent flow regime", *Chemical Engineering Science (15) 52* (1997) *2557-2565*.

NIENOW, A.W. and BUJALSKI, W., "The versatility of up-pumping hydrofoil agitators", *Chemical Engineering Research & Design (A9) 82* (2004) *1073-1081*.

NIENOW, A.W. and MILES, D., "A dynamometer for the accurate measurement of mixing torque", *Journal of Physics E: Scientific Instruments (11) 2* (1969) *994-995*.

NORRISH, R.S., "Selected Tables of Physical Properties of Sugar Solutions" (*The British Food Manufacturing Industries Research Association,* 1967).

NOURI, J.M. and HOCKEY, R.M., "Power number correlation between Newtonian and non-Newtonian fluids in a mixing vessel", *Journal of Chemical Engineering of Japan (5) 31* (1998) *848-852*.

PARKER, D.J., BROADBENT, C.J., FOWLES, P., HAWKESWORTH, M.R. and MCNEIL, P., "Positron emission particle tracking - a technique for studying flow within engineering equipment", *Nuclear Instruments and Methods in Physics Research, Section A: Accelerators, Spectrometers, Detectors and Associated Equipment (3) A326* (1993) *592-607*.

PARKER, D.J., DIJKSTRA, A.E., MARTIN, T.W. and SEVILLE, J.P.K., "Positron emission particle tracking studies of spherical particle motion in rotating drums", *Chemical Engineering Science (13) 52* (1997) *2011-2022*.

PARKER, D.J., FORSTER, R.N., FOWLES, P. and TAKHAR, P.S., "Positron emission particle tracking using the new Birmingham positron camera", *Nuclear Instruments and Methods in Physics Research, Section A: Accelerators, Spectrometers, Detectors and Associated Equipment (1-3) 477* (2002) *540-545*.

PERICLEOUS, K.A. and PATEL, M.K., "Source-Sink Approach in the Modelling of Stirred Reactors", *PCH. Physicochemical hydrodynamics (1-2) 9* (1987) *279-297*.

PITIOT, P., "Caracterisation, Par Trajectographie Tridimensionnelle, Du Melange Dans Un Reacteur Agite: Characterisation, By Three-Dimensional Trajectography, Of Mixing In A Stirred Tank", *Université de soutenance,* 1999.

PRESS, W., TEUKOLSKY, S., VETTERLING, W. and FLANNERY, B., "Numerical Recipes in Fortran" (*Cambridge University Press, New York,* 1992).

RAMMOHAN, A.R., KEMOUN, A., AL-DAHHAN, M.H. and DUDUKOVIC, M.P., "A lagrangian description of flows in stirred tanks via computer-automated radioactive particle tracking (CARPT)", *Chemical Engineering Science (8) 56* (2001) *2629-2639*.

RANADE, V.V., "An efficient computational model for simulating flow in stirred vessels: A case of Rushton turbine", *Chemical Engineering Science (24) 52* (1997) *4473-4484*.

RANADE, V.V. and JOSHI, J.B., "Flow generated by pitched blade turbines 1: Measurements using laser Doppler anemometer", *CHEMICAL ENGINEERING COMMUNICATIONS 81 , 1989* (1966) *197-224*.

RANADE, V.V., JOSHI, J.B. and MARATHE, A.G., "Flow generated by pitched blade turbines 2: simulation using k-ε model", *Chemical Engineering Communications 81 , 1989* (1989) *225-248*.

REVSTEDT, J., FUCHS, L. and GARDH, C., "Large eddy simulations of the turbulent flow in a stirred reactor", *Chemical Engineering Science (24) 53* (1998) *4041-4053*.

RIGOPOULOS, S. and JONES, A., "A hybrid CFD-reaction engineering framework for multiphase reactor modelling: Basic concept and application to bubble column reactors", *Chemical Engineering Science (14) 58* (2003) *3077-3089*.

ROBERTS, R.M., GRAY, M.R., THOMPSON, B. and KRESTA, S.M., "Effect of impeller and tank geometry on circulation time distributions in stirred tanks", *Chemical Engineering Research and Design (A1) 73* (1995) *78-86*.

RODI, W., "Turbulence models and their application in hydraulics - A state of the art review" (*Research supported by the Deutsche Forschungsgemeinschaft. International Association for Hydraulic Research, Delft,* 1980).

ROUSSINOVA, V., KRESTA, S.M. and WEETMAN, R., "Low frequency macroinstabilities in a stirred tank: Scale-up and prediction based on large eddy simulations", *Chemical Engineering Science (11) 58* (2003) *2297-2311*.

ROUSSINOVA, V.T., GRGIC, B. and KRESTA, S.M., "Study of macro-instabilities in stirred tanks using a velocity decomposition technique", *Chemical Engineering Research and Design (7) 78* (2000) *1040-1052*.

ROUSSINOVA, V.T., KRESTA, S.M. and WEETMAN, R., "Resonant geometries for circulation pattern macroinstabilities in a stirred tank", *Fluid Mechanics and Tranport Phenomena (12) 50* (2004) *2986-3005*.

RUSZKOWSKI, S., 'A Rational Method for Measuring Blending Performance and Comparison of Different Impeller Types.' *Proc. 8th Europ. Mixing Conf.* (*Rugby, U.K.,* 1994).

RUTHERFORD, K., MAHMOUDI, S.M.S., LEE, K.C. and YIANNESKIS, M., "The influence of rushton impeller blade and disk thickness on the mixing characteristics of stirred vessels", *Chemical Engineering Research and Design (3) 74* (1996) *369-378*.

SCARGLE, J., "Studies in astronomical time series analysis. II. Statistical aspects of spectral analysis of unevely spaced data", *The Astrophisical Journal 263* (1982) *835-853*.

SCHÄFER, M., HÖFKEN, M. and DURST, F., "Detailed LDV measurements for visualization of the flow field within a stirred-tank reactor equipped with a rushton turbine", *Chemical Engineering Research and Design (8) 75* (1997) *729-736*.

SCHÄFER, M., YIANNESKIS, M., WÄCHTER, P. and DURST, F., "Trailing vortices around a 45° pitched-blade impeller", *AIChE Journal (6) 44* (1998) *1233-1246*.

SCHETZ, J.A.F., A.E., "Handbook of Fluid Dynamics and Fluid Machinery" (*Wiley, New York, NY,* 1996).

SCHMITZ, R., "Circulation Time Studies in Newtonian and non-Newtonian Fluids in Stirred Tanks", *PhD Thesis, University of Birmingham,* 1996.

SCOTT, J.A., "An Arnoldi code for computing selected Eigenvalues of Sparse, Real, Unsymmetric Matrices", *ACM Transaction on Mathematical Software (4) 21* (1995) *432-475*.

SHARP, K.V. and ADRIAN, R.J., "PIV Study of small-scale flow structure around a Rushton turbine", *AIChE Journal (4) 47* (2001) *766-778*.

SIMMONS, M.J.H., ZHU, H., BUJALSKI, W., HEWITT, C.J. and NIENOW, A.W., "Mixing in a model bioreactor using agitators with a high solidity ratio and deep blades", *Chemical Engineering Research & Design (A5) 85* (2007) *551-559*.

SOMMERFELD, M. and DECKER, S., "State of the art and future trends in CFD simulation of stirred vessel hydrodynamics", *Chemical Engineering and Technology (3) 27* (2004) *215-224*.

STELLEMA, C.S., VLEK, J., MUDDE, R.F., DE GOEIJ, J.J.M. and VAN DEN BLEEK, C.M., "Development of an improved positron emission particle tracking system", *Nuclear Instruments and Methods in Physics Research, Section A: Accelerators, Spectrometers, Detectors and Associated Equipment (2-3) 404* (1998) *334-348*.

STEWART, R.L., BRIDGWATER, J., ZHOU, Y.C. and YU, A.B., "Simulated and measured flow of granules in a bladed mixer- A detailed comparison", *Chemical Engineering Science (19) 56* (2001) *5457-5471*.

STOOTS, C.M. and CALABRESE, R.V., "Mean velocity field relative to a rushton turbine blade", *AIChE Journal (1) 41* (1995) *1-11*.

SVENSSON, F.J.E. and RASMUSON, A., "LDA-measurements in a stirred tank with a liquid-liquid system at high volume percentage dispersed phase", *Chemical Engineering and Technology (3) 27* (2004) *335-339*.

TABOR, G., GOSMAN, A.D. and ISSA, R., "Numerical simulation of the flow in a mixing vessel stirred by a Rushton turbine. " *IChemE Symp. Ser. 140* (1996) *23-40*.

TRAN, A.T.T., LITSTER, J.D., SEVILLE, J.P.K., INGRAM, A. and FAN, X., 'Dry and cohesive powders in vertical axis high shear mixers using positron emission particle tracking (Pept)', *Fifth World Congress on Particle Technology* (*The American Institute of Chemical Engineers,* 2006).

VAN BARNEVELD, J., SMIT, W., OOSTERHUIS, N.M.G. and PRAGT, H.J., "Measuring the liquid circulation time in a large gas-liquid contactor by means of a radio pill. Part 1. Flow pattern and mean circulation time", *Industrial & Engineering Chemistry Research (11) 26* (1987a) *2185-2192*.

VAN BARNEVELD, J., SMIT, W., OOSTERHUIS, N.M.G. and PRAGT, H.J., "Measuring the liquid circulation time in a large gas-liquid contactor by means of a radio pill. Part 2. Circulation time distribution", *Industrial & Engineering Chemistry Research (11) 26* (1987b) *2192-2195*.

VAN DER MOLEN, K. and VAN MAANEN, H.R.E., "Laser-Doppler Measurements of the Turbulent Flow in Stirred Vessels to Establish Scaling Rules", *Chemical Engineering Science (9) 33* (1978) *1161-1168*.

VERSTEEG, H.K. and MALALASEKERA, W., "An introduction to Computational Fluid dynamics. The finite volume method" (*Longman Group Ltd, London,* 1995).

WILCOX, D.C., "Multiscale model for turbulent flows", *AIAA journal (11) 26* (1988) *1311-1320*.

WINARDI, S. and NAGASE, Y., "Unstable phenomenon of flow in a mixing vessel with a marine propeller", *Journal of Chemical Engineering of Japan (2) 24* (1991) *243-249*.

WITTMER, S., FALK, L., PITIOT, P. and VIVIER, H., "Characterization of stirred vessel hydrodynamics by three dimensional trajectography", *Canadian Journal of Chemical Engineering (3) 76* (1998) *600-610*.

WOLF, D. and MANNING, F.S., "Impact tube measurement of flow patterns, velocity profiles and pumping capacities in stirred vessels", *Canadian Journal of Chemical Engineering 44* (1966) *137-142*.

WONG, Y.S., "Particle motion in relatively thin fluidised bed models", *Chemical Engineering Science (18) 61* (2006) *6234-6238*.

WU, H. and PATTERSON, G.K., "Laser-doppler measurements of turbulent-flow parameters in a stirred mixer", *Chemical Engineering Science (10) 44* (1989) *2207-2221*.

WU, J., GRAHAM, L.J., NGUYEN, B. and MEHIDI, M.N.N., "Energy efficiency study on axial flow impellers", *Chemical Engineering and Processing (8) 45* (2006) *625-632*.

YAKHOT, V. and ORSZAG, S.A., "Renormalization-Group Analysis of Turbulence", *Physical Review Letters (14) 57* (1986) *1722*.

YEOH, S.L., PAPADAKIS, G., LEE, K.C. and YIANNESKIS, M., "Large Eddy Simulation of turbulent flow in a Rushton impeller stirred reactor with sliding-deforming mesh methodology", *Chemical Engineering and Technology (3) 27* (2004a) *257-263*.

YEOH, S.L., PAPADAKIS, G. and YIANNESKIS, M., "Numerical simulation of turbulent flow characteristics in a stirred vessel using the LES and RANS approaches with the sliding/deforming mesh methodology", *Chemical Engineering Research and Design (7) 82* (2004b) *834-848*.

YIANNESKIS, M., POPIOLEK, Z. and WHITELAW, J.H., "Experimental Study Of The Steady And Unsteady Flow Characteristics Of Stirred Reactors", *Journal of Fluid Mechanics 175* (1987) *537-555*.

YIANNESKIS, M. and WHITELAW, J.H., "On the structure of the trailing vortices around Rushton turbine blades", *Chemical Engineering Research and Design (A5) 71* (1993) *543-550*.

YOON, H.S., HILL, D.F., BALACHANDAR, S., ADRIAN, R.J. and HA, M.Y., "Reynolds number scaling of flow in a Rushton turbine stirred tank. Part I - Mean flow, circular jet and tip vortex scaling", *Chemical Engineering Science (12) 60* (2005) *3169-3183*.

YOON, H.S., SHARP, K.V., HILL, D.F., ADRIAN, R.J., BALACHANDAR, S., HA, M.Y. and KAR, K., "Integrated experimental and computational approach to simulation of flow in a stirred tank", *Chemical Engineering Science (23) 56* (2001) *6635-6649*.

Appendix A

Homemade routines developed in Matlab to analyse PEPT data.

The main routine `startscript.m` developed in Matlab is used as basis for processing PEPT data. From this script all the rest of routine are called for the different purposes. The Matlab code is here reported:

```
%% Starting Script for analysing PEPT Data
clc;
disp('Do you want load: ')
disp('1. new or ')
disp('2. old file or  ');
risp=input('3. already loaded?   ');
if risp==1
    cut             %call the routine to assemble files and cut da
%% Geometry parameters
    H=287;
    T=287;
    vtip=1.52;
    x_0=0;           %x_0, y_0 are the origin of the coordinate axes
    y_0=0;
    clear t x y z a filename risp
elseif risp==2
    filename=input('Please insert the MAT file name (file.mat): ');
    load(filename);
    clear filename risp
elseif risp==3
    clear risp
end
data=data(:,1:4);

%% Choice of the reference system
disp('Coordinate reference system: [2]');
disp('1. Cartesian  ');
risp=input('2. Cylindrical   ');
if isempty(risp)
    risp = 2;
end
if risp==1
    coord = {'car'}
elseif risp==2
    coord = {'cyl'}
end
clear risp

%% Filtering Stage and Centering
disp('Filtering...')
f_data=filtra(data,{'ON'});  %'ON' to activate the filter
                             %'OFF' to deactivate the filter
z_0=min(f_data(:,4));        % always set as minimum
f_data(:,2)=f_data(:,2)-x_0;
f_data(:,3)=f_data(:,3)-y_0;
f_data(:,4)=f_data(:,4)-z_0;

%% Velocity Routine Calls
disp('Calculating velocities...')
if strcmpi(coord,{'car'})
    [car]=prep(f_data,T,vtip);
    ndis=length(data)-length(car);
elseif strcmpi(coord,{'cyl'})
    [th,R,phi]=cart2pol(f_data(:,2),f_data(:,3),f_data(:,4));

    delta=0;                %Converting theta from [-pi,pi] to [0,n*pi]
```

```
    th1=zeros(length(th),1);
    th1(1)=th(1);
    for i=2:length(th)
        if(th(i)-th(i-1)<-pi)
            delta=delta+2*pi;
        elseif(th(i)-th(i-1)>pi)
            delta=delta-2*pi;
        end
        th1(i)=th(i)+delta;
    end
    th=th1; clear delta i th1;
    [cyl]=prep([f_data(:,1) R th phi],T,vtip);
    cyl(:,5)=cyl(:,5)*1000;  %convert from [rad ms^-1] to [rad s^-1]
                             %and overwriting the vel magnitude
    cyl(:,7)=(cyl(:,4).^2+(cyl(:,5).*cyl(:,1)/1000).^2+cyl(:,6).^2).^.5;
    clear R th phi;
    ndis=length(data)-length(cyl);
    disp('Calculating Occupancy file...')
    Occ=O2d(cyl,H,T,vtip);
end
disp([num2str(ndis),' locations have been discharged.']);
clear ndis coord
```

The first routine called by the `startscript.m` is `cut.m`. This routine is used to open single PEPT files and to attach them in a single one; furthermore, it gives also the possibility of cutting portion of data where for example the tracer got stuck or similar cases.

The Matlab code for `cut.m` is here reported:

```
%% Routine to load new files and to remove zones where the tracer got stuck
clc
clear all
clear java
close all
n_files=input('insert number of files to join: ');
id_start=input('insert first file number: ');
%% File Location Path
dir_out=['D:\Work\out\'];                %file folder output
dir_in=['D:\Work\in\'];                  %file folder input
filename=['PEPTfile01.a'];               %PEPT filename
%% Open successive files
data1(1,1:4)=0;
for i=1:n_files
    if id_start<10
        add=['0' num2str(id_start)];
    else
        add=[num2str(id_start)];
    end
id_start=id_start+1;

[t,x,y,z,a,a,a,a]=textread([dir_in filename add],...
    '%f %f %f %f %f %f %f %f',-1,'headerlines',16);
data=[t,x,y,z];
data(:,1)=data(:,1)+data1(end,1);
```

```
data1=[data1; data];
end
data1(1,:)=[];
%% Showing portion of file to be cut
data=data1;
clear a* data1 dir_in i* n* t x y z
gap=25000;
data_orig=data;
fig = figure;id=gap+1;i=1;
final_id=length(data);
while id<final_id+gap
    if id<final_id
        intv=id-gap:id;
    else
        intv=id-gap:final_id;
    end
    plot(data(intv,1)/1000,data(intv,3))
    figure(1)
    dcm_obj = datacursormode(fig);
    set(dcm_obj,'DisplayStyle','datatip','SnapToDataVertex','on')
    datacursormode('on')
    n_int=input('# of times particle got stuck:[0] ');
    if isempty(n_int)
        n_int = 0;
    end
    if n_int>0
        for j=1:n_int
            figure(1)
            pause
            c_info = getCursorInfo(dcm_obj);
            a(i)=c_info.DataIndex+intv(1);
            figure(1)
            pause
            c_info = getCursorInfo(dcm_obj);
            b(i)=c_info.DataIndex+intv(1);
            i=i+1;
        end
    end
    id=id+gap;
end
for i=1:length(a)
    data(a(i):b(i),:)=0;
end
data(data(:,1)==0,:)=[];
clear i j gap n_int c_info a b intv id final_id dcm_obj fig
close
sav=input('insert name of file to save in: ');
save([dir_out sav '_bis.mat'])        %file name to save the final results
clc
```

After `cut.m`, the function `filtra.m` is called; this function filters the raw data eliminating all those point which position is not aligned with the locations preceding and following it. The code is:

```
function f_data=filtra(data,flag)
%% This function passes the PEPT data and gets rid of those points that are
%% not 'aligned' with the rest.  It can be disabled calling it with
%% flag ='OFF'
```

```
figure(100)
data1=diff(data(2:4,:));
data1=diff(data(:,2:4));
dist=(data1(:,1).^2+data1(:,2).^2+data1(:,3).^2).^.5; %distance between 2
points
hist(dist,50);
clear data1 dist;
data_tm=data;
t=data_tm(:,1);
x=data_tm(:,2);
y=data_tm(:,4);                    % swapping y & z
z=data_tm(:,3);
if strcmpi(flag,{'on'})
    e=input('insert error: ');     %[mm]  maximum gap expected
    n_el=length(x);
    point=[x y z];
    index=ones(n_el,1);
    dist=zeros(n_el,1);
    count1=1;
    count2=2;
    skip=0;
    while count2<=n_el
        l=point(count2,:)-point(count1,:);
        dist(count2)=norm(l);

        if (dist(count2)>(skip+1)*e)
            skip=skip+1;
            if(skip<3)
                index(count2)=0;
                count2=count2+1;
            elseif(skip==3)
                index(count2)=0;
                count1=count2;
                count2=count2+1;
                skip=0;
            else
                error('sth went wrong!!!!');
            end
        else
            count1=count2;
            count2=count2+1;
            skip=0;
        end
    end
    temp=find(index==0);
    x(temp,:)=[]; y(temp,:)=[];z(temp,:)=[];t(temp,:)=[];
end
close 100; pause(0.01);
f_data=[t x y z];
```

To calculate Lagrangian velocities from PEPT locations the function `prep.m` has been employed. This routine calls within itself a further function called `velfit.m` which calculates the tracer velocity given a certain number of locations and time across them. Here it follows the codes:

```
%Prep.m
function [vel]=prep(f_data,H,vtip)
%% Routine to calculate Lagrangian velocities
%% Data=(T,X,Y,Z,...,...,...) to A=(X,Y,Z,u,v,w,Vel,T) or
%% Data=(T,r,rho,phi,...,...,...) to A=(r,rho,phi,u_r,u_rho,u_phi,Vel,T)
tic
pnt=5;              %number of points used to calculate the velocities
step=1;             %step is create to cut the number of data, if (step=1)
                    %all the data are calculated.
n_el=size(f_data,1);
T=f_data(:,1);   %[msec]
X=f_data(:,2);   %X & Z are in [mm]
Y=f_data(:,3);   %Y might be either in [mm] or [rad]
Z=f_data(:,4);

%% Find the max DT to calculate the velocities
dtime=diff(T);
L=H/1000;               %[m]             %Characteristic length [m]
mdt=(L/vtip)*1000;      %[ms]            %max DT=chararactristic lenght over
                                         %max V expected.
stdt=std(dtime(dtime<mdt));              %STD of the time of the real values
if mdt>(mean(dtime(dtime<mdt))+3*stdt)   %it takes the smaller among max DT
    mdt=mean(dtime(dtime<mdt))+3*stdt;   %and mean(DT) + 3*STD(DT)
                                         %(confidence int 99%)
end

%% Creating the velocity matrix
j=0;
vel=zeros(n_el,8);
err=zeros(n_el,3);
for i=pnt:step:n_el,
    if (diff(T((i-(pnt-1)):i))<mdt)  %checks if all the dt<mdt
        j=j+1;
        vel(j,1)=mean(X((i-(pnt-1)):i));              %[mm]
        vel(j,2)=mean(Y((i-(pnt-1)):i));              %[mm] or [rad]
        vel(j,3)=mean(Z((i-(pnt-1)):i));              %[mm]
        [Vx,err(j,1)]=velfit(T((i-(pnt-1)):i),X((i-(pnt-1)):i),pnt);
        vel(j,4)=Vx;                                  %[m sec^-1]
        [Vy,err(j,2)]=velfit(T((i-(pnt-1)):i),Y((i-(pnt-1)):i),pnt);
        vel(j,5)=Vy;                                %[m sec^-1] or [rad ms^-1]
        [Vz,err(j,3)]=velfit(T((i-(pnt-1)):i),Z((i-(pnt-1)):i),pnt);
        vel(j,6)=Vz;                                  %[m sec^-1]
        vel(j,7)=(vel(j,4).^2+vel(j,5).^2+vel(j,6).^2)^0.5;%[m sec^-1]
        vel(j,8)=mean(T((i-(pnt-1)):i));              %[sec]

    end
end
vel(j+1:end,:)=[];
toc
t=toc;
================================================================================
%velfit.m
function [vel,err]=velfit (xdat,ydat,m)
%% Least square dx/dt interpolation using m points to find velocities
%xdat is time, whilst ydat is the coordinate
sigmax=sum(xdat);
sigmay=sum(ydat);
sigmxy=sum(xdat.*ydat);
sigmx2=sum(xdat.^2);
%sigmy2=sum(ydat.^2);
det=m*sigmx2-sigmax^2;
ycept=(sigmx2*sigmay-sigmax*sigmxy)/det;
vel=(m*sigmxy-sigmax*sigmay)/det;
err=sum((ycept+vel*xdat-ydat).^2);
err=sqrt(err/m);            %STD for the velocities
```

To transform the Lagrangian velocities in Eulerian maps, the routine `O2d.m` has been developed:

```
function Occ = O2d(A,H1,T,vtip)
%% Routine to calculate the azimuthal average variables
%Occupancy:
%from A=(r,rho,phi,u_r,u_rho,u_phi,T) to structured
%Occupancy(frequency DATA) (r,rho,phi,u_r,u_rho,u_phi,O)
n_el=size(A,1);
n_r=50; n_rho=36; n_phi=100;  % Grid definition.  The R will be divided to
                              % get equal volume bins
%% Equal volume radius spacing
r_m=max(A(:,1));
phi_m=min(A(:,3));
H=max(A(:,3))-min(A(:,3));
Vcell=((r_m^2)*H*pi)/(n_r*n_rho*n_phi);
drho=2*pi/n_rho;
dphi=(max(A(:,3))-min(A(:,3)))/n_phi;
R=zeros(n_r,1);
i=1;
while (R(i)<r_m)
    i=i+1;
    R(i)=(R(i-1)^2+Vcell*n_rho/(pi*dphi))^0.5;
end
H=zeros(n_r+1,n_phi+1,5);
pass=zeros(n_r+1,n_phi+1);
total_T=A(end,8);
xx=1;yy=1;zz=1;

%% first loop to calculate the Time averaged velocity for each cell
for i=2:n_el-1,
    x=max(find(R<=A(i,1)));
    z=floor((A(i,3)-phi_m)/dphi)+1;
    dt=(A(i+1,8)-A(i-1,8))/2;
    H(x,z,1)=H(x,z,1)+A(i,4)*dt;                %u
    H(x,z,2)=H(x,z,2)+A(i,5)*dt;                %v
    H(x,z,3)=H(x,z,3)+A(i,6)*dt;                %w
    H(x,z,4)=H(x,z,4)+1;                        %locations
    if (x~=xx|z~=zz)
        pass(x,z)=pass(x,z)+1;                  %passes
    end
    H(x,z,5)=H(x,z,5)+dt;                       %time in the cell
    xx=x;  zz=z;                   %ad majora
end

%% Loop to find standard deviation for each velocity component
for i=2:n_el-1,
    %x=floor((A(i,1))/dr)+1;            %x,z are the index of r,phi
    x=max(find(R<=A(i,1)));
    z=floor((A(i,3)-phi_m)/dphi)+1;
    H(x,z,6)=(H(x,z,1)/H(x,z,5)-A(i,4))^2;                %su
    H(x,z,7)=(H(x,z,2)/H(x,z,5)-A(i,5))^2;                %sv
    H(x,z,8)=(H(x,z,3)/H(x,z,5)-A(i,6))^2;                %sw
end

%% Final form matrix
j=1;
Occ=zeros(n_r*n_phi,11);
for i1=1:n_r,
    for i3=1:n_phi,
        Occ(j,1)=(R(i1)+R(i1+1))/2;                    %positions
        Occ(j,2)=i3*dphi+phi_m;
```

```
        if (H(i1,i3,4)>2)
            Occ(j,3)=Occ(j,3)+(H(i1,i3,1)/H(i1,i3,5));%mean velocities
            Occ(j,4)=Occ(j,4)+(H(i1,i3,2)/H(i1,i3,5));
            Occ(j,5)=Occ(j,5)+(H(i1,i3,3)/H(i1,i3,5));

            Occ(j,8)=Occ(j,8)+H(i1,i3,6)/H(i1,i3,4); %std
            Occ(j,9)=Occ(j,9)+H(i1,i3,7)/H(i1,i3,4);
            Occ(j,10)=Occ(j,10)+H(i1,i3,8)/H(i1,i3,4);
        end
        Occ(j,6)=Occ(j,6)+H(i1,i3,5)/total_T;        %Occupancy
%         Occ(j,7)=Occ(j,7)+H(i1,i3,4);              %Total number of loc
        Occ(j,7)=Occ(j,7)+pass(i1,i3);               %Total number of pass
        j=j+1;
    end
end
%% sqrt for STD
Occ(:,8)=sqrt(Occ(:,8));Occ(:,9)=sqrt(Occ(:,9));Occ(:,10)=sqrt(Occ(:,10));

%% Adimensional variables

Occ(:,3)=Occ(:,3)/vtip;
Occ(:,4)=Occ(:,4).*Occ(:,1)/(vtip*1000);
Occ(:,5)=Occ(:,5)/vtip;
Occ(:,11)=(Occ(:,3).^2+Occ(:,4).^2+Occ(:,5).^2).^.5;
Occ(:,1)=Occ(:,1)/T;
Occ(:,2)=Occ(:,2)/H1;
```

Finally, the routine `selinterp.m` used to interpolate locations in the zones where high velocity gradients occur is here reported:

```
%% Interpolating data where the point are missing (RAW data)
% This function passes all the original file and monitors the distance
% between two consecutive points. If this distance is larger than dmin
% interpolates the points between using a linear interpolation until
% the distance is  now smaller than dmin.  There is also other two vars:
% - dmax: maximum gap to be interpolated, if the two points are larger than
%         this value the interpolation is not applied;

%% Main routine
function mat2=intrpselective(mat,dmin,dmax)
clc
tic
mat2=zeros(3*length(mat),4);
mat2(1,:)=mat(1,:); k=2;
%hbar = waitbar(0,'computing pleas wait...');
for i=2:length(mat)
    p1=mat(i-1,:);
    p2=mat(i,:);
    d=distcar(p1,p2);
    if (d>dmin & d<dmax)
        Nint=floor(d/dmin);
        t=linspace(p1(1),p2(1),Nint+2);
        k=k-1;
        mat2(k:k+Nint+1,1)=t;
        mat2(k:k+Nint+1,2)=intfab([p1(1) p2(1)],[p1(2) p2(2)],t);
        mat2(k:k+Nint+1,3)=intfab([p1(1) p2(1)],[p1(3) p2(3)],t);
        mat2(k:k+Nint+1,4)=intfab([p1(1) p2(1)],[p1(4) p2(4)],t);
        k=k+Nint+2;
    else
        mat2(k,:)=mat(i,:);
        k=k+1;
    end
end
```

```
mat2(k:end,:)=[];
toc

%% ======================================================================%%
%% Subfunction to calculate cartesian distance                           %%
%% ======================================================================%%
function d=distcar(p1,p2)
d=((p1(4)-p2(4))^2 + ...
    (p1(2)-p2(2))^2 + ...
    (p1(3)-p2(3))^2)^.5;

%% ========================================================== ========== %%
%% Interpolation first order                                             %%
%% xdat is time, whilst ydat is the coordinateSubfunction to calculate%%
%% cartesian distance                                                    %%
%% ======================================================================%%
function int=intfab (xdat,ydat,t)
a=(ydat(2)-ydat(1))/(xdat(2)-xdat(1));
b=ydat(1)-a*xdat(1);
int=a*t+b;
```

Appendix B

File used in Ansys-CFX to resolve the CFD Particle tracking simulations

In order to be able to perform the 3 steps simulation for particle tracking in CFD, the following file `.cll` is needed to be added to the definition file of the second simulation step. This file will make the solver able to import the right velocities as initial conditions for the non-rotating simulation.

```
#include "cfx5ext.h"
C=======================================================================
dllexport(usr_init_alg_av)
C=======================================================================
      SUBROUTINE USR_INIT_ALG_AV(NLOC,NRET,NARG,RET,ARGS,CRESLT,
     &                           CZ,DZ,IZ,LZ,RZ)
CC
CD Controls the initialisation of the MHD algebraic variables,
CD they are properly computed in junction box routines.
CC --------------------
CC        Input
CC --------------------
CC NLOC       : Number of locations for source.
CC NRET       : Number of returned data fields.
CC NARG       : Number of argument fields.
CC ARGS       : Argument fields array.
CC --------------------
CC        Output
CO RET        : Computed data fields (source values).
CO CRESLT     : Result of attempting computation.
CC=======================================================================
C     Preprocessor includes
C ------------------------------
#include "locale_params.h"
#include "MMS.h"
#include "stack_point.h"
C ------------------------------
C        Argument list
C ------------------------------
C
      INTEGER NLOC,NARG,NRET
      CHARACTER CRESLT*(*)
      REAL ARGS(NLOC,NARG), RET(NLOC,NRET)
      INTEGER IZ(*)
      CHARACTER CZ(*)*(1)
      DOUBLE PRECISION DZ(*)
      LOGICAL LZ(*)
      REAL RZ(*)
C
C ------------------------------
C        Local Parameters
C ------------------------------
C
      CHARACTER*(*) ROUTIN
      PARAMETER (ROUTIN='USR_INIT_ALG_AV')
C
C ------------------------------
C        Local variables
C ------------------------------
C
      INTEGER IRET,ILOC
      INTEGER ILOCS,ILOCF,IENTS,IENTF,NVX
C
```

```
      CHARACTER*(4) CERACT,CRES,CDTYPE
      CHARACTER*(MXDNAM) CVAR,CZONE,LOCALE,ENTITY,WHEN,WHO,CALIAS
C
C--Saved data.
C ------------------------------
C        Stack pointers.
C ------------------------------
      __stack_point__ pVAR
C ------------------------------
C    Executable statements
C ------------------------------
C
C---- Find out where we are - special treatment on vertices, just zero
C     on other locales as this will only be for hybrid.
C
      CALL USER_CALC_INFO(WHO,'GET',CVAR,LOCALE,ENTITY,WHEN,
     &                    CALIAS,CERACT,CRES,
     &                    CZONE,ILOCS,ILOCF,IENTS,IENTF,
     &                    CZ,DZ,IZ,LZ,RZ)
C
      IF (LOCALE.NE.'VERTICES') THEN
        CALL SET_A_0(RET,NLOC*NRET)
      ELSE
        CALL LOCDAT('/FLOW/SOLUTION/LATEST/' //CZONE //'/VERTICES/'
     &              //CVAR,CDTYPE,'SKIP',NVX,pVAR,CRES)
        IF (CRES.NE.'GOOD') THEN
C
C---- Simply initialise.
C
          IF (CRES.EQ.'NONE') THEN
            CALL SET_A_B(RET,ARGS,NLOC)
          ELSE
            CRESLT = CRES
          ENDIF
        ELSE
C
C---- Use old vertex solution and overwrite as 'RECALC' must have been
C     used and we do not wish to corrupt user junction box calc.
C
          CALL SET_A_B(RET,RZ(pVAR),NVX)
        ENDIF
      ENDIF
C
      END
```

Appendix C

The use of Eigenvalues as a tool to characterise mixing

The theory

The modelling of compartmental systems is typically based on mass balances. This always leads to a system of differential equations, where the state variables represent masses or related quantities, e.g. concentration or amount of material. Further properties like pressure or temperature usually appear only as parameters. A general form of compartmental equations for a system with *n* compartments is:

$$\frac{dx_i}{dt} = f_{0i} + \sum_{j \neq i} f_{ji} - \sum_{j \neq i} f_{ij} - f_{i0}, \qquad i = 1,\ldots,n \tag{C.1}$$

where x_i is the variable associated with compartment i, f_{ij} is the flow rate to compartment j from compartment i, and the subscript 0 denotes the environment. If all the flows to/from the environment are zero ($f_{i0}= f_{0i}=0,\ i=1,\ldots,n$) the system is said to be closed, otherwise it is open. It is clear that compartmental models are simply sets of constrained first-order differential equations; the constraints are that the physical flow rates cannot be negative. In this form, equation (C.1) is too general to be useful and it is helpful to relate flows to the state variable. In fact, in this application the flow rates are directly proportional to the state variable in the donor compartment. Therefore, equation (C.1) becomes:

$$\frac{dx_i}{dt} = k_{0i}x_0 + \sum_{j \neq i} k_{ji}x_j - \sum_{j \neq i} k_{ij}x_i - k_{i0}x_i, \quad i,j = 1,\ldots,n \tag{C.2}$$

The previous equation can be written for open or closed systems as follows:

$$\frac{dx_i}{dt} = \sum_{j \neq i} k_{ji} x_j - x_i \sum_{j \neq i} k_{ij} \,, \quad i, j = 0,\ldots,n \tag{C.3}$$

Note that in this model, the flow rate from compartment j to compartment i is $k_{ji}\, x_j$, i.e. directly proportional to the quantity x_j in the donor compartment but independent of the quantity x_i in the receptor compartment.

For a closed network of Continuous Stirred Tank(s) (CSTs), the expression of the concentration as a function of time for every tank can be evaluated using equation (C.3) expressing it as:

$$V_i \frac{dc_i}{dt} = \sum_{j \neq i} Q_{ji} c_j - c_i \sum_{j \neq i} Q_{ij} \,, \qquad i = 1,\ldots,n \tag{C.4}$$

where c_i is the concentration in every single tank having V_i volume and Q_{ij} is the volumetric flow rate from the i-th tank to the j-th tank.

To solve the first Ordinary Differential Equation (ODE) system the initial conditions (I.C.) are needed, so presuming they are defined for $t=0$; the complete system can be rewritten as:

$$\begin{cases} \dfrac{dc_1}{dt} = \displaystyle\sum_{j \neq 1} \frac{Q_{j1}}{V_1} c_1 - c_1 \sum_{j \neq 1} \frac{Q_{1j}}{V_1} \\ \vdots \\ \dfrac{dc_n}{dt} = \displaystyle\sum_{j \neq n} \frac{Q_{jn}}{V_n} c_n - c_n \sum_{j \neq n} \frac{Q_{nj}}{V_n} \end{cases}, \qquad I.C. = \begin{cases} c_1(t_0) = c_1(t=0) = c_1^0 \\ \vdots \\ c_n(t_0) = c_n(t=0) = c_n^0 \end{cases} \tag{C.5}$$

in which the $\dfrac{Q_{ji}}{V_i}$ are constant. By letting

$$\mathbf{c} = \begin{pmatrix} c_1 \\ \vdots \\ c_n \end{pmatrix}, \; \mathbf{c}' = \frac{d\mathbf{c}}{dt} = \begin{pmatrix} \dfrac{dc_1}{dt} \\ \vdots \\ \dfrac{dc_n}{dt} \end{pmatrix}, \text{ and } \; \mathbf{c}^0 = \mathbf{c}(t=0) = \begin{pmatrix} c_1^0 \\ \vdots \\ c_n^0 \end{pmatrix} \tag{C.6}$$

this system can be expressed in matrix form as

$$\frac{d\mathbf{c}}{dt} = \begin{pmatrix} \frac{-\sum_{j\neq 1} Q_{j1}}{V_1} & \cdots & \cdots & \frac{Q_{n1}}{V_1} \\ \vdots & \ddots & & \vdots \\ \vdots & & \ddots & \vdots \\ \frac{Q_{1n}}{V_n} & \cdots & \cdots & \frac{-\sum_{j\neq n} Q_{jn}}{V_n} \end{pmatrix} \cdot \mathbf{c}, \text{ with I.C. } \mathbf{c}^0 = \begin{pmatrix} c_1^0 \\ \vdots \\ c_n^0 \end{pmatrix} \qquad \text{(C.7)}$$

And in a more compact form it becomes:

$$\frac{d\mathbf{c}}{dt} = \mathbf{M} \cdot \mathbf{c}, \text{ with I.C. } \mathbf{c}(t_0) = \mathbf{c}^0 \qquad \text{(C.8)}$$

An $N \times N$ matrix $\mathbf{A}$ is said to have an eigenvector $\mathbf{x}$ and corresponding eigenvalue λ if

$$\mathbf{A} \cdot \mathbf{x} = \lambda \cdot \mathbf{x} \qquad \text{(C.9)}$$

Obviously any multiple of an eigenvector $\mathbf{x}$ will also be an eigenvector; furthermore the zero vector is not consider to be an eigenvector at all. Evidently expression (C.9) can hold only if

$$\det|\mathbf{A} - \lambda \cdot \mathbf{I}| = 0 \qquad \text{(C.10)}$$

which, if expanded out, is an N^{th} degree polynomial in λ whose roots are the eigenvalues. This proves that there are always N (not necessarily real and distinct) eigenvalues (see section 11.0 of Press *et al.*, 1992).

Supposing that $\mathbf{V}^{-1} \cdot \mathbf{M} \cdot \mathbf{V} = \mathbf{D} = diag(\lambda_1, ..., \lambda_n)$, then changing variable $\mathbf{c} = \mathbf{V} \cdot \mathbf{z}$, satisfies $\frac{d\mathbf{c}}{dt} = \mathbf{V} \cdot \frac{d\mathbf{z}}{dt}$ because V is not time dependant, so

$$\mathbf{V} \cdot \frac{d\mathbf{z}}{dt} = \mathbf{M} \cdot (\mathbf{V} \cdot \mathbf{z}), \quad \text{with I.C.} \quad \mathbf{V} \cdot \mathbf{z}(t_0) = \mathbf{c}^0$$

.

But $\mathbf{V}^{-1}\cdot\mathbf{M}\cdot\mathbf{V}=\mathbf{D}$, so upon premultipling by $\mathbf{V}^{-1}$, one gets $\frac{d\mathbf{z}}{dt}=\mathbf{D}\cdot\mathbf{z}$ with the I.C. $\mathbf{z}(t_0)=\mathbf{z}^0$ where the new initial conditions are $\mathbf{z}^0=\mathbf{V}^{-1}\cdot\mathbf{c}^0=\begin{pmatrix} z_1^0 \\ \vdots \\ z_n^0 \end{pmatrix}$.

The equations represented by this diagonal system are

$$\begin{cases} \dfrac{dz_1}{dt}=\lambda_1\cdot z_1 \\ \quad\vdots \\ \dfrac{dz_n}{dt}=\lambda_n\cdot z_n \end{cases}, \qquad \begin{cases} z_1(t_0)=\mathrm{z}_1^0 \\ \quad\vdots \\ z_n(t_0)=\mathrm{z}_n^0 \end{cases} \tag{C.11}$$

Since $\frac{dz_i}{dt}$ depends only on z_i, the solution of the system is

$$\begin{cases} z_1(t)=\mathrm{z}_1^0\cdot\exp\left(\lambda_1(t-t_0)\right) \\ \quad\vdots \\ z_n(t)=\mathrm{z}_n^0\cdot\exp\left(\lambda_n(t-t_0)\right) \end{cases} \tag{C.12}$$

Hence, if $\mathbf{c}=\mathbf{V}\cdot\mathbf{z}$, then

$$\mathbf{c}(t)=\mathrm{z}_1^0\cdot\exp\left(\lambda_1(t-t_0)\right)\cdot\mathbf{v}_1+\ldots+\mathrm{z}_n^0\cdot\exp\left(\lambda_n(t-t_0)\right)\cdot\mathbf{v}_n \tag{C.13}$$

Where $\mathbf{v}_i$ are the columns of the matrix $\mathbf{V}$, which are also the eigenvectors of $\mathbf{M}$ (see section 9.1c of Maron, 1982)

This expression leads immediately to some useful information about the whole system. In fact for every time it is possible to define the state of the system (concentration distribution across the compartments) just as a simple vector. A possible initial injection point can be expressed with a vector $\mathbf{c}^0=(0,\ldots,0,1,0,\ldots 0)^T$; e.g. that means it is possible also to study the effect of the injection point on the mixing time only

changing the $\mathbf{c}^0$. Finally, the long mixing time behaviour is described by the slowest decaying eigenvectors (or smallest eigenvalues) of the matrix **M.**

1st Theory extension: CSTR Network with chemical reactions.

The theory above described concerns a simple network of interconnected tanks that exchange material flows. If a chemical reaction is present inside the reactors equation (C.4) becomes:

$$V_i \frac{dc_i}{dt} = \sum_{j \neq i} Q_{ji} c_j - c_i \sum_{j \neq i} Q_{ij} - V_i < r_a >_i, \qquad i = 1,...,n \tag{C.14}$$

Where $< r_a >_i$ is the rate of chemical reaction consuming the component per unit of volume. For simplicity, it is assumed to depend only on the concentration *C* and the temperature *T*. Common expressions for the rate of the reaction are of the form

$$< r_a >_i = c^n k \exp\left(-\frac{E_a}{RT} \right) \tag{C.15}$$

n is called the order of reaction. If a first order reaction is present and the temperature can be assumed constant, equation (C.14) can be rewritten in a simpler form:

$$\begin{aligned} V_i \frac{dc_i}{dt} &= \sum_{j \neq i} Q_{ji} c_j - c_i \sum_{j \neq i} Q_{ij} - V_i c_i k' \\ \frac{dc_i}{dt} &= \sum_{j \neq i} \frac{Q_{ji}}{V_i} c_j - \left(\sum_{j \neq i} Q_{ij} + k' \right) c_i \end{aligned}, \qquad i = 1,...,n \tag{C.16}$$

Where *k'* includes the exponential term. This system can be expressed in matrix form as follows:

$$\begin{aligned} \frac{d\mathbf{c}}{dt} &= \mathbf{M} \cdot \mathbf{c} - k' \cdot \mathbf{I} \cdot \mathbf{c} \\ &= (\mathbf{M} - k' \cdot \mathbf{I}) \cdot \mathbf{c} \end{aligned} \tag{C.17}$$

By letting $\mathbf{M'} = (\mathbf{M} - k' \cdot \mathbf{I})$ with λ' its eigenvalues can be written

$$|\mathbf{M'} - \lambda' \cdot \mathbf{I}| = |(\mathbf{M} - k' \cdot \mathbf{I}) - \lambda' \cdot \mathbf{I}| = |\mathbf{M} - (k' + \lambda') \cdot \mathbf{I}| \tag{C.18}$$

So the eigenvalues of a first order reaction system (at constant *T*) can be evaluated as $\lambda' = \lambda - k'$, where λ are the eigenvectors of the matrix describing the same system without chemical reaction inside, while *k'* is the rate constant of the chemical reaction.

2nd Theory extension: from mass to thermal energy balance.

For a general stirred tank without chemical reactions belonging at a network, it is possible to express the mass balance with equation (C.4).

$$V_i \frac{dc_i}{dt} = \sum_{j \neq i} Q_{ji} c_j - c_i \sum_{j \neq i} Q_{ij} \,, \quad i = 1,\ldots,n \tag{C.19}$$

If the same approach is used for thermal balance, it is possible to find a similar form for it (section 2.5 of Friedly, 1972)

$$C_P \rho V_i \frac{dT_i}{dt} = C_P \rho \sum_{j \neq i} Q_{ji} T_j - T_i C_P \rho \sum_{j \neq i} Q_{ij} \quad \text{that in matrix form becomes}$$
$$\frac{d\theta}{dt} = \mathbf{M} \cdot \theta \quad , \qquad i = 1,\ldots,n \tag{C.20}$$

Where C_P is the specific mass thermal coefficient and θ is the vector containing the T_i of every tank.

All the same considerations about the eigensystem applied to the mass balance can be here applied as well. The case where chemical reaction is present needs further studies, because the previous section assumed an isothermal process. That, of course, is not interesting for thermal balances.

Cases studied and Results

Case 1

The first case that has been studied concerns a simple closed network of CST. The network is a double loop of tanks, and there are exchange flows between a tank in one

loop and a tank in the other, which link the two loops. This simple network, shown in Figure C.1, has got n_1 tanks for the first loop and n_2 for the second one. Every tank can have a different volume, however the flow circulating around each loop has to be constant; also the two flows between tank 1 and tank n_1+1 have to be equal.

The matrix **M** containing all the flows has the following structure (for simplicity each tank has got unit volume):

$$\begin{pmatrix} -\sum Q_{ji} & & f_1 & & EF & \\ f_1 & \ddots & & & & \\ & \ddots & \ddots & & & \\ & & f_1 & -\sum Q_{ji} & & \\ EF & & & & -\sum Q_{ji} & & f_2 \\ & & & & f_2 & \ddots & \\ & & & & & \ddots & \ddots \\ & & & & & & f_2 & -\sum Q_{ji} \end{pmatrix} \quad \text{(C.21)}$$

where f_1 and f_2 are the flows inside the two loops, while EF are the two flows exchanged among the loops. For this system the main diagonal of the matrix is always equal to minus the sum of all the other components of the row. Every time a loop of CSTs appears in a system, it will be a block with the structure highlighted by the red

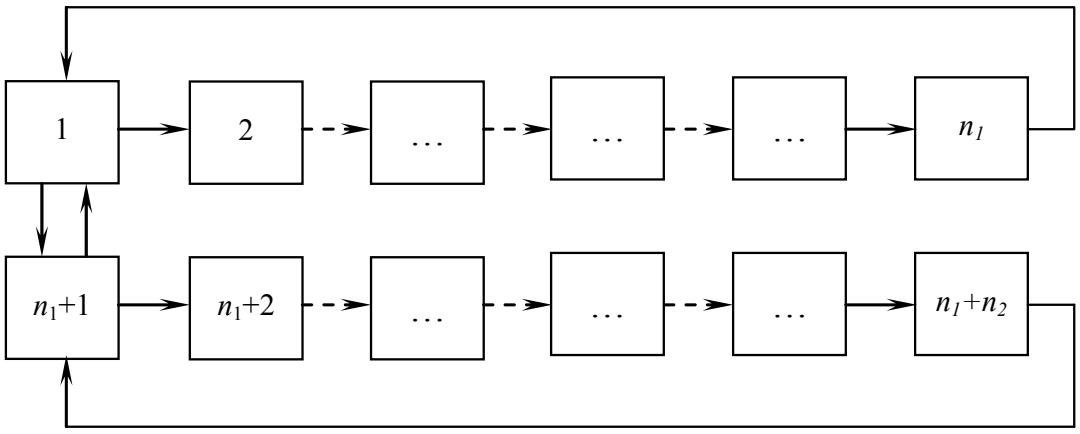

Figure C.1: 2 loop network of CSTs

square inside the matrix describing the system.

To find out the eigenvalues and the eigenvectors of the matrix **M**, at first a Visual basic (VBA) program was written for use in Excel (see chapter 11 of Press *et al.*, 1992). After that, aiming to reach a larger number of compartments, the use of `Matlab` was needed. In the following figure an example of a matrix and its eigensystem are reported (negative values are shown in red, and positive values in blue).

From this example the structure of the matrix of the flows is clear; furthermore it is also obvious that because the matrix M is non-Hermitian the eigenvalues can be both real and pairs of complex conjugates. For this type of system, it always happen that one eigenvalue, $\overline{\lambda}$, is zero and the associated eigenvector, $\overline{\mathbf{x}}$, has all its terms equal to 1:

This is the matrix of flows, consisting of a loop 1→2→3→4→5→1
another loop (6→7→8→9→10→6), which is faster, and
with fast exchange (1↔6). All the volumes are equal to 1 unit.

	-101	0	0	0	1	100	0	0	0	0
	1	-1	0	0	0	0	0	0	0	0
	0	1	-1	0	0	0	0	0	0	0
	0	0	1	-1	0	0	0	0	0	0
	0	0	0	1	-1	0	0	0	0	0
	100	0	0	0	0	-200	0	0	0	100
	0	0	0	0	0	100	-100	0	0	0
	0	0	0	0	0	0	100	-100	0	0
	0	0	0	0	0	0	0	100	-100	0
	0	0	0	0	0	0	0	0	100	-100

These are the eigenvectors (as columns), increasingly shortlived.

Eigenvalues										
Real	5E-15	-0.641	-0.641	-1.441	-1.441	-76.62	-76.62	-101	-199.5	-247.1
Imag	0	0.577	-0.577	0.377	-0.377	79.36	-79.36	0	0	0
	0.32	0.21	0.00	0.13	0.00	0.43	0.00	0.71	0.41	0.45
	0.32	0.04	0.28	-0.30	0.19	0.00	0.00	-0.01	0.00	0.00
	0.32	-0.40	0.44	0.40	-0.49	0.00	0.00	0.00	0.00	0.00
	0.32	-0.71	0.07	-0.15	0.72	0.00	0.00	0.00	0.00	0.00
	0.32	-0.24	-0.85	-0.78	-0.45	0.00	0.00	0.00	0.00	0.00
	0.32	0.22	0.01	0.14	0.00	0.17	-0.40	0.00	-0.40	-0.66
	0.32	0.22	0.01	0.14	0.00	0.43	0.01	0.00	0.41	0.45
	0.32	0.22	0.01	0.14	0.01	0.04	0.59	0.00	-0.41	-0.31
	0.32	0.22	0.01	0.14	0.01	-0.61	0.39	0.01	0.41	0.21
	0.32	0.22	0.01	0.14	0.01	-0.47	-0.59	-0.71	-0.41	-0.14

Figure C.2: An example of matrices describing a double loop system

$\begin{pmatrix} -\sum Q_{ji} & & \\ & \ddots & \\ & & -\sum Q_{ji} \end{pmatrix} \cdot \begin{pmatrix} 1 \\ \vdots \\ 1 \end{pmatrix} = \begin{pmatrix} 0 \\ \vdots \\ 0 \end{pmatrix}$, because for every row there is an element equal to minus the sum of all the others (the one on the diagonal). So by equation (C.9) can be written $\mathbf{A} \cdot \overline{\mathbf{x}} = 0 = \overline{\lambda} \cdot \overline{\mathbf{x}}$, which means $\overline{\lambda} = 0$.

Another interesting issue is the position of the eigenvalues on the real/complex plane. Starting from an easier system where instead of a double loop, a single loop is studied with a flow equal to *k*. The **M** matrix becomes:

$$\begin{pmatrix} -k & & & k \\ k & \ddots & & \\ & \ddots & \ddots & \\ & & k & -k \end{pmatrix} \qquad \text{(C.22)}$$

The eigenvalues are the solutions of

$$\begin{vmatrix} \lambda + k & & & -k \\ -k & \ddots & & \\ & \ddots & \ddots & \\ & & -k & \lambda + k \end{vmatrix} = 0 \qquad \text{(C.23)}$$

i.e. $(\lambda + k)^p - k^p = 0$

$$\lambda + k = \left(k^p\right)^{1/p}$$

whence $\lambda = -k + k\left(\cos\frac{2\pi m}{p} + j\sin\frac{2\pi m}{p}\right), \quad m = 1,2,...,p$.

The eigenvalues thus lie on a unit circle in the complex plane, with centre –*k* and radius *k,* as shown in Figure C.3. One eigenvalue is at the origin and for *p* even, one

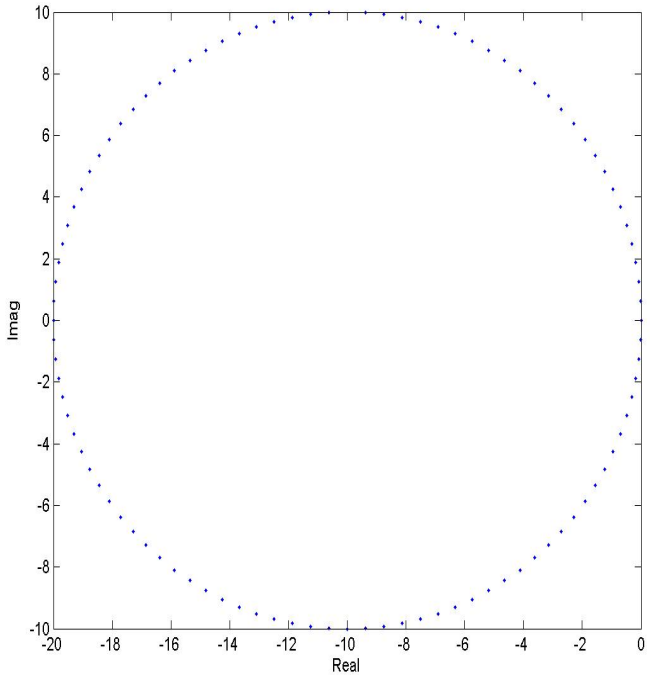

Figure C.3: Positions, on the complex plane, of the eigenvalues for a single loop system (shown for p = 100 and k = 10)

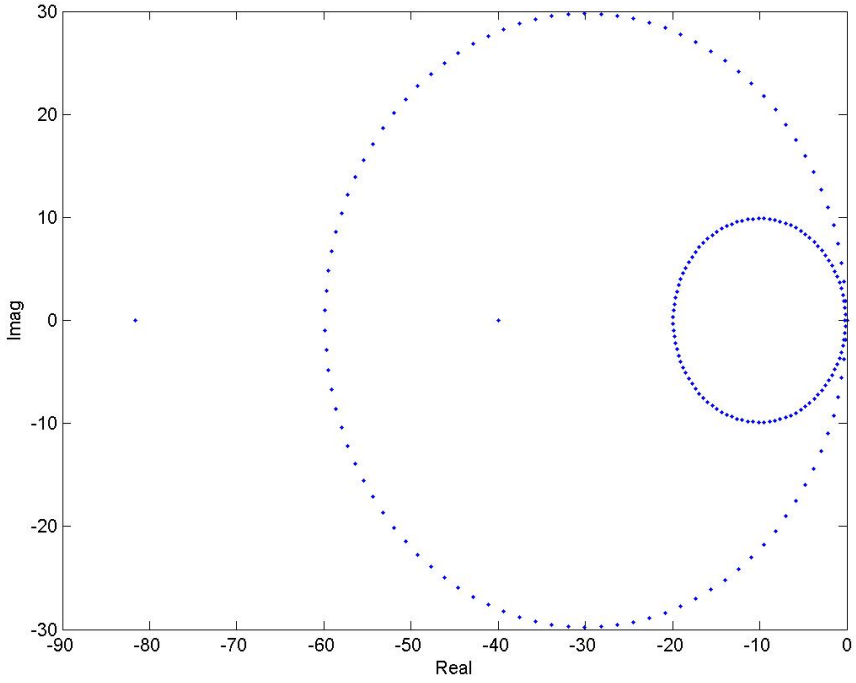

Figure C.4: Positions, on the complex plane, of the eigenvalues for a double loop system of Figure C.1 (shown for $f_1 = 10$, $f_2 = 30$ and $EF = 30$)

eigenvalue is equal to $-2k$; the remaining eigenvalues form complex conjugate pairs (see section 4.2.5 of Godfrey, 1983).

Passing to the study of the original system with double loops, it is possible to see how the property of the position of the eigenvalues is still kept, although the position of the circle is less clear. However, the radius is still equal to the flow rate, as shown in Figure C.4. Further studies should be focused on the full understanding of the position of the eigenvalues for the reason that they are quite simple to define, so it will be possible to deduce properties of the system simply by looking at their positions.

To check if this approach would work for the two-loop system, a concentration profile has been calculated and plotted as shown in Figure C.5. The previous graph has been plotted using equation (C.13); naturally that is possible only after having calculated the eigenvalues and the eigenvectors of the system. Concerning the initial conditions, the $\mathbf{c}^0$ has been chosen equal to $\mathbf{c}^0 = (0,1,0,\ldots 0)^T$, which simulates an injection point on the second CST of the network. The concentrations are normalized such that all concentrations will approach unity for $t \to \infty$. Again, naturally the curves concerning the second loop are not properly distinguishable because, with the second loop faster than the first, every introduction in the 11^{th} tank passes immediately to all the other CSTs belonging to the 2nd loop.

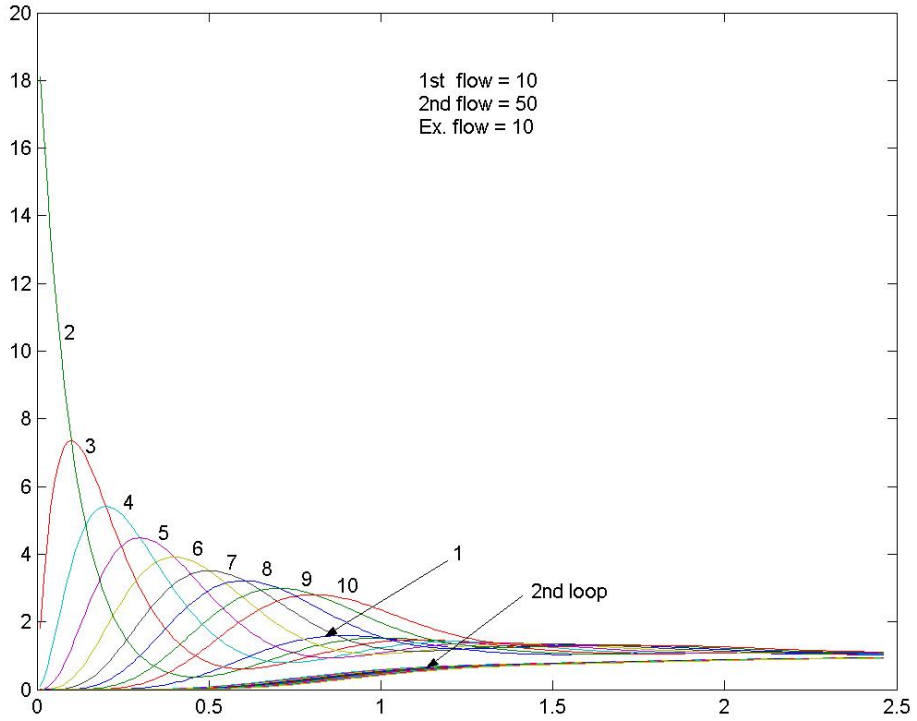

Figure C.5: Concentration profile of every CST of a double loop system (shown for $f_1 = 10$, $f_2 = 50$ and $EF = 10$, injection point on the 2nd tank)

Case 2.

The second case studied was intended to be closer to real processes and it concerns the model of the flow in a pipe. For simplicity, only a cross section of the pipe was analysed generating a 2D-network as shown in Figure C.6.

This is the case of an open system. It is possible to implement the eigensystem approach also in this case considering the environment as a further compartment (with a very large volume) which collects the outlet flows from the zones of the last column and donates the same total flow to the first column, as shown in Figure C.6. Supposing that the cell-to-cell interchange flow rates of every compartment are known, it is possible to create the matrix **M**.

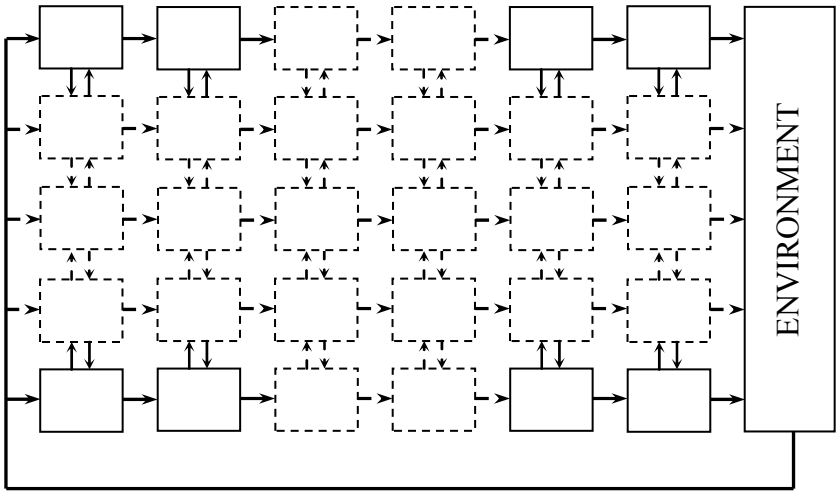

Figure C.6: 2D-network simulating a section of a flow in a pipe.

By letting *nc* and *nr* represent the numbers of columns and rows, respectively, of the network shown above, *MF* the main horizontal flow and, finally, *EF* the exchange flowrate between cells belonging to different rows; again, the matrix of the flowrates has got a particular structure, which can be summarized as follows:

$$\mathbf{M} = \left(\begin{array}{ccccc|c} \mathbf{A_r} & & & & \mathbf{0} & \mathbf{e} \\ \mathbf{B} & \mathbf{A_r} & & & & 0 \\ & \ddots & \ddots & & & \vdots \\ & & \mathbf{B} & \mathbf{A_r} & & \vdots \\ \mathbf{0} & & & \mathbf{B} & \mathbf{A_r} & 0 \\ \hline 0 & \cdots & \cdots & 0 & \mathbf{e}'/V_e & * \end{array}\right) \qquad \text{(C.24)}$$

where $\mathbf{A_r} = \begin{pmatrix} * & EF & & \\ EF & \ddots & \ddots & \\ & \ddots & \ddots & EF \\ & & EF & * \end{pmatrix}$ and $\mathbf{B} = \begin{pmatrix} MF & & \\ & \ddots & \\ & & MF \end{pmatrix}$; $* = -\sum Q_{ji}$, the

vector **e** has the dimension of *nr* and its element are all equal to *MF*. The blocks **Ar** and **B** have the dimension of *nr* by *nr,* while the number of times **Ar** appears in **M** is equal to *nc*.

In Figure C.7 the positions of the eigenvalues for a pipe system are shown with *nc* = 20 and *nr* = 3, 5, 7 and 10 respectively. From the previous case, it can be assumed that the

circles reveal the presence of the loops – actually, the number of the eigenvalues for each circle is equal to the number of columns of cells, and the total number of circles is equal to the number of rows. Furthermore, the radius of the little circles is not always the same. Like in the previous case, a full understanding of the radius and the position of the circles is a subject for future studies.

Further possible developments

The cases studied showed how this new approach to the modelling of mixing process can became an innovative and potentially useful tool in the description of real problems, though the this initial work needs a better insight, specially regarding the positions of

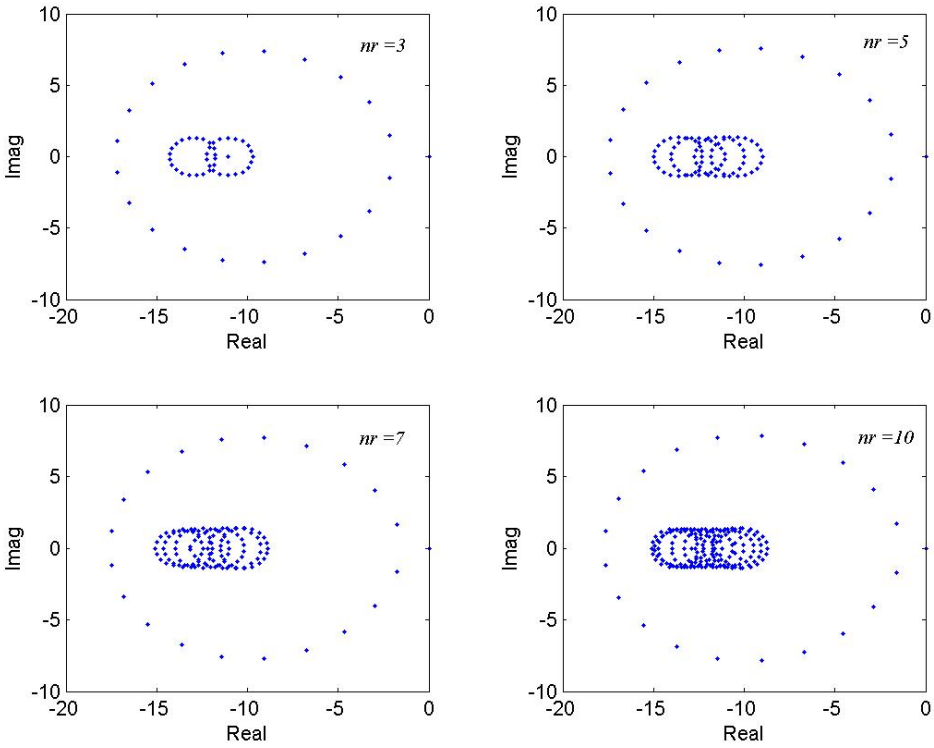

Figure C.7: Positions, on the complex plane, of the eigenvalues for the pipe system (shown for *nr* = 3,5,7,10 and *nc* = 20)

the eigenvalues in the complex plane.

In order to be able to apply the method to a real problem, a proper CST network should be defined. The next development of this study would be to create a natural way to generate that network of zones; in fact, both CFD and PIV/LDV create a file where a certain number of cells and the interchanged volumetric flow rates are collected. Starting from the simulated (CFD) or real (PIV/LDV) flow field of a mixing process, the eigensystem method will be developed. Thinking to the file mentioned above it is clear that the biggest limit of this new method lies in the dimension of the network, because the matrix **M** has always the dimension of the number of the cells (plus the environment cell if the system is open). To find all the eigenvalues and the eigenvectors of large matrices (up to 1,000,000 × 1,000,000 or more) requires huge computational efforts and/or special numerical methods based on advanced linear algebra. Two possible different approaches might be helpful in finding a good solution:

- as it can be observed in the simple cases already studied, the matrix **M** is sparse, which means it is almost full of zeros with few values. In addition, thinking of a more complex 3D-network, every cell cannot exchange flows with more than six other cells, which means every row of **M** will have all zeros apart from six values and the one on the diagonal. For the resolution of generalised eigenvalue problem for large sparse matrices, some particular numerical methods have been developed in the literature. `Arpack` (Lehoucq et al., 1998) and its `Matlab` counterpart (`eigs`) are packages of routines that calculate some eigenvalues of large non-symmetric sparse matrix by the implicit restarted Arnoldi's method. Some specific mathematical studies using this method have been implemented for matrices with dimension up to 400,000 (Duff and Scott, 1993; Scott, 1995).

- to avoid the management of really large matrices, a hybrid multizonal/CFD model can be developed (Rigopoulos and Jones, 2003; Bezzo et al., 2004). In mixing processes where the fluid dynamics operate on a faster time-scale than other phenomena, larger areas can be found with the same characteristics. Thus, it should be possible to simplify the original network grouping together more cells having the same main characteristics, hence reducing the dimension of **M**. A major issue in setting up this kind of model is the definition of a suitable network of zones. Bezzo and Macchietto, 2004, proposed some criteria to implement an automatic zoning system.

Finally, further work includes a study of how to extend the eigensystem approach to other fields or subjects apart from mixing, as already introduced in the section of the theory.